19th ANNUAL
UC Systemwide
Bioengineering Symposium

ABSTRACTS BOOK

June 21-23, 2018

Bioengineering
Institute of
California

Meeting Biomedical Needs with Cutting Edge Science and Technology

Hosted by

UCR

**Marlan and Rosemary Bourns
College of Engineering**
Bioengineering

Table of Contents

Edwards Lifesciences Foundation is proud to support the 19th Annual Bioengineering Symposium

Because Every Heartbeat Matters

Edwards.com/corporategiving
@EdwardsGiving

Edwards Lifesciences Foundation
One Edwards Way, Irvine CA 92614 USA
edwards.com

EDWARDS
LIFESCIENCES
FOUNDATION

Edwards

BOARD ROOM

MR 4   MR 5

BALLROOMS A AND B

MR 1   MR 2   MR 3

RESTROOM

CONCOURSE 101

ESCALATOR

PLAZA

ENTRANCE
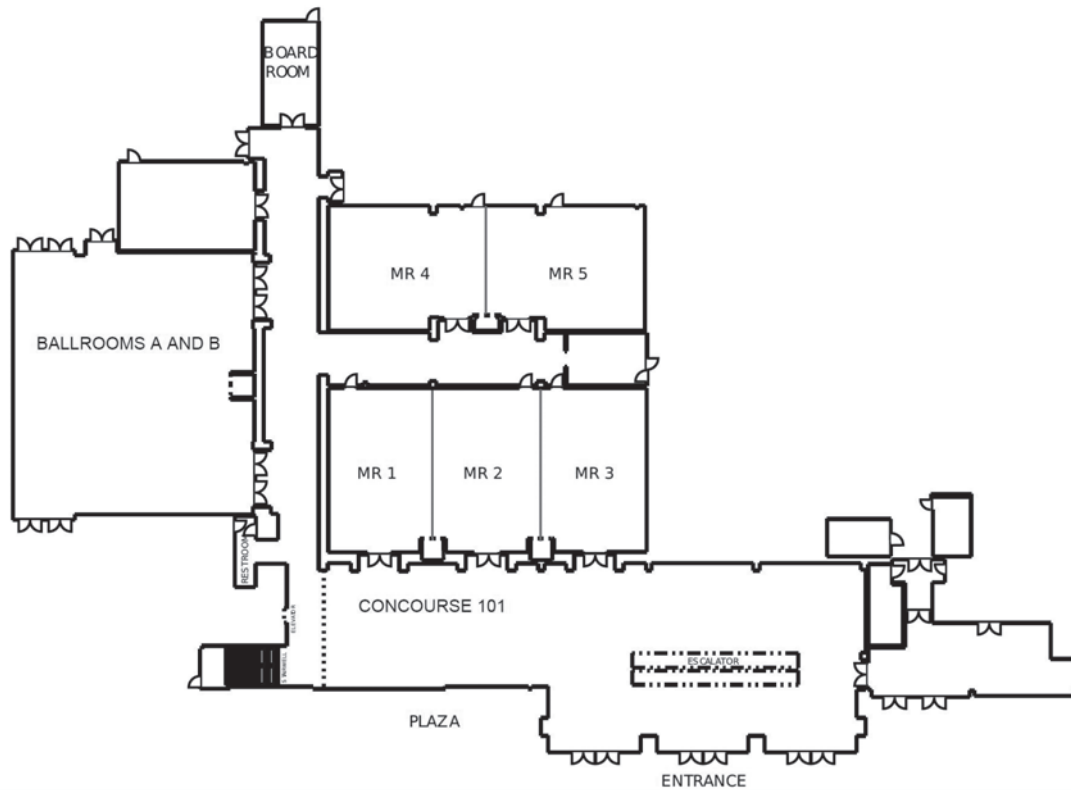
Poster Number Layout for MR 4 and MR 5

Thursday: Poster Session I   Friday: Poster Session II   Saturday: Poster Session III

Room Entrance

Thursday, June 21st

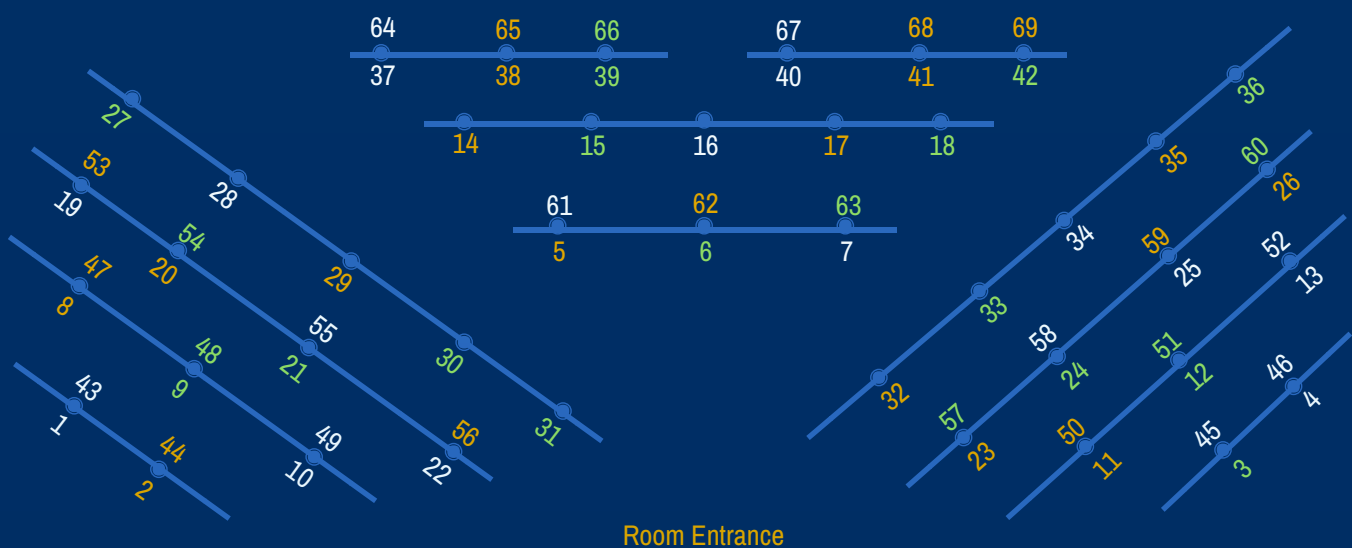|	
9:00 am – 5:00 pm	**Registration (Concourse 101)**
9:00 am – 11:00 am	**Exhibitor Setup (Concourse 101)**
11:00 am – 1:00 pm	**Poster Setup (MR 4 and MR 5)**
11:30 am – 1:00 pm	**Lunch (Concourse 101 and Plaza)**
1:00 pm – 1:20 pm	**Welcome Remarks (Ballrooms A and B)** Xiaoping Hu, Ph.D., Professor and Chair Department of Bioengineering, UC Riverside Chinya Ravishankar, Ph.D., Associate Dean, Research and Graduate Education UC Riverside Marlan and Rosemary Bourns College of Engineering Chris Lynch, Ph.D., Incoming Dean UC Riverside Marlan and Rosemary Bourns College of Engineering
1:20 pm – 2:10 pm	**Plenary Talk 1: Ed Boyden, Y. Eva Tan Professor in Neurotechnology, Massachusetts Institute of Technology (Ballrooms A and B)**
2:15 pm – 3:45 pm	**Computational Bioengineering (MR 1)** Chair: Dimitrios Morikis, UC Riverside Co-Chair: Justin Chartron, UC Riverside **Medical Devices and Instrumentation 1 (MR 2)** Chair: William Grover, UC Riverside Co-Chair: Victor G. J. Rodgers, UC Riverside **Biomaterials and Drug Delivery 1 (MR 3)** Chair: Huinan Liu, UC Riverside Co-Chair: Kaustabh Ghosh, UC Riverside **Molecular and Cellular Engineering 1 (Ballrooms A and B)** Chair: Jiayu Liao, UC Riverside Co-Chair: Jered Haun, UC Irvine
3:45 pm – 4:00 pm	**Break (Concourse 101 and Plaza)**
4:00 pm – 6:00 pm	**Poster Session I (MR 4 and MR 5)**
4:00 pm – 4:30 pm	**Rapid-Fire Poster Presentations (Ballrooms A and B)**
6:00 pm– 6:15 pm	**Break (Concourse 101 and Plaza)**
6:15 pm – 7:00 pm	**Plenary Talk 2: Milan Yager, Executive Director American Institute for Medical and Biological Engineering (Ballrooms A and B)**
6:00 pm – 8:00 pm	**Cash Bar (Concourse 101 and Plaza)**
7:00 pm – 9:00 pm	**Dinner (Concourse 101 and Plaza)**

2:15 pm – 3:45 pm	**Computational Bioengineering (MR 1)**
	Chair: Dimitrios Morikis, UC Riverside
	Co-Chair: Justin Chartron, UC Riverside
2:15 pm – 2:45 pm	Invited Speaker: Aaron Meyer, UC Los Angeles
	Dissecting Fcγ Receptor Regulation through a Multivalent Binding Model
2:45 pm – 3:00 pm	Jose Zamora, UC Merced
	ODE Modeling of Vascular Differentiation. Stochastic Spatial and Temporal Population-based Model for the Coemergence of Vascular Patterns
3:00 pm – 3:15 pm	Ali Nematbakhsh, UC Riverside
	Contribution of Cellular Mechanics on Morphology of Epithelia
3:15 pm – 3:30 pm	Danielle Behrens, UC Irvine
	A Conceptual Piezoelectric Sensor to Monitor Blood Flow in Coronary Stents
3:30 pm – 3:45 pm	J.J. Lawrence, UC San Diego
	Steady-streaming Effects on the Motion of the Cerebrospinal Fluid (CSF) in the Spinal Canal
2:15 pm – 3:45 pm	**Medical Devices and Instrumentation 1 (MR 2)**
	Chair: William Grover, UC Riverside
	Co-Chair: Victor G. J. Rodgers, UC Riverside
2:15 pm – 2:55 pm	Invited Speaker: Mohammad Al Faruque, UC Irvine
	Side-Channel Vulnerabilities of Cyber-Physical Systems in Biomedical Applications
2:55 pm – 3:15 pm	Harish Dixit, UC Riverside
	Achieving Cell Delivery of Exogenous Molecules Via Ultrahigh Throughput Mechanoporation
3:15 pm – 3:35 pm	M. Sinha, UC San Diego
	A Rapid Microbial Profiling Technology based on dPCR, DNA Melting, and Machine Learning
2:15 pm – 3:45 pm	**Biomaterials and Drug Delivery 1 (MR 3)**
	Chair: Huinan Liu, UC Riverside
	Co-Chair: Kaustabh Ghosh, UC Riverside
2:15 pm – 2:45 pm	The BIC Shu Chien Lecturer: Song Li, UC Los Angeles
	Reprogramming of Dermal Cells into Skeletal Muscle by Controlled Release of Small Molecules
2:45 pm – 3:00 pm	Jamal Lewis, UC Davis
	Epitope-functionalized Nanoparticles for Entrapment of Autism Autoantibodies
3:00 pm – 3:15 pm	J. T. Mac, UC Riverside
	Erythrocyte-derived Nano-constructs for Combined Chemo-photodestruction of Cancer Cells
3:15 pm – 3:30 pm	Noah Pacifici, UC Davis
	Responsive Two-fluorophore Reporter System: a Potential Tool to Monitor Particulate Vomocytosis
3:30 pm – 3:45 pm	J. Pazzani, UC Merced
	Using Cellulose Paper to Assemble and Load Cargo Into Polymersomes
2:15 pm – 3:45 pm	**Molecular and Cellular Engineering 1 (Ballrooms A and B)**
	Chair: Jiayu Liao, UC Riverside
	Co-Chair: Jered Haun, UC Irvine
2:15 pm – 2:30 pm	J. M. Corbin, UC Davis
	Process Development for Production of Recombinant Butyrylcholinesterase in Metabolically-regulated, Transgenic Rice Cell Suspension Cultures
2:30 pm – 2:45 pm	T. Lopez, UC Riverside
	Generation of Highly Selective Protease Inhibitory Antibodies by Function-based Selection
2:45 pm – 3:00 pm	A. Leung, UC Berkeley
	Introducing Antiterminator Paralog Genes to Activate the Expression of Biosynthetic Gene Clusters to Induce Production of Natural Products in Clostridium Species
3:00 pm – 3:15 pm	G. Way, UC Riverside
	Identification of Sumoylation Site of Influenza Virus Protein by FRET Technology
3:15 pm – 3:30 pm	Leland Howard, UC Davis
	Transgenic Expression of Type II Collagen for Tissue Engineering
3:30 pm – 3:45 pm	Z. Huang, UC San Diego
	A Light Inducible Gene Activation System Toward Controllable Cell-based Therapeutics

DISSECTING FCγ RECEPTOR REGULATION THROUGH A MULTIVALENT BINDING MODEL

[1]Ryan A. Robinett, [1]Ning Guan, [2]Anja Lux, [2]Markus Biburger, [2]Falk Nimmerjahn, [3]Aaron S. Meyer

[1]Koch Institute for Integrative Cancer Research, Massachusetts Institute of Technology, Cambridge, MA

[2]Division of Genetics, University of Erlangen-Nürnberg, Germany

[3]Department of Bioengineering, University of California, Los Angeles, CA; Contact: *ameyer@ucla.edu*

Introduction: Antibodies (Abs) are critical and central regulators of the immune response. Abs of the IgG isotype interact with Fcγ receptors (FcγRs) expressed widely on immune effector cells. IgG effector function occurs through multiple cell types (e.g. macrophages and monocytes) and through multiple processes (e.g. Ab-dependent cell-mediated cytotoxicity and cytokine response). IgGs operating through effector cell function are used in both cancer and autoimmune disease treatment. These biologic agents are particularly versatile therapeutic agents on account of their immunotherapeutic effects and ability to operate directly through antigen binding/opsonization. Quantitatively predicting IgG function would aid the understanding and treatment of cancer and autoimmune/infectious diseases.

Materials & Methods: Immune complex (IC) binding to FcγRs was analyzed using hFcγR-expressing CHO cells. FcγR expression was quantified using Abs against each FcγR and flow cytometry. Association constants for all combinations of IgG and FcγR were obtained from literature. All analysis was implemented in Python. TNP-BSA binding to FcγRs was modeled using a two-parameter equilibrium model of multivalent ICs binding to FcγRs expressed uniformly on a cell surface. We fit our model to binding measurements for each hFcγR-hIgG pair using an Markov chain Monte Carlo sampler. We assayed convergence using the Geweke diagnostic and autocorrelation. Using an assumed ligand concentration and valency, as well as mFcγR expression, activities of each cell population were calculated and regressed against *in vivo* effectiveness, represented as the percent reduction in the number of lung metastases, by least-squares.
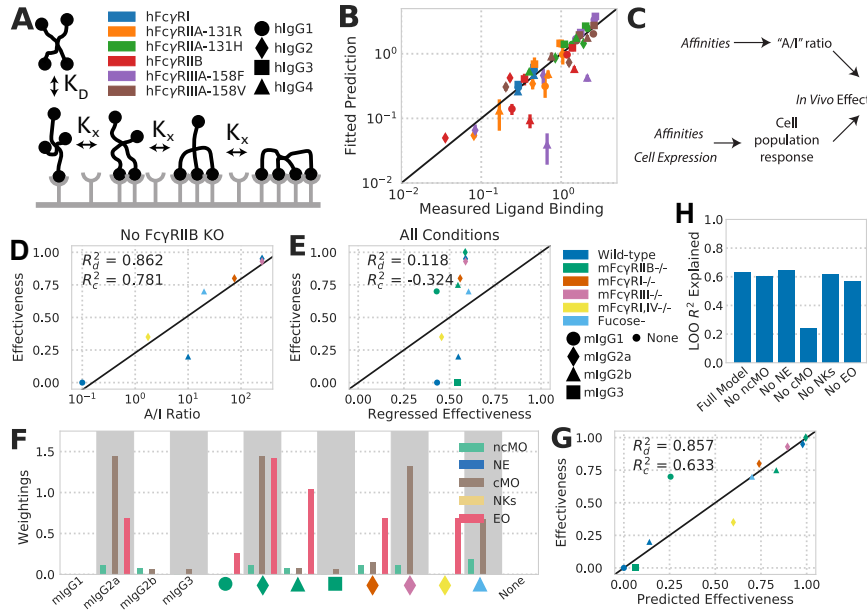
Figure 1: (A) Model schematic for single IgG IC-FcγR interaction. (B) Predicted vs. measured binding for each hFcγR-hIgG pair and valency. (C) Schematic of earlier IgG subclass experiments (top) and our approach (bottom). (D) Effectiveness of individual IgG treatments vs. A/I ratio for each IgG. (E) Predicted vs. regressed effectiveness of A/I ratio for IgG treatments upon FcγR knockout. (F) Individual activities calculated for each treatments using multimerization predicted by multivalent binding model (scaled by regression model fit). (G) Effectiveness predicted vs. actual using the multivalent binding model. (H) Model prediction R^2 with individual populations removed. R_d^2 and R_c^2 represent R^2 upon fitting or cross-validation, respectively.

Results & Discussion: IC binding to CHO cells expressing each single FcγR was quantified and then fit to a two-component binding model (A-B). With confidence that such a model could predict IC binding to FcγR-expressing cells, we then applied the model to predict *in vivo* effector function in the B16F10 melanoma model. An A/I ratio, or ratio of activating to inhibitory receptor affinity, has previously been used for predicting the effect of IgG treatments (C). While the A/I ratio could predict treatment efficacy in conditions where it has been previously applied, we observed that it failed to predict a wider panel of interventions (D-E). In contrast, our model was able to predict outcome in this wider panel, and implicated classical monocytes as a critical cell population, as has been validated by *in vivo* experiments (F-H).

Conclusions: A unified multivalent binding model accounting for IC valency and affinity provides a framework for reasoning about how IC binding is affected by changing antibody-antigen binding or constant region composition. In addition to enabling rationally designed immunotherapeutic interventions, our model of IC engagement makes it feasible to infer the factors contributing to the *in vivo* efficacy of existing immunotherapies. More generally, these results demonstrate the ability of molecular models linked to data-driven inference to deconvolve *in vivo* function.

STOCHASTIC SPATIAL AND TEMPORAL POPULATION-BASED MODEL FOR THE CO-EMERGENCE OF VASCULAR PATTERNS

[1]Jose Zamora, [2]Ajay Gopinathan, [3]Kara E. McCloskey
[1]Graduate Program in Biological Engineering and Small-scale Technologies (BEST), University of California Merced
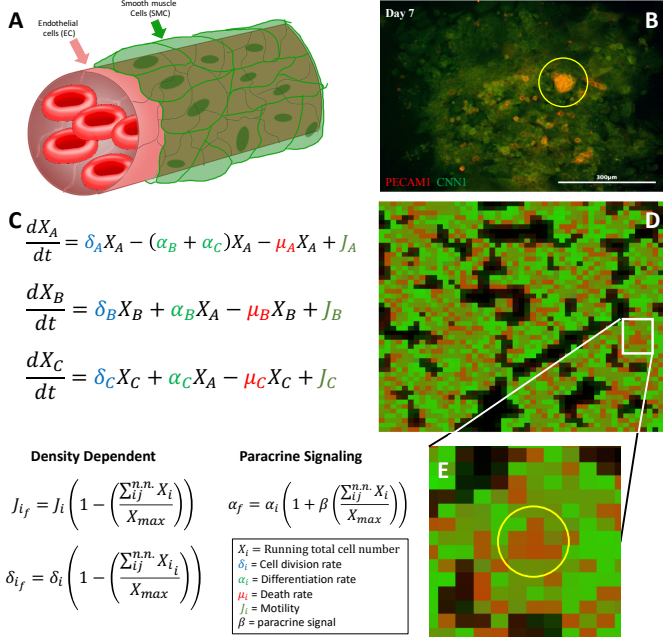[2]School of Natural Sciences, University of California Merced
[3]School of Engineering, University of California Merced

Introduction: Stem cells differentiation is often examined as cell responding to biochemical signals in two-dimensional (2D) cultures. However, cellular microenvironment in vivo is a much more complex 3D environment with multiple cell types and materials. To that end, we have developed a computational model that incorporates multiple cell types, as well as, biochemical and physical cues in directing stem cell differentiation in order to explore the relationship and co-emergence and spatial patterning of two cell types; endothelial cells (EC) and vascular smooth muscle cells (vSMC) from a common vascular progenitor cell.

Materials and Methods: Our spatio-temporal computational model consists of three differential equations for three changing cell populations; VPC (X_A), EC (X_B), and vSMC (X_C). Within these equations, we account for cell division (δ_i), differentiation (α_i), cell death (μ_i), motility (J_i). Additionally, functions that measured cell density and signaling from adjacent cells were added as functions of motility, cell division, and differentiation (see Fig. 1). In Matlab, the growth of the cell populations are tracked overtime, resulting in videos of the 2D cell patterns evolving in time. Empirical data was first used to estimate values for the variables, followed by regression analysis techniques to find true values that are analogous to experimental conditions. Lastly, phase space sweeps were conducted to determine which variables lead to the development of micropatterns.

Results and Discussion: The current model is able to reproduce experimental patterns (see Fig. 1). Results show that the cell segregated spatial pattern can be recreated using a few different input combinations. When analyzing phase space, we discovered that a well-defined step function emerged when varying the motility and division variable; indicating a region where micropatterning will form and a region where one cell type will out preform the other (data not shown). This was not true for the differentiation variable; indicating that differentiation does not play as significant role in cell pattern formations. This trend held true for conditions that did and did not included density sensing and/or paracrine signaling.

$$\frac{dX_A}{dt} = \delta_A X_A - (\alpha_B + \alpha_C)X_A - \mu_A X_A + J_A$$

$$\frac{dX_B}{dt} = \delta_B X_B + \alpha_B X_A - \mu_B X_B + J_B$$

$$\frac{dX_C}{dt} = \delta_C X_C + \alpha_C X_A - \mu_C X_C + J_C$$

Density Dependent

$$J_{i_f} = J_i\left(1 - \left(\frac{\sum_{ij}^{n.n.} X_i}{X_{max}}\right)\right)$$

$$\delta_{i_f} = \delta_i\left(1 - \left(\frac{\sum_{ij}^{n.n.} X_{i_i}}{X_{max}}\right)\right)$$

Paracrine Signaling

$$\alpha_f = \alpha_i\left(1 + \beta\left(\frac{\sum_{ij}^{n.n.} X_i}{X_{max}}\right)\right)$$

X_i = Running total cell number
δ_i = Cell division rate
α_i = Differentiation rate
μ_i = Death rate
J_i = Motility
β = paracrine signal

Fig 1. Computational Model. A) The 3D structure of a blood vessel with EC shown red and SMCs in green. B) Two-dimensional cell outgrowths from vascular progenitor cells (day 7 of total differentiation, day 4 since VPC differentiation) showing a cluster of EC (PECAM-1, red) surrounded by vSMCs (green). C) The differential equations used to calculate the evolution of the cell types; progenitor cell (X_A), EC (X_B), vSMC (X_C). Variables rates include cell division (δ_i), differentiation (α_i), cell death (μ_i), motility (J_i), paracrine signaling (β_i). Also, additional regulations to determine density influence and paracrine signaling influence. n.n. = nearest neighbors D) Results show that after 96 iterations (simulated hrs), equivalent to a 4-day differentiation and comparable to image in Figure 1B.

Conclusions: Our co-culture experiments indicate self-patterning during differentiation of ECs and vSMCs from VPCs. A computational model was developed that recapitulates this spatio-temporal phenomenon. Simulations suggest that the patterning is to due to self-sorting after differentiation rather than neighboring cell-directed differentiation.

CONTRIBUTION OF CELLULAR MECHANICS ON MORPHOLOGY OF EPITHELIA

[1]A. Nematbakhsh, [2]J. Janugula, [1]W. Chen, [2]J. Zartman, and [1]M. Alber

[1]Department of Mathematics, University of California, Riverside, CA

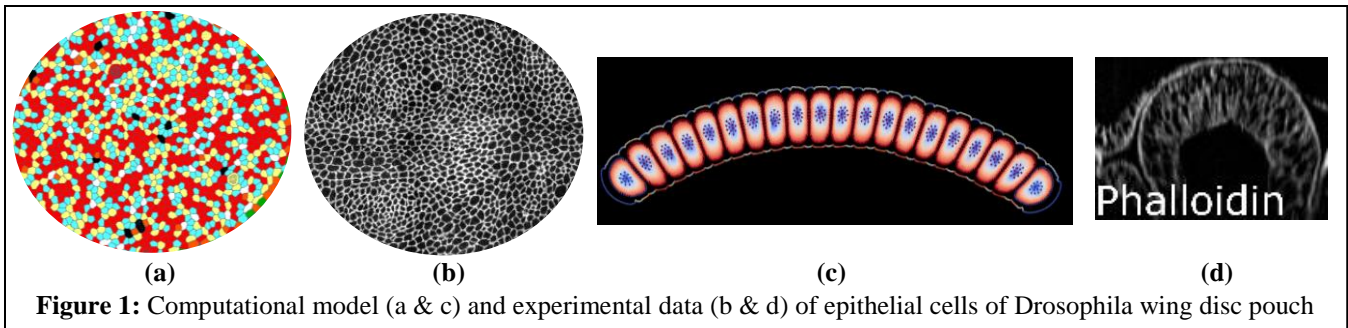[2]Department of Chemical and Biomolecular Engineering, University of Notre Dame, Notre Dame, IN

Contact: *jeremiah.zartman.3@nd.edu & mark.alber@ucr.edu*

Introduction: Epithelia serve as barriers between the environment and internal structures of organs. Epithelial morphogenesis and growth must be carefully controlled through coordination of cellular properties to specify organ shape and function. This is critical because uncontrolled epithelial growth is the underlying cause of more than ninety percent of tumors. However, how mechanical properties of epithelia are patterned and contribute to the overall tissue morphology of tissue is still poorly understood. Here, we introduce an advanced subcellular element model incorporating cytoplasmic pressure, cell-cell adhesion, and nuclear positioning to simulate epithelial cell mechanics. In this model, force contributions of the extracellular matrix have also been taken into account. We investigated the contribution of each of these cellular properties to the size and shape of cells and tissue. Simulation results considering apical side of epithelial cells revealed that cytoplasmic pressure is the main driver of cell area expansion in mitotic phase, while cortical stiffness and cell-cell adhesion promote cell rounding before division. This model has recently been expanded to study cross-section of epithelia cells as well to predict the underlining mechanism driving the curvature profile of tissue. It has been shown that a critical ratio of apical to basal contractility gave rise to the curvature profile obtained from experiments. Simulations results are calibrated and verified with experimental data obtained from epithelial cells of *Drosophila* imaginal wing disc, a valuable model to study epithelial tissue.

Materials and Methods: A subcellular element computational model used here is composed of three different type of nodes: nuclear nodes, representing the nucleus, membrane nodes, representing the lipid bilayer and cortical stiffness of the cells, and ECM nodes that represent extra cellular matrix. Cytoplasmic volume is modeled using the Lagrangian multiplier technique. These elements are interacting with each other by potential energy functions and Langevin equations are used to advance the system in time.

Experimental images of wing discs were obtained using confocal microscopy of organs cultured ex vivo. Wing discs were stained with the actin marker, phalloidin, to enable visualization of cell boundaries. The apical and basal surfaces were segmented, and a circle was fitted to the coordinates of each surface. Global curvatures were calculated as the inverse of the radii of these fitted circles.

Results and Discussion: The subcellular element model has been used to study epithelial cells shapes of *Drosophila* imaginal wing disc from apical surface (Figure 1a) and results are compared with experimental data (Figure 1b). It has been shown that pressure is dominant factor on the expansion size of mitotic cells, while adhesion and cortical stiffness are responsible for roundness of mitotic cells. Also by studying cross sectional profile of the epithelial cells (Figure 1c) and comparing with experimental data (Figure 1d), it has been shown that pattern in the contraction level can give rise the right curvature profile of epithelial cells.

(a)   **(b)**   **(c)**   **(d)**

Figure 1: Computational model (a & c) and experimental data (b & d) of epithelial cells of Drosophila wing disc pouch

Conclusions: The results from apical surface of epithelia have shown that increase in cytoplasmic pressure is the main driver of expansion of cells in mitotic phase, while variation in cell-cell adhesion and cortical stiffness contribute to the roundness of mitotic cells. Also the results from the cross-section of epithelial cells revealed that difference in apical versus basal contraction level of epithelia can give rise to the global curvature profile measured experimentally for *Drosophila* wing disc.

A CONCEPTUAL PIEZOELECTRIC SENSOR TO MONITOR BLOOD FLOW IN CORONARY STENTS

D. M. Behrens, W. J. Agnew, A. Kheradvar, W. C. Tang.
UC Irvine Department of Biomedical Engineering
Contact: dbehrens@uci.edu, wagnew@uci.edu, araskhk@uci.edu, wctang@uci.edu

Introduction: After implanting a stent, re-occlusion of coronary arteries presents a severe risk and it would be advantageous to measure the blood flow through the stent in real time to detect potential re-occlusion. Here, we propose incorporating piezoelectric cantilevers at the beginning and end of an arterial stent, and by measuring the voltage generated, we aim to calculate the blood velocity and characterize the flow.

Materials and Methods: To test a concept coronary artery flow velocity in the event of mild to moderate stenosis as well as the normal patient data were adopted from literature. The pressure drop from the beginning to end of a 15.45 mm stent, the average stent length [2], was calculated based on both a laminar flow model and a pulsatile flow in a rigid tube, assuming the stent creates a rigid wall scenario. This pressure drop was then used to calculate the expected voltage difference from two piezoelectric cantilevers made of Polyvinylidene difluoride (PVDF). Cantilevers were considered such that with two boundary plates, assuming a capacitor model [1]. Cantilever geometry were assumed to be: 1000 x 100 x 100 µm. Then by using the following equation we associated pressure changes with voltage:

$$V = \sigma dt/e,$$

where V is voltage generated, σ is the stress exerted on the cantilever, d and e are piezoelectric properties. This equation was obtained from [1] by taking equations (11) and (14) and solving for voltage. We can then calculate the pressure difference, ΔP, across the tube from equations 3.3.6 and 3.4.1 for the steady state flow and equations 4.6.1 and 5.5.1 from [2], we arrive at the following equations for ΔP:

$$\Delta P_{steady\ state} = 4v_{max} * \mu * \frac{L^2}{a^2}, \qquad and \qquad \Delta P_{puslatile\ flow} = \frac{v_{max} * \mu * \Omega^2 * L}{i * a^2 \left(1 - J_0\left(\frac{i-1}{\sqrt{2}} * \Omega\right)^{-1}\right)},$$

where v_{max} is maximum velocity, μ is blood viscosity, L is the length of the stent, a is radius of the artery, and Ω is the Womersley number. By assuming that the pressure drop $kL = \sigma$, we can solve for expected voltage.

Results and Discussions: Our results demonstrate that given a maximum blood velocity and assuming either laminar or pulsatile flow, we can predict the voltage difference between the two cantilever sensors in µV, a measurable value.

Table 1. Demonstrating the resulting µV & Pa difference across cantilevers given different flow assumptions across three different conditions.

Resulting Voltage and Pressure Differences		Assumption Used			
		Pulsatile Flow Assumption		Laminar Flow Assumption	
		Diseased Patients	Healthy Patients	Diseased Patients	Healthy Patients
Minimumal Voltage Difference	Voltage Difference [µV]	112.45	56.23	333.94	166.97
	Pressure Difference [Pa]	-3.61	-1.81	-10.73	-5.36
Average Voltage Difference	Voltage Difference [µV]	351.53	351.53	744.03	608.75
	Pressure Difference [Pa]	-11.29	-9.24	-23.90	-19.55
Maximumal Voltage Difference	Voltage Difference [µV]	915.54	894.74	1625.36	1588.42
	Pressure Difference [Pa]	-29.41	-28.74	-52.21	-51.02

Minimal and maximal conditions were chosen to optimize these voltage conditions. In the case of minimal voltage difference, the lowest measured blood velocity was computed along with the largest artery diameter to stress test the model, vice versa for the maximal condition.

Conclusions: Through our preliminary calculations, we have proposed a proof of concept for a piezoelectric dual cantilever pressure sensor to detect variations in blood flow patterns through a coronary artery stent. Based on our calculations, changes in blood flow should produce a measurable voltage difference. This is a stepping stone to perform more sophisticated experimental and computational studies with the aim of developing a sensor that can monitor stent re-occlusions.

References:
1. Sirohi, Jayant, and Inderjit Chopra. "Fundamental Understanding of Piezoelectric Strain Sensors." Smart Structures and Materials 1999: Smart Structures and Integrated Systems, 1999, doi:10.1117/12.350731.
2. Dilmanian, Hajir, et al. "The Average Stent Length is Longer and the Average Stent Diameter is shorter in Patients with Drug-Eluting Stents versus Bare-Metals Stents During Percutaneous Coronary Intervention." American Journal of Therapeutics. 14(3):277-279, May 2007.
3. Zamir, M. The Physics of Pulsatile Flow. AIP Press, 2000.

STEADY-STREAMING EFFECTS ON THE MOTION OF THE CEREBROSPINAL FLUID (CSF) IN THE SPINAL CANAL

[1]J. J. Lawrence, [1]W. Coenen, [1]A. L. Sánchez, [1,2]J. C. Lasheras
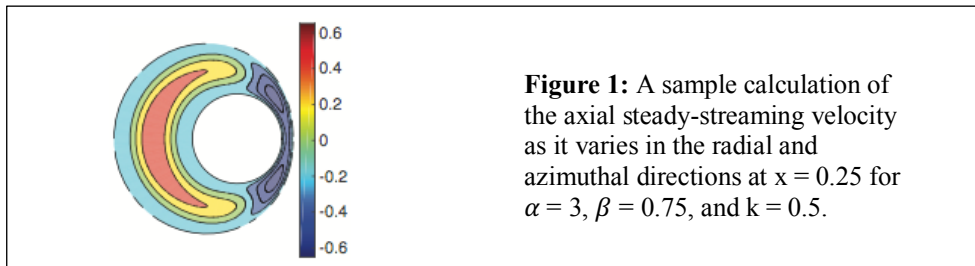[1]Deparment of Mechanical and Aerospace Engineering, University of California, San Diego, CA
[4]Deparment of Bioengineering, University of California, San Diego, CA
Contact: jjlawren@eng.ucsd.edu

Introduction: With each heartbeat the oscillatory blood supply to the rigid cranial vault produces a time-periodic variation of the intracranial pressure that drives the cerebrospinal fluid (CSF) periodically in and out of the compliant spinal canal, which is a main driving force for CSF motion in the spinal canal. However, despite radiological measurements by Di Chiro (1964) and many others which confirm the bulk circulation of CSF in the spinal canal, there has been no comprehensive physical explanation for the mechanism responsible for such a bulk motion. Understanding this mechanism has important implications in optimizing targeted drug delivery systems to the intrathecal space and in improving the current understanding of the etiology of a large class of neurological conditions.

Materials and Methods: The theoretical portion of this work was done by hand, with computations done in MATLAB using several built-in numerical integration methods. Additionally, the results are computed without a mesh using Chebyshev polynomials so that further manipulations are quick and accurate. The experimental portion of this work utilized particle image velocimetry with silver-coated microparticles as well as a CCD camera with a resolution of 2000×2000 pixels and fluorescent dye.

Results and Discussion: We take a simple model of the subarachnoid space as the volume between two eccentric cylinders, with an open top and closed distal end, imposing a periodic pressure gradient at the open end to model the pressure in the brain. For a large Strouhal number ($St = 1/\varepsilon \gg 1$), we asymptotically expand in ε and compute the resulting leading-order and first-order flow. We find that the steady-streaming motion associated with this periodic flow, resulting from the cumulative nonlinear effects of convective acceleration, causes steady motion of CSF inside the spinal canal. A sample calculation of the steady-streaming flow is shown in figure 1, where the negative velocity on the wide side of the canal indicates bulk motion toward the brain and the positive velocity on the narrow side indicates bulk motion toward the sacrum, matching the trends shown in experiments.

Figure 1: A sample calculation of the axial steady-streaming velocity as it varies in the radial and azimuthal directions at x = 0.25 for $\alpha = 3$, $\beta = 0.75$, and k = 0.5.

Conclusions: We have shown that the small pressure pulsation imposed at the entrance results in an oscillatory motion whose amplitude decreases along the length of the compliant canal. These results match MRI data from human subjects which shows velocities at the entrance that are approximately 1-2 cm/s. We have also demonstrated that this oscillatory motion induces a steady-streaming motion with velocities two orders of magnitude smaller, establishing a slower bulk motion. These results match radionuclide cisternography data which estimates that the bulk motion occurs with velocities that are roughly 1-2 cm/min. Therefore, we suggest that steady-streaming is a possible mechanism for the net CSF motion in the spinal canal.

SIDE-CHANNEL VULNERABILITIES OF CYBER-PHYSICAL SYSTEMS IN BIOMEDICAL APPLICATIONS

[1]Mohammad Abdullah Al Faruque,

[1]Department of Electrical Engineering and Computer Science, University of California, Irvine, CA

Contact: alfaruqu@uci.edu

Introduction:

In recent years, emergence of automation in biomedical science through Cyber-Physical Systems (CPS) has resulted in tremendous advancements. For instance, 3D printing technologies are revolutionizing medicine by allowing customization for prosthetics development and tissue engineering, while low cost oligonucleotides synthesized by fully automated DNA synthesizers are providing solutions for treating variety of diseases. However, systems with cyber-domain processes and physical-domain components are prone to security breaches like any other computing system. To this end, we present a novel attack methodology which can be used to steal the sensitive information often incorporated with using such machine through unintended emissions (also known as side-channels) from the machine. By identifying these type of vulnerabilities, we hope to encourage commercial biomedical equipment manufacturers to strengthen their products confidentiality.

Materials and Methods:

The approach that we use to attack the corresponding CPS consist of two phases: the training phase and the attack phase. In the training phase, we profile the CPS into a statistical model by providing labels for each emitted acoustic signal from the machine, and then in the attack phase, the model predicts the labels (sensitive data) for a given signal. In both phases, we apply signal segmentation and feature extraction to magnify the information carried in the emitted signals. We carry the presented attack over Printrbot Simple Maker 3D printer and Applied Biosystems 3400 DNA synthesizer.

Results and Discussion: The results of applying the presented attack methodology over the 3D printer shows that an attacker can reconstruct a 3D printed object by 92.54% accuracy for the axis prediction and 6.35% error on length prediction for a given object such as key. Also, the results show that the attack methodology can predict the order and type of bases in a synthesized DNA sequence by 88.07% accuracy on average.
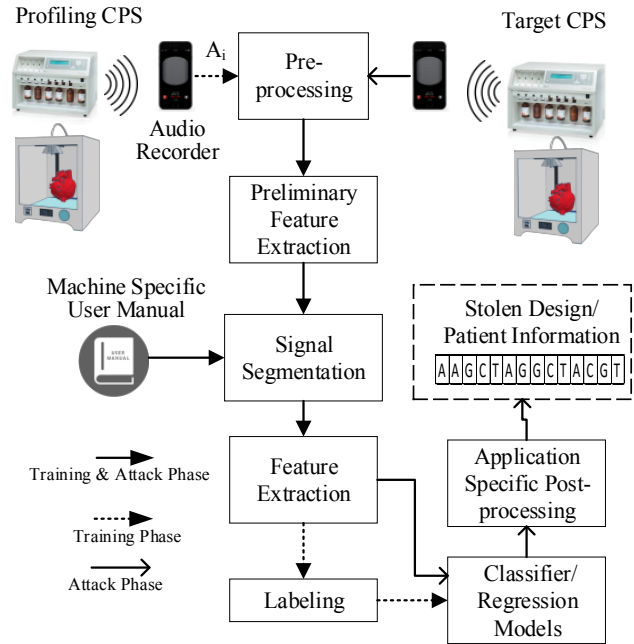
Figure 1: Side-channel attack methodology
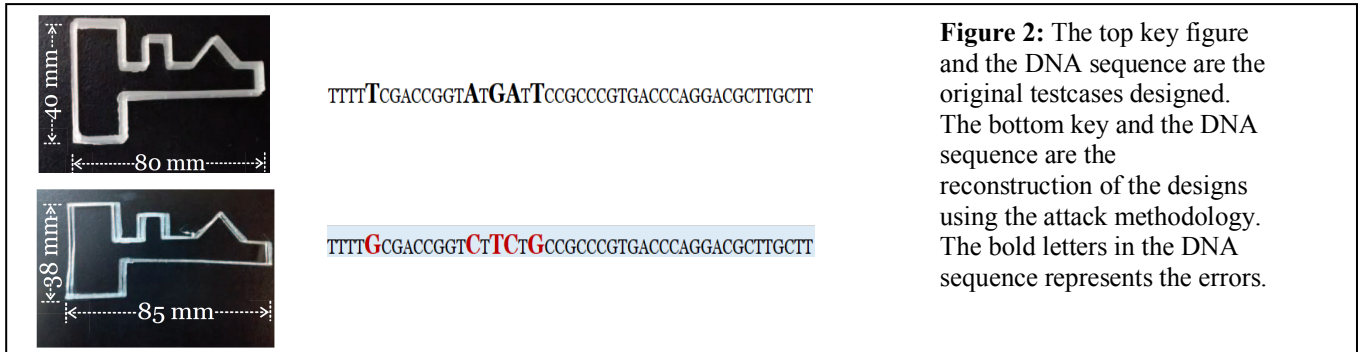
Figure 2: The top key figure and the DNA sequence are the original testcases designed. The bottom key and the DNA sequence are the reconstruction of the designs using the attack methodology. The bold letters in the DNA sequence represents the errors.

Conclusions: The results presented here show existence of side-channel confidentiality vulnerabilities in the CPS used in biomedical application.

ACHIEVING CELL DELIVERY OF EXOGENOUS MOLECULES VIA ULTRAHIGH THROUGHPUT MECHANOPORATION

[1]Harish G. Dixit, [2,3]Renate Starr, [1]Daniel Nampe, [4]Yanyan Zhang, [5]Christopher B. Ballas, [1,4]Hideaki Tsutsui, [2,3]Christine Brown, [2,3]Stephen J. Forman, and [1,4]Masaru P. Rao

[1] Department of Bioengineering, University of California – Riverside, Riverside, CA, USA
[2] Department of Cancer Immunotherapy and Tumor Immunology, City of Hope – Duarte, CA, USA
[3] Department of Hematology and Hematopoietic Cell Transplantation, City of Hope – Duarte, CA, USA
[4] Department of Mechanical Engineering, University of California – Riverside, Riverside, CA
[5] Division of Hematology/Oncology, Indiana University School of Medicine – Indianapolis, IN, USA

Introduction: Cancer immunotherapies have had promising clinical results and show great potential as an alternative to chemotherapy or radiation. However, the methods used to genetically engineer cancer fighting T lymphocytes possess limitations in automation and cost. There is a critical need for the development of a new cell modification strategy that addresses these shortcomings. Microinjection, which physically punctures the cell membrane for delivery of molecules, may represent the basis of an effective solution, but is limited in throughput.

We outline preliminary efforts to develop a new form of microinjection using silicon microfabrication. As a proof-of-concept, we have created a device for ultrahigh throughput (UHT) cellular manipulation via mechanical membrane poration, i.e. UHT mechanoporation. This technology represents an interim step towards our overall microinjection concept. Primary device operation stems from a microelectromechanical systems (MEMS) functional core composed of cell capture sites with integrated, sub-micrometer scale solid penetrators. The transient nature of membrane disruption enables transfection via diffusion-driven influx of exogenous molecules, while parallelization provides for UHT operation (e.g. 10k capture sites in the current device).

Materials and Methods: We use a combination of photolithography, reactive ion etching (RIE), and deep reactive ion etching (DRIE) to realize our micron scale and sub-micron scale UHT mechanoporation device features [Fig 1(a)]. Device testing on Jurkat cells is completed using a custom designed housing capable of integrating with an upright fluorescence microscope and a syringe pump for precise device control, and real time monitoring of cell testing. Successfully treated cells are assayed for viability and cell treatment efficiency across various time regimes using a combination of fluorescent molecules and plasmids (calcein AM blue, propidium iodide, and green fluorescent protein) via flow cytometry.

Results and Discussion: Our preliminary studies validated concept feasibility, but resulted in low cell delivery efficiencies (~8%). The implementation of high-resolution fluorescence imaging during device operation and precise flow rate control has provided a means for improved device characterization. Through our efforts, we have been able to increase our efficiencies by optimizing several device parameters, and have thus improved our delivery efficiency for recovered cells at 30-minute (~90%) [Fig. 1(b)] and 12-hour time points (~90%) [Fig. 1(c)].
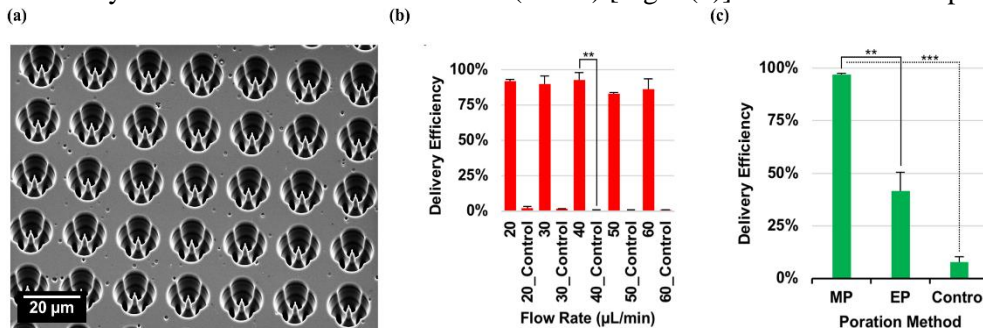
Figure 1. (a) Scanning electron image of our device array. **(b)** Delivery efficiency of propidium iodide into Jurkat cells across a range of aspiration flow rates. **(c)** Delivery efficiency of GFP into Jurkat cells using optimum parameters, compared to electroporation.

Conclusions: The results from our optimization studies demonstrate effective molecule delivery to cells using the UHT mechanoporation device. They indicate high delivery efficiencies across our parameter window. However, we observed a low efficiency of cell recovery from the device. Our results thus identify directions for the future development of the UHT mechanoporation device.

A RAPID MICROBIAL PROFILING TECHNOLOGY BASED ON DPCR, DNA MELTING AND MACHINE LEARNING

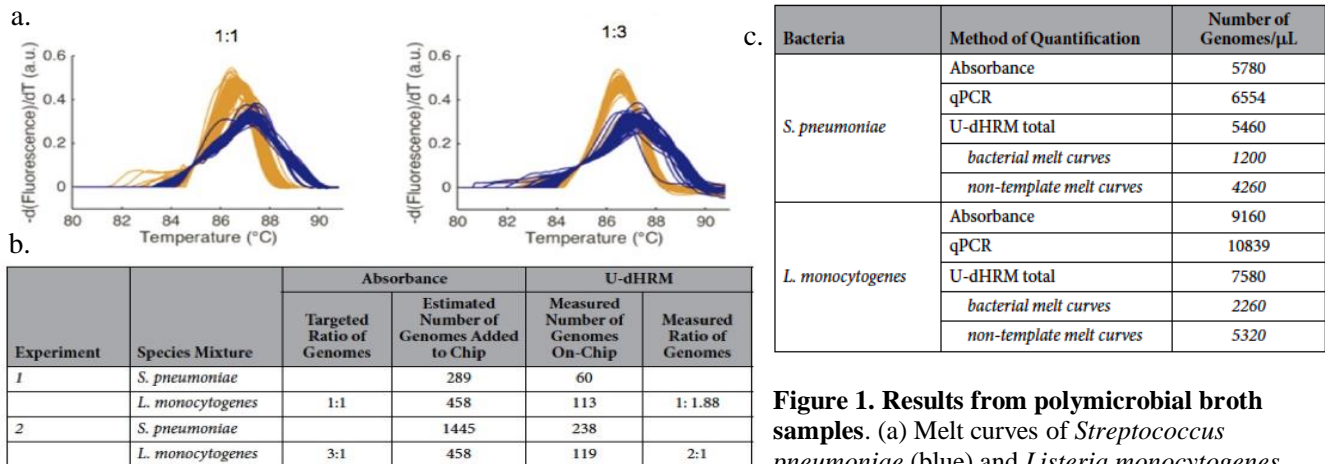[1]M. Sinha, [2]S. Lawrence, [1]T.P. Coleman, and [1]S.I. Fraley
[1]Department of Bioengineering, University of California, San Diego, CA
[2]Department of Pediatrics, University of California, San Diego, CA
Contact: sifraley@*ucsd.edu*

Introduction: Emerging technologies for microbial profiling and infectious disease diagnostics that use broad-based amplification are limited by background contaminating DNA, inability to sensitively detect multiple microbes in a single sample, and semi-quantitative nature. We developed a platform incorporating Universal Digital PCR amplification with High Resolution Melting (U-dHRM) and machine learning algorithms, to overcome these limitations. Here, our goal was to determine if the U-dHRM platform can accurately identify and quantify mixtures of two clinically relevant pathogens.

Materials and Methods: Previously, we generated melt curve signatures of the 16S rRNA gene for 37 clinically relevant bacterial organisms using universal qPCR. Our Support Vector Machine (SVM) learning algorithm demonstrated 99.9% accuracy for identifying these organisms in monomicrobial samples. Here, to address the need for polymicrobial identification and quantification, we apply our SVM algorithm to 16S melt analysis accomplished in a dPCR format. Both broth and 1 mL mock blood samples were created to mimic polymicrobial infection with *S. pneumoniae* and *L. monocytogenes* in 1:1 and 1:3 ratios, respectively, at concentrations spanning the low and high end of typical clinical pathogen load for neonatal bacteremia (50-2,000 copies). Total extracted DNA was spread across 20,000 picoliter scale dPCR reactions such that each reaction contained only zero or one genome. Then, a custom dHRM device was used for melt curve generation.

Bacteria	Method of Quantification	Number of Genomes/μL
S. pneumoniae	Absorbance	5780
	qPCR	6554
	U-dHRM total	5460
	bacterial melt curves	*1200*
	non-template melt curves	*4260*
L. monocytogenes	Absorbance	9160
	qPCR	10839
	U-dHRM total	7580
	bacterial melt curves	*2260*
	non-template melt curves	*5320*

		Absorbance		U-dHRM	
Experiment	**Species Mixture**	**Targeted Ratio of Genomes**	**Estimated Number of Genomes Added to Chip**	**Measured Number of Genomes On-Chip**	**Measured Ratio of Genomes**
1	*S. pneumoniae*		289	60	
	L. monocytogenes	1:1	458	113	1:1.88
2	*S. pneumoniae*		1445	238	
	L. monocytogenes	3:1	458	119	2:1

Figure 1. Results from polymicrobial broth samples. (a) Melt curves of *Streptococcus pneumoniae* (blue) and *Listeria monocytogenes* (yellow) in mixed samples containing 1:1 or 1:3 ratios, respectively, were automatically identified by SVM. (b) Table showing number of genomes of each organism estimated by absorbance measurement versus quantified by U-dHRM on the NeoChip. (c) Table showing different methods used to quantify bacterial genomic DNA content of samples. U-dHRM on the NeoChip detects less target DNA than other methods by distinguishing true copies from background DNA.

Results and Discussion: U-dHRM correctly identified and quantified *S. pneumoniae* and *L. monocytogenes* at typical pathogen loads in broth samples with 99.9% accuracy and estimated type I and II error rates of 0.07 and 0.00%, respectively (Figure 1). Total DNA concentrations detected were consistent with two commonly employed methods, but the U-dHRM distinguished target from background DNA (Figure 1). The identification of microbial DNA in mock blood samples gave comparable results and was not inhibited by high human DNA background or inhibitors from the DNA extraction process.

Conclusions: U-dHRM is an inexpensive (~$15 per chip) and rapid (<4 hours) platform enabling the identification and quantification of microbes in mixtures.

REPROGRAMMING OF DERMAL CELLS INTO SKELETAL MUSCLE BY CONTROLLED RELEASE OF SMALL MOLECULES

Jun Fang, Jaekyung Koh, Junren Sia, Dong Wang, Pingping Wang, Dino Di Carlo, Song Li*
Department of Bioengineering and Medicine, University of California, Los Angeles, CA
Contact: songli@ucla.edu

Introduction: Skeletal muscle has a remarkable ability to repair after minor injury, mediated by a resident population of satellite cells. However, their self-renewal potential is limited and further compromised with aging, excessive trauma, or genetic defects. Direct reprogramming somatic cells into alternative lineages have highlighted a promising strategy for regenerative therapy, via defined factors including transcription factors, RNA, proteins, and small molecules. Among them, small molecules offer powerful tools for manipulating cell fate in cell reprogramming. Meanwhile, material/physical cues suggest other exciting possibilities in specifying cell behaviors.

Here, we screened a cocktail of chemicals for direct skeletal muscle reprogramming, and developed a novel particle-micro gel system to control the release of the small molecules for cell reprogramming, which has potential for in situ cell regulation for tissue regeneration.

Materials and Methods: Neonatal dermal derived cells isolated from C57/B6 mice, Fsp1-Cre/ROSA26-tdTomato, and Pax7-CreER/ROSA26-EYFP mice were used for screening the optimal components and concentrations of small molecules. Drug loaded nano-/micro-particles were prepared by using an emulsification solvent evaporation technique. Then the drug-loaded particles were further encapsulated into an injectable microporous annealed particle (MAP) gel, made by 4-arm PEG precursor solution and crosslinker solution in the microfluidics device.

Results and Discussion: We found that the combination of repsox and forskolin can induce the appearance of myogenic cells. Together, bFGF and ascorbic acid synergistically enhanced the reprogramming efficiency (**Fig. 1A**). By seeding the initial cells on a microgrooved substrate, more muscle spherical colonies formed than the flat substrate, which allowed easy purification of muscle progenitor cells and benefited to engraft and repair the injured muscle (**Fig. 1C**). To explore the potential of in situ reprogramming via small molecules, drug-loaded PLGA particle-microsphere gel system was engineered with uniform particle distribution and high loading rate. Microsphere gel could avoid cellular uptake of particles and the encapsulated drugs can be released gradually to reprogram dermal cells into skeletal myotubes (**Fig. 1D**).
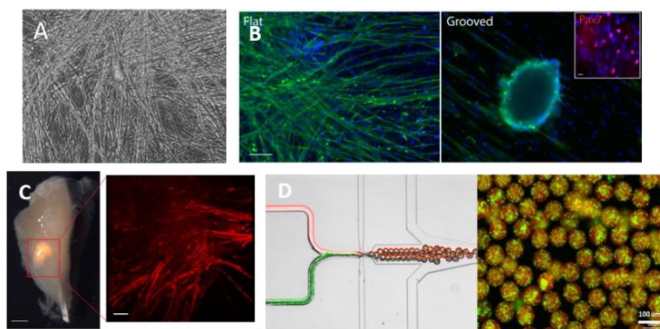
Fig. 1. Chemical induced skeletal muscle reprogramming from dermal derived cells. **A)** Long myotubes formation with screened chemicals at 2 week; **B)** Skeletal spherical colony formation on grooved substrate; **C)** Purified skeletal muscle cells injected into cardiotoxin-injured tibialis anterior engrafted after 1 week; **D)** Microfluidic generation of particle loading in microsphere hydrogel.

Conclusions: A chemical cocktail was found that can efficiently reprogram dermal fibroblasts into skeletal muscle cells. These drugs are loaded into particle-micro gel system for controlled release, which provides a basis for in situ cell reprogramming. This in situ chemical reprogramming strategy opens up an exciting new avenue for skeletal muscle repair and regeneration.

EPITOPE-FUNCTIONALIZED NANOPARTICLES FOR ENTRAPMENT OF AUTISM AUTOANTIBODIES

[1]A. Bolandparvaz, [2]E. Edmiston, [1]K. Alvarez, [2]J. Van De Water, [1*]J. S. Lewis

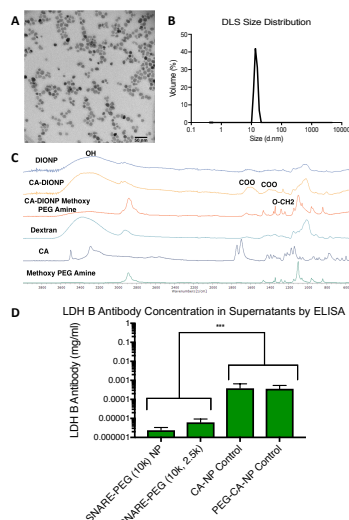[1]Department of Biomedical Engineering, University of California, Davis

[2]M.I.N.D. (Medical Investigation of Neurodevelopmental Disorders) Institute, University of California, Davis

Introduction: Autism Spectrum Disorder (ASD) comprises a range of developmental disorders diagnosed in early childhood, where the ability to communicate and interact are impaired. In the U.S., an estimated 1 in 68 children[1] is born with ASD and the economic burden is a staggering $268 billion per year[2]. Current therapies are post-symptomatic and include behavioral interventions or symptom-derived pharmacological treatments. Recently, the *Van De Water* group discovered that about a quarter of ASD cases are caused by maternal auto-antibodies that can hinder normal neurodevelopment in the fetus. Moreover, they elucidated the seven proteins targeted by these auto-antibodies in the fetal brain, including lactate dehydrogenase A and B (LDHA, LDHB)[3]. Herein, we aim to develop a **S**ystem for **N**anoparticle-based **A**utoantibody **R**etention and **E**ntrapment (**SNARE**) prophylactic as a biomagnetic-trap for sequestration of disease-propagating Maternal Autoantibody-Related (MAR) autoantibodies. Our *central hypothesis* is that upon intravenous injection, the iron oxide NPs surface-conjugated with autoantigens will circulate throughout the maternal vasculature, and specifically ligate MAR auto-antibodies, thereby limiting antibody (Ab) transport across the placenta and preventing MAR autism. Currently, investigative aims are to synthesize an epitope-functionalized DIONP system, assess Ab binding capacity, cytotoxicity *in vitro*, and determine maximum tolerated dose *in vivo*.

Fig 1: A-B. TEM and DLS of DIONPs **C.** FTIR confirming presence of surface moieties **D.** Anti-LDH B antibody capture on SNAREs *in vitro* P<.05(*), P<.01(**), P<.001 (***)

Materials and Methods: We synthesized magnetite dextran iron oxide NPs (DIONPs) by a standard co-precipitation method using Fe(II) and Fe(III) Chloride with dextran (MW 10k) and adding ammonium hydroxide dropwise. Subsequently, DIONPs were surface-modified with citric acid (CA) by overnight refluxing and methoxy poly(ethylene glycol) (PEG) amine via EDC chemistry. We performed physicochemical characterization of the DIONPs with TEM, DLS, and verified chemical modifications by FTIR and a zeta potential assay. Furthermore, DIONPs were surface-conjugated with FITC-LDH B (15 amino acids) peptide via EDC reaction (finalized formulation referred to as SNAREs). Moreover, LDH B Ab capture was demonstrated by incubating SNAREs with LDH B-specific Ab and performing a modified ELISA on the supernatant to detect Ab concentration. Finally, we confirmed SNARE repulsion of BSA protein by a bradford calorimetric assay, assessed cytotoxicity on RAW276.4 macrophages by propidium iodide viability stain via flow cytometry, and NP cellular uptake by Prussian Blue stain.

Results and Discussion: Based on TEM analysis and DLS measurements, the unmodified DIONPs demonstrate desired size and shape of ~15 nm in diameter (**Fig 1: A-B**). Moreover, PEG surface-conjugation of DIONPs was confirmed by FT-IR spectroscopy showing a characteristic peak at 1053 cm^{-1} (O-CH$_2$) (**Fig 1: C**). Next, surface moieties were confirmed by determining zeta potential surface-charge in different pH solutions and performing thermogravimetric analysis (TGA) (**not shown**). Furthermore, FITC-LDH B peptide conjugation to PEGylated DIONPs was quantified at 33.8 μg peptide/cm^2 DIONP with 70% efficiency (**not shown**). Notably, entrapment of anti-LDH B Abs by SNAREs was demonstrated *in vitro* with 95% capture efficiency (**Fig 1: D**). SNARE cytotoxicity on macrophage cells for 25% lethal concentration (LC25) dose was at 500 μg/ml (**not shown**). BSA adsorption on DIONP formulations exhibited maximum repulsion by PEG 10k/20k and NP uptake by macrophages at different incubation times demonstrated lower uptake of SNAREs vs CA-DIONPs (**not shown**).

Conclusion: We demonstrated that we can surface-functionalize DIONPs with PEG and LDH B peptide and entrap anti-LDH B autoantibodies *in vitro*. Current studies underway will assess maximum tolerated dose (MTD) by tail vein injection of (0.1-10)*LC25 SNARE dose on Gestation Day 12 in C57/BL6 pregnant mice. Post-mortem necropsy of fetuses and dams will assess for toxicity and iron biodistribution in all major organs. Our future studies will include (a) *in vitro* epitope specificity of the antigen-conjugated NPs (b) *in vivo* biodistribution and clearance via MRI in pregnant mice, and (c) efficacy of the NP system in MAR autism mice model by assessing behavioral changes in offspring.

References: 1. WHO; **2.** JP. Leigh, 2015 J Autism Dev. Disorder **3.** Braunschweig, 2012 Neurological Review

ERYTHROCYTE-DERIVED NANO-CONSTRUCTS FOR COMBINED CHEMO-PHOTDESTRUCTION OF CANCER CELLS

[1]**J.T Mac**, [2]D. Patel, [3]R. Vankayala, [2]J.M. Burns, and [1,2]B. Anvari
[1]Department of Biochemistry, University of California, Riverside, CA
[2]Department of Bioengineering, University of California, Riverside, CA
[3]Radoptics LLC, Irvine, CA
Contact: *anvarib@ucr.edu*

Introduction: Erythrocyte-derived delivery platforms have potential for personalized cancer theranostics. Key advantages of using this platform include improved biocompatibility based on fabrication of the constructs from autologously-derived blood, extended in vivo circulation time, encapsulation of various payloads (e.g., fluorescent probes and/or chemotherapeutic drugs), and surface modification to target specific biomarkers. Herein, we present the fabrication of erythrocyte-derived nanoparticles co-loaded with two FDA-approved agents: indocyanine green (ICG) as the near-infrared (NIR) absorbing agent to induce photothermal heating, and chemotherapeutic drug doxorubicin (DOX) released by the photothermal action of ICG. We refer to these constructs DOX+ICG NIR erythrocyte-derived transducers (NETs).

Materials and Methods: Erythrocytes are isolated from whole blood and undergo hypotonic treatment to remove the cytoskeletal constituents. The resulting erythrocyte ghosts undergo extrusion to form nano-sized vesicles. ICG and DOX are pre-mixed and loaded into the nano-sized vesicles in a hypotonic buffer. To evaluate the combined chemo-phototherapeutic response, SKOV3 ovarian cancer cells are incubated with nanoparticles, and subsequently, laser-irradiated at 808 nm and assessed for viability.

Results and Discussion: Both ICG and DOX can be co-loaded into NETs. DOX+ICG NETs are localized to SKOV3 cells in vitro at a greater extent as compared to non-encapsulated ICG+DOX (Figure 1).
In response to laser irradiation, DOX+ICG NETs mediate greater extent of cellular death as compared to NETs containing only ICG, which can be contributed to a combined chemo-photothermal effect.
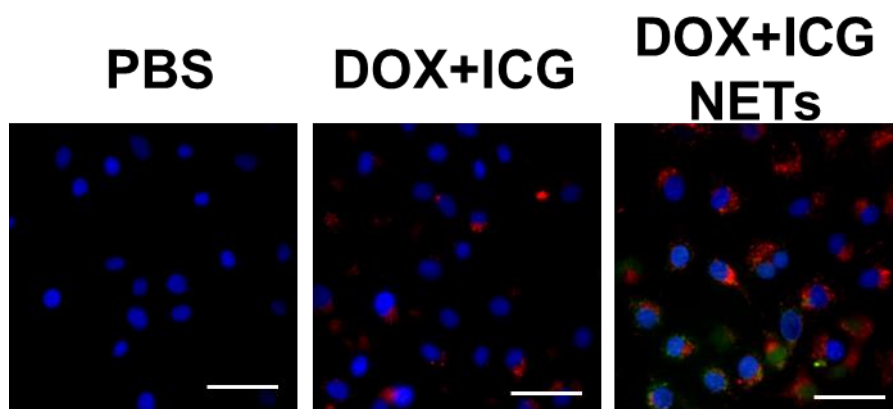

Figure 1: Falsely-colored fluorescent images of SKOV3 ovarian cancer cells after 2 hours of incubation with various agents. Blue channel: DAPI-stained nucleus; Green channel: DOX; Red channel: ICG. Scale bar = 50 µm.

Conclusions: We demonstrate erythrocyte-derived nanoparticles can be co-loaded with ICG and DOX, and subsequently, utilized to induce combined chemo-photodestruction of ovarian cancer cells in vitro.

Introduction: Pathogens have evolved over time to evade the host immune system in various ways. Specifically, the fungal species *Cryptococcus neoformans*, following engulfment by phagocytes, has been observed to stay alive within the acidic phagolysosome and escape through a process called **vomocytosis**[1]. Using this phenomenon, *C. neoformans* utilizes host immune cells to disseminate infection throughout the body. This condition, cryptococcal meningitis, is a serious risk to immunocompromised individuals, affecting an estimated 220K HIV/AIDS patients and causing 181K deaths per year worldwide[2]. Greater understanding of vomocytosis could lead to the development of new meningitis treatments for patients, as well as new biomaterial particulate vaccines. However, the underlying mechanisms of this phenomenon are unknown. To study vomocytosis, a method for quantifying phagocytosis and expulsion rates is required. Current studies use manual counting of vomocytosis events[3] (**Fig. 1**) or flow cytometry staining[4] with limited success. **This work characterizes a novel dual fluorescent reporter system that for precise monitoring of phagocytic entry and vomocytic expulsion**. The molecular signaling system is composed of tethered Enzyme-Labeled Fluorescence (ELF-97), a fluorogenic substrate that activates upon cleavage by internal lysosomal β-galactosidase (B-Gal), and Fluorogen Activating Peptide (FAP), a peptide that activates with a cell-impermeable fluorogen (αRED-np) added outside of the cytoplasm. Here, poly(lactic-co-glycolic acid) (PLGA) maleimide (PLGA-Mal) microparticles (MPs) are used to demonstrate proof-of-concept to eventually transfer the reporter system to *C. neoformans* and particulates.

Figure 1: *C. neoformans* observed to escape a RAW 264.7 macrophage 3 hours after phagocytosis.

Materials and Methods: PLGA-Mal (10% PLGA-mal + 90% PLGA) MPs were synthesized using an oil/water emulsion. Dynamic light scattering (DLS) was used to size these particles as ~1 μm. To these MPs, ELF-97 was conjugated using EDC/NHS chemistry (200μM ELF-97 in 1mg/ml MPs) and FAP (Silva Lab) was conjugated using an amine/maleimide linkage (0.1uM FAP in 1mg/ml MPs). 1mg/ml B-Gal enzyme was used to activate ELF-97 and 125nM cell-impermeable fluorogen (αRED-np, SpectraGenetics) was used to activate FAP. A plate reader was used to detect ELF-97 (Ex: 345nm, Em: 530nm) and FAP (Ex: 620nm, Em: 670nm). Images were taken using a fluorescent microscope.

Results and Discussion: The reporter molecules ELF-97 and FAP successfully tethered to the PLGA-Mal MPs, producing Reporter MPs that display strong fluorescence under distinct activation prompts (**Fig. 2**). More specifically, Reporter MPs do not fluoresce without B-Gal or αRED-np. However, when incubated with B-Gal, these particles exhibit strong ELF-97 fluorescence and low FAP fluorescence. After exposure to αRED-np, the particles show high FAP and weak ELF-97 signal. Upon Reporter MP dual activation by αRED-np and B-Gal, both ELF-97 and FAP fluorescence signals are significantly raised. Curiously, unconjugated ELF-97 with αRED-np produces FAP fluorescence. Finally, blank MPs exhibit negligible autofluorescence under all conditions.
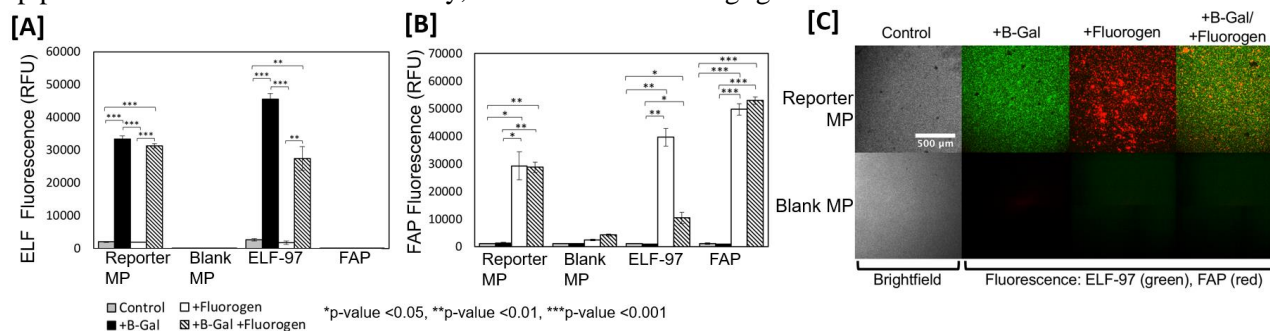
Figure 2: Reporter MPs, blank MPs, ELF-97, and FAP (n=3) with B-Gal and/or αRED-np exposure were tested for (**A**) ELF fluorescence and (**B**) FAP fluorescence. (**C**) Fluorescent images of Reporter MPs and blank MPs with B-Gal and/or αRED-np.

Conclusions: These data demonstrate successful synthesis of MP dual-reporters that show robust fluorescent responsiveness to distinct activation prompts (B-Gal and αRED-np). Future work will quantify surface-tethered fluorescence agents and optimize fluorescence signal (reduce ELF-97 signal during FAP-specific fluorescence). These particles will be fed to phagocytes to assess efficacy of the system *in vitro*. Further, this simple approach will be applied to the *C. neoformans* cell wall for investigation of vomocytosis *in vitro* and *in vivo*.

USING CELLULOSE PAPER TO ASSEMBLE AND LOAD CARGO INTO POLYMERSOMES

[1]J. Pazzi, [1]A. Li, [1]M. Xu, [1]A.B. Subramaniam
[1]Department of Bioengineering, University of California, Merced, CA
Contact: *asubramaniam@ucmerced.edu*

Introduction: Polymersomes are vesicle-like structures composed of self-assembled membranes of amphiphilic diblock copolymers, such as polybutadiene-block-polyethyleneoxide (PBD-PEO). Polymersomes are attractive drug-delivery vehicles since the PEO chains confer the polymersomes with stealth capabilities that prolongs circulation lifetime. Here we show that cellulose paper can be used to assemble polymersomes from a variety of amphiphilic diblock and triblock copolymers[1]. The cellulose paper simplifies the production of polymersomes in comparison to other techniques and allows for a sustainable and economic means of scaling up the production of polymersomes. A multistep process can be used to encapsulate a model protein in the polymersomes.

Materials and Methods: We prepared amphiphile solutions of poly(ethylene glycol)-*block*-poly(propylene glycol)-*block*-poly(ethylene glycol) (Pluronic L121) and poly(butadiene-*b*-ethylene oxide) ($PBD_{46}PEO_{30}$) as well as protein solutions of fluorescein-bovine serum albumin (FITC-BSA). We dissolved the amphiphiles in chloroform and added 0.5 mol % of the fluorescent molecule Nile Red to serve as a probe for our membranes. We deposited the desired amphiphiles onto Whatman filter paper at a nominal surface concentration between O (0.1-1) $nmol/mm^2$. We allowed the chloroform to completely evaporate and hydrated the paper in an aqueous growth buffer under conditions specific to each amphiphile. After 90 minutes, we extracted the polymersomes from the paper and into a gasket on a glass slide. We imaged the polymersomes using a confocal laser scanning fluorescence microscope. We collected tile scans covering an area of approximately 850 μm^2 and quantified the images using a custom routine in Matlab.

Results and Discussion: We show that the growth of polymersomes on cellulose paper is dependent on both the nominal surface concentration of amphiphile deposited onto the paper as well as the conditions of the growth buffer used during hydration of the paper. Polymersomes from $PBD_{46}PEO_{30}$ require temperatures of around 80 C for rapid assembly. Lowering the temperature to 25 C allows encapsulation of a model protein FITC-BSA. We find that encapsulation of the FITC-BSA protein is efficient with most of the polymersomes paper showing fluorescence within their lumens (Figure 1c,d).
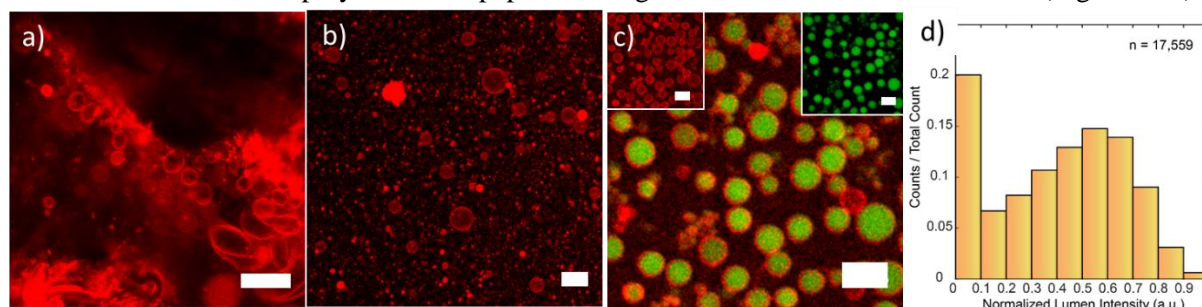
Figure 1: a) Confocal fluorescence image of polymersomes (red rings) growing on cellulose paper. b) Typical image of polymersomes after extraction from the paper. c) Composite image of the Nile Red and FITC (green) channels showing successful encapsulation of the FITC-BSA protein into polymersomes. Insets are the separate channels. d) Histogram of the normalized lumen intensities of a population. Scale bars: a,c) 10 μm, b) 25 μm

Conclusions: We show the production of polymersomes on cellulose paper is possible under the appropriate initial growth conditions and that encapsulation of a FITC-BSA molecule into the polymersomes is efficient. This technique creates an economic and scalable avenue for the production of polymersomes loaded with cargo with potential drug delivery applications.

References:

1) Li, A.; Pazzi, J.; Xu, M.; Subramaniam, A. B. *Biomacromolecules* **2018**.

PROCESS DEVELOPMENT FOR PRODUCTION OF RECOMBINANT BUTYRYLCHOLINESTERASE IN METABOLICALLY-REGULATED, TRANSGENIC RICE CELL SUSPENSION CULTURES

[1]Jasmine M. Corbin, [1]Matthew J. McNulty, [2]Muchena J. Kailemia, [3]C. Linn Cadieux, [1]Zachary R. Kyser, [2]Carlito B. Lebrilla, [3]Douglas M. Cerasoli, [1,4]Karen A. McDonald, and [1,4]Somen Nandi

[1]Department of Chemical Engineering, University of California, Davis, CA, USA
[2]Department of Chemistry, University of California, Davis, CA, USA
[3]Medical Toxicology Division, US Army Medical Research Institute of Chemical Defense, Aberdeen Proving Ground, MD, USA
[4]Global HealthShare Initiative, University of California, Davis, CA, USA
Contact: *jmcorbin@ucdavis.edu*

Introduction: The human enzyme butyrylcholinesterase (BChE) has been studied as a therapeutic and prophylactic treatment against organophosphate poisoning and cocaine toxicity, though its use has been limited by the prohibitive costs of production and purification of BChE from human plasma (estimated US$20,000 per dose). To address the need for an affordable and reliable supply of this life-saving drug, we have developed a process for producing a recombinant version of BChE in a metabolically-regulated transgenic rice cell suspension culture (rrBChE). Plant cell cultures are well suited to BChE production due to their inherent biosafety, controllability, reproducibility, conformance to cGMP requirements, capacity to perform complex glycosylation, and ability to grow in simple, low-cost medium.

Materials and Methods: After design of the gene construct and transformation of the cells, independent transformation events were screened to select a single cell line. The culture was scaled up to a lab scale bioreactor to determine culture kinetics when operated in a semicontinuous mode. We then developed a downstream process to isolate an active, >95% molecule using operations such as tangential flow filtration, diethylaminoethanol (DEAE) anion-exchange chromatography, and affinity chromatography. To assess the impact of these cost-saving measures at the manufacturing scale, we scaled up the process *in silico* using SuperPro Designer (Intelligen, Inc.) and used the model for techno-economic analysis.

Results and Discussion: Our data demonstrate that rrBChE can be produced at 20 mg/L and higher through multiple cycles of growth and expression at multiple process scales without a decrease in expression levels. Our downstream process recovers 42% of an active, >95% pure molecule using manufacturing-friendly operations. The molecule was extensively characterized and found to function comparably to the native human protein. Results from our techno-economic simulation indicate that this novel process is expected to reduce the production cost of each dose of rBChE from $20,000 to $620.
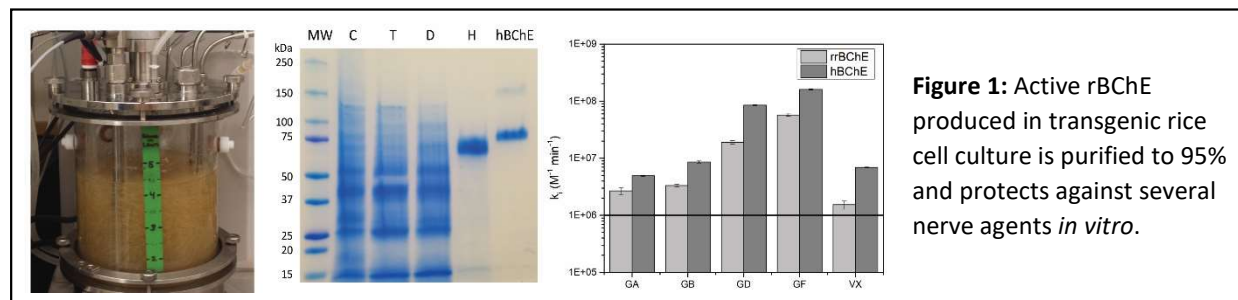
Figure 1: Active rBChE produced in transgenic rice cell culture is purified to 95% and protects against several nerve agents *in vitro*.

Conclusions: Functional rrBChE can be efficiently produced in a transgenic rice cell suspension culture, potentially reducing production costs over 30-fold compared with purification from human plasma and significantly increasing the accessibility of this important drug.

GENERATION OF HIGHLY SELECTIVE PROTEASE INHIBITORY ANTIBODIES BY FUNCTION-BASED SELECTION

[1]Tyler Lopez, [1]Zahid Mustafa, [1]Aaron Ramirez, [1]Chuan Chen, [2]Xin Luo, [1]Chris Benitez, [1]Henry Pham, [1]Ramon Sanchez, [2]Ru-Rong Ji, [1]Xin Ge

[1]Department of Chemical and Environmental Engineering, Bourns College of Engineering,
[2]Department of Anesthesiology and Neurobiology, Duke University Medical Center
Contact: xge@engr.ucr.edu

Introduction: As extremely important signaling molecules, proteases precisely control a wide variety of physiological processes, and thus represent one of the largest families of potential pharmaceutical targets. Mounting evidence suggested that specificity is desired for any protease inhibition therapy, but the proteolytic mechanisms are highly conserved among the same class or family of proteases. As a result, distinguishing proteases using small molecule inhibitors is exceedingly difficult (e.g. fails of board spectrum MMP inhibitors in clinical trials), and thus monoclonal antibodies (mAbs) with their exclusive specificity have emerged as attractive agents to inhibit biomedically important proteases. However, current antibody selection methods are essentially binding based assays without control on inhibition function.

Materials and Methods: To facilitate the isolation of protease inhibitory antibodies, this study used synthetic antibody libraries enriched with convex conformation CDR-H3, and developed functional rather than binding based screening methods. More specifically, epitope-specific FACS and genetic selection approaches were designed, optimized and applied for the discovery of a panel of highly potent and selective Fab inhibitors targeting all four main classes of proteases: matrix metalloproteinases (MMP-14, a predominant target in cancer metastasis; MMP-9, in neuropathic pains), beta-secretase 1 (BACE1, an aspartic protease in Alzheimer), cathepsin B (a cysteine protease in cancer), and Alp2 (a serine protease in aspergillosis).

Results: For each target, multiple inhibitory mAbs (5-8 unique clones) were discovered. Many of them exhibited nM affinity and similar inhibition strength (**Table**, only top three clones for each studied protease are shown). Inhibition kinetics demonstrated most of them are competitive inhibitors with excellent selectivity. Particularly, Fab B3B12 blocked BACE-1 catalyzing on its physiological substrates with a binding affinity of 10 nM and an inhibition potency of 19 nM. In addition, mAb L13, an anti-MMP9 inhibitor exhibited a potency of 20 nM. Intravenous application of L13 showed significant pain attenuation effects in paclitaxel mouse model. Works on improving stability and selectivity of MMP inhibitory mAbs by epitope-specific FACS will also be discussed.

Protease Type	Target (indication)	Fab	Binding Affinity K_D (nM)	Inhibition Potency K_I (nM)
Metallo-	MMP-9 (neuropathic pain)	H3	82	97
		H4	6.9	100
		L13	120	250
	MMP-14 (cancer)	2B4	62	110
		2B12	76	130
		1A5	57	170
Aspartic	BACE1 (Alzheimer's)	B3B12	10	19
		B1A4	21	55
		r2B5	130	97
Serine	Alp2 (aspergillosis)	r4A2	110	240
		r4A7	420	360
		r4A6	700	790
Cysteine	Cathepsin B (cancer)	In progress		

Conclusions: Highly potent mAb inhibitors with exclusive selectivity have been discovered for many proteases of biomedical importance with the potentials to deliver desired therapeutic efficacy.

INTRODUCING ANTITERMINATOR PARALOG GENES TO ACTIVATE THE EXPRESSION OF BIOSYNTHETIC GENE CLUSTERS TO INDUCE PRODUCTION OF NATURAL PRODUCTS IN *CLOSTRIDIUM* SPECIES

[1]A. Leung, [2]J. Li, and [3]W. Zhang

[1, 2, 3] Department of Bioengineering, University of California, Berkeley, CA

Contact: *a.leung@berkeley.edu*

Introduction: Antimicrobial resistance is a significant worldwide problem, contributing to $21-$34 billion in healthcare costs and 8 million additional hospital days in the US. Due to the increased demand for antibiotics with new mechanisms of action, bacteria are being investigated for their ability to form natural products useful for drug development and novel antibiotics. These include secondary metabolites, which are difficult to produce *in vitro*. However, in one study, overexpression of the anti-terminator gene nusG corresponding to biosynthetic gene clusters in *Clostridium celluloyticum* yielded the antibiotic closthioamide and related thioamides [1]. Using the knowledge that a paralog of nusG (LoaP) was discovered in *Clostridium beijerinckii* (B-598), it was hypothesized that if LoaP were excised from B-598's genome and inserted into B-598, the biosynthetic gene cluster Cluster 10 would be activated under a cryptic biosynthetic pathway, driving B-598 to yield novel secondary metabolites.

Materials and Methods: PJL9 was created by cutting the native nusG sequence out of PJL5, and ligating B-598's nusG (LoaP) sequence to it using cloning and Gibson assembly. PJL9 was transformed into *E. coli* and into B-598 colonies using a transformation procedure developed by the Zhang Lab. Transformants were grown in TYA media and chemically extracted. Compounds were separated out through mass spec and HPLC.
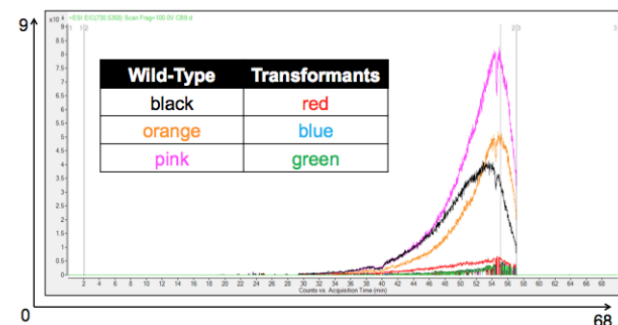
Results and Discussion: Figure 1a indicates a significant difference between the LoaP overexpression and control samples. The wild-type curves showed high-counts, indicating that the mass was present in a higher quantity than the LoaP overexpression samples.

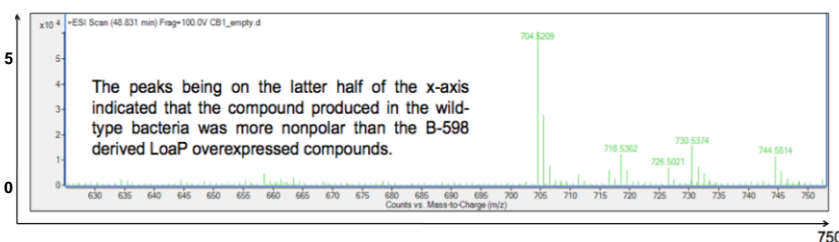**Figure 1a:** Chromatogram Comparing B-598 LoaP Overexpression Strains Versus Wild Type

Figure 1b shows a QTOF data file comparing counts to mass to charge ratio. Mass is present in the wild-type, indicating that a nonpolar compound was produced in the wild-type bacteria, but not the B-598 derived LoaP overexpression samples.

Figure 1b: Counts Versus Mass Charge Confirming the Presence of the 730.5358 m/z in the Wild Type Bacteria

Conclusions: Theoretically, overexpression of the nusG vector in bacteria would induce it into creating natural products such as antibiotics. However, Figure 1a indicates that the wild-type bacteria contained a peak with a mass that the transformant strain lacked. The sequence inserted into B-598 decreased production in the bacteria, suggesting that the sequence used produced secondary effects that inhibited creation of the expected product. In the future, another LoaP sequence associated with a saccharide gene cluster and similar proteins will be inserted into the B-598 genome and studied for secondary metabolite activity.

References:
[1] Behnken, S., Lincke, T., Kloss, F., Ishida, K. and Hertweck, C., Antiterminator-Mediated Unveiling of Cryptic Polythioamides in an Anaerobic Bacterium. Angewandte, 51, 2425–2428, 2012

IDENTIFICATION OF SUMOYLATION SITE OF INFLUENZA VIRUS PROTEIN
by FRET TECHNOLOGY

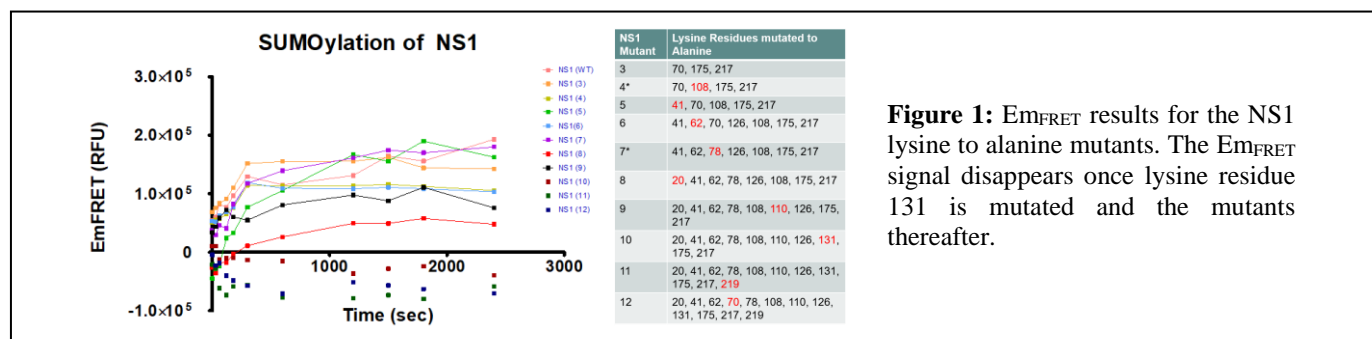[1]G. Way, [1]Z. Xiong, [1]J. Jiang, and [1]J. Liao
[1]Department of Bioengineering, University of California, Riverside, CA
Contact: *JLiao@engr.ucr.edu*

Introduction: SUMOylation is a post-translational modification which is important for protein function regulation and cellular processes. The dysregulation of SUMOylation has been observed in many different types of cancers and neurodegenerative diseases. More recently, SUMOylation has been shown to be an important host factor for the replication of the influenza A virus and other viruses. The obligatory relationship between SUMOylation and the influenza A virus remains to be elucidated. Currently, identification of SUMOylated lysine residues relies on the Western-blot methods after site-directed mutagenesis. Because SUMOylation is a dynamic process, the Western-blot may give false positives due to a lack of sensitivity or the breakdown of the isopeptide bond from endogenous SENP. We have developed a highly sensitive FRET-based methodology to identify the specific lysine residue(s) responsible for SUMOylation. Our method can be applied to other proteins and post-translational modifications homologous to SUMO in the identification of conjugated residues and the evaluation of PTMs as druggable targets for cancer and antiviral therapies.

Materials and Methods: The expression constructs for pET28 (b) CyPet-SUMO1, pET 28 (b) UBA2, pET28 (b) AOS1, pET28 (b) UBC9 were described in Song, et al. 2011 and pET28 (b) YPet-Linker 2- NS1 was cloned from the pDZ NS construct. Site-directed mutagenesis was conducted by PCR as described in Walker et al. 2009. Expression and purification were performed as outlined in Jiang et al 2014. Quantitative FRET was used to subtract the ratiometric contributions from the FRET pair to determine the real FRET emission. The SUMOylation assays were performed in the presence of all enzymes, CyPet-SUMO1 and YPet-NS1.

Results and Discussion: From our mutagenesis, we were able to determine the lysine residue 131(K131) is SUMOylated. According to several predictive tools, the SUMOylated lysine residues with the highest probabilities were K70, K175, and K219. Our finding is contrary to the computational prediction and previous reports, showing that K70 and K219 of NS1 were SUMOylated. Our FRET approach for the identification of SUMOylation sites is sensitive and more accurate than the previously described methods. We have also shown that the NS1 K131 is critical for influenza virus replication supported by the data presented here.

NS1 Mutant	Lysine Residues mutated to Alanine
3	70, 175, 217
4*	70, 108, 175, 217
5	41, 70, 108, 175, 217
6	41, 62, 70, 126, 108, 175, 217
7*	41, 62, 78, 126, 108, 175, 217
8	20, 41, 62, 78, 126, 108, 175, 217
9	20, 41, 62, 78, 108, 110, 126, 175, 217
10	20, 41, 62, 78, 108, 110, 126, 131, 175, 217
11	20, 41, 62, 78, 108, 110, 126, 131, 175, 217, 219
12	20, 41, 62, 70, 78, 108, 110, 126, 131, 175, 217, 219

Figure 1: Em$_{FRET}$ results for the NS1 lysine to alanine mutants. The Em$_{FRET}$ signal disappears once lysine residue 131 is mutated and the mutants thereafter.

Conclusions: Our newly FRET-based methodology to identify SUMOylation sites in proteins has demonstrated its power and convenience. Our method can be applied to residues that are targeted by post-translational modifications by Ubiquitin-related peptides (UBLs) and can significantly push mechanistic studies and translational research.

References (optional):
1. Song, Y., Madahar, V. & Liao, J. Development of FRET assay into quantitative and high-throughput screening technology platforms for protein-protein interactions. *Annals of Biomedical Engineering* **39,** 1224–1234 (2011).
2. Jiang, L. *et al.* Specific substrate recognition and thioester intermediate determinations in ubiquitin and SUMO conjugation cascades revealed by a high-sensitive FRET assay. *Molecular BioSystems* **10,** 778 (2014)
3. Walker, J. M. *Enzyme Engineering, Methods and Protocols*. *Life Sciences* **531,** 588 (2009).

TRANSGENIC EXPRESSION OF TYPE II COLLAGEN FOR TISSUE ENGINEERING

J. Doong, F. Murolo, L. Howard, S. Yamada, A. Passerini, A. Yao, M. Facciotti
Department of Biomedical Engineering, University of California, Davis, CA
Contact: *lwhoward@ucdavis.edu*

Introduction: Joint cartilage injuries are some of the most costly injuries in the United States. Current artificial joint replacements are unsuitable as long-term treatments due to metal toxicity and fracture. Tissue engineered cartilage promises to produce a long-term solution by growing impantable cartilage *in vitro* with comparable physical properties to native tissue. Unfortunately, state-of-the-art engineered cartilage has lower levels of the major structural protein Type II Collagen (Col II) when compared to native tissue which contributes to its mechanical insufficiency. To address this, we built a transgenic construct to test the application of genetic engineering for increasing Col II production in bovine chondrocytes. The construct consists of a Tet-ON incubile Col II gene that is available for genomic integration with the piggyBac transposon system.

Materials & Methods: Bovine COL2A1 transcript IIB cDNA was partially codon optimized and separated into four fragments for chemical synthesis. The cDNA was assembled into an intermediate backbone using restriction enzyme digestion and then transferred via Gateway Cloning to a doxycycline inducible Tet-ON vector with piggyBac inverted repeats. The final construct was transiently transfected into monolayer HEK 293T cells using lipofection and induced with 1μM doxycycline (dox). Western Blot assessed Col II production in non-induced HEK cells, non-transfected HEK cells, and primary bovine articular chondrocytes.

Results and Discussion: Western blot results demonstrated that dox induced production of Procollagen II protein in transfected cells. Procollagen II is the preprocessed form of Col II and is higher in molecular weight than the purified Col II protein standard. The Col II protein detected in transfected HEK293T cells matched in weight with the procollagen II in the control chondrocyte lysate. qRTPCR assays are in progress to assess changes in mRNA abundance of native and transgenes. The system will soon be tested in bovine chondrocytes with a range of inducer concentrations to quantitatively assess the inducer/RNA/protein transfer function. Finally, the transgene will be genomically integrated to create stable cell lines for testing in 3D tissue constructs whose histological and mechanical properties will be evaluated.
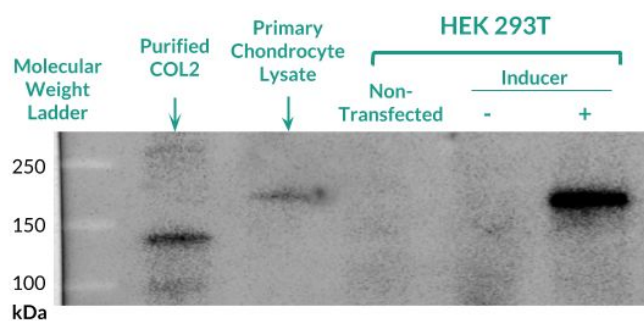
Figure 1: Western Blot showing Col II production. Lane 2: Purified mature Col II proteins is 140kDa.
Lane 3: Primary bovine articular chondrocyte lysate display 200kDa intracellular procollagen II.
Lanes 4 & 5: Non-transfected and non-induced cells show no Col II expression.
Lane 6: Dox-induced cells produced significant procollagen II with comparable cell counts to Lane 4 and 5.

Conclusion: The preliminary results demonstrates that the construct is capable of inducible Col II protein expression in a mammalian cell line and indicates potential applicability in articular chondrocytes for culturing viable cartilage tissue.

A LIGHT INDUCIBLE GENE ACTIVATION SYSTEM TOWARD CONTROLLABLE CELL-BASED THERAPEUTICS

[1]Ziliang Huang, [1]Yiqian Wu, [1]Yijia Pan, [1]Molly Allen, [1]Ya-Ju Chang, [1,2]Shu Chien, and [1,2]Yingxiao Wang

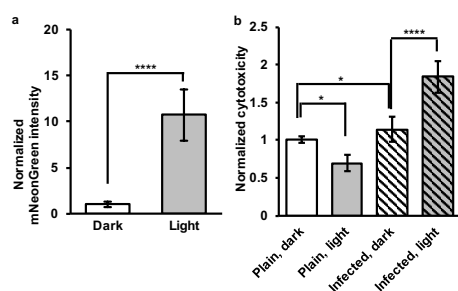[1]Department of Bioengineering, University of California, San Diego, CA

[2]Institute of Engineering in Medicine, University of California, San Diego, CA

Contact: *yiw015@eng.ucsd.edu*

Introduction: T cells engineered to express chimeric antigen receptors (CARs) on cell surface can recognize and engage with target cancer cells with redirected specificity. This CAR T cell-mediated immunotherapy is under intensive investigation as a revolutionary therapy for cancer. However, adverse effects have been reported, including on-target off-tumor cytotoxicity, cytokine release syndrome and tumor lysis syndrome. One of the solutions is to engineer on/off-switchable cells to achieve high-precision control over their activation. Optogenetics utilizing genetically encoded dimerizers has been applied to remotely activate gene expression. Here, we developed a new blue light-mediated light-inducible nuclear translocation and dimerization (LINTAD) system for gene regulation to control cell activation, by integrating a LOV2-based light-inducible nuclear localization signal with CRY2-CIB1 dimerization. We demonstrated light-controllable gene expression and functional modulation in HEK 293T and Jurkat T cell lines. We further applied the LINTAD system in primary human CAR T cells and showed that the light-stimulated cells possessed a significantly stronger cytotoxicity against target cancer cells than the non-stimulated ones. We also extended the LINTAD system to activate the expression of the TNF-related apoptosis-inducing ligand (TRAIL) in HEK 293T cells, and observed a gain of cytotoxicity upon light stimulation. Therefore, our newly developed LINTAD system can serve as an efficient and general tool to remotely and non-invasively control gene activation in live cells for therapeutic applications.

Materials and Methods: Human peripheral blood mononuclear cells (PBMCs) were isolated from buffy coats (San Diego Blood Bank) using Ficoll gradients (Amersham Biosciences). For lentiviral transduction, cells were first activated for 72 h using 2 mg/L phytohemagglutinin (Thermo Fisher) in complete RPMI medium. The cells were then transduced with concentrated lentivirus at a MOI of 10 for each construct by spinoculation on Retronectin (Takara)-coated plates at 1,800 g, 32 °C for 1 h.

Results and Discussion: We have demonstrated that the LINTAD system can be used to control gene expression in HEK 293T and Jurkat cell lines (Figure 1a). Through delivering the LINTAD system into PBMCs, the activity/cytotoxicity of CAR-T cells can be controlled by blue light illumination (Figure 1b).

Figure 1: (a) Light-inducible mNeonGreen expression in HEK 293T cells transfected with LINTAD.Dark, without light treatment. Light, with 24 hr blue light illumination (n=20). (b) Light-inducible cytotoxicity of PBMCs. Plain, without infection. Infected, cells infected with LINTAD system. Dark, without light treatment. Light, with 24 hr blue light illumination. ($n = 9$).

Conclusions: In summary, we have developed a light-inducible gene activation system LINTAD by combining the light-inducible nuclear translocation and CIB1-CRY2 dimerization. We have demonstrated that LINTAD has high efficiency in controlling gene expression in mammalian cells, and that it can remotely and non-invasively regulate the activation of CAR T cells for cancer immunotherapy with high spatiotemporal precision.

Poster #	Track	Rapid Fire	Lead Author	Affiliation	Title
16	Biomaterials and Drug Delivery	Yes	Crysthal Alvarez	UC Riverside	Femtosecond Laser Assisted Antibacterial Activity of Zno Nanoparticles
19	Biomaterials and Drug Delivery	Yes	Wayne Leu	UC Riverside	Polycaprolactone With Citric Acid Coated Iron Oxide Composite for Biomedical Applications
22	Biomaterials and Drug Delivery		S. Hoang	UC Riverside	Size and Concentration Analysis of Nanoliposomes Using a Single Nanoparticle Sensor
25	Biomedical Imaging	Yes	Amirhessam Aminfar	UC Riverside	Application of Optical Flow Algorithms to Visualize Pulsatile Blood Flow
28	Biomedical Imaging	Yes	Asa F. Gardner	UC Merced	A Method of Tissue Clearing to Identify Cell Types in the Thymus
34	Computational Bioengineering		J. C-N. Chang	UCSC	Identifying Coreferent Genotypes in One-way Cryptographic Hash Using Haplotype Information
49	Medical Devices and Instrumentation	Yes	M.F. Yee	UCLA	Ionic Liquid Aqueous Two-phase Systems for Enhanced Detection of Transferrin and E. Coli
52	Medical Devices and Instrumentation		Jianhou Zhang	UC Riverside	Effect of Hybridization Time and Concentration of Dna Linker on Aggregate Size of Dna-conjugated Microspheres
55	Medical Devices and Instrumentation		S. Modha	UC Riverside	Towards the Development of a Multiplexed Paper-based Biossensor
58	Medical Devices and Instrumentation		Sherine Cheung	UCLA	Nucleic Acid Enrichment and Isothermal Amplification on Paper
61	Medical Devices and Instrumentation		R. Yeung	UC Riverside	Modeling of Solid-fluid Flow in Microfluidic Systems for Sorting Aspherical Particles
64	Medical Devices and Instrumentation		So You Lee	UCLA	Modeling Flow Separation of Aqueous Two-phase System Imbibition in Porous Media
67	Medical Devices and Instrumentation		F. Lopot	Czech Technical University	Respiratory Sounds as a Source of Diagnostic Information in Pulmonary Obstruction Diseases
68	Medical Devices and Instrumentation		A. S. Abrams	UCSB	Measuring Changes in Nanofluidic Current as a Continuous Multi-Analyte Biosensor for Biological Fluids
1	Molecular & Cellular Engineering	Yes	J. Morival	UC Irvine	Epigenetic Regulation During Topography-induced Cardiomyocyte Maturation
4	Molecular & Cellular Engineering	Yes	J. Soto	UCLA	Role of Intracellular Structures in the Direct Conversion of Fibroblasts Into Neurons
7	Molecular & Cellular Engineering		Zaira Alibay	UC Riverside	Assessment of Template Tuning Properties for Viral-directed Synthesis of Inorganic Materials
10	Molecular & Cellular Engineering		Ki Baek Lee	UC Riverside	The Study of Mmp-14 Inhibitory Antibody Isolated From a Long Cdr-h3 Synthetic Fab Library
13	Molecular & Cellular Engineering		Ssu-Chieh J. Hsu	UC Irvine	Investigating the Effects of Homotypic Paracrine Signaling in Macrophage Activation
37	Neuroengineering	Yes	C. M. Laine	USC	Emg Coherence: a Physiological Biomarker for Parkinson's Disease
40	Stem Cells and Regenerative Medicine		Anna A. Kim	UCSB	Mechanical Signaling in Intestinal Stem Cell Biology of Fruit Flies
43	Stem Cells and Regenerative Medicine		D. utherford	UC Riverside	Window to the Brain: in Vitro Cell Studies With Yttria Stabilized Zirconia Nanopowder (8ysz, 6ysz, 3ysz, and Zro2)
45	Stem Cells and Regenerative Medicine	Yes	D. Horne	UCSF	Low-intensity Pulsed Ultrasound Increases Collagen Production in Bovine Annulus Fibrosus Cells
46	Stem Cells and Regenerative Medicine		Daniel Ortiz	UCSD	3d Collagen Architecture Modules Cell Adhesion and Mmp Activity to Promote Cancer Cell Invasiveness

FEMTOSECOND LASER ASSISTED ANTIBACTERIAL ACTIVITY OF ZNO NANOPARTICLES

Crysthal Alvarez, Natanael Cuando, and Guillermo Aguilar
Department of Mechanical Engineering, University of California, Riverside, CA
Contact: *gaguilar@ucr.edu*

Introduction: According to recent studies [1] up to 40% of PMMA cranioplasties show complications such as migration of the implant, infection, chronic pain, and hematoma. About 35% of the complication cases end in implant removal and about 90% of the implant removal cases involves infected implants. Infection inside the skull represents a major therapeutic challenge as the blood-brain barrier exclude most of the conventional drugs used to treat infection. A novel approach of transparent ceramic implants [4] brings the possibility of laser based treatments for infections of cranial implants. Here we present a study of a treatment that combines ZnO nanoparticles and femtosecond laser pulses to inhibit the growing rate of Escherichia coli (E. coli).

Materials and Methods: Lyophilized cells of K12 E. coli of clinic relevance were obtained from Sigma-Aldrich and grown in Luria-Bertani (LB) broth while shaking at 100 rpm at 37°C. Overnight cultures of bacteria were grown in 10 mL of LB broth (with and without ZnO nanoparticles). A femtosecond pulsed laser (Mikan, Amplitude) at 1030nm, 54MHz and pulse duration of 250fs was used to irradiate liquid samples of E. coli with and without ZnO nanoparticles. Cultures of E. coli with no treatment (i.e. no ZnO nanoparticles and no irradiation) were used as a control. Dilutions of E. coli solution (3×10^3 CFU/mL) with and without ZnO nanoparticles (0.2mg/mL) were plated in a 48 well plate and placed on a hot plate to perform laser irradiation for a given time. Following irradiation, the samples were incubated at 37°C for 20hr.

Results and Discussion: As expected, the minimum number of CFU/mL is presented at the longest irradiation time period tested. A reduction of 3 orders of magnitude was observed in CFU/mL when comparing 60 min of irradiation versus no irradiation (~5×10^{13} vs. ~4×10^{10} CFU/mL). The proposed treatment presents a nearly two-fold inhibition on the mean value after 15min of treatment. When comparing the laser-assisted ZnO nanoparticles treatment with its non-irradiated counterpart, one can see that laser light clearly enhances the antibacterial activity of ZnO nanoparticles. Although antibacterial activity of ZnO has been extensively reported in literature [7], the interaction of femtosecond laser pulses and ZnO as antibacterial treatment has not been reported. Notice that the same initial concentrations of cells were used for all cultures, and the same concentration of ZnO nanoparticles were used for cultures with and without laser irradiation.

Conclusions: In this work, we investigate a combined treatment strategy where ZnO nanoparticles and fs laser pulses may be acting independently, or alternatively, a combined effect (e.g. excitation of the ZnO nanoparticles by absorption of laser energy) may be responsible for the observed reduction in bacterial concentration. Optimization of the treatment strategy and elucidation of the specific antibacterial mechanism are subjects of ongoing work.

References (optional):
[1] Joby Jaberi, Kenneth Gambrell, Paul Tiwana, Chris Madden and Rick Finn, "Long-Term Clinical Outcome Analysis of Poly-Methyl-Methacrylate Cranioplasty for Large Skull Defects," Journal of Oral and Maxillofacial Surgery, 71, e81-e88 (2013).
[2] Yasaman Damestani, Diego E Galan-Hoffman, Daniel Ortiz, Pedro Cabrales and Guillermo Aguilar, "Inflammatory response to implantation of transparent nanocrystalline yttria-stabilized zirconia using a dorsal window chamber model," Nanomedicine: Nanotechnology, Biology and Medicine, 12(7), 1757–1763 (2016).
[3] Amna Sirelkhatim, Shahrom Mahmud, Azman Seeni, Noor Haida Mohamad Kaus, Ling Chuo Ann, Siti Khadijah Mohd Bakhori, Habsah Hasan and Dasmawati Mohamad, "Review on Zinc Oxide Nanoparticles: Antibacterial Activity and Toxicity Mechanism," Nano-Micro Letters, 7(3), 219–242 (2015).

Polycaprolactone with Citric Acid Coated Iron Oxide Composite for Biomedical Applications

[1]W.F. Leu, [2]L.V. Salmeron, [3]C.G. Azevedo, [1]H. Liu

[1]Department of Bioengineering, University of California, Riverside, CA

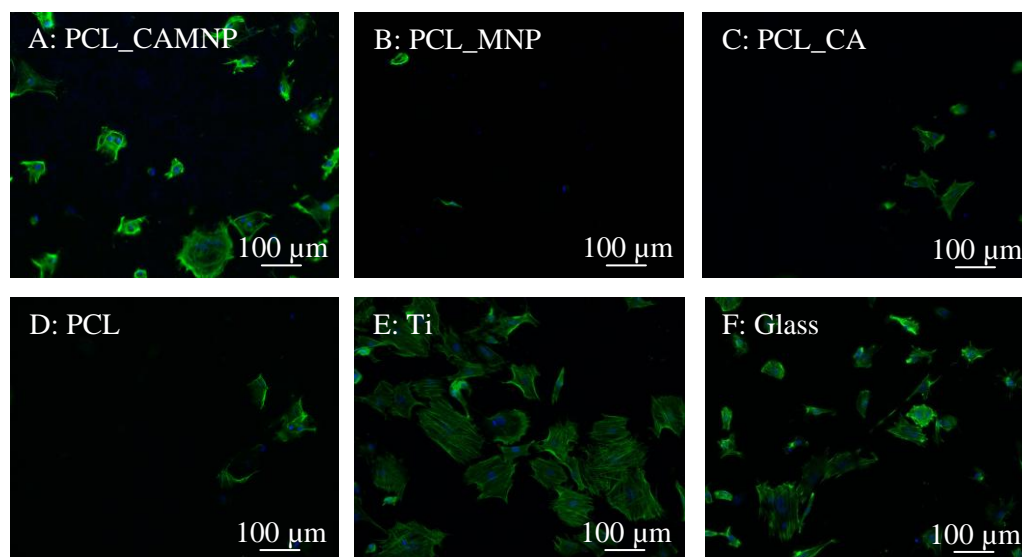[2]Department of Bioengineering, University of California, Merced, CA

[3]Materials Science and Engineering, University of California, Riverside, CA

Contact: *huinanliu@engr.ucr.edu*

Introduction: Magnetic nanoparticles (MNPs) are instrumental to a multitude of research disciplines, which include catalysis, magnetic fluids, data storage, and biomedical applications. Biomedical applications for MNPs consists of detection of biological entities and magnetic bio-separation, clinic diagnosis and therapy, biological labels, and targeted drug delivery. Therefore, it is crucial to choose the constituents for the construction of nanostructure materials and devices with adaptable physical and chemical properties. Biodegradable polymers like polycaprolactone (PCL) have a multitude of biomedical applications which include implants and drug delivery. This study focuses on synthesizing citric acid coated iron oxide (Fe_4O_4) nanoparticles and embedding them inside PCL to create a biocompatible polymer composite. This citric acid (CA) coating maintains proper pharmacokinetic properties and bio-distribution characteristics for iron oxide (Fe_3O_4) MNP and sterically stabilizes the hydrophobic nature of iron oxide nanoparticles. Finally, scaffolds of the polymer composite were made by solvent casting. These nanocomposites, PCL, and Fe_3O_4 controls were assessed for cytocompatibility with Bone Marrow derived Mesenchymal Stem Cells (BMSC).

Materials and Methods: Iron oxide MNPs were synthesized by the co-precipitation method, and the citric acid coated MNPs were synthesized by adding citric acid to the iron chloride mixture during the co-precipitation method. The MNPs were then embedded in PCL thin film by solvent casting. The 10 % w/w MNPs to PCL were then assessed with Scanning Electron Microscopy (SEM) and cytocompatibility study with BMSCs. Ionic concentrations were assessed with ICP-OES.

Results and Discussion: PCL_CAMNP and PCL_MNP maintained magnetic properties of the magnetic nanoparticles. The citric acid coated iron oxide improved cell adhesion on PCL as shown in Figure 1.

Figure 1: Fluorescence images of BMSCs adhesion and morphology when cultured on materials of interest. Original magnification at 100x.

Conclusions: PCL_CAMNP presents an opportunity where a biodegradable polymer can be directed to a targeted location and can be potentially visualized in a non-invasive method such as MRI.

SIZE AND CONCENTRATION ANALYSIS OF NANOLIPOSOMES USING A SINGLE NANOPARTICLE SENSOR

[1]S. Hoang, [1]N. Palegar, [1]K. Ghosh, [1]K. Freedman
[1]Department of Bioengineering, University of California, Riverside, CA
Contact: kfreedman@engr.ucr.edu

Introduction: Nanoliposomes represent a core technology in pharmaceutical sciences allowing drugs to be delivered to target tissues. Composed of a phospholipid bilayer, these submicron particles package drugs within its aqueous interior until their payload is delivered through endocytosis or fusion with a target cell. Although nanoparticle sizing technology, such as dynamic light scattering, has been the technique of choice for liposome characterization, there is a surprising deficit in the number of tools capable of measuring concentration. An alternative approach which can measure both size and concentration makes use of nanopipettes. Nanopipettes are fabricated from quartz capillaries and are characterized by a nanoscale opening at the tip (i.e. a nanopore). By nature of the size of the opening, nanopipettes are capable of detecting individual translocation events (i.e. the process of an analyte passing through the pore) making them suitable for the analysis of nanoliposomes.

Materials and Methods: The sizes of the nanoliposomes were characterized using resistive pulse sensing, a technique that allows for single-particle characterization. For this study, the nanoliposomes (~150-200 nm) were diluted in 50 mM KCl and driven through a nanopipette using externally applied voltages in the range of 100 and 800 mV. The resulting current (nA range) and corresponding resistive spikes (pA range) were measured using an Axopatch 200B (Molecular Devices). The concentration of the nanoliposomes was characterized by analyzing how frequently the particles flowed through the pore within a known volume of liquid. By driving the particles through the pore using a combination of electrophoretic force and negative pressure, the volume flow was calculated as a function of the pressure and the hydrodynamic resistance of the nanopipette. Nanopipettes were fabricated using a Sutter P2000 with an internal diameter of approximately 500 nm.

Results and Discussion: For a given nanopore, the current measured across it is a function of the pore size and the conductive solution (KCl) concentration, both of which are reflected in the measured conductance of the pore (Figure 1a). Once the nanoliposomes passed through the pore, drops in current from this baseline value were produced due to the particles occupying space inside the pore. Ions that were originally present within the nanopore are excluded, thus causing a single particle event (Figure 1b). A larger current drop indicates a larger molecule or particle which can be measured independently from all other particles. From these event detections, each particle was binned and placed on a histogram. The relative current drop ($\Delta I/I$) and event duration are the main properties which are extracted and will be used for future nanoliposome characterization. (Figure 1c and 1d respectively).
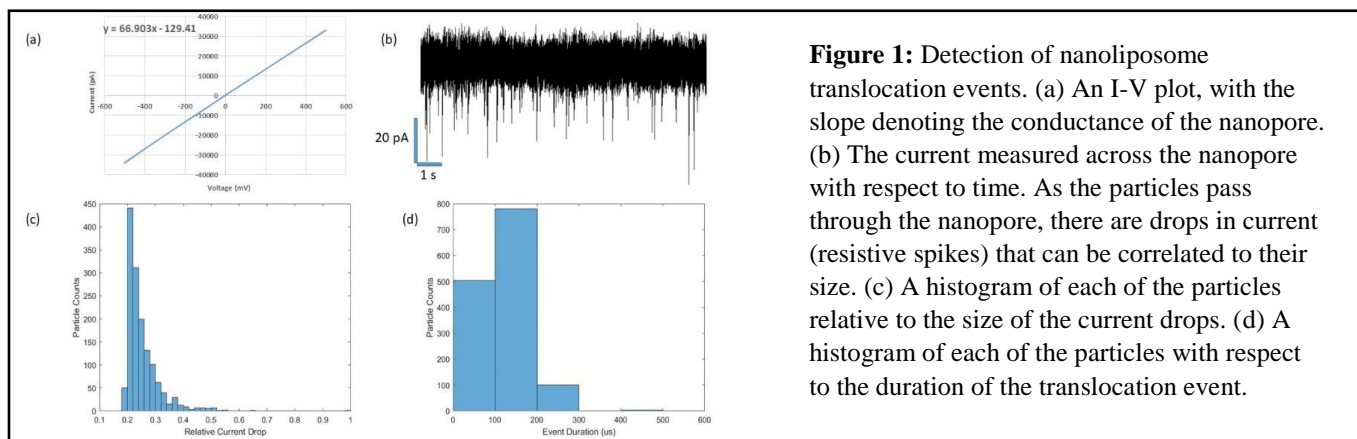
Figure 1: Detection of nanoliposome translocation events. (a) An I-V plot, with the slope denoting the conductance of the nanopore. (b) The current measured across the nanopore with respect to time. As the particles pass through the nanopore, there are drops in current (resistive spikes) that can be correlated to their size. (c) A histogram of each of the particles relative to the size of the current drops. (d) A histogram of each of the particles with respect to the duration of the translocation event.

Conclusion: As shown in this study, nanopore sensing allows for single-particle analysis of the translocated nanoliposomes. Because the drop in current is a function of the geometry of the nanopipette and the diameter of the nanoparticles, using a ratio of the particle diameter to the tip diameter, the size of each of the particles can be extracted. The particle size and concentration are essential metrics for performing dosing experiments with nanoliposomes and for their success as a future nano-therapeutic.

APPLICATION OF OPTICAL FLOW ALGORITHMS TO VISUALIZE PULSATILE BLOOD FLOW

[1]A. Aminfar, N. Davoodzadeh, G. Aguilar, and M. Princevac
[1]Department of Mechanical Engineering, University of California, Riverside, CA
Contact: *aamin006@ucr.edu*

Introduction:
Imaging and measuring blood flow has critical applications in a clinical environment. A high spatiotemporal resolution imaging system can provide accurate measurement of velocity fields and shear stresses. Laser speckle imaging methods are one of the categories of imagery that are gaining interest because of their simplicity and ease of use. Laser speckle effect occurs when a coherent light, such as laser beam, illuminates a rough diffuse surface, which leads to random interference effects. This effect is visualized by a granular pattern consisting of dark and bright spots. Blood vessels can be considered as thin-walled elastic tubes. Once illuminated by laser speckle patterns, the pulsatile flow within thin-walled elastic tubes causes fluctuations in the speckle pattern on the detector. These fluctuations are then correlated to the blood flow.

Materials and Methods:
The apparent displacement of the laser speckle pattern in the image is calculated for all the pixels in the image using optical flow algorithms. Since the apparent optical motion of the pulsatile flow is different from the surrounding tissue, the optical displacement can be used to map the blood vessels.

The mapped image has a high spatiotemporal resolution and is used for visualization and measurement of blood flow inside veins. This methodology, hereafter referred as the Laser Speckle Optical Flow Imaging (LSOFI), is similar to the laser speckle velocimetry.

The architecture of LSOFI is optimal for GPU computing platforms such as Nvidia's CUDA Platform. This enables faster optical flow calculation and therefore a quasi-real time imaging of the arteries.

Results and Discussion:
LSOFI was applied to image the blood flow inside a mouse brain. Although cranial bone limits the spatial resolution and the imaging depth, we were able to visualize the blood veins under the cranial bone. Figure 1 shows the comparison of Laser Speckle Contrast Analysis (LASCA) and LSOFI to the dataset. LSOFI has higher spatial resolution compared to LASCA. It must be stated that for this Dataset LSOFI converges faster, especially when the algorithm runs on CUDA platform.
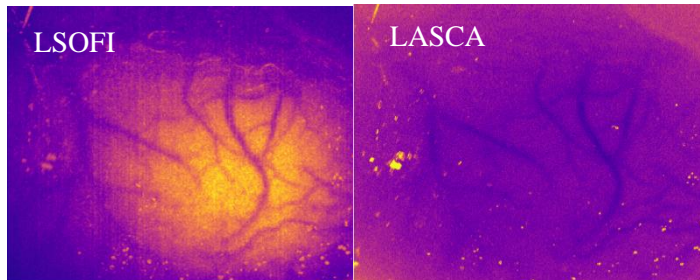
Figure 1: Comparison of spatial resolution of LSOFI and LASCA on the dataset. LSOFI(left) has higher spatial resolution than common LASCA method(right)

Conclusions: The successful deployment of LSOFI technique enabled high spatiotemporal resolution noninvasive imaging method for visualization of blood arteries. CUDA platform reduced the computation time allowing for quasi-real time imaging of the blood flow. This method can be deployed to emended systems such as Nvidia's JETSON to create a fully functional imaging system.

A METHOD OF TISSUE CLEARING TO IDENTIFY CELL TYPES IN THE THYMUS

[1]A. F. Gardner and [1,2,3]J. A. Spencer
[1]Quantitative and Systems Biology Graduate Program, University of California, Merced, CA
[2]Biological Engineering and Small-Scale Technologies Program, University of California, Merced, CA
[3]Department of Bioengineering, University of California, Merced, CA
Contact: *joel.spencer@ucmerced.edu*

Introduction: Clinically, recipients of hematopoietic stem cell transplantation (HSCT) retain a greatly diminished capacity to produce mature T cells in the thymus long after the initial treatment. One of the causes of this delayed capacity lies in the complex relationship between the regeneration of the thymus stroma (mainly composed of vascular endothelial cells, mesenchymal cells, and thymic epithelial cells) and the recruitment of de novo "seeding" thymic progenitor cells (TPCs) from the regenerated bone marrow. Vascular endothelial cells (ECs) are radio-resistant and are involved in TPC recruitment to the thymus. However, in the context of HSCT, it is unknown which type of EC (arterial, venous, or capillary) is radio-resistant, whether all or only a subset of surviving ECs contributes to thymus regeneration, and what role each type of EC plays in TPC recruitment or niche formation. Furthermore, functional damage to the vascular compartment may lead to other microenvironmental changes (e.g., diminished perfusion, hypoxia, and/or increased vascular permeability) that have the potential to negatively impact thymus regeneration and TPC recruitment. Understanding how ECs and the thymus microenvironment respond to cytotoxic therapy may lead to improved therapies for restoring adaptive immunity after cytoreductive therapy. This project seeks to investigate the cells and molecules involved in thymus regeneration and T-cell production after HSCT. Traditionally, to study this, either flow cytometry or immunohistochemistry would be utilized, but these methods lack the sensitivity and/or resolution to detect the arrival of the first TPCs in the context of the whole organ. Therefore, we developed a methodology to fix, stain, and image the whole thymus ex vivo enabling us to observe the recruitment of single TPCs in the context of the whole thymus.

Materials and Methods: Wild-type C57BL/6 mice were irradiated with a lethal dose (9.5 Gy) of gamma irradiation one day prior to transplantation. GFP+ Lymphoid Progenitor Cells (LPCs) from a Ubiquitin-GFP mouse (on a C57BL/6 background) were adoptively transferred into these irradiated mice 24 hours later. On days 1-7 after transplantation, these mice were perfused with 1x PBS, followed by 4% PFA, and then the thymus was removed. The fixed thymus was incubated in donkey serum with fluorescent antibodies that bind to the cell surface markers of interest. Next, the tissue was cleared involving a series of *tert*-butanol dehydration steps followed by incubation in dichloromethane and BABB-D4 and eventually the addition of vitamin E to prevent peroxidase formation. Lastly, the thymus was imaged for 5-10 hours using a two-photon microscope to capture the whole thymus with subcellular resolution.

Results and Discussion: Using our methodology, we were able to locate and identify single TPCs in the thymus. We discovered that TPCs arrive by Day 5 and quickly expand in number within the first few days. We are using this knowledge to design and implement RNAseq analysis of TPCs and stromal cells on Day 5. We also observed TPCs still within the lumen of blood vessels suggesting that live imaging may be used on Day 5 to directly observe cell trafficking in vivo.
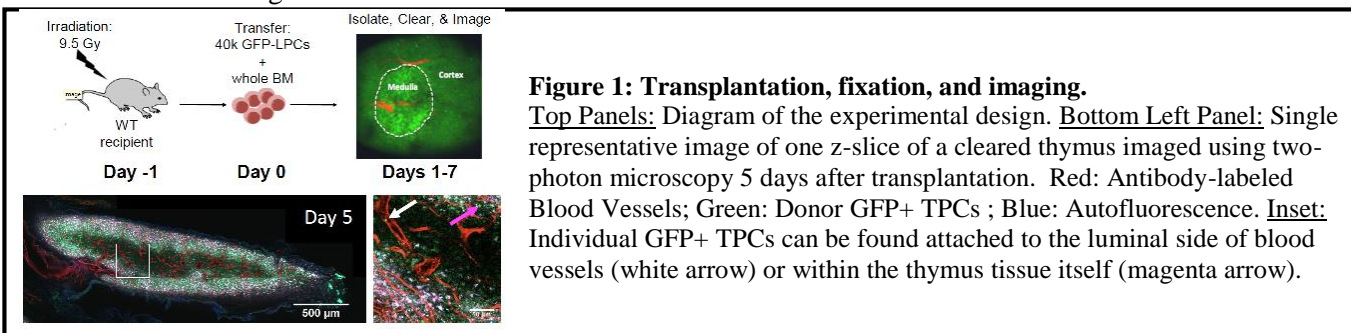
Figure 1: Transplantation, fixation, and imaging.
Top Panels: Diagram of the experimental design. Bottom Left Panel: Single representative image of one z-slice of a cleared thymus imaged using two-photon microscopy 5 days after transplantation. Red: Antibody-labeled Blood Vessels; Green: Donor GFP+ TPCs ; Blue: Autofluorescence. Inset: Individual GFP+ TPCs can be found attached to the luminal side of blood vessels (white arrow) or within the thymus tissue itself (magenta arrow).

Conclusions: We have been able to detect homed cells on day 5 due to the fact that with tissue clearing and imaging we can detect as few as 1 TPC in the whole thymus. Other methods do not have that sensitivity and/or resolution. This methodology is informing us when to isolate TPCs and other thymic populations for characterization and when to attempt live imaging for studying TPC trafficking to the thymus.

IDENTIFYING COREFERENT GENOTYPES IN ONE-WAY CRYPTOGRAPHIC HASH USING HAPLOTYPE INFORMATION

[1]J. C-N. Chang and [2]M. S. Cline

[1]Department of Computer Science, University of California, Sana Cruz, CA
[2]UC Santa Cruz Genomics Institute, Sana Cruz, CA

Contact: [1]*cchan60@ucsc.edu*, [2]*mcline@ucsc.edu*

Introduction: Genome-wide association studies (GWASs) are powered by analyzing and learning from large amounts of data. Due to the sensitive nature of individual-level genotype data, such large datasets are sometimes hard to come by. A common strategy is to merge smaller datasets by identifying and removing duplicate individuals using one-way cryptographic hashing of the genotype [1]. In practice, however, we are often unable to obtain the entire genotype array due to privacy concerns and divergent data collecting purposes. Therefore, we want to find a small subset of SNPs to represent each individual that provides sufficiently low collision rate. In this study, we approach the challenge in selecting SNPs to identify duplicate individuals and explore methods using entropy and Linkage Disequilibrium (LD) [2] information.

Materials and Methods: In this study, we use the 1000 Genome Project dataset [3], with 2504 individuals, each with 5756 SNPs. We filter out all intronic SNPs and genes other than BRCA1 and BRCA2, as our target data sources focus on analyses of the BRCA genes, leaving 525 SNPs. We consider two methods to eliminate SNPs from this set, namely Shannon Entropy and LD information. A low entropy indicates similar allele distribution for a large proportion of patients and hence low distinguishability, so we want to remove SNPs with low entropy. We also use r^2 values in LD information from SNP Annotation and Proxy Search (SNAP) [4] to identify haplotypes, SNPs in which are inherited together and tend to provide similar information. Hence, for SNPs in the same haplotype, we want to only keep a few in our selection. We combine these two methods in two ways: Composite, where we simply apply the two methods sequentially, and Knapsack, where we solve a knapsack problem [5], an optimization problem, with value and weight functions based on entropy and LD.

Results and Discussion: Both methods achieve high identifiability with a relatively small set of SNPs, where identifiability is computed as the fraction of uniquely identified patients. For Composite, we remove SNPs with high r^2 and select the top k SNPs ranked by entropy, varying k. For Knapsack, we empirically determine the maximum weight and vary the selection size k. As a baseline, we simply select SNPs according to their entropy ranking. The results are below. Composite performs best overall. While Knapsack is reasonably good, the baseline surpasses when k is large. We also consider various levels of birth information (not presented). As expected, the granularity in birth information has a positive effect on identifiability.
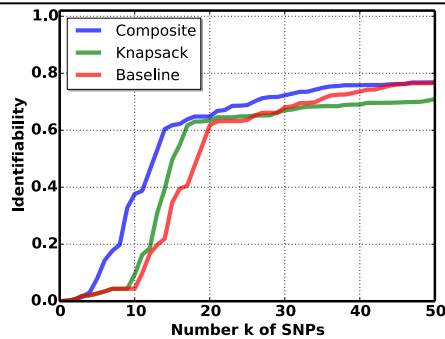
Figure 1: Identifiability versus number of SNPs used. Composite corresponds to results where SNPs with high r^2 are removed, and the top k SNPs, ranked by entropy, are selected; Knapsack corresponds to results where we solve a knapsack problem with a fixed maximum weight; and Baseline corresponds to selecting SNPs based on the entropy ranking only.

Conclusions: We can identify 60% of the individuals with 14 SNPs using the Composite solution. This can be boosted to 93% with 9 SNPs if we also consider the birth year of the individuals.

References:
[1] Turchin, Michael C., and Joel N. Hirschhorn. "Gencrypt: one-way cryptographic hashes to detect overlapping individuals across samples." *Bioinformatics* 28.6 (2012): 886-888
[2]Slatkin, Montgomery. "Linkage disequilibriumâ€"understanding the evolutionary past and mapping the medical future." Nature Reviews Genetics 9.6 (2008): 477.
[3]1000 Genomes Project Consortium. "A global reference for human genetic variation." Nature 526.7571 (2015): 68.
[4]Johnson, Andrew D., et al. "SNAP: a web-based tool for identification and annotation of proxy SNPs using HapMap." Bioinformatics 24.24 (2008): 2938-2939.
[5] Andonov, Rumen, Vincent Poirriez, and Sanjay Rajopadhye. "Unbounded knapsack problem: Dynamic programming revisited." European Journal of Operational Research 123.2 (2000): 394-407.

IONIC LIQUID AQUEOUS TWO-PHASE SYSTEMS
FOR ENHANCED DETECTION OF TRANSFERRIN AND E. COLI

[1]M.F. Yee, [1]G.N. Emmel, [1]E.J. Yang, [1]E. Lee, [1]J.H. Paek, [1,2]B.M. Wu, and [1]D.T. Kamei

[1]Department of Bioengineering, University of California, Los Angeles, CA 90095
[2]School of Dentistry, University of California, Los Angeles, CA 90095
Contact: kamei@seas.ucla.edu

Introduction: Aqueous two-phase systems (ATPSs) have been widely utilized for liquid-liquid extraction and purification of biomolecules, with some studies also demonstrating their capacity as a concentration technique for use in diagnostic settings. As the limited polarity range of conventional polymer-based ATPSs can restrict their use, ionic liquid (IL)-based ATPSs have been recently proposed as a promising alternative, since ILs are regarded as tunable solvents with excellent solvation capabilities for a variety of natural compounds and proteins. This study demonstrates the first application of IL ATPSs to point-of-care diagnostics. ATPSs consisting of 1-butyl-3-methylimidazolium tetrafluoroborate ([Bmim][BF$_4$]) and sodium phosphate salt were utilized to concentrate *Escherichia coli* (*E. coli*) and transferrin (Tf) prior to detection utilizing the lateral-flow immunoassay (LFA).

Materials and Methods: LFAs were constructed in competitive and sandwich formats by printing Tf and anti-*E. coli* antibodies as test line components onto nitrocellulose membranes, respectively. Cherry-colored gold nanoprobes (GNPs) and purple-colored dextran-coated gold nanoprobes (DGNPs) were synthesized by conjugating anti-Tf antibodies onto gold nanoparticles and anti-*E.coli* antibodies onto dextran-coated gold nanoparticles, respectively. [Bmim][BF$_4$], sodium phosphate salt, phosphate-buffered saline, *E. coli* or Tf, and the corresponding colorimetric probe were combined to form a mixed ATPS. The suspension was left to phase separate at room temperature, after which the salt-rich top phase was isolated and applied to an LFA. Positive results would be indicated by the appearance of two lines, in the case of *E. coli*, or one line, in the case of Tf.

Results and Discussion: The phase separation speed of the IL ATPS was found to be very rapid, complete macroscopic phase formation observed within 5 minutes, with both GNPs and DGNPs partitioning preferentially into the top phase. We then compared detection of our ATPS + LFA system with LFA-only tests for both Tf and *E. coli*, the data for which are shown in Figure 1. Tf detection was found to improve 20-fold, while *E. coli* detection was found to improve 8-fold, the difference likely due to screening effects from the ionic nature of the ATPS influencing antigen/antibody binding. Regardless, this constituted significant improvement in the sensitivity of the LFA tests for both competitive and sandwich formats.
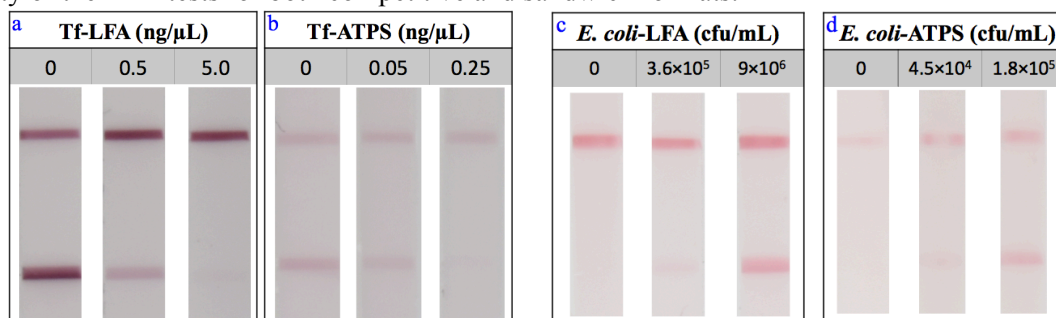
Figure 1: Comparison of tests of LFA only and enhancement with ATPS. Panels a) and b) show 20-fold improvement in transferrin (Tf) through the competitive assay. Panels c) and d) show 8-fold improvement in *E. coli* using the sandwich assay.

Conclusions: We successfully implemented novel use of an IL ATPS for the enhanced detection of biomarkers through the use of the LFA. We found the macroscopic phase separation speed of the IL ATPS to be very rapid and a significant improvement upon the separation speed of both polymer-salt and micellar ATPSs, allowing for direct application to LFA without necessitating modifications to existing LFA structures. This system was successfully applied to both sandwich and competitive LFA formats and enhanced the detection of *E. coli* and Tf up to 8-fold and 20-fold, respectively. We envision that the combination of tunability and speed would allow this system to be used as a flexible, powerful enhancement tool for a wide variety of biomarkers and pathogens.

EFFECT OF HYBRIDIZATION TIME AND CONCENTRATION OF DNA LINKER ON AGGREGATE SIZE OF DNA-CONJUGATED MICROSPHERES

[1]Jianhou Zhang, [1]Brent Kalish, and [1,2,3]Hideaki Tsutsui
[1]Department of Mechanical Engineering, University of California, Riverside, CA
[2]Department of Bioengineering, University of California, Riverside, CA
[3]Stem Cell Center, University of California, Riverside, CA
Contact: *htsutsui@engr.ucr.edu*

Introduction: In recent years, paper-based microfluidics have become an innovative and easy-to-use method for point-of-care (POC) diagnostic microdevices. Microsphere aggregation is a potential method of paper-based microfluidics for DNA sensing and detection. This research looks at the aggregate size and population distribution of DNA oligomer-conjugated microspheres as a function of hybridization time as well as the concentration of the target single-stranded DNA oligomer. The microspheres were conjugated with ssDNA, mixed with linkers of different concentration, and then incubated in the oven for different durations. This research will provide a solid foundation for the development of quantitative paper-based DNA sensors.

Materials and Methods: 1 μm red and blue polystyrene latex carboxylated microspheres were diluted and washed in 2- (N-morpholino) ethanesulfonic acid (MES) and mixed with ssDNA and some related buffer solutions such as phosphate-buffered saline (PBS) and Tris-acetate-EDTA (TAE). Microsphere solutions comprising equal parts two non-complementary strands both partially complementary to a third strand, were incubated and then deposited onto a slide. By microscopy, the aggregate size and population distribution of the microspheres were obtained.

Results and Discussion: At incubation time t=0, there were no visible aggregates for the unconjugated microspheres, 2.31×10^5 aggregates/μL with an average diameter of 2.63 μm for conjugated microspheres without DNA linker and 2.45×10^5 aggregates/μL with an average diameter of 2.87 μm for conjugated microspheres with linker. As time went on, there was no noticeable change in the aggregation of unconjugated microspheres. The aggregate size and quantity increased for both sets of conjugated microspheres, but at a much faster rate for the microspheres with DNA linker. At t=30 min, there were 1.59×10^5 aggregates/μL with an average diameter of 2.89 μm for conjugated microspheres without linker and 2.74×10^5 aggregates/μL with an average diameter of 5.28 μm for conjugated microspheres with linker (Figure 1). After overnight incubation, the aggregate size and quantities did not significantly change compared with those at t=30 min. There were several aggregates of microspheres of same color for all the 3 microspheres mix solutions, likely due to insufficient resuspension after centrifugal washing.
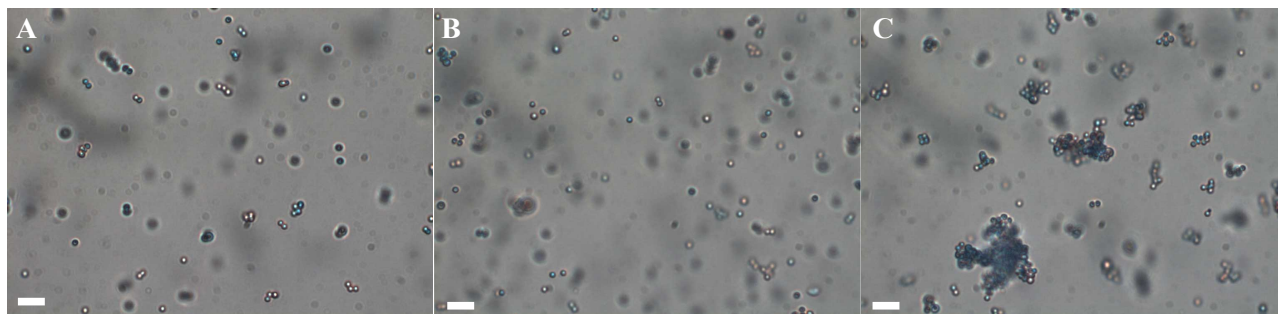
Figure 1: Aggregate size of microspheres solutions (1 μL, 0.13% solid) after a 30-min-long incubation. A) Microspheres unconjugated with DNA Probes. B) Microspheres conjugated with DNA Probes but without DNA linker. C) Microspheres conjugated with DNA Probes with 1 μM DNA linker. Scale bar is 5 μm.

Conclusions: The above work show that the aggregate size of DNA oligomer-conjugated microspheres increases as time goes on. For the specified quantities of ssDNA, the aggregation reaches the maximum value after a 30-min-long incubation.

TOWARDS THE DEVELOPMENT OF A MULTIPLEXD PAPER-BASED BIOSENSOR

[1]S. Modha, [2]Y. Shen, [2,3]A. Mulchandani, and [4]H. Tsutsui
[1]Department of Bioengineering, University of California, Riverside, CA
[2]Department of Chemical and Environmental Engineering, University of California, Riverside, CA
[3]Chair, Material Science & Engineering Program, University of California, Riverside, CA
[4]Department of Mechanical Engineering, University of California, Riverside, CA
Contact: *smodh001@ucr.edu*

Introduction: Substantial efforts have been made to scale down laboratory processes for use in resource-limited settings. Since paper-based microfluidic analytical devices (µPADs) were introduced, the field has grown rapidly in the last decade. The advantages of using paper are lower costs compared to traditional microfluidics and capillary flow, which enables fluid transport without the need for an external pump. The WHO has laid out a set of criteria for diagnostic tools known as the ASSURED (Affordable, Sensitive, Specific, User-friendly, Rapid and Delivered) criteria. Measurement of electrical signals on paper is being pursued to allow qualitative measurement of analytes. Paramount to the functionality of paper-based sensors is the precise control of fluids within the device. Most laboratory procedures require multiple reagents in a specific order. Several electric paper-biosensors are being developed alongside different fluid handling techniques with the overall goal of combining them into a single, multiplexed paper-based sensor.

Materials and Methods: Preliminary studies have been conducted on the measurement of glucose using glucose oxidase (GoX). A Xerox ColorQube 8880 was used to pattern Whatman 5 filter paper to define wax channels in the paper. The wax was then melted, creating hydrophobic regions throughout the thickness of the paper. Carbon graphite paste and Ag/AgCl ink were screen-printed onto the paper to create the conductive electrodes (working, counter and reference electrodes). GoX oxidase solution was dropcasted onto the center of the working electrode (WE) and dried. Various concentrations of glucose were flown into the WE and cyclic voltammetry (CV) and chronoamperometry were used to classify electrode performance and determine glucose concentration on the electrode surface.

Results and Discussion: Electrode performance was classified using a glucose/GoX system. Fig. 1 plots steady-state current response to various concentrations of glucose. A linear dynamic range was established between 0mM and 100mM. These data help validate the utility of paper-based electrochemical sensors. Additional research needs to be done on the robustness of this sensing platform (i.e. effect of sample impurities on device performance). This sensor will be one of several that will be combined onto a single paper-based device. Further research will explore the use of combined enzymatic/immune detection coupled with various fluid control strategies to develop a multiplexed, automated sensor for detection of multiple analytes
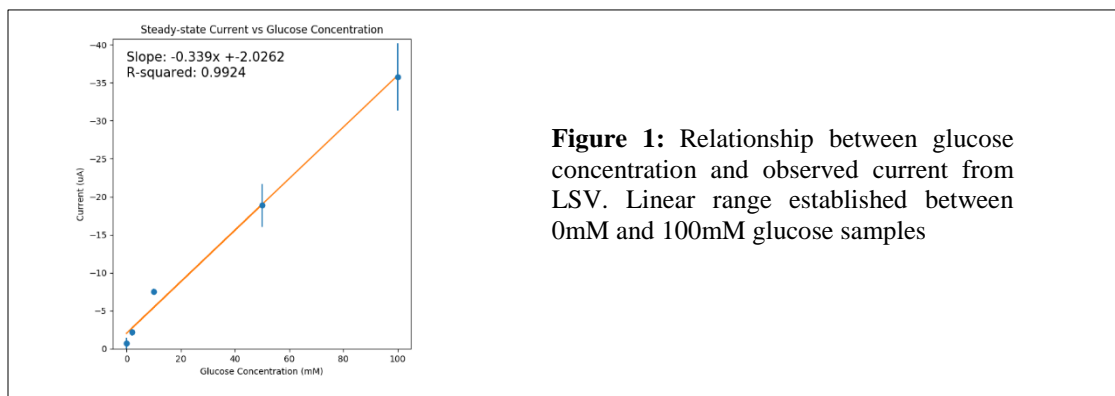
Figure 1: Relationship between glucose concentration and observed current from LSV. Linear range established between 0mM and 100mM glucose samples

Conclusions: Paper-based electric biosensors can offer robust, quantitative measurements for a variety of different analytes. Moreover, these devices can be readily engineered to offer simultaneous detection of different molecules from a single sample. The fabrication techniques used in the study are also amenable to mass-production, meaning that these devices can shipped quickly for field use.

NUCLEIC ACID ENRICHMENT AND ISOTHERMAL AMPLIFICATION ON PAPER

Sherine F. Cheung[1], Benjamin M. Wu[1,2], and Daniel T. Kamei[1]
[1]Department of Bioengineering, University of California, Los Angeles, CA 90095
[2]School of Dentistry, University of California, Los Angeles, CA 90095
Contact: *kamei@seas.ucla.edu*

Introduction: The nucleic acid amplification test (NAAT) is a category of diagnostics that detects for genetic material of bacteria or viruses associated with a disease. Unfortunately, implementation of NAATs in resource-poor settings is limited due to its complex steps, which require expensive equipment, liquid handling, and trained personnel. Thus, we aimed to develop a simplified, paper-based NAAT. We chose to use recombinase polymerase amplification (RPA) – an isothermal DNA amplification method that can be performed entirely at 37°C, thereby mitigating the need for a thermocycler. By dehydrating the RPA reagents on paper, the reagents can be easily stored and transported. In place of centrifugation, DNA sample preparation can be performed in a Triton X-114 (TX-114) micellar aqueous two-phase system (ATPS) – a lightweight and affordable liquid-liquid extraction method. We have previously demonstrated that, upon phase separation, DNA partitions preferentially to the micelle-poor top phase and is concentrated. Thus, genomic DNA samples can be concentrated without equipment, prior to direct application to dehydrated RPA paper pads for amplification.

Methods and Materials: We designed our assay to detect for the model organism enterohemorrhagic *Escherichia coli (E. coli)* O157:H7. Appropriate amounts of RPA reaction components (buffers, nucleotide bases, gene-specific primers, and enzyme mixture) were dehydrated onto fiberglass membranes along with polyethylene glycol 20K and trehalose. Triton X-114 ATPSs with a 1:9 top to bottom volume ratio were made containing the appropriate concentration of magnesium acetate required to initiate the RPA reaction. Varying concentrations of *E. coli* genomic DNA was then added, and the entire suspension was mixed to form a mixed micellar ATPS. Upon phase separation at 37°C, the micelle-poor top phase was extracted, and directly added to the paper membranes containing dehydrated RPA reagents. The paper membrane was heated at 37°C for 20 minutes to allow for amplification. The reaction products were eluted and analyzed via gel electrophoresis.

Results and Discussion: We determined that RPA could be successfully dehydrated and rehydrated on paper membranes for amplification. Specifically, RPA activity was also retained when resolubilized using the ATPS, confirming its compatibility with the micellar ATPS. We identified the detection limit for RPA alone on paper to be 10^3 copies of genomic DNA per reaction. However, when the ATPS was integrated with the RPA on paper, a lower detection limit was achieved, allowing for successful detection and amplification from reactions containing as low as 10^1 copies. These results can be visualized in Figure 1. Thus, combining ATPS with dehydrated RPA on paper led to a 100-fold improvement in the detection limit.
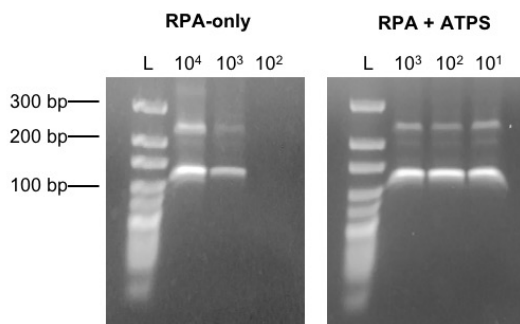
Figure 1. Results of DNA amplification with RPA-only (left) and integrated RPA + ATPS (right). Successful amplification was determined by the presence of a band corresponding to the expected 229 bp DNA product. The RPA-only reaction successfully amplified DNA from a reaction containing 10^3 copies of genomic DNA, while RPA + ATPS successfully amplified DNA from samples containing as low as 10^1 copies. "L" denotes the lanes containing the DNA ladder, and the numbers above the image are the number of copies of genomic DNA per reaction. The secondary ~120 bp band that appears is a primer artifact common to RPA reactions.

Conclusions: In this study, we have developed an improved NAAT for *E. coli* O157:H7 by combining a micellar ATPS for DNA sample preparation with RPA DNA amplification in a paper platform. This is also the first known application of ATPS with an isothermal DNA amplification on paper. Furthermore, we have demonstrated that the paper-based RPA + ATPS integrated method has an improved limit of detection compared to the RPA on paper alone. By pairing this DNA concentration and paper-based amplification with a sequence-specific probe for downstream lateral-flow detection, we anticipate that a fully integrated and low-cost sample-to-detection device can be achieved. We envision that our platform can be applied to other pathogens, and its minimized dependence on laboratory equipment can help advance NAAT technology for point-of-care use.

MODELING OF SOLID-FLUID FLOW IN MICROFLUIDIC SYSTEMS
FOR SORTING ASPHERICAL PARTICLES

[1]R. Yeung, [1]W. Grover, [2]P. Brisk, [1]V. G. J. Rodgers
[1]Department of Bioengineering, University of California, Riverside, CA
[2]Department of Computer Science and Engineering, University of California, Riverside, CA
Contact: *ryeun003@ucr.edu*

Introduction: The ability to predict the motion of particles in arbitrary fluid flow fields is critical for the design and optimization of particle sorting-based microfluidic devices. Particle tracing methods from commercial computational fluid dynamics (CFD) software treat particles as point masses and resolves the forces on the particles using spherical particle size-dependent correlations. Many particle sorting applications, however, deal with non-spherical particles, many of whose force coefficient expressions are not well-characterized and whose surfaces are not continuously differentiable [1,2]. The particle tracing methods are also not well-suited to model particle-wall interactions [3]. In this study, we present a finite element CFD model that takes into account solid bodies using an arbitrary Lagrangian-Eulerian (ALE) framework for two-way coupled fluid-structure interaction (FSI) with extension to the case of fluid-immersed, non-spherical solids interacting through contact. To validate the performance of the simulations, we used the method to model the motion of flat, rectangular particles in various microfluidic designs and compared the results to the trajectories observed in particle sorting experiments.

Materials and Methods: The finite element analysis software, COMSOL Multiphysics (COMSOL Inc., Burlington, MA), was used for the two-dimensional CFD simulations. The FSI interface was utilized to combine fluid flow with solid mechanics to capture the interaction between the fluid and the solid structure. A Lagrangian formulation is used for the solid mesh and an ALE formulation is specified for the deforming fluid mesh.

Designs for the microfluidic chips were constructed using the Inkscape vector graphics software. Single-layered microchannels were etched from acrylic sheets using a computer numerical control (CNC) mill and subsequently sealed onto flat acrylic sheets. Square micron-sized particles ($600 \times 600 \times 100 \, \mu m$) diced from a silicon wafer were seeded into the microfluidic chips with fluid (deionized water) being delivered by a syringe pump at set flow rates. Particle trajectories were captured using a high-speed complementary metal-oxide-semiconductor (CMOS) camera at 1600 frames per second and the videos were analyzed using the Open Computer Vision Library (OpenCV) implemented by the Python programming language.

Results and Discussion: The CFD simulations for the transport of rectangular particles in fluid flow along microchannels are able to resolve fluid-particle and particle-particle interactions. As shown in Fig. 1, the wake of the leading particle influences the drag which the trailing particle experiences. Parametric studies of the initial longitudinal spacing between two particles for simulations with an inlet flow velocity of 0.01 m/s indicate spacing of less than 1.4 mm is necessary for the trajectories of the particles to be affected by the presence of one another. Evaluation of the velocity profiles for models with inlet flow velocities of 0.02 m/s and 0.1 m/s reflect that the wake-influenced region between the two interacting particles can be longer at higher Reynolds number.
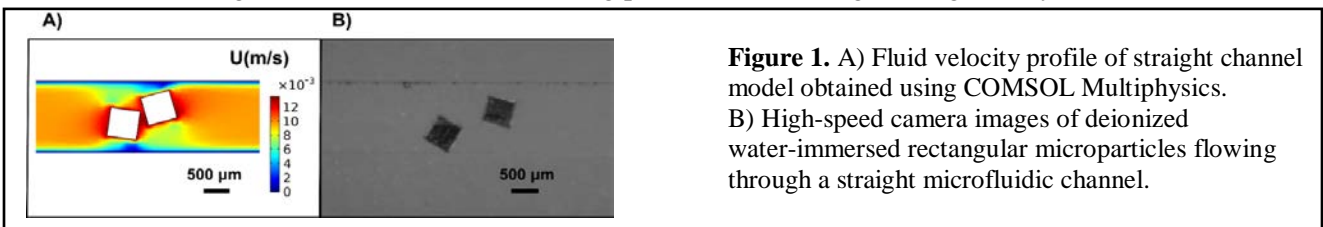
Figure 1. A) Fluid velocity profile of straight channel model obtained using COMSOL Multiphysics. B) High-speed camera images of deionized water-immersed rectangular microparticles flowing through a straight microfluidic channel.

Conclusions: The results of the finite element CFD simulations using the ALE-Lagrangian formulations for the respective fluid and solid domains indicate the method can solve fluid-structure coupling problems to determine trajectories of aspherical particles. For future work, methods for resolving submerged solid contact will be incorporated into the models. Three-dimensional models will also be used to evaluate particle tumbling.

References:

[1] Hur, S. C., Choi, S., Kwon, S., Di Carlo, D. Appl. Phys. Lett., **99**, 044101 (2011).
[2] Zastawny, M., Mallouppas, G., Zhao, F., Van Wachem, B. Int. J. of Multiph. Flow, **39**, 227-239, (2012).
[3] Wang, J., Rodgers, V. G., Brisk, P., & Grover, W. H. Biomicrofluidics, **11**(3), 034121 (2017).

Modeling Flow Separation of Aqueous Two-Phase System Imbibition in Porous Media

[1]So Youn Lee, [1]David Y. Pereira, [1]Chloe M. Wu, [1,2]Benjamin M. Wu, and [1]Daniel T. Kamei
[1]Department of Bioengineering, University of California, Los Angeles, CA 90095, USA
[2]School of Dentistry, University of California, Los Angeles, CA 90095, USA
Contact: emilylee1107@g.ucla.edu

Introduction: Although the lateral-flow immunoassay (LFA) is an inexpensive and rapid paper-based assay that is promising for detecting infectious disease biomarkers, its sensitivity needs to be improved. Previously, our group successfully demonstrated that aqueous two-phase systems (ATPSs) can be used to concentrate biomolecules and improve their LFA limit of detection by 10-fold. We then subsequently discovered that the application of the mixed ATPS solution directly onto a paper membrane enhances its phase separation, significantly reducing the required separation time. However, since this phenomenon is not fully understood, we applied a mathematical model to more accurately predict two-phase system wicking behavior in paper-based devices. Such a model could then be used to determine the optimal concentrations and volumes of two-phase components that are required to produce a specific flow pattern.

Materials and Methods: In order to model the phase separation phenomenon, we examined the Washburn equation, where the fluid in a porous medium is modeled as flowing through a bundle of identical capillary tubes. We first measured the bulk phase fluid properties of four different ATPSs: polyethylene glycol (PEG)-potassium salt, Triton X-114, PEG-dextran, and PEG-polyacrylic acid. We then used these measured properties in the Washburn model to analyze and predict the phase separation capabilities of each ATPS when wicking in fiberglass paper. Finally, we further tested the model by investigating its ability to predict enhancement of ATPS phase separation in completely different porous media, the microporous polyethylene glycol dimethacrylate (PEGDMA)-based hydrogels.

Results and Discussion: Analysis of the PEG-salt and Triton X-114 ATPSs confirmed that the flow of their individual phases followed the Washburn equation (Figure 1). Comparing the fluid phase properties involved in determining the flow rate in the Washburn equation, we identified the viscosity difference between the two phases of an ATPS to be a key determinant of enhanced phase separation on paper. Using this information, we successfully predicted the phase separation behavior of PEG-dextran and PEG-polyacrylic acid ATPSs on paper. Lastly, the model was successfully extended to predict the phase separation behavior of the four ATPSs in hydrogels, generalizing our observations to porous media other than paper.
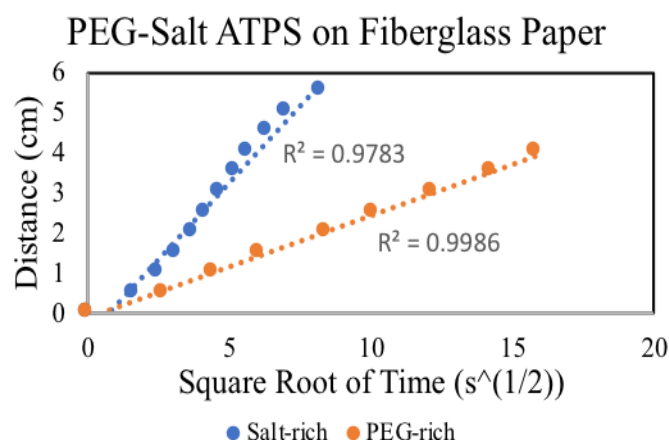
Figure 1. Both PEG-rich and salt-rich phases demonstrated linear relationships between distance and the square root of time, following the Washburn equation.

Conclusions: In the current study, we made the first step toward developing a theoretical framework to model and describe the phase separation of ATPSs applied to paper membranes. Using this framework, we identified the viscosity difference between the two phases of an ATPS as a dominant factor in determining the leading and lagging phases on paper. We also extended this framework to predict and demonstrate phase separation of ATPSs in PEGDMA hydrogels, demonstrating that the phase separation enhancement can potentially apply to porous media in general.

RESPIRATORY SOUNDS AS A SOURCE OF DIAGNOSTIC INFORMATION IN PULMONARY OBSTRUCTION DISEASES

[1,4]F. Lopot, [1,4]D. Skalický, [2]V. Koucký, [3]M. Vítězník, [3]A. Holubová, [1]D. Hadraba, [1]K. Jelen, [3]P. Smrčka, [2]P. Pohunek

[1]Department of Anatomy and Biomechanics, Charles University, Prague, Czech Republic
[2]Dep. of Information and Communication Technology in Medicine, Czech Technical University, Czech Republic
[3]Department of Paediatrics, Charles University and Motol University Hospital, Prague, Czech Republic
[4]Dep. of Designing and Machine Elements, Czech Technical University, Czech Republic

Contact: *flopot@seznam.cz*

Introduction: Around 300 million people worldwide at widely varying age suffer from asthma [1]. Patients with this disease have primarily difficult breathing with wheezing in respiratory sounds, cough and feeling of constricted chest and their physical activity is therefore strongly limited. Early diagnosis of asthma improves its treatment by allowing choose optimal medication. However, symptoms of asthma can be confused with other respiratory diseases and without appropriate collaboration of the patient, exact asthma diagnose is quite complicated [2]. This paper presents our idea of non-invasive method of pulmonary obstruction diseases diagnosis based on detection of typical wheezing phenomena in respiratory sound records.

Materials and Methods: In an ongoing project, respiratory sounds records are obtained from pediatric patients at Pneumology Department of the University Hospital in Prague – Motol in frame of their standard planned examination. The broad-band recording instrumentation for acquisition of bioacoustig signals is designed for use in pediatric patients whom it evokes conventional stethoscope. The system consists of the following components: combined sensor set, amplifier, A/D converter and operational software. Innovative construction of the sensor set combines several different methods for bioacoustic signals synchronized in time domain. Input signals are first amplified by a low-noise pre-amplifier of our own construction and then digitalized by means of multiple channel interface with sampling frequency of 192 kHz and 24 bit resolution. The system has an internal storage. The data can be further transferred to a PC via an USB or Bluetooth for final processing and investigation. Operational software offers graphical interpretation of the data and enables highlight specific frequency range, suppression of artifacts etc. Signal processing is based on the Fourier and Wavelet transforms.

Results and Discussion: The measurements performed so far exhibit 100% correspondence with spirometry considered nowadays a golden standard. It is encouraging that some obstruction phenomena undetectable by conventional auscultation are reliably identified by our method. Our results are also supported by a number of works which has found wheezings in asthmatic patients in the frequency range from 400 to 800 Hz, e.g. [3].
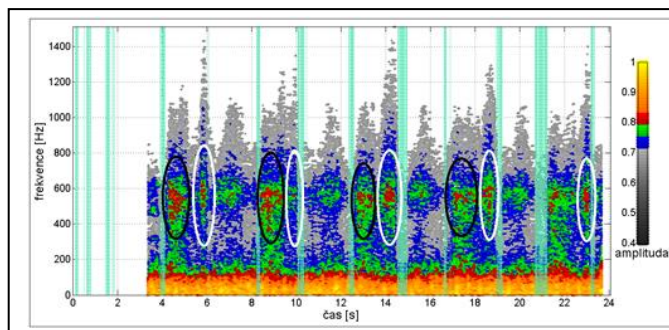
Figure 1: Graphical data interpretation (wheezings marked by black ovals are detected both by auscultation and our method; those marked by white ovals by our method only)

Conclusions: Development of the instrumentation and the method is still going on. From medical point of view, current results prove that detailed analysis of respiratory sounds may bring highly significant additional information about the obstruction disease character and patients condition.

References:
[1] Teřl, M., Pohunek, P. Strategie diagnostiky, prevence a léčby astmatu: uvedení globální strategie do praxe v ČR. Praha: Jalna, 2012.
[2] Ayres, Jon G. Asthma. 1. vyd. Praha: Grada, 2001. ISBN 80-247-0091-3.
[3] Sengupta, N., Sahidullah, Md., Saha, G. Lung sound classification using cepstral-based statistical features, Computers in Biology and Medicine, vol. 75, pg. 118-129, Elsevier, 2016

MEASURING CHANGES IN NANOFLUIDIC CURRENT AS A CONTINUOUS MULTI-ANALYTE BIOSENSOR FOR BIOLOGICAL FLUIDS

Austin S. Abrams, Bing Wang, Bridget N. Queenan, Guillermo C. Bazan, and Sumita Pennathur
University of California, Santa Barbara, Santa Barbara, CA

Introduction: In this work, we show a novel scheme for monitoring biological reactions through the change of current in a nanochannel. Our versatile system incorporates a bioreceptor onto the surface of a nanochannel that converts a target binding event into a change of surface potential, which can be subsequently monitored via changes in current.

Materials and Methods: To validate this scheme, we chose glucose binding to diboronic acid (DBA) as a model system. Specifically, we functionalized inner surfaces of fused silica capillary tubing with a DBA compound that changes pKa upon glucose binding. Consequently, DBA switches its net charge from positive (– glucose) to neutral (+ glucose) in physiological pH ~7.4, which in turn changes the surface potential (ζ) of the channel. Therefore, simply measuring surface charge can allow for a unique indirect measurement of glucose concentration. To do so, we apply a well-known technique known as current monitoring. In this technique, we measure the time to traverse the channel through changing solution concentrations on either side of the channel, thereby changing the current. From monitoring current, we can determine the zeta potential though the Helmholtz–Smoluchowski equation.[1]

Results and Discussion: Results are shown in the figure below, where we tested our glucose sensor by measuring ζ of DBA-modified capillaries in phosphate-buffered saline (PBS) solution with varying concentrations of glucose. Following DBA-surface modification, we measured ζ to increase by more than 170 mV. This significant increase in ζ agrees with the expected change in surface charge as positive DBA groups replace negative silanol sites on the surface. Consequently, we observed ζ to decrease over 110 mV after exposure to glucose (10 mM in PBS). Thus, we observed that in the presence of glucose, DBA surface sites are neutralized. These preliminary findings demonstrate the promising capability of this tailored yet versatile design to sense glucose and eventually multiple analytes in biological fluids. Furthermore, this compact, affordable, reagentless, and reusable platform is far superior to the handful of systems currently offered for point-of-care or on-body health monitoring.
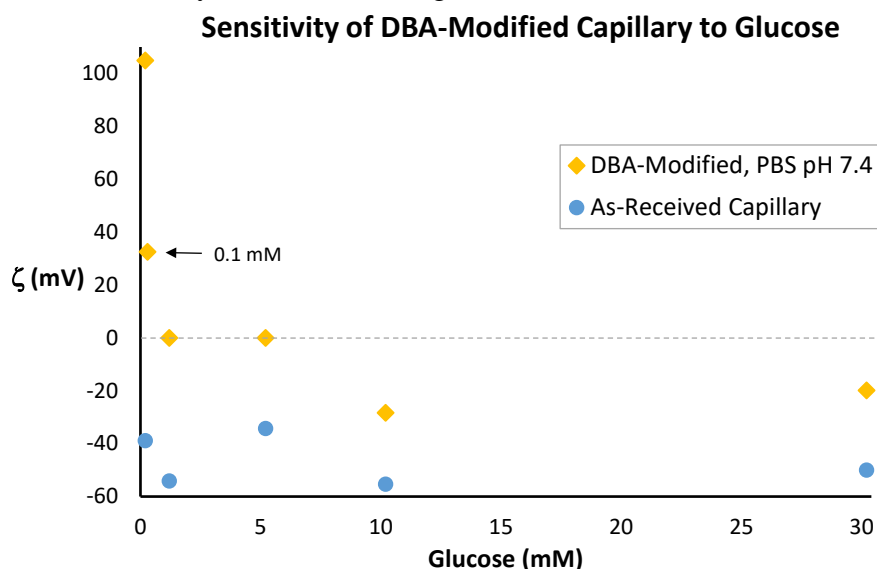
(1) Rice, C. L.; Whitehead, R. Electrokinetic Flow in a Narrow Cylindrical Capillary. *J. Phys. Chem.* **1965**, *69* (11), 4017–4024.

EPIGENETIC REGULATION DURING TOPOGRAPHY-INDUCED CARDIOMYOCYTE MATURATION

[1]J. Morival, [2]J. Naik, [1]K. Phan, [1]A. Grosberg, and [1]T. Downing
[1]Department of Biomedical Engineering, University of California, Irvine, CA
[2]Department of Chemical Engineering and Materials Science, University of California, Irvine, CA
Contact: *tim.downing@uci.edu*

Introduction: Stem cell-derived cardiomyocytes have great therapeutic potential for the treatment of heart diseases. Although promising, protocols used to differentiate stem cells into cardiomyocytes often retain properties of immature cells. It was recently shown that neonatal rat ventricular myocytes (NRVMs), when seeded on patterned substrates that mimic the anisotropic structure of the native myocardium, had a gene expression closer to mature cardiomyocytes than when seeded on an unpatterened (isotropic) substrate. Our lab and others have demonstrated that substrate topography can influence cell behavior through epigenetic mechanisms. Understanding how NRVM maturity is affected by topography through epigenetics can therefore be beneficial for future tissue engineering applications. We aim to characterize differences in the epigenetic landscape that are induced through surface topography and assist in cardiomyocyte maturation.

Materials and Methods: Coverslips were coated with PDMS and stamped with fibronectin (FN) either over the entire coverslip (isotropic surface) or patterned into 20µm wide lines spaced every 5µm (anisotropic surface). Primary NRVMs were harvested and left to adhere onto the coverslips for 24 hours (Fig. 1A). To understand how DNA methylation may be involved in cardiomyocyte maturation, cells were then treated with RG108, a DNA methylation inhibitor, for either 24 or 48 hours (Fig. 1B). Coverslips were then fixed and stained to reveal the nuclear, actin, and sarcomere structures of the cells. Following image acquisition, the orientational order parameter (OOP), which returns a value between zero (unorganized tissue) and one (perfectly aligned), was calculated for actin and sarcomere structures (Fig. 1C,D). The effect of topography on histone modifications was tested for by staining cells for H3K4me3 (Fig. 1E).
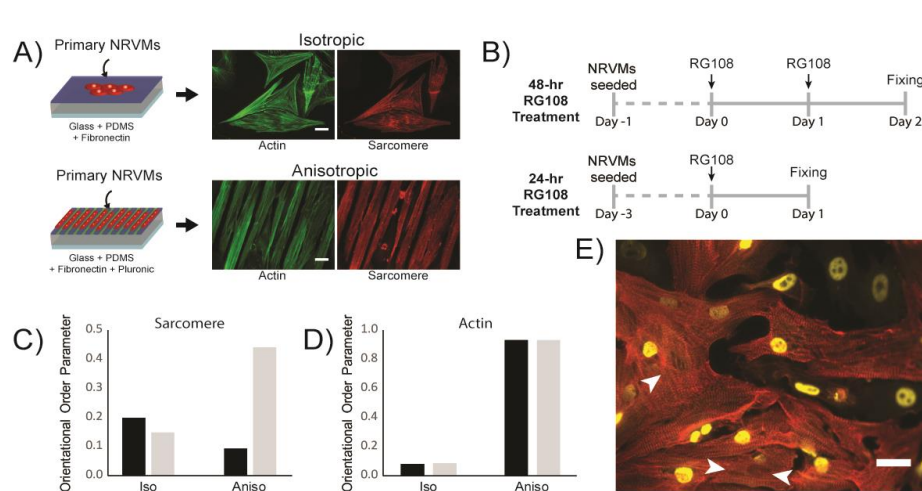
Figure 1. (A) Immunostaining of actin and sarcomere structures for isotropic (top row) and anisotropic (bottom row) conditions. (B) Timeline for RG108 treatment of NRVMs. (C) Plot showing the OOP values for sarcomere, in 24-hr treatment of RG108 (black) and control (grey) conditions. (D) Similar plot showing the OOP values for actin. (E) Immunostaining of isotropic 48hr RG108-treated NRVMs. Stains show sarcomere structures (red), and H3K4me3 (yellow). White arrowheads indicate nuclei locations without H3K4me3 staining. Scalebars = 50 µm.

Results and Discussion: We observed that cells seeded on anisotropic surfaces, when treated with RG108 for 24 hours, had a sarcomere OOP of 0.09, while non-treated controls exhibited a sarcomere OOP of ~0.5 (Fig. 1C). Interestingly, this value returned to 0.42 in the 48-hour treatment condition. This apparent delay in sarcomere OOP could suggest that RG108 is slowing down cardiomyocyte maturity. This deviation from control OOP values, however, was not present in isotropic cells or in actin OOP for both conditions (Fig. 1C,D). Finally, staining cardiomyocytes with H3K4me3 revealed that some cells exhibited nuclear localization of the histone modification, while others had it dispersed in the cytoplasm (Fig. 1E). Analysis of OOP between nuclear and non-nuclear H3K4me3-containing cells, however, did not show any significant difference for both sarcomeres and actin, in any of the studied conditions.

Conclusions: These preliminary findings suggest that epigenetic mechanisms may be important for topography-induced cardiomyocyte maturation.

Role of Intracellular Structures in the Direct Conversion of Fibroblasts into Neurons

Jennifer Soto[1], Sze Yue Wong[2], Julia Chu[2], Song Li[1]
[1]Department of Bioengineering, University of California Los Angeles, Los Angeles, CA
[2]Department of Bioengineering, University of California Berkeley, Berkeley, CA
Contact: *Jennifer.soto@ucla.edu*

Introduction: Direct reprogramming is the process of converting from one cell type into a very distantly related cell type without proceeding through an intermediate proliferative stem-cell like stage. In 2010, Vierbuchen *et al* demonstrated that mouse embryonic and postnatal tail-tip fibroblasts can be converted into induced neuronal (iN) cells via the forced expression of three transcription factors Brn2, Ascl1, and Myt1l. Since then, multiple groups have shown how various combination of transcription factors and microRNAs can be used to yield different neuronal subtypes. More recently, it has been shown that chemical cocktails can be used to directly convert fibroblasts into neurons. Although the roles of transcription factors and soluble biochemical factors in direct reprograming have been widely studied, how the cell cytoskeleton may regulate induced neuronal reprograming through mechanotransductive pathways is not well understood. Thus, the objective of this study was to investigate the role of various intracellular structures in the direct conversion of mouse fibroblasts into functional neurons.

Materials and Methods: To elucidate the role of the cytoskeleton, focal adhesions and nuclear matrix in direct iN reprogramming, we have utilized reprogramming technology in conjunction with small molecule compounds that are known to modulate these intracellular structures. For reprogramming experiments, adult mouse fibroblasts were transduced with doxycycline-inducible lentiviral vectors encoding the three key reprogramming factors, Ascl1, Brn2, and Myt1l (BAM), and seeded onto laminin-coated tissue culture dishes wherein fibroblasts were treated with various chemical inhibitors. After two weeks, induced neuronal cells were identified via immunostaining for neuronal beta-III tubulin (TUJ1) and the reprogramming efficiency was determined. For mechanistic studies, fibroblasts were treated with chemical inhibitors or siRNA and analyzed using Western blotting, immunostaining, and qRT-PCR techniques.

Results and Discussion: Here we show, for the first time, that disruption of actin-myosin contractility via treatment with blebbistatin can enhance the efficiency of induced neuronal conversion (Figure 1). The derived iN cells displayed a typical neuronal morphology, expressed neuronal markers and exhibited functional neuronal properties. The involved mechanism relied on the modulation of fibroblast and neuronal marker expression by blebbistatin. We found that blebbistatin downregulated fibroblast markers while concurrently upregulated neuronal genes. Furthermore, our findings suggest that focal adhesions and the nuclear lamina play a critical role in this direct reprogramming process.
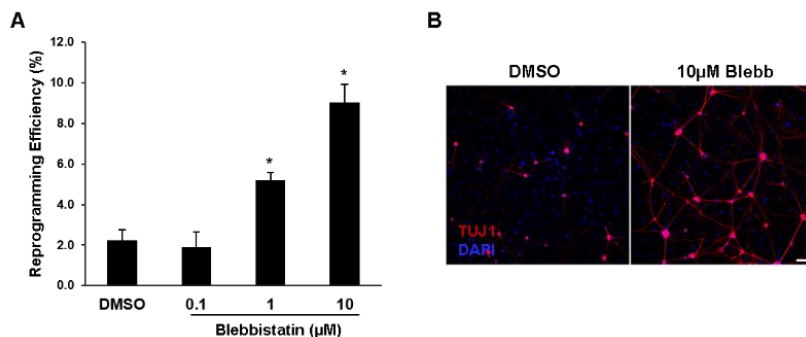
Figure 1 Inhibition of actin-myosin contractility improves induced neuronal conversion. **A.** Reprogramming efficiency of fibroblasts transduced with BAM and cultured in the presence of blebbistatin at various concentrations. **B.** Representative fluorescent micrographs of iNs generated in the absence and presence of blebbistatin.

Conclusions: In essence, our findings highlight that the disruption of intracellular mechano-structures can regulate the direct reprogramming of fibroblasts into induced neurons. By investigating signaling pathways, these novel findings can provide insights into the mechanisms that determine cell fate as well as identify potential targets that can be used to further enhance this process for potential applications in neurological disease modeling and drug discovery.

ASSESSMENT OF TEMPLATE TUNING PROPERTIES FOR VIRAL-DIRECTED SYNTHESIS OF INORGANIC MATERIALS

[1]Zaira Alibay, [2]Joshua M. Plank, [1]Tam-Triet Ngo-Duc, [1,2]Elaine D. Haberer

[1]Materials Science and Engineering Program, University of California, Riverside
[2]Department of Electrical and Computer Engineering, University of California, Riverside
Contact: *haberer@ucr.edu*

Introduction: Viruses are widely known biological macromolecules with self-assembly and molecular recognition capabilities. Genetic modification of viruses to include high affinity peptide fusions allows templating of a variety of materials, and formation of hierarchical nanoarchitectures. Despite the success of biotemplate employment, there is a significant disadvantage: the geometry of the scaffold cannot be drastically changed. A different virus with the required architecture must be individually engineered. The desire to develop a viral scaffold with geometry tuning capability, while preserving its material binding properties has led us to study M13 bacteriophage transformation. The M13 bacteriophage is a high aspect ratio, 880 nm long and 6.5 nm diameter filamentous virus. It contains approximately 2700 copies of p8 major coat protein along its length and 5 copies of p3 minor coat protein at the proximal end of the filament. An extensive collection of peptides with affinity for an array of materials has been developed for and is compatible with this biotemplate. Moreover, during the infection process, the M13 can contract from nanowire to rod and spheroidal structures upon exposure to nonpolar media. This is a considerable advantage, since it enables low-cost manufacturing of variable nanoarchitectures under mild conditions.

Materials and Methods: Circular dichroism spectroscopy was employed to study the structural changes which accompanied the morphological modification. I-form peptide fusion functionality was assessed through templated Au synthesis. Size, growth rate and crystallinity of the resulting Au nanostructures were investigated by transmission electron microscopy and electron diffraction techniques (see Figure 1).

Results and Discussion: In this work, genetically-modified bacteriophage with Au- and ZnS-binding peptides displayed on the p8 and p3 sites, respectively, have been transformed via chloroform treatment into 182 nm long and 20 nm diameter rod structures, known as intermediate- or i-forms. Synthesis of Au on the the transformed virus showed the preservation of binding peptides on the surface of the templates.
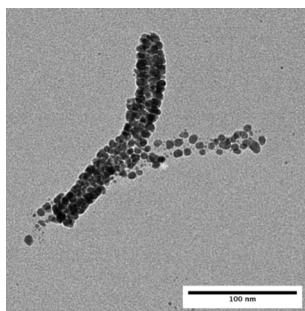
Figure 1: Transmission electron microscope images of Au-ZnS-binding i-forms after synthesis of gold. Distinct gold nanoparticles formation was observed on the templates.
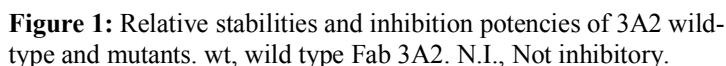
Conclusions: This research shows that fine-tuning of the virus geometry allows assembly of inorganic materials with desired morphological and optical properties.

The study of MMP-14 inhibitory antibody isolated from a long CDR-H3 synthetic Fab library

Ki Baek Lee, Xin Ge

Department of Chemical and Environmental Engineering, University of California, Riverside, CA

Contact: *xge@engr.ucr.edu*

Introduction: Playing pivotal roles in tumor growth and metastasis, matrix metalloproteinase-14 (MMP-14) is an important cancer target. Potent inhibitor fragment antigen-binding (Fab) 3A2 with therapy-desired high selectivity has been isolated from a synthetic antibody library carrying convex paratopes. However, the inhibition mechanism of Fab 3A2 has not been extensively studied. In addition, like many standard mechanism protease inhibitors, Fab 3A2 can be cleaved by high concentrations of MMP-14 after extended incubation, and thus could result in relatively short half-lives and even untoward side effects caused by truncated proteins. For therapeutic applications, it is necessary to identify the paratope of Fab 3A2 and improve its proteolytic stability while retaining its binding affinity, inhibition potency and high selectivity.

Materials and Methods: To identify the binding site on Fab 3A2, the complex of Fab 3A2 and MMP-14 catalytic domain (cd) was simulated and six residues on CDR-H2/H3 were identified for Ala scanning mutagenesis. These 3A2 mutants were then tested for binding affinity and inhibition functions. To precisely identify the cleavage position on 3A2 by MMP-14, the generated Fab 3A2 fragment was subjected to Adman degradation for N-terminal amino acid sequencing. By comparing the cleavage site sequence of Fab 3A2 with MMP-14 substrate specificity, we chose three residues P1 (N100h), P1' (L100i), and P3' (A100k) as the target positions for performing site-saturation mutagenesis. Periplasmic fractions including produced Fab 3A2 variants were prepared and incubated with cdMMP-14, then analyzed by western blotting with anti-Fab-HRP to compare both full-length Fab and truncated HC and LC fragments.

Results and Discussion: For improving the proteolytic stability of Fab 3A2, by introducing site-directed mutagenesis at its cleavage site, mutations at P1' (L100i) resulted in loss of inhibition function (Fig 1), suggesting that Leu at P1' was needed for the inhibitory activity of Fab 3A2. Among tested 3A2 Fab mutants at P1 (N100h) and P3' (A100k) positions, three P1 mutants, two P3' mutants, and two double mutants exhibited stability improvements, however with 1.3-2.6 fold decreases of inhibition potency (Fig 1). On the contrary, five P1 mutants, one P3' mutant, and three double mutants showed significant improvements in both stability and inhibition potency (Fig 1). The majority of these mutants with improved stability were substitutions to either hydrophobic (e.g. Lue, Ile, Trp) or basic residues (Arg, Lys). Particularly, double mutant N100hR/A100kR exhibited a 7.5-fold of stability enhancement and inhibition potency of 10 nM. Results on paratope mapping Fab 3A2 will also be discussed.

Figure 1: Relative stabilities and inhibition potencies of 3A2 wild-type and mutants. wt, wild type Fab 3A2. N.I., Not inhibitory.

Conclusions: In this study, the role of residues of a MMP-14 inhibitory antibody interacting with MMP-14 has been extensively identified. In addition, the cleavage site on a standard mechanism inhibitory antibody was identified, and site saturation mutagenesis near its cleavage site was introduced and tested for improved proteolytic stability.

Investigating the Effects of Homotypic Paracrine Signaling in Macrophage Activation

[1]S.J. Hsu, and [1]W.F. Liu

[1]Department of Biomedical Engineering, University of California, Irvine, Irvine, CA, 92697
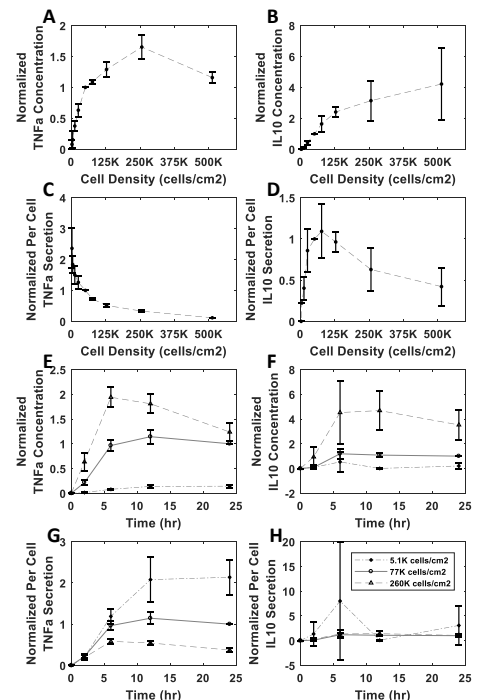
Contact: *wendy.liu@uci.edu*

Introduction: Macrophages perform an important role in mediating inflammation following injury and infection. Recent studies on single cell transcriptional and secretory responses of immune cells have highlighted the significance of paracrine signaling from a small population of cells in coordinating innate immune responses, but much details regarding the role of paracrine interactions remain to be explored [1,2]. Thus, better understanding of this process could provide new strategies to modulate inflammatory responses. In this study, we aim to characterize the effect of the cellular environment on LPS and IFNγ induced macrophage activation by stimulating bone-marrow derived macrophages (BMDM) cultured at different cell densities. Our findings suggest that soluble paracrine signals inhibit secretion of inflammatory cytokine TNFα, and while secreted product is necessary for IL10 secretion, excess signals inhibit IL10 responses.

Materials and Methods: BMDM were obtained by harvesting bone marrow from C57BL/6J mice and culturing in DMEM containing FBS and M-CSF for 7 days to induce differentiation. Cells were seeded in different densities ranging from $5.1x10^5$ to $2.6x10^3$ cells/cm^2 onto glass slides, allowed to adhere overnight, and stimulated with 10 ng/ml of LPS and IFNγ for 24 hours before supernatants were collected. In addition, cells were seeded onto tissue culture polystyrene at the density of $5.1x10^3$, $7.7x10^4$, and $2.6x10^5$ cells/cm^2, supernatants were collected at 2, 6, 12, and 24 hours following stimulation for time course analysis. The supernatants were analyzed with ELISA to determine secreted TNFα and IL10 concentrations.

Results and Discussion: We found that cells seeded at different densities secreted different amounts of TNFα and IL10 following LPS/IFNγ stimulation. As cell densities were increased from $2.6x10^3$ to $2.6x10^5$ cells/cm^2, secreted TNFα levels concomitantly increased. However, at densities higher than $2.6x10^5$ cells/cm^2, levels of TNF-a decreased, suggesting that paracrine interactions may feed-back inhibit further secretion. IL10 concentration exhibited a similar increasing trend but without a decrease at higher cell densities. Analysis of TNFα secretion per cell showed a consistent decrease with increasing cell density, further supporting the inhibition of TNFα by paracrine signaling. IL10 secretion rose sharply from $2.6x10^3$ to $7.7x10^4$ cells/cm^2, but gradually dropped at densities higher than $7.7x10^4$ cells/cm^2, although the drop may not be significant. The results indicated that paracrine signaling is necessary for IL10 production, but it could also suppress IL10 secretion at higher densities. Analysis of TNFα secretion over a time course revealed that at 2 h after stimulation, per-cell TNFα secretion was comparable among all culture densities, but differences were observed in later hours. This suggested that paracrine interactions exert their effects only beyond 2 h after inflammatory stimulation. IL10 secretion was noisy at lowest density, but for the two other densities, per cell IL10 was similar. Although IL10 secretions from the initial density experiment did not have statistical significance for the two densities tested above, it could also suggested that adherent substrates may affect the responses caused by secreted products.

Figure 1: (A, B) total and (C, D) per cell TNFα and IL10 secretion of BMDM at different seeding densities (E, F) total and (G, H) per cell time course TNFα and IL10 secretion for stimulated BMDM at selected densities

Conclusions: Our studies revealed that paracrine interaction inhibits TNFα secretion upon stimulation with LPS/IFNγ, and that paracrine signaling is implicated in the production of IL10. Current work is focused on using engineered microwell substrates to culture macrophages in isolation or in small groups to more precisely investigate the effects of cell-cell communication on macrophage activation.

Reference: [1] Xue, Q. Sci. Signal. 2015(8): ra59 [2] Shalek, A. Nature. 2014(510): 363-9

EMG COHERENCE: A PHYSIOLOGICAL BIOMARKER FOR PARKINSON'S DISEASE

[1]C.M. Laine, [1,2]F.J. Valero-Cuevas

[1]Division of Biokinesiology and Physical Therapy, University of Southern California, Los Angeles, CA
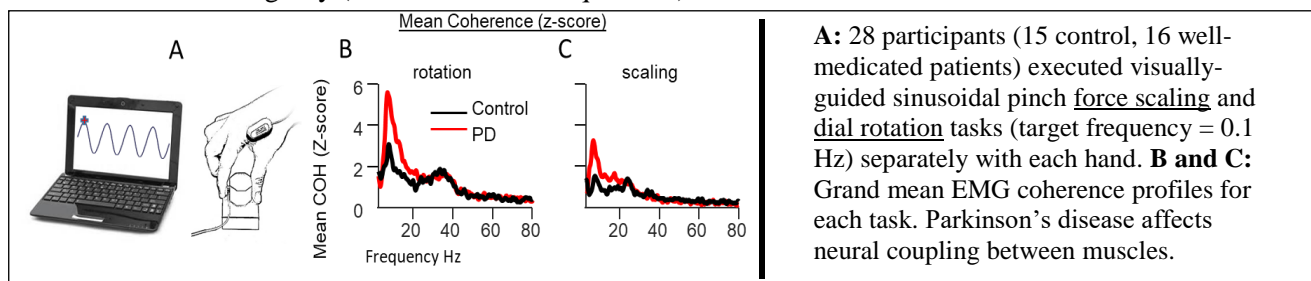[2]Department of Biomedical Engineering, University of Southern California, Los Angeles, CA
Contact: *claine@usc.edu*

Introduction: Parkinson's disease is a common progressive neurodegenerative disease which is typically diagnosed definitively only after irreversible damage to the nervous system has occurred [1]. Although it may remain undetected for many years, it is possible that neural circuit activity may become abnormal even before overt symptoms lead to diagnosis. Parkinson's disease is associated with changes in the oscillatory content of neural drive to muscles (e.g. ~20 Hz and ~40 Hz) [2]. When the mechanical demands of a task require strict coordination among muscles, they share a portion of their neural drive in common, which allows the technique of EMG-EMG coherence analysis to reveal the frequency spectrum of this shared drive [3]. Here, we tested the hypothesis that coherence between the muscles of the fingers would show an abnormal frequency spectrum of synchronization (as measured by EMG-EMG coherence analysis) in those with mild-moderate severity Parkinson's disease, compared with age-matched controls.

Materials and Methods: EMG-EMG coherence was measured between the *first dorsal interosseous* (FDI) of the index finger and the *abductor pollicis brevis* (APB) of the thumb while participants performed 3-minute manual tasks with each hand. The patient group consisted of 16 individuals (ages 62.3 ± 8.6(SD), 8 male) with Parkinson's disease, all on medication, and a control group of 15 individuals (61.3 ± 10.3, 8 male). Two tasks were executed with each hand. The first was an isometric precision pinch where forces were varied at 0.1 Hz from 1 to 3 N. using visual feedback for guidance. The second task was to pinch-and-rotate a small dial (1-3 N. force, rotation angle ± 22.5 deg, rate 0.1 Hz). Again, visual feedback was provided for guidance. EMG-EMG coherence was calculated for each hand and task, with an average 'alpha ratio' per participant. This represented the proportion of coherence within the 6-15 Hz frequency range for each task. To evaluate differences across groups, we used an unequal variance t-test on ranked data, calculated effect sizes using Cohen's D, and discriminability using area under a Receiver Operating Characteristic curve (ROC_AUC).

Results and Discussion: EMG-EMG coherence was markedly different between participants with Parkinson's disease and age-matched controls. There was greater ~10 Hz coherence in both tasks, as well as increased beta-band coherence (~20 Hz) and decreased gamma-band coherence (~40 Hz). Differences were clearest when alpha-ratios were combined across tasks to create a single diagnostic measure (Cohen's D = 1.53, ROC_AUC = 0.94, and p = 3.2 e-6). In the rotation task, the magnitude of coherence correlated with clinical measures of rigidity (rho ~ 0.7 for all frequencies).

A: 28 participants (15 control, 16 well-medicated patients) executed visually-guided sinusoidal pinch force scaling and dial rotation tasks (target frequency = 0.1 Hz) separately with each hand. **B and C:** Grand mean EMG coherence profiles for each task. Parkinson's disease affects neural coupling between muscles.

Conclusions: Our work demonstrates that Parkinson's disease has a profound and easily-detectable impact on the frequency spectrum of synchronization between muscles of the hand. Simple, inexpensive, and non-invasive tests for Parkinson's-associated neural dysfunction are therefore possible using surface EMG of hand muscles.

References:
[1] Cheng et al. *Ann Neurol* **67**, 715–25, 2010
[2] McAuley et al. *J Neurol Neurosurg Psychiatry* **70**, 471–475, 2001
[3] Laine & Valero-Cuevas. *J Neurophys.* doi: 10.1152/jn.00204.2017

MECHANICAL SIGNALING IN INTESTINAL STEM CELL BIOLOGY OF FRUIT FLIES

[1, 2, 3]Anna A. Kim, [2]Adam L. Nekimken, [1, 2]Beth L. Pruitt, and [2]Lucy E. O'Brien
[1]University of California, Santa Barbara, CA
[2]Stanford University, CA
[3]Uppsala University, Sweden
Contact: *anna_kim@engineering.ucsb.edu*

Introduction: Adult stem cells are key players in processes that govern tissue homeostasis, such as renewal and repair. Understanding how various cues influence the behavior of adult stem cells is essential to developing novel therapeutic approaches for maintaining healthy organs and combating the development of pathological states. However, a particular aspect—mechanical signaling—has remained unexplored to a large extent, in particular due to lack of appropriate experimental techniques. Despite significant evidence that mechanical forces play an integral role in organ development and maintenance, we are still missing a deep understanding of how they may direct cell behavior in tissues (*ex vivo*) and animals (*in vivo*).

Materials and Methods: We exploit the powerful genetic tools and high experimental tractability of adult Drosophila intestine (midgut) in combination with customizable micro-scale technologies to address the knowledge gap described above. Microfluidic devices[1] are adapted for targeted mechanical stimulation and optogenetics with a programmable light delivery system is used to mimic peristaltic or segmentation contractions in Drosophila midgut tissues.

Results and Discussion: Currently, we are testing midgut muscle drivers, including their potential for optogenetic applications. Figure 1 is an example of midgut tissue from transgenic flies with light-gated channelrhodopsin-2 expressed in midgut muscle cells using the *mef2GAL4/UAS system*.
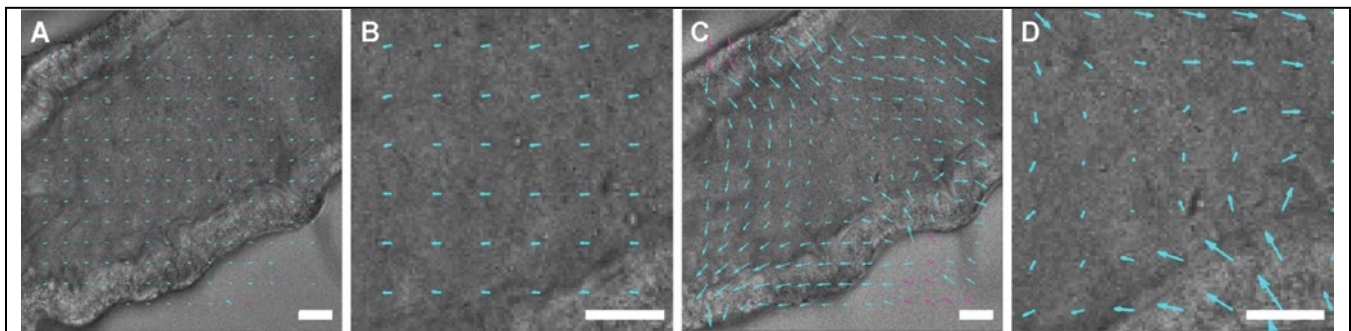
Figure 1: Preliminary data: representative frames of particle velocimetry (cyan) on *ex vivo* peristalsis in midguts expressing channelrhodopsin-2 (ChR2) in muscle cells (*Mef2-GAL4 > UAS-H134R-ChR2*). Purple arrows represent interpolated data. A) Prior to blue-light stimulation, with B) inset. C) Following blue-light stimulation with D) inset. Scale bars 25 μm.

Conclusions: Preliminary data indicate that it is possible to induce muscle contractions *ex vivo*, as shown by Particle Image Velocimetry (PIV) analysis[2] in Figure 1.

References:
1. Nekimken, A. L., H. Fehlauer, A. A. Kim, S. N. Manosalvas-Kjono, P. Ladpli, F. Memon, D. Gopisetty, V. Sanchez, M. B. Goodman and B. L. Pruitt (2017). "Pneumatic stimulation of C. elegans mechanoreceptor neurons in a microfluidic trap." *Lab on a Chip* **17**(6): 1116-1127.
2. Thielicke, W. and E. Stamhuis (2014). "PIVlab–towards user-friendly, affordable and accurate digital particle image velocimetry in MATLAB." *Journal of Open Research Software* **2**(1).

WINDOW TO THE BRAIN: IN VITRO CELL STUDIES WITH YTTRIA STABILIZED ZIRCONIA NANOPOWDER (8YSZ, 6YSZ, 3YSZ, AND ZrO₂)

[1]D. Rutherford, [3]S. Exarhos, [1]M. Niacaris, [1]C. Mariano, [3]L. Mangolini, [1,2]H. Liu

[1]Department of Bioengineering, University of California, Riverside, CA
[2]Material Science and Engineering Program, University of California, Riverside, CA
[3]Department of Mechanical Engineering, University of California, Riverside, CA

Contact: *huinanliu@engr.ucr.edu, lmangolini@engr.ucr.edu, druth001@ucr.edu, sexar001@ucr.edu, mniac001@ucr.edu, cmari010@ucr.edu*

Introduction: The NSF PIRE Window to the Brain (WttB) Project is comprised of nine different labs (six in California and three at top academic institutions in Mexico), collaborating to develop a ceramic, yttria-stabilized zirconia (8YSZ) cranial implant as a modality for treatment of brain injuries, as well as providing a platform for noninvasive, long-term monitoring of neural activity. The Mangolini lab has developed a scalable protocol for the synthesis of YSZ nanoparticles using aerosol spray pyrolysis, which are the basis for the cranial implant. The Liu group has developed cell protocols for cytocompatibility studies with the YSZ nanoparticles. The Liu Lab hypothesized that bone marrow mesenchymal stem cells (BMSCs), from rat weanlings, would grow successfully in culture with the YSZ nanoparticles. This work, in concert with additional work studying the cytotoxicity of bulk-YSZ disks, indicates that nanoparticle-derived bulk-YSZ is viable for implementation in human skull models. These particles will later be formed into solid, optically clear, disks, using high temperature and compression.

Materials and Methods: The YSZ nanoparticle precursor solution contains of zirconium (IV) chloride and varying amounts of yttrium (III) chloride hexahydrate, dissolved in deionized water and sprayed with argon gas into a furnace of 900°C. The solvent droplets are evaporated, and the precursor is thermally processed into nanoparticles. Particles were characterized morphologically by transmission electron microscopy, structurally by Raman spectroscopy and X-Ray diffraction, and compositionally by energy dispersive X-Ray spectroscopy. Post synthesis, three concentrations (60mMol/L, 30mMol/L, and 10mMol/L) of 8YSZ (8 mol% Y_2O_3), 6YSZ, 3YSZ, ZrO_2 (starting material), and commercial 8YSZ were grown with BMSCs for 24 hours in 37 C and 5.0% CO_2. At time t = 0 cells were seeded onto culture wells in a sequential seeding process. After 24 hours incubation, culture media was removed and saved for analysis, YSZ nanoparticles were suspended in fresh culture media and transferred into cell culture wells, over the existing monolayer of BMSCs. Cells and YSZ nanopowder were left to incubate for an additional 24 hours and at t = 48 hours, media and nanoparticles were harvested, tested for pH. BMSCs were fixed with 4% paraformaldehyde and stained with DAPI and Alexa Fluor to assess cellular morphology and BMSC adhesion density.

Results and Discussions: ZrO_2 and the different molar concentrations of YSZ were successfully synthesized to the desired size and crystalline composition. Post cytocompatibility study, media was collected and pH was measured for differences between nanopowder groups. Overall, a decrease in pH was observed in the culture media post 24-hour exposure to YSZ and ZrO_2 nanopowder. BMSCs were able to survive culture in the presence of ZrO_2 and YSZ nanopowder.
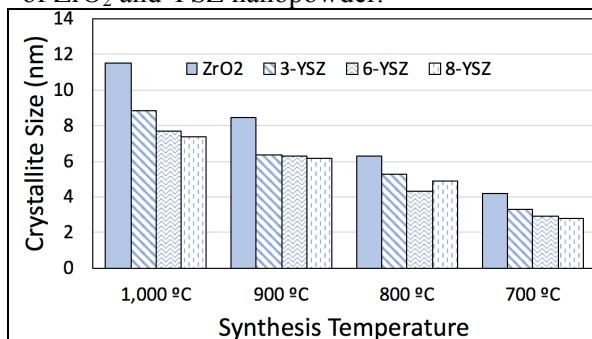
Figure 1: YSZ Sample crystalline size based on increasing synthesis temperature. At 800 C, ZrO_2 the sample Scherrer estimate is ~6.7 nm.

Conclusions: Through varying the temperature, flow rate, and precursor solvent, the crystalline phase and particle size were controlled. BMSCs were viable while in culture with YSZ and ZrO_2 nanopowder. This experiment provides a basis for uses in future applications of cranial implants.

LOW-INTENSITY PULSED ULTRASOUND INCREASES COLLAGEN PRODUCTION IN BOVINE ANNULUS FIBROSUS CELLS

[1]D. Horne, [2]P. Jones, [2]M. Adams, [2]C. Diederich, [1]J. Lotz

[1]Department of Orthopaedic Surgery | [2]Department of Radiation Oncology, University of California, San Francisco, CA

Introduction: Low back pain (LBP) is the most common musculoskeletal condition, affecting 80% of the population at some point in their lifetime. Common causes of LBP include annulus fibrosus (AF) tears and herniations of the intervertebral disc (IVD). The standard treatment for IVD herniation is discectomy; however, the reherniation rate following discectomy is reported to be up to 21%, likely due to inefficient healing of the remaining AF defect. Oftentimes, surgeons opt to leave the AF defect to heal on its own. However, the IVD has limited healing capacity due to it being sparsely cellularized and having a poor blood supply.

Currently, there is no effective treatment to repair AF damage that effectively promotes tissue regeneration. Recently emerging biologic therapies, such as growth factor injection, have been introduced clinically with variable success. The primary limitations of these invasive intra-discal injection procedures are their sustainability and biological safety concerns. These findings indicate a clinical need for an effective noninvasive therapy for repairing annular defects.

Mechanical stimulation of IVD cells may be a safer therapeutic mechanism that could be used alone or in conjunction with other forms of biological treatments. It is well known that IVD cells respond to mechanical stimulation by increasing proteoglycan and collagen synthesis. Low-intensity pulsed ultrasound (LIPUS) is a mechanical stimulus that is potentially both noninvasive and regenerative. LIPUS has been shown to stimulate matrix metabolism in several cell types including IVD cells. However, the efficacy demonstrated in these *in-vitro* studies are highly variable and do not consider several confounding factors. Nonetheless, detailed descriptions of system characterization and LIPUS parameters are largely missing from published work. These deficiencies have likely contributed to the lack of experimental reproducibility and successful transfer to *in-vivo* conditions.

In this study, a custom LIPUS *in-vitro* exposimetry system was designed and characterized to mitigate potentially confounding factors including ultrasound beam inhomogeneity, beam reflections, and temperature rise within the target sample. This fully characterized system was used to test the hypothesis that collagen synthesis in annulus fibrosus cells can be increased by LIPUS mechanical energy.

Materials and Methods: Bovine AF cells were encapsulated in 1.2% sodium alginate beads at a density of 4×10^6 cells/mL. Twelve alginate beads per well (one sample) were cultured in 6-well plates with 3mL of supplemented DMEM. There were 12 total samples divided among 3 treatment groups: control, BMP-7, and LIPUS. The BMP-7 group received media supplemented with 200ng/mL of Human Bone Morphogenetic Protein-7 (BMP-7). The LIPUS group was exposed to a LIPUS waveform (1.5MHz frequency, 600mW/cm^2 spatial peak intensity, 1kHz pulse repetition frequency, and 20% duty) for 20 minutes each treatment day. To simulate the environmental conditions without LIPUS, control and BMP-7 samples were placed in the LIPUS exposimetry system for 20 minutes with the ultrasound turned off. All samples were cultured for 14 total days, with treatments taking place on 8 of the 14 days. On day 14, beads were collected and collagen content was evaluated by hydroxyproline assay.

Results and Discussion: BMP-7 treatment demonstrated greater total collagen per bead compared to control by 85.3% ($2.18 \pm 0.20\mu g$ vs $1.18 \pm 0.14\mu g$). LIPUS treatment demonstrated greater total collagen per bead compared to control by 98.2% ($2.33 \pm 0.26\mu g$ vs $1.18 \pm 0.14\mu g$). There was no significant difference between the BMP-7 and LIPUS groups.

Conclusions: The findings of this study provide evidence that LIPUS exposure can increases collagen production in bovine annulus fibrosus cells at a magnitude similar to BMP-7 treatment. These results suggest that LIPUS treatment may be an effective noninvasive therapy for enhancing IVD repair.

Figure 1: LIPUS and BMP-7 groups demonstrated greater total collagen compared to the control group (n=6). Collagen content was normalized by number of beads in well.

3D COLLAGEN ARCHITECTURE MODULATES DEGRADABILITY AND CELL ADHESION

[1]D.O. Velez, [2]B. Tsui, [1]S. Ranamukhaarachchi, [3]H. Carter, and [1]S.I. Fraley
[1]Department of Bioengineering, University of California, San Diego, CA
[2] Bioinformatics and Systems Biology Program, University of California, San Diego, CA
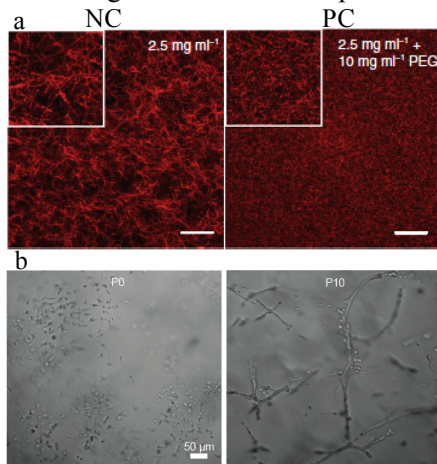[3] Department Medicine, University of California, San Diego, CA
Contact: *sifraley@ucsd.edu*

Introduction: Metastasis is the cause of 90% of cancer related deaths. An initial step in metastasis is the migration of cancer cells through collagen-rich tumor stroma and into the lymphatic or vascular systems. Despite an appreciation for the role of collagen in promoting tumor growth and progression, the field is generally lacking an understanding of how native collagen architecture, independent of stiffness and density, regulates cell migration and metastasis. We have developed a collagen matrix engineering technique to study the role of matrix architecture on cell-ECM interactions and cell migration outcomes.

Materials and Methods: The density of acid-extracted Type I collagen was held constant, and fibril architecture was tuned by the addition of free polyethylene glycol (PEG) during polymerization. PEG was then removed by washing. Biochemical assessment and quantitative microscopy were used to measure four core cell-ECM interactions (cytoskeletal polymerization, matrix remodeling, contractility, and adhesion) and cell migration.

Results and Discussion: PEG crowding (PC) created matrices with smaller pores, shorter fibers, and lowered degradability compared to non-crowded matrices (NC) (Fig. 1A). However, local and bulk stiffness was not significantly different. PC matrices triggered a migration response in breast cancer (BRCA) cells and several other cancer types, resulting in collective migration and the formation of multicellular network structures (Fig. 1B). We linked these structures to an aggressive clinical phenotype known as vasculogenic mimicry (VM) through phenotypic, histological, and transcriptional evidence. Clinically, the VM phenotype is correlated with advanced metastatic disease in 16 tumor types, but mechanistically, it is poorly understood. To better understand induction of this phenotype, we closely analyzed cell-ECM interactions. Cells initially interacting with PC matrices produced smaller and shorter-lived protrusions compared to cells embedded in NC matrices. Actin FRAP studies revealed that this difference in protrusion lifetime was not caused by differences in actin polymerization rates. TFM and protrusion-ECM displacement correlation showed that in PC architectures, cells fail to stabilize protrusions and sustain pulling force on the surrounding matrix. Likewise, FAK is significantly less phosphorylated, suggesting that adhesion is limited. Higher reactive oxygen species levels, lowered glucose consumption, and downregulation of mTOR signaling revealed that PC matrix architecture triggered oxidative and metabolic stress consistent with a low adhesion state. MMP inhibition led to lowered adhesive coupling in both conditions, suggesting that the PC matrix's resistance to degradation may be the feature driving cell stress and transdifferentiation.

Figure 1. (a) Reflection confocal micrograph of non-crowded (NC) 2.5 mg/ml collagen matrix (left) and 2.5 mg/ml collagen crowded with PEG (PC, right). (b) Brightfield micrographs of MDA-MB-231 cells cultured in NC and PC conditions after seven days.

Conclusions: These preliminary results suggest that collagen matrix degradability is regulated by fiber architecture, and that degradation activity modulates the extent of cell-ECM coupling. Thus, cells can experience low-adhesion stress even when surrounded by matrix. Low adhesion stress in 3D collagen leads to cancer transdifferentiation into an aggressive migratory phenotype.

Friday, June 22nd

7:00 am – 5:00 pm	**Registration (Concourse 101)**
7:00 am – 9:00 am	**Exhibitor Setup (Concourse 101)**
7:00 am – 8:00 am	**Breakfast (Concourse 101 and Plaza)**
8:00 am – 8:50 am	**Plenary Talk 3: Gilda Barabino, Ph.D., Dean and Daniel Frances Berg Professor, The Grove School of Engineering, The City College of New York (Ballrooms A and B)**
9:00 am – 10:30 am	**Special Session on Computational Microfluidics (MR 2)** Organizers: William Grover, Philip Brisk, Justin Chartron, Jiayu Liao, Victor G. J. Rodgers
9:00 am – 10:30 am	**Neuroengineering (MR 3)** Chair: Megan Peters, UC Riverside Co-Chair: Kevin Freedman, UC Riverside
9:00 am – 10:30 am	**Biomedical Imaging 1 (Ballrooms A and B)** Chair: Hyle Park, UC Riverside Co-Chair: Xiaoping Hu, UC Riverside
10:30 am – 11:00 am	**Break (Concourse 101 and Plaza)**
11:10 am – 12:00 pm	**Plenary Talk 4: Susan Tousi, Senior Vice President, Product Development, Illumina, Inc. (Ballrooms A and B)**
12:00 pm – 1:00 pm	**Lunch (Concourse 101 and Plaza)**
1:00 pm – 3:00 pm	**Poster Session II (MR 4 and MR 5)**
1:00 pm – 1:30 pm	**Rapid-Fire Poster Presentations (Ballrooms A and B)**
3:00 pm – 4:20 pm	**Break (Concourse 101 and Plaza)**
4:20 pm – 5:50 pm	**Stem Cells and Regenerative Medicine (MR 1)** Chair: Jin Nam, UC Riverside Co-Chair: Joshua Morgan, UC Riverside
4:20 pm – 5:50 pm	**Biomedical Imaging 2 (MR 2)** Chair: Hyle Park, UC Riverside Co-Chair: Xiaoping Hu, UC Riverside
4:20 pm – 5:50 pm	**Medical Devices and Instrumentation 2 (MR 3)** Chair: William Grover, UC Riverside Co-Chair: Victor G. J. Rodgers, UC Riverside
4:20 pm – 5:50 pm	**Molecular and Cellular Engineering 2 (Ballrooms A and B)** Chair: Val Vullev, UC Riverside Co-Chair: Stephanie Fraley, UC San Diego
6:00 pm – 6:30 pm	**Plenary Talk 5: Hayley J. Lam, Ph.D., Senior Science Officer, Portfolio Development and Review, California Institute for Regenerative Medicine (Ballrooms A and B)**
6:30 pm – 10:00 pm	**Reception (Concourse 101 and Plaza)**

9:00 am – 10:30 am	**Special Session on Computational Microfluidics (MR 2)**
	Organizers: William Grover, Philip Brisk, Justin Chartron, Jiayu Liao, Victor G. J. Rodgers
9:00 am – 9:40 am	Elliot Hui, UC Irvine Computing with Microfluidics
9:40 am – 10:20 am	Philip Brisk, UC Riverside Design Automation for Microfluidics
10:20 am – 10:30 am	Discussion: The Future of Computational Microfluidics at the University of California Moderator: William Grover, UC Riverside
9:00 am – 10:30 am	**Neuroengineering (MR 3)**
	Chair: Megan Peters, UC Riverside Co-Chair: Kevin Freedman, UC Riverside
9:00 am – 9:30 am	Invited faculty speaker: Karen Moxon, UC Davis Beyond Neuroprosthetics: the New Science of Cognitive Neuroengineering
9:30 am – 9:45 am	Beth Lopour, UC Irvine EEG Functional Networks Reflect Treatment Response in Infantile Spasms
9:45 am – 10:00 am	Lebo Wang, UC Riverside Application of Convolutional Recurrent Neural Network for Individual Identification Using Resting-State fMRI Data
10:00 am – 10:15 am	Jason Langley, UC Riverside Accurate Assessment of Locus Coeruleus Function
10:15 am – 10:30 am	Karen Low and Gerardo Ico, UC Riverside Acoustic Activation of Piezoelectric Scaffold System for Functional Nerve Regeneration
9:00 am – 10:30 am	**Biomedical Imaging 1 (Ballrooms A and B)**
	Chair: Hyle Park, UC Riverside Co-Chair: Xiaoping Hu, UC Riverside
9:00 am – 9:30 am	Invited faculty speaker: Vivek Srinivasan, UC Davis Human Brain Interferometers for Blood Flow
9:30 am – 9:45 am	David L. Halaney, UC Riverside Optical Coherence Tomography and Laser Speckle Imaging of the Brain Through a Transparent Cranial Implant in a Chronic Mouse Model
9:45 am – 10:00 am	Nami Davoodzadeh, UC Riverside Long-Term Brain Blood Perfusion Imaging and Bacterial Growth Monitoring Using Laser Speckle Imaging
10:00 am – 10:15 am	Hossein S. Yazdi, Beckman Laser Institute and Medical Clinic, UC Irvine Measuring Blood Flow, Oxygenation and Metabolism in Human Skeletal Muscle using Combined Diffused Optical Spectroscopic Imaging and Diffuse Correlation Spectroscopy
10:15 am – 10:30 am	Sana Hussain, UC Riverside Resting State Locus Coeruleus Functional Connectivity Profiles With Various Brain Networks

EEG FUNCTIONAL NETWORKS REFLECT TREATMENT RESPONSE IN INFANTILE SPASMS

[1]B. Lopour, [2,3]D. W. Shrey, [2,4]O. K. McManus, [5]R. Rajaraman, [6,7]H. Ombao, [5]S. A. Hussain

[1]Department of Biomedical Engineering, University of California, Irvine, CA, USA
[2]Division of Neurology, Children's Hospital Orange County, Orange, CA, USA
[3]Department of Pediatrics, University of California, Irvine, CA, USA
[4]Division of Pediatric Neurology, University of California, San Diego, CA, USA
[5]Division of Pediatric Neurology, University of California, Los Angeles, CA, USA
[6]Department of Statistics, University of California, Irvine, CA, USA
[7]Statistics Program, King Abdullah University of Science and Technology, Saudi Arabia
Contact: *beth.lopour@uci.edu*

Introduction: Infantile spasms is associated with hundreds of underlying etiologies, yet the brain activity of children with this disease, measured with electroencephalography (EEG), tends to exhibit common characteristics. This suggests that common underlying networks may mediate this activity, and prior studies have supported this idea. However, the role played by EEG-based functional networks in IS with respect to treatment response and outcome prediction has never been evaluated. Therefore, we set out to compare functional connectivity to known electrographic signatures of infantile spasms and evaluate it as a potential biomarker of both treatment response and long-term outcomes.

Materials and Methods: We retrospectively identified 21 patients with newly diagnosed infantile spasms and 21 controls. Spontaneous awake scalp EEG data recorded prior to treatment initiation and after ten or more days of treatment were visually assessed in a blinded fashion and functional connectivity was independently measured using cross-correlation techniques. Relevant clinical data, including short-term treatment response and long-term outcomes, were collected for each subject.

Results and Discussion: In patients with newly diagnosed infantile spasms, 42% of electrode pairs exhibited stronger functional connections compared to controls, with the strongest connections occurring between parietal and frontal head regions (Figures 1A, 1B). These functional networks were highly individualized, and they were more stable than those of control subjects. Successful treatment was associated with a reduction in strength and stability to control levels (Figures 1C, 1D). Six subjects with extremely strong pre-treatment functional connectivity were all responders, suggesting that this characteristic may be predictive of favorable response; this group was clinically diverse and represented over half of all responders.

Figure 1: Average network maps for (A) controls (n=21), (B) pre-treatment infantile spasms (n=21), (C) post-treatment responders (n=11), (D) post-treatment non-responders (n=10). Connection strength is indicated by color (red = high).
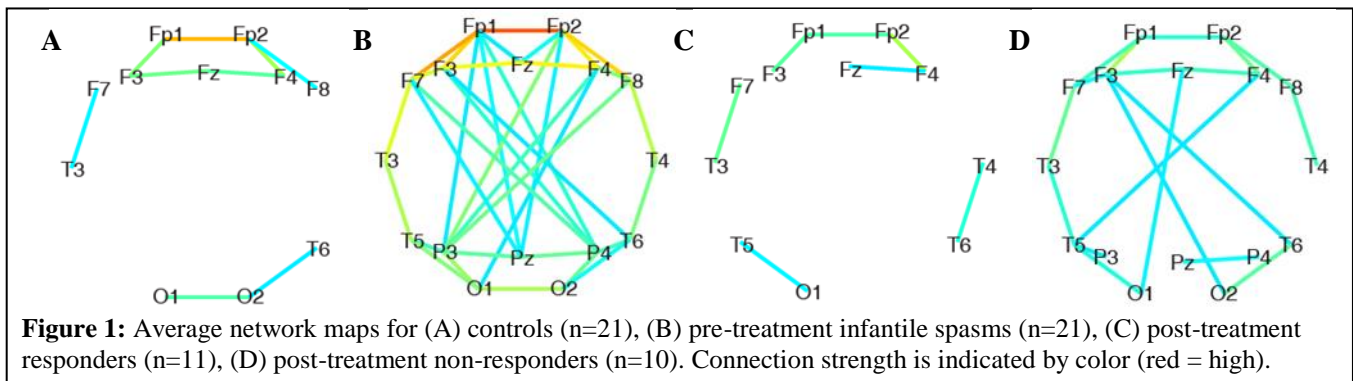
Conclusions: Changes in network connectivity and stability correlate to treatment response for infantile spasms, and pre-treatment connectivity may specifically predict favorable short-term treatment response in a subset of patients. Standard visual EEG analysis did not produce any measures that were correlated to treatment response or long-term outcome in a clinically meaningful way. Further study is needed to fully validate functional connectivity's role as a predictor of treatment response and its relationship to long-term epilepsy and neurocognitive outcomes.

APPLICATION OF CONVOLUTIONAL RECURRENT NEURAL NETWORK FOR INDIVIDUAL IDENTIFICATION USING RESTING-STATE FMRI DATA

[1]Lebo Wang and [2]Xiaoping Hu

[1]Department of Electrical and Computer Engineering, University of California, Riverside, CA
[2]Department of Bioengineering, University of California, Riverside, CA
Contact: *xhu@engr.ucr.edu*

Introduction: While neuroimaging studies have been focusing on the homogeneity of the general patterns of brain activity, functional connectivity (FC) studies have revealed high individual variability, leading to a viable individual identifying fingerprint [1]. Understanding the uniqueness of the brain connectivity opens up an avenue to unveil the brain mechanism. A recurrent neural network (RNN) was recently applied to extract both temporal and spatial features from a short fMRI clip (100 frames, 72 sec) for individual identification [2], demonstrating a better identification accuracy than considering only the spatial features by FC. To make more use of the spatiotemporal information, we adopt the Convolutional RNN (ConvRNN) model with stacked layers in the present work, achieving further improvement in accuracy.

Materials and Methods: In artificial systems, successive non-linear transformations with convolutional structures can convert raw inputs into sophisticated features. Instead of a fully connected network with a collection of neurons in hidden layers, ConvRNN utilizes convolutional structures in both the input-to-state and state-to-state transitions. The final classification is done based on the state of the last frame. As shown in Figure 1, our ConvRNN consists of two convolutional layers followed by BatchNormalization layers to accelerate the neural network training. Most of the parameters are from the final fully-connected layer. No pooling layer is used so that the temporal and spatial resolutions are preserved. For a fair comparison, both the traditional RNN [2] (404K) and our ConvRNN (382K) have similar number of parameters.

We applied our network to the ICA-FIX denoised resting-state fMRI data of 100 unrelated subjects in the Human Connectome Project database (54 females, 46 males, mean age = 29.1 ± 3.7 years, repetition time = 0.72 sec) [3]. Two scans on the first day were used for training. Two scans on the second day were used for validation and test, respectively. Each scan (1200 frames in total) was divided into multiple 100-frame clips. The brain data were spatially down-sampled onto 236 regions of interest (ROIs) over the cerebral cortex.

Figure 1. The architecture of ConvRNN

Figure 2. The outputs from the 2nd-level convolutional filters in ConvRNN

Results and Discussion: The accuracy of the ConvRNN is 99.17% on validation set and 98.50% on test set, which is 2.6% higher compared to that of the conventional RNN. The improved identification accuracy indicates that the ConvRNN can successfully extract spatiotemporal information. Figure 2 presents outputs from the 2nd-level convolutional filters on the validation dataset. It is clear to see that each convolutional filter consistently focuses on some certain ROIs and generates robust features across the 100 subjects.

Conclusions: In this study, we exploited the ConvRNN to distill spatial and temporal features from resting-state fMRI data. Our results showed that the ConvRNN has a better identification accuracy than that of the normal RNN model. Further study of the hidden patterns could be deployed to have a better understanding of the brain mechanism.

References:
[1] Finn, Emily, et al. "Functional connectome fingerprinting: identifying individuals using patterns of brain connectivity." Nature neuroscience 18.11 (2015): 1664. [2] Chen, Shiyang, et al. "Individual Identification Using Functional Brain Fingerprint Detected by Recurrent Neural Network." Brain connectivity ja (2018). [3] Van Essen, David, et al. "The WU-Minn human connectome project: an overview." Neuroimage 80 (2013): 62-79.
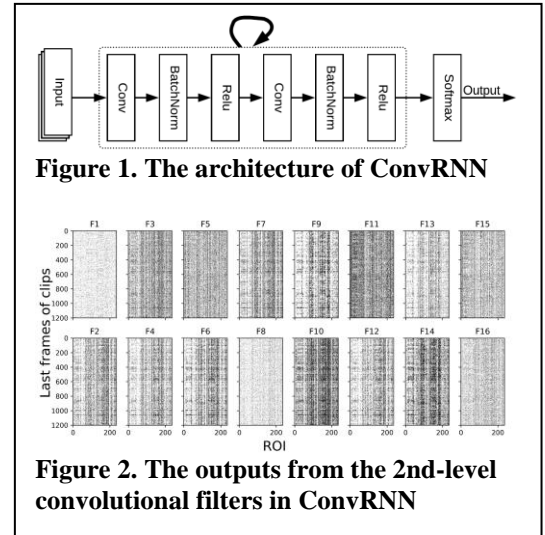
ACCURATE ASSESSMENT OF LOCUS COERULEUS FUNCTION

[1,2]J. Langley, [1,2]S. Hussain, [1,2]X. Chen, and [1,2]X. Hu

[1]Department of Bioengineering, University of California, Riverside, CA
[2]Center for Advanced Neuroimaging, University of California, Riverside, CA
**Contact:** xhu@engr.ucr.edu

Introduction: The locus coeruleus (LC) is a small bilateral catecholaminergic nucleus, approximately 15 mm long and 2.5 mm in diameter, located on the anterior edge of the fourth ventricle in the pons of brainstem. LC is deeply involved in many cognitive functions such as attention and arousal. Further, LC dysfunction occurs in the early stages of Parkinson's disease and Alzheimer's disease. New MRI acquisition methods allow for delineation of LC and for LC function to be probed. However, many functional studies do not correct susceptibility induced distortions and regions of interest (ROIs) used to localize LC may be misaligned with the actual location of LC.

Materials and Methods: A cohort of 13 healthy subjects (7 female; mean age: 23.8 years) participated in this study. All participants were right-handed, normal hearing status, and no history of psychiatric or neurological disease. Data were acquired on a 3 T MRI scanner (Prisma, Siemens Healthineers, Malvern, PA) using a 32-channel receive-only coil. T_1-weighted images (echo time (TE)/repetition time (TR)/inversion time=3.02 ms/2600 ms/800 ms, flip angle (FA)=8°, voxel size=0.8×0.8×0.8 mm^3) were used for registration from subject space to common space. All participants performed three trials of an auditory oddball task during fMRI scans. For each trial, participants were instructed to maintain fixation at a centrally presented cross (white against a black background) and listened to a series of sequentially presented standard and target stimuli. All stimuli were presented for 1 second and targets were pseudorandomly interspersed. Functional data were collected during this task with an echo planer imaging (EPI) sequence with 36 slices, covering the brainstem and auditory cortex in each subject. Scan parameters were as follows: TE/TR=32 ms / 1400 ms; slices = 36; voxel size=2×2×3 mm^3. A total of 327 volumes were collected for each trial. A pair of spin echo EPI acquisitions with identical parameters but opposite phase encoding directions were collected to correct for susceptibility related distortions.

To examine displacement due to susceptibility related distortions, a pair of ROIs were drawn dorsal edge of the brain stem at midline along the fourth ventricle in both susceptibility-corrected and uncorrected spin echo EPI images. The ROIs were then transformed to common space. Functional MRI (fMRI) images were processed using FMRIB Software Library (FSL) using standard preprocessing steps (motion correction, susceptibility distortion correction, spatial smoothing, and common space transformation). Two activation analyses were performed: one whole brain analysis and one analysis restricted to the brainstem.

Results and Discussion: The mean magnetic field inhomogeneity in LC was 7.0 Hz ± 2.6 Hz. This shift resulted in a displacement approximately 2.6 mm for both left and right LC when susceptibility corrected and uncorrected images were compared. As LC is smaller than this displacement, care must be taken in interpreting activation or functional connectivity derived from uncorrected fMRI images. In the oddball analysis, bilateral activation clusters were observed in the auditory cortex. Interestingly, we observed unilateral activation in the region of LC on the dorsal edge of the brainstem (Fig. 1). No other clusters of activation were seen in the brainstem.
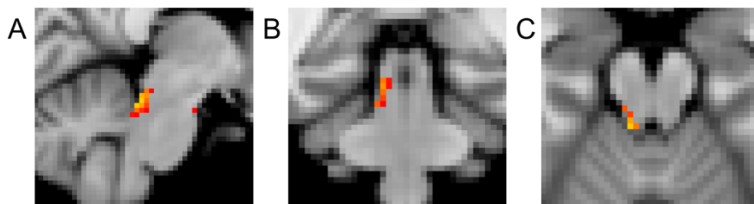
Figure 1. Sagittal (A), coronal (B), and axial (C) views of the activation cluster from the oddball task (p<0.01). Activation was observed on the right side of the dorsal edge of the brain stem.

Conclusions: Susceptibility induced distortions in uncorrected EPI images will result in misalignment between structural images and functional images. The displacement due to susceptibility is larger than the size of LC. Functional activation was observed along the dorsal edge of the brainstem in proximity to LC and correction of susceptibility-induced distortions will lead to more accurate assessment of LC function.

ACOUSTIC ACTIVATION OF PIEZOELECTRIC SCAFFOLD SYSTEM FOR FUNCTIONAL NERVE REGENERATION

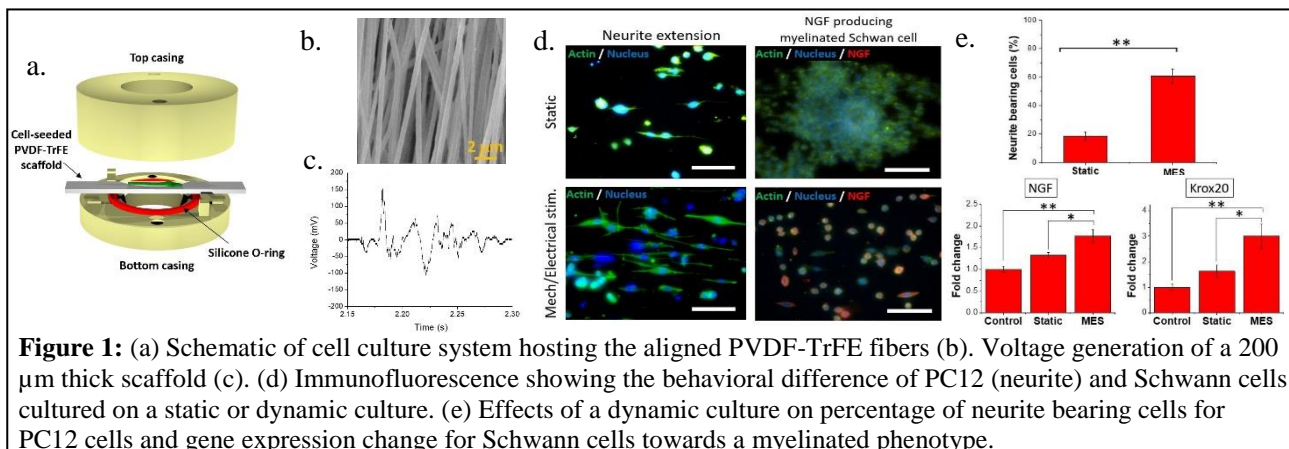[1]K. Low, [1]G. Ico, [1]D.Garcia-Viramontes, and [1]J. Nam
[1]Department of Bioengineering, University of California, Riverside, CA, 92521
Contact: *jnam@engr.ucr.edu*

Introduction: A lack of therapeutic technologies that enable electrically stimulating nervous tissues in a facile and clinically relevant manner has partly hindered the advancement in treating nerve injuries for full functional recovery. Currently, the gold standard for nerve repair is autologous nerve grafting. However, this method has several disadvantages, such as necessity for multiple surgeries, creation of functionally impaired region where graft was taken from, disproportion of graft to nerve tissue in size and structure, and most substantially, high risk of neuroma formation. Therefore, there is an increasing need for the development of alternative strategies to enhance nerve regeneration. To address these limitations, the development of a piezoelectric neuroconduit that can self-generate optimized levels of electrical stimulation can be utilized to wrap a damaged nerve and remotely activated by acoustically-driven piezoelectricity. In this regard, a piezoelectric scaffold was developed using electrospinning technology and its piezoelectric performance was optimized by controlling the fiber diameter and scaffold thickness to induce favorable cellular behaviors.

Materials and Methods: Electrospun P(VDF-TrFE) nanofibers were synthesized for optimal piezoelectric performance by controlling the fiber diameter and scaffold thickness. A custom 3-D printed cell culture system was designed to deliver a non-contact mechanical/electrical stimulation to the scaffolds, while simultaneously providing a sterile culture environment to the adherent cells on the scaffolds. Two types of neural cells (PC12 cells and Schwann cells) were separately seeded onto the scaffolds with a pre-culture period of 24 hr. Mechanical/electrical stimulation was introduced for 3 days (Schwann cells: 7 days) at 2 hours per day. To examine the effects of mechanical/electrical stimulation the cellular behavioral changes were observed with immunofluorescence, feature characterization, and gene expression.

Results and Discussion: Aligned nanofibers of approx. 500 nm in diameter were collected to produce a scaffold with a thickness of 200 µm. Utilizing the cell culture system, the scaffold was measured to generate a voltage of 200 mV$_{p-p}$. When PC12 cells, a model system for neurons, were subjected to multi-day application of mechanical/electrical stimulation, enhancements in neurite formation and elongation were observed. Alternatively, mechanical/electrical stimulation induced Schwan cells, the glial cell of the peripheral nervous system, to differentiate into its myelinating phenotype and induced the enhanced production of the neurotrophic protein, nerve growth factor.

Figure 1: (a) Schematic of cell culture system hosting the aligned PVDF-TrFE fibers (b). Voltage generation of a 200 µm thick scaffold (c). (d) Immunofluorescence showing the behavioral difference of PC12 (neurite) and Schwann cells cultured on a static or dynamic culture. (e) Effects of a dynamic culture on percentage of neurite bearing cells for PC12 cells and gene expression change for Schwann cells towards a myelinated phenotype.

Conclusions: The utilization of a piezoelectric scaffold to induce favorable cellular behavior shows the potential applicability of the scaffold as a conduit platform for the regeneration of neural injuries.

OPTICAL COHERENCE TOMOGRAPHY AND LASER SPECKLE IMAGING OF THE BRAIN THOUGH A TRANSPARENT CRANIAL IMPLANT IN A CHRONIC MOUSE MODEL

David L. Halaney, Carrie R. Jonak, Nami Davoodzadeh, Junze Liu, Pasha Ehtiyatkar, Hyle Park, Devin K. Binder, Guillermo Aguilar

University of California, Riverside, Riverside, CA

Optical diagnostic and therapeutic neuro-procedures are hindered by the highly scattering cranial bone, necessitating craniotomy (i.e. removal of a section of skull) to provide optical access each time a procedure is performed. Repeated cranial surgeries are expensive and increase risk to the patient. We have proposed a solution to this issue previously by introducing a novel transparent cranial implant made of nanocrystalline yttria-stabilized zirconia (nc-YSZ), which we call the Window to the Brain (WttB) implant. In our previous work, we demonstrated that imaging depth and contrast of optical coherence tomography (OCT) imaging is improved though the WttB implant compared to the native skull in an acute murine model. In this present work, we extend this acute study with OCT performed through the WttB implant immediately following cranioplasty, and at multiple subsequent time points over 30 days in a chronic murine implant model. Additionally, we present complementary laser speckle imaging blood flow mapping across the WttB implant over corresponding time points. Factors influencing the stability of this model such as cranial bone regeneration will be discussed. This work represents the next step towards a viable transparent implant for chronic use, and demonstrates the potential value of this murine implant model as a tool to evaluate the neurological effects of new drugs, procedures, or to study neurological physiology and disease longitudinally over time in a single animal.

LONG-TERM BRAIN BLOOD PERFUSION IMAGING AND BACTERIAL GROWTH MONITORING USING LASER SPECKLE IMAGING

[1]Nami Davoodzadeh, [2]Mildred S. Cano-Velázquez, [1]David Halaney, [3]Carrie R. Jonak, [1]Natanael Cuando, [3]Devin K. Binder, and [1]Guillermo Aguilar

[1]Department of Mechanical Engineering, University of California, Riverside, CA
[2]Instituto de Investigaciones en Materiales, Universidad Nacional Autonoma de Mexico
[3]Department of Neuroscience, University of California, Riverside, CA
Contact: *Ndavo001@ucr.edu*

Introduction: Laser speckle contrast imaging methods have attracted extensive attention recently because they can image brain blood flow with high spatiotemporal resolution. However, the poor transparency of the cranial bone limits the spatial resolution and the imaging depth. This problem has previously been addressed in animal studies by removing or thinning the skull to transparency. Nevertheless, a permanent and reliable solution has not yet been developed. Our study demonstrates a new method to address this challenge in biomedical imaging research, through the use of novel transparent cranial implants made from nanocrystalline yttria-stabilized zirconia (nc-YSZ). The transparency of our implant may provide a unique opportunity for non-invasive imaging of the underlying tissue layer dynamics using laser speckle imaging (LSI). In general, an LSI system includes a camera which records the changes in the speckle pattern created by a diffused coherent light source. The magnitude of the changes is measured by the speckle contrast. The contrast has been found to correlate with blood flow and bacterial growth. In this study, we investigated brain blood perfusion imaging in a set of in-vivo experiments. In addition, we evaluated LSI for monitoring bacterial growth under the cranial implant, which is the leading factor for biofilm formation (fouling), infection, and implant failure.

Materials and Methods: Two sets of *in-vivo* and *in-vitro* imaging experiments including mouse brain blood flow mapping and bacterial growth assessment, respectively, were performed. The speckle images were acquired using a 12 bit CMOS camera (Thorlabs DCC1545M). A continuous wave (CW) laser (632.8 nm) was used to illuminate the region of interest at a 45° incidence. A pair of negative-positive lenses was used to expand the laser beam and a diffuser was used to homogenize the intensity of the laser beam. A sequence of laser speckle images reflected from the illuminated regions was then acquired by the camera attached to a microscope mount (10X). For acquiring the speckle images, the microscope was focused 0.3 mm below the implant surface. Collimated laser light was shown onto the cortex through the implant. The images (1024 x 1280 pixels) were acquired with a frame rate of 14.5 Hz and exposure times of 2, 5, and 10ms. The contrast images were constructed by calculating the speckle temporal contrast, Kt, of each image pixel in the time sequence.

Results and Discussion: By applying LSI to underlying brain in an acute murine model, we show that spatial resolution of blood flow measurement are improved when imaging through transparent nc-YSZ implants relative to native cranium. The results of *in-vitro* bacterial mass growth monitoring show good agreement with the previous studies on bacterial mass growth monitoring using optical density measurements.

Conclusions: As such, these results provide evidence supporting the feasibility of nc-YSZ transparent cranial implant as a clinically-viable long-term optical access for LSI on a chronically-recurring basis, thereby suppressing the need for repeated craniotomies. LSI show promise as a non-invasive tool for brain blood flow imaging and early detection of bacterial infection and assessment of antibacterial treatments.

MEASURING BLOOD FLOW, OXYGENATION AND METABOLISM IN HUMAN SKELETAL MUSCLE USING COMBINED DIFFUSE OPTICAL SPECTROSCOPIC IMAGING AND DIFFUSE CORRELATION SPECTROSCOPY

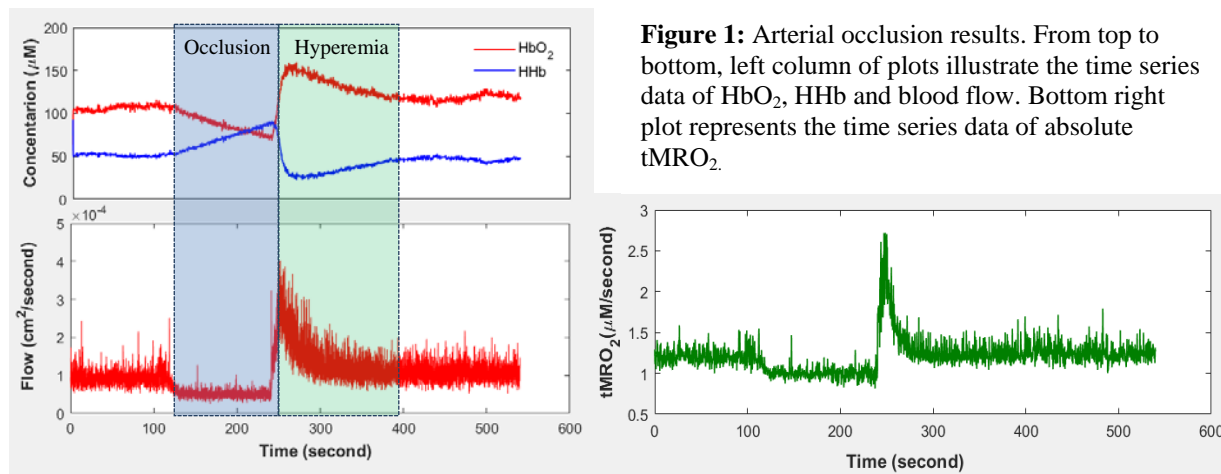[1]Hossein S. Yazdi,[1]Jesse Lam,[1] Mohammad Torabzadeh and [1] Bruce J.Tromberg
[1]University of California, Beckman Laser Institute and Medical Clinic, Irvine, California, United States
Contact: *hseddigh@uci.edu*

Introduction: Diffuse optical spectroscopic imaging (DOSI) and diffuse correlation spectroscopy (DCS) are model based near-infrared (NIR) methods that quantitatively measure tissue oxygenation (oxyhemoglobin (HbO_2), deoxy hemoglobin (HHb)) and blood flow respectively. When taken together, DCS and DOSI can provide a noninvasive measurement of metabolic rate of oxygen consumption ($tMRO_2$) in centimeter thick tissue. Decrease in tMRO2 is known to be an indicator of pathological conditions such as peripheral arterial disease, chronic wounds, and diabetes. Thus, assessment of $tMRO_2$ can provide information for early diagnosis, screening, and treatment response monitoring. In this study, we applied a combined DOSI/DCS instrument to an arterial occlusion protocol and demonstrate the ability to provide quantitate information of HbO_2, HHb, blood flow and $tMRO_2$ during ischemia and reperfusion in a human subject.

Materials and Methods: In this study, a previously developed and characterized DOSI/DCS probe has been applied to a 2-minutes arterial cuff occlusion on a healthy 33-year-old male subject. Total measurement time was 9 minutes including 2 minutes baseline, 2 minutes arterial occlusion and 5 minutes post occlusion. The study was carried out under a UC Irvine IRB-approved protocol (HS #2004-3626).

Results and Discussion: *In vivo* arterial occlusion studies illustrate that DOSI/DCS can measure dynamic changes of HbO_2, HHb and blood flow during the arterial occlusion and hyperemia (post occlusion) Fig1. Oxygen metabolism ($tMRO_2$) is calculated by combining oxygenation and blood flow information.

Figure 1: Arterial occlusion results. From top to bottom, left column of plots illustrate the time series data of HbO_2, HHb and blood flow. Bottom right plot represents the time series data of absolute $tMRO_2$.

Conclusions: Quantitative DOSI/DCS instrument provides a more complete view of tissue composition and metabolism, which may aid in diagnosis, and treatment response monitoring in wide variety of diseases.

References:
Yazdi, Hossein S., et al. "Mapping breast cancer blood flow index, composition, and metabolism in a human subject using combined diffuse optical spectroscopic imaging and diffuse correlation spectroscopy." *Journal of biomedical optics* 22.4 (2017): 045003.
Ghijsen, Michael, et al. "Quantitative real-time optical imaging of the tissue metabolic rate of oxygen consumption." *Journal of biomedical optics* 23.3 (2018): 036013.
Wilson, Robert H., et al. "High-speed spatial frequency domain imaging of rat cortex detects dynamic optical and physiological properties following cardiac arrest and resuscitation." *Neurophotonics* 4.4 (2017): 045008.
Najdahmadi, Avid, Jonathan RT Lakey, and Elliot Botvinick. "Diffusion coefficient of alginate microcapsules used in pancreatic islet transplantation, a method to cure type 1 diabetes." *Nanoscale Imaging, Sensing, and Actuation for Biomedical Applications XV*. Vol. 10506. International Society for Optics and Photonics, 2018.

RESTING STATE LOCUS COERULEUS FUNCTIONAL CONNECTIVITY PROFILES WITH VARIOUS BRAIN NETWORKS

[1]S. Hussain, [2]J. Langley, [3]A. Seitz, [1]M. Peters, [1,2]X. Hu

[1]Department of Bioengineering, University of California, Riverside, CA
[2]Center for Advanced Neuroimaging, University of California, Riverside, CA
[3]Department of Psychology, University of California, Riverside, CA

Contact: xhu@engr.ucr.edu

Introduction: The locus coeruleus (LC) is a 2 mm in diameter noradrenergic nucleus bilaterally located just under the fourth ventricle that projects to the entire brain. LC is deeply involved in modulating arousal, and even when the brain is at rest, it continues to control corresponding functions. It is thought that LC influences the switching between various networks, and dysfunction of LC and its control over these networks lead to neurodegenerative disorders including Alzheimer's and Parkinson's diseases. We currently understand little of how LC controls arousal, and understanding this circuit can provide insight into how and why brain dysfunctions occur, ultimately paving the way towards correcting them.

Materials and Methods: A 3T (Siemens Prisma) with 64-channel receive only head coil was used to scan 10 right-handed human subjects (mean age 24 ± 5 Years, 5 male) at UC Riverside. Resting state data (52 slices with echo time 32ms, repetition time 2000ms, flip angle 77º, and voxel size $2\times2\times3$ mm^3) was collected for 5 minutes while the subjects stared at a white fixation cross on a black screen and were told not to dwell on anything in particular. Then subjects squeezed a squeeze-ball for 30 seconds, followed by another 5 minute resting state scan. FMRIB Software Library (FSL) was utilized to perform standard preprocessing steps: motion correlation, brain extraction, smoothing, slice time correction, and registration to standard space. Matlab was utilized to implement temporal smoothing, regression of CSF, and a sliding time window correlation analysis using a window of 40 time points. The mean within-network correlation was found for four networks of interest (default mode network (DMN), fronto-parietal control network (FPCN), dorsal attention network (DAN), and salience network (SN)) along with the connectivity between these networks and LC. The first and last ten time points were excluded for edge effects. Standard Package for the Social Sciences (SPSS) was used to perform paired t-tests before and after squeezing for the within network connectivity, connectivity between the networks and LC, and variance.

Results and Discussion: Mean within network connectivity was found to be more positive for all networks after squeezing (Figure 1), and statistical analysis showed this increase in connectivity to be significant for DMN, DAN, and SN. The connectivity between LC and the networks was found to become more negative, except for FPCN, which became more positive. Statistical testing confirmed that this shift is significant for connectivity between LC and FPCN, DAN, and SN. The dots representing the correlation coefficients become less clumped after squeezing, indicating a possible increase in variance. While the R^2 value of the linear regression decreased after squeezing, with the exception of SN, a paired t-test showed that there is no significant change in variance.
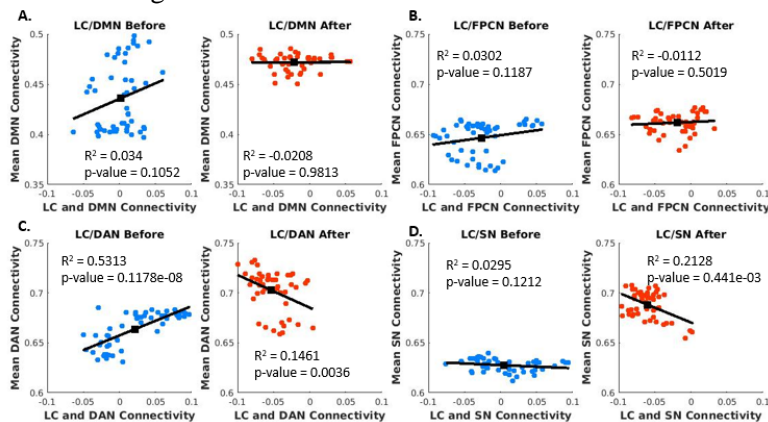
Figure 1: Connectivity between LC and DMN (**A**), FPCN (**B**), DAN (**C**), and SN (**D**) before and after squeezing, averaged across all 10 subjects. Dots show the correlation coefficients in each time window, and the black square shows the mean value of each axis.

Conclusions: Our results suggest that arousal induces a slight anti-correlation between LC and DAN, and LC and SN, indicating that when LC turns on, the networks turn off. Similarly, arousal causes a more positive connection between LC and FPCN suggesting that both are turning on at the same time. Moreover, there appears to be no significant decrease in network variability upon arousal.

4:20 pm – 5:50 pm	**Stem Cells and Regenerative Medicine (MR 1)**
	Chair: Jin Nam, UC Riverside Co-Chair: Joshua Morgan, UC Riverside
4:20 pm – 4:35 pm	Caleb Lee, UC Berkeley Human iPSC-Derived Liver-Microphysiological Systems for Drug Development
4:35 pm – 4:50 pm	Gagandip Singh, UC Merced Perfusable Vasculature Enhanced by Cardiomyocyte Co-Culture
4:50 pm – 5:05 pm	Atena Zahedi, UC Riverside Quality Control Methods for Monitoring Stem Cells in Health and Disease
5:05 pm – 5:20 pm	Gauree Chendke, UC San Francisco Controlled Release of Amino Acids for Enhancement of Islet Viability in Encapsulation and Transplantation
5:20 pm – 5:35 pm	Tri Andrew Q. Phan, UC Irvine Dynamic Adhesome Gene Regulation in Somatic Cell Reprogramming
5:35 pm – 5:50 pm	Mehrsa Mehrabi, UC Irvine In Vitro Modeling of Variable Heart Diseases due to LaminA/C Mutation via Patient induced Pluripotent Stem Cell-Derived Cardiomyocytes
4:20 pm – 5:50 pm	**Biomedical Imaging 2 (MR 2)**
	Chair: Hyle Park, UC Riverside Co-Chair: Xiaoping Hu, UC Riverside
4:20 pm – 4:35 pm	Yichen Wu, UC Los Angeles Deep Learning Achieves Auto-focusing and Phase Recovery to Extend the Depth-of-field in Digital Holographic Microscopy
4:35 pm – 4:50 pm	Michael C. Lun, UC Merced Development of a Focused X-ray Luminescence Tomography (Fxlt) Imaging System
4:50 pm – 5:05 pm	Maha K.Rahim, UC Irvine Transforming FLIM into a High-Content Molecular Analysis Platform
5:05 pm – 5:20 pm	Yibo Zhang, UC Los Angeles On-Chip Microscopy for 3D Imaging of Optically Cleared Tissue
5:20 pm – 5:35 pm	Mohammad Torabzadeh, UC Irvine Broadband Spatial Frequency Domain Imaging Using a Supercontinuum Laser Source
5:35 pm – 5:50 pm	Chih-Chiang Chang, UC Los Angeles Integrating 4-D Light-Sheet Imaging with Interactive Virtual Reality to Recapitulate Developmental Cardiac Mechanics and Physiology
4:20 pm – 5:50 pm	**Medical Devices and Instrumentation 2 (MR 3)**
	Chair: William Grover, UC Riverside Co-Chair: Victor G. J. Rodgers, UC Riverside
4:20 pm – 4:40 pm	Junming Cai, UC Irvine A Novel Synthetic Artificial Cornea with Biomimetic Nanotopography, from Device Fabrication to Animal Study
4:40 pm – 5:00 pm	Brittney McKenzie, UC Riverside "Microfluidic Thermometers" for Analyzing Biomedical Samples
5:00 pm – 5:20 pm	Y. Chung, UC Los Angeles Laser Generated Shockwave Treatment Increases Bacterial Cell Membrane Permeability In Vitro
5:20 pm – 5:40 pm	A. Downs, UC Santa Barbara Electrokinetic Sensing of Immunoglobulin G: A Preliminary Study of IgG Conductivity in Physiologically-relevant Buffer
4:20 pm – 5:50 pm	**Molecular and Cellular Engineering 2 (Ballrooms A and B)**
	Chair: Val Vullev, UC Riverside Co-Chair: Stephanie Fraley, UC San Diego
4:20 pm – 4:35 pm	J. C. Tang, UC Riverside Characterization of Phosphatidylserine Expression on Erythrocyte-derived Nanoparticles
4:35 pm – 4:50 pm	V. Herrera, UC Irvine Measuring Protein Secretion From Single Cells at Single Molecule Resolution Using Quantum Dots
4:50 pm – 5:05 pm	P. Kyriakakis, UC San Diego Genetically Encoded PhyB Optogenetics in Animal Cells
5:05 pm – 5:20 pm	E. M. Espinoza, UC Riverside Dipole Modulation of Charge Transfer
5:20 pm – 5:35 pm	K. Chen, UC San Diego Assessing Cancer Heterogeneity Through Phenotypic Cell Sorting
5:35 pm – 5:50 pm	G. Way, UC Riverside Develop Sumoylation Inhibition as a Novel-influenza A Virus Agent

HUMAN IPSC-DERIVED LIVER-MICROPHYSIOLOGICAL SYSTEMS FOR DRUG DEVELOPMENT

C.S. Lee[1,2*], F.T. Lee-Montiel[1,2*], A. Laemmle[3*], B. Siemons[1,2], H. Willenbring[3] and K.E. Healy[1,2]

[1]Department of Bioengineering and California Institute for Quantitative Biosciences (QB3), University of California, Berkeley, CA

[2]Department of Materials Science and Engineering, University of California, Berkeley, CA

[3]Department of Surgery, Division of Transplantation and Eli and Edythe Broad Center of Regeneration Medicine and Stem Cell Research, University of California, San Francisco, CA.

*These authors contributed equally to the work.
Contact: *Holger.Willenbring@ucsf.edu* and *kehealy@berkeley.edu*

Introduction: Microphysiological Systems (MPS) have been proposed as in vitro models for drug screening that can potentially replace animal models. Here, we report a liver-MPS (L-MPS) that contains human iPSC-derived hepatocytes and partner cells that exhibit normal physiological responses, such as stable albumin and urea secre-tion, lipid storage, low number of immature hepatocytes, regulation of glucose metabolism, and liver specific drug response.

Materials and Methods: Our L-MPS models a single liver sinusoid using two micropatterned PDMS layers (cell chamber and media channel) and an isoporous PET membrane in between to allow media flow. Each layer was made by first creating a mold via photolithography then replica molding with PDMS soft lithography. Next, we loaded human iPSC-derived cells, of which 80% were albumin positive, 7% endothelial, and 2% stromal cells, with the remaining cells undefined. Once the hepatocytes and their supporting cells were fully loaded in the chamber, culture (or conditioned) media was hydrostatically perfused. COMSOL simulations were performed to assess the microenvironment for the cells (i.e., shear stress, oxygen level, and distribution of a small molecule following me-dia). Lastly, drug response within the L-MPS was performed by measuring CYP3A4 metabolism in the presence of cisapride and then while blocking activity with ketoconazole.

Results and Discussion: Live/dead (calcein AM/ethidium homodimer-1) staining showed strong viability of the cells after loading (Fig. 1A center). They were also functionally robust, as the immunofluorescence images illustrate high albumin expression, suppression of the immature hepatocyte marker alpha-fetoprotein (AFP), and formation of lipid droplets over time (Fig. 1A bottom). Moreover, functional superiority of cells in 3D L-MPS over 2D culture was shown by comparing albumin and urea production (Fig. 1B top). As an indicator of liver-like function, change in mean glucose level responding to physiologically relevant insulin and glucagon media was observed (Fig. 1B bottom-left). CYP3A4 activity within the L-MPS was confirmed by exposure to cisapride, and inhibition was con-firmed under ketoconazole-treated conditions (Fig. 1B bottom-right).
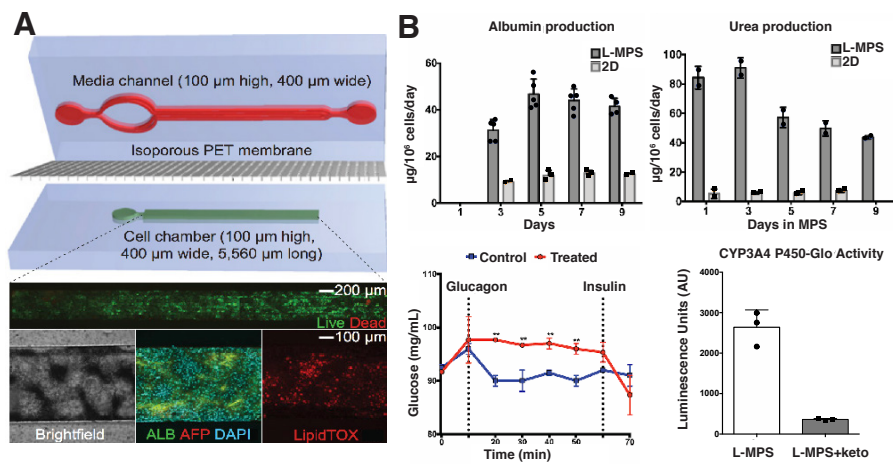
Figure 1. (A) Design of the L-MPS and cell viability/functionality. Immu-nofluorescence showed strong albumin and weak DAPI expressions, and Lip-idTOX staining indicated lipid droplet formation. (B) Cell functionality and metabolism in 3D L-MPS compared to that in 2D culture. Mean productions of albumin and urea were significantly higher in L-MPS (top). Response of the hepatocytes to glucagon and insulin was measured by change in mean glucose levels (bottom-left). Drug metabolism of cisapride exposed to the L-MPS demon-strated CYP3A4 activity, and inactivity when inhibited by ketoconazole (bot-tom-right).

Conclusions: We developed a liver MPS that integrates human iPSC-derived hepatocytes into an environment that replicates essential characteristics of liver physiology. Continuous and homogenous diffusion-mediated nutrient exchange through fenestrated sinusoidal endothelial cells in vivo was reproduced with continuous and hydrostat-ic perfusion of media in vitro. Ample oxygen and shear stress protection for cells inside the liver MPS were also confirmed using COMSOL simulations (data not shown). Resulting immunofluorescence images supported strong viability and liver-like functionality of the cells, including: (i) stable albumin and urea secretion; (ii) lipid droplet formation; and, (iii) physiological regulation of glucose release. We propose our liver MPS will be an effective tool at reducing the current gap between in vitro liver animal models and in vivo human liver function.

PERFUSABLE VASCULATURE ENHANCED BY CARDIOMYOCTE CO-CULTURE

[1]G. Singh, [2]L. Wong, and [2]K. McCloskey

[1]School of Natural Sciences, University of California, Merced, CA

[2] Graduate Program in Biological Engineering and Small-scale Technologies, University of California, Merced

Contact: *kmccloskey@ucmerced.edu*

Introduction: Cardiovascular disease is one of the leading causes of death around the world. After a myocardial infarction, heart tissue is injured and heart cells, or cardiomyocytes, are not able to regenerate. Regenerative medicine investigates how to produce these tissues in vitro to repair the damaged tissue. However, engineered tissues are limited in size due to oxygen's diffusion limit of 250 μm [1]. Vascular networks and three-dimensional cardiac muscle can be formed in vitro, but merging these two tissues has proven difficult. Stem cells are a promising tool for cardiovascular tissue engineering, as they can be directed to differentiate into endothelial cells (ECs) which can be used to form vascular networks and cardiomyocytes (CMs) to form heart tissue. Therefore, we set out to combine stem cell derived-ECs and CMs in a fibrin bead assay and microfluidic device to investigate vascular network formation in the presence of CMs.

Materials and Methods: Undifferentiated human embryonic stem cells (hESC-H9) were induced into ECs on fibronectin coated plates with stage 1 medium containing VEGF and BMP-4. KDR^+ cells were selected and plated with medium containing VEGF and bFGF. After 7 days, SB431542 is added and on day 25 the cells were purified based on VE-cadherin expression. The same hESC-H9 cells were also used to generate cardiomyocytes from an established protocol [2]. We first examine the sprouting capacity of the hESC-derived ECs in a fibrin bead assay. Cytodex 1 microcarrier beads were coated with fibronectin to increase attachment followed by EC seeding. The EC-coated beads were then suspended in fibrin gels with either normal human lung fibroblasts (NHLF) or both NHLF and hESC-derived CM cultured on top of the fibrin gels. Next, perfusable vasculature was generated within microfluidic devices (designs generously provided by Roger Kamm, MIT) made from polydimethylsiloxane (PDMS). A combination of human umbilical vein endothelial cells (HUVEC) or hESC-EC, NHLF, and hESC-derived CM were suspended in fibrin in the center channel at various ratios.

Results and Discussion: In the fibrin bead assay, greater EC sprouting was observed in the presence of NHLF and hESC-derived CM, compared to the control of NHLF only (Figure 1A and B). Perfusable vascular networks were formed from HUVEC in the presence of hESC-derived CM and NHLF. However, attempts to form perfusable networks using the more migratory hESC-derived EC remain a challenge.
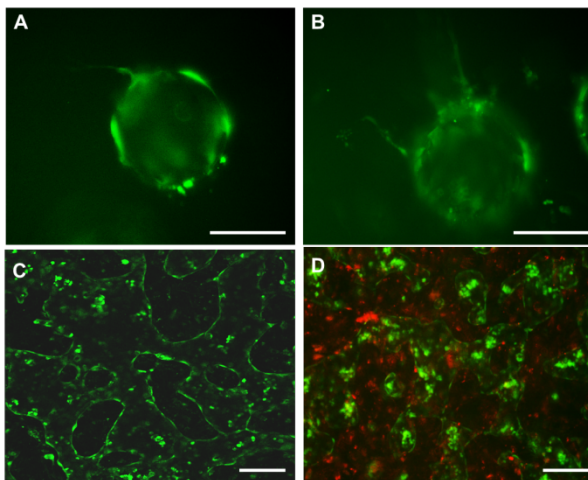
Figure 1: (A) Fibrin bead sprouting assay of hESC-derived EC (Cell Tracker Green) on day 4 co-cultured with only NHLF or **(B)** NHLF and hESC-derived CM. **(C)** HUVEC (Cell Tracker Green) forming perfusable microvasculature in a microfluidic device **(D)** co-cultured with hESC-H9 derived CM (Cell Tracker Red). Scale bars=100μm

Conclusions: The findings show that co-culturing EC with hESC-derived CM can enhance sprouting and lumen formation. Although the hESC-derived EC do form angiogenic sprouts and exhibit some potential to form sprouts and assemble into vascular networks, more optimization is necessary for enhancing stability of vasculature using hESC-derived EC.

References:
1. Lovett, M., et al., *Vascularization strategies for tissue engineering.* Tissue Eng Part B Rev, 2009. **15**(3): p. 353-70.
2. Lian, X., et al., *Directed cardiomyocyte differentiation from human pluripotent stem cells by modulating Wnt/beta-catenin signaling under fully defined conditions.* Nat Protoc, 2013. **8**(1): p. 162-75.

QUALITY CONTROL METHODS FOR MONITORING STEM CELLS
IN HEALTH AND DISEASE

[1]A. Zahedi, [2]R. Phandthong, [3]V. On, and [1,2]P. Talbot

[1]Department of Bioengineering, University of California, Riverside, CA

[2]Department of Molecular, Cell and Systems Biology University of California, Riverside, CA

[3]Department of Electrical Engineering, University of California, Riverside, CA

Contact: *talbot@ucr.edu* (corresponding author: Dr. Prue Talbot)

Introduction: The application of stem cells in regenerative medicine and disease modeling have enormous potential; however, systematic approaches are needed to ensure that stem cells meet the standards necessary for basic research, clinical use, and commercial therapeutics. Here, we introduce StemCellQC, a pipeline to non-invasively assess the health of pluripotent stem cell colonies, including induced pluripotent stem cells, during culture and experimental conditions. In addition, we introduce MitoMo, a user-friendly software toolkit that can be used with single cells to assess mitochondrial health, which is a sensitive barometer for detecting stress. Lastly, we introduce bioinformatics methods for evaluating epithelial-to-mesenchymal transitions (EMT) in cancer cells and tracking changes in the context of disease progression.

Materials and Methods: StemCellQC and MitoMo were written and developed with MATLAB 2016a. The source codes and executable versions are available online at http://vislab.ucr.edu/SOFTWARE/software.php. EMT analysis was conducted using a combination of software including MATLAB and CL-Quant (DR Vision).

Results and Discussion: StemCellQC provided quantifiable real-time data on human embryonic stem cell (hESC) colonies to identify biomarkers of health/harm, which are not detectable by manual inspection. Feature analysis, when combined with machine-learning classification, enabled identification of healthy, unhealthy, and dying colonies. The software was used to determine that cigarette smoke inhibited growth, increased motility, and increased apoptosis (Figure 1A-B) [1]. MitoMo was used to show that mouse neural stem cells (mNSC) treated with a toxicant experienced stress-induced mitochondrial hyperfusion (SIMH), a protective mechanism (Figure 1C). MitoMo enables automatic analysis of mitochondrial morphology, intra-organelle motion, texture, morphogenesis, and cell health classification. Lastly, a set of tools were developed to classify cancer cell morphology into normal, elongated (EMT-like), and enlarged phenotypes (Figure 1D). Other capabilities include motility and cell-cycle regulation analysis, which are all hallmarks of cancer metastasis and progression.
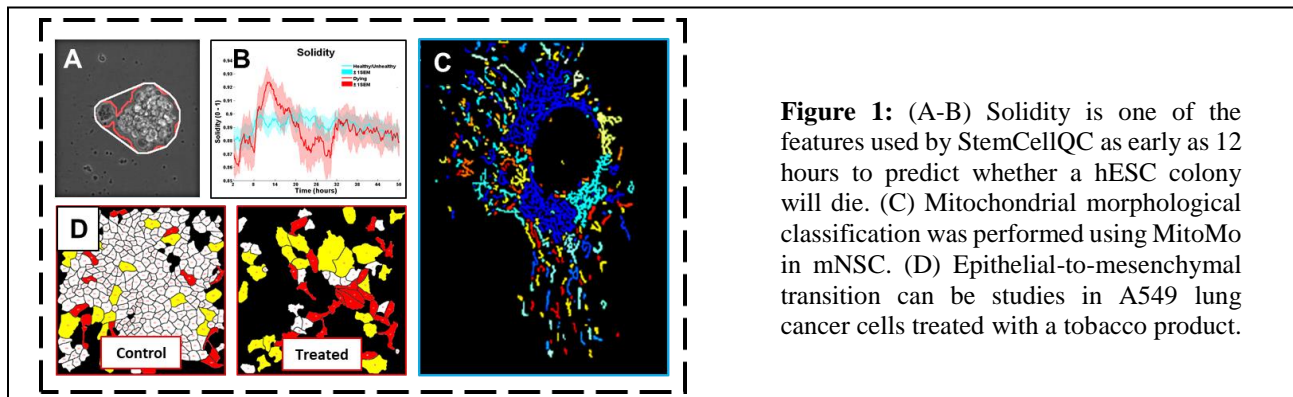
Figure 1: (A-B) Solidity is one of the features used by StemCellQC as early as 12 hours to predict whether a hESC colony will die. (C) Mitochondrial morphological classification was performed using MitoMo in mNSC. (D) Epithelial-to-mesenchymal transition can be studies in A549 lung cancer cells treated with a tobacco product.

Conclusions: Automated image and video bioinformatics software enable fast, accurate, and unbiased analysis of complex biological processes at the cellular, subcellular, and even intra-organelle levels. These software have broad utility in cell biology, drug discovery, toxicology, and medicine in that they permits deep quantitative evaluation of stem cell health, stress, and disease.

References (optional): 1. Zahedi A, On V, Lin SC, Bays BC, Omaiye E, Bhanu B, et al. Evaluating cell processes, quality, and biomarkers in pluripotent stem cells using video bioinformatics. PLoS One. 2016;11: 1–22. doi:10.1371/journal.pone.0148642

CONTROLLED RELEASE OF AMINO ACIDS FOR ENHANCEMENT OF ISLET VIABILITY IN ENCAPSULATION AND TRANSPLANTATION

*Gauree Chendke, [a]Gaetano Faleo, [a]Charity Juang, [a]Matthias Hebrok, [a]Qizhi Tang, and *Tejal Desai
* Department of Bioengineering and Therapeutic Sciences, University of California, San Francisco, CA
[a] Diabetes Center, University of California, San Francisco, CA
Contact: gauree.chendke@ucsf.edu

Introduction: Transplantation of encapsulated pancreatic islets is a developing treatment for Type 1 diabetes mellitus (T1D), which affects approximately 34.6 million Americans today.[1] Since T1D is a chronic autoimmune disease in which host immune cells attack the insulin producing beta cells in pancreatic islets, it is crucial to provide immune protection to the transplanted islets. Cell encapsulation addresses this problem by providing a physical barrier between transplanted islets and the transplant recipient, thereby protecting the islets from immune rejection without the need for life-long immunosuppressants. Previous research conducted in the Desai lab has shown that nanoporous polycaprolactone (PCL) encapsulation devices serve as ideal encapsulation device that allows stem cell derived insulin producing cells (SCIPC's) to survive and function *in vivo*. This treatment, although promising, has some challenges since encapsulation devices are prone to ischemia, which results in a loss of 50-80% of cell mass post-transplantation. Therefore, the aim of this work is to develop a device that will enhance the survival of the encapsulated cells immediately after transplantation. Past research has shown that supplementation of single amino acids (glutamine and alanine in particular) to the cells can prevent beta cell death in vitro[2]. Using this information, our aim is to support cell survival for up to 2 weeks until the exterior of the device is vascularized. Therefore, we have developed a biocompatible to enhance cell survival post-transplantation.

Materials and Methods: For the assembly of the encapsulation devices, nanoporous PCL thin-film devices were fabricated as described in Nyitray et al. (2015)[3] and Chang et al. (2017)[2]. Following the same techniques used to make the encapsulation devices, amino acid compartment was embedded inside the encapsulation device. After demonstrating sustained release over two weeks, the amino acid supplemented devices were tested to assess viability enhancement of the encapsulated cells *in vitro*. In order to simulate the nutrient-depleted conditions encountered by encapsulated cells *in vivo* immediately after transplant, cells and devices were placed in deplete media, which contains no supplemental nutrients. After various time points, flow cytometry following propidium iodide staining was performed to determine cell viability.

Results and Discussion: By manipulating the thickness and porosity of the PCL films used to make the devices, long-term release of amino acids was achieved. Using 80 kDa non-porous PCL, the release rate of glutamine and alanine from the amino acid devices was 163 µg/day and 12.9 µg/day, respectively. Cell viability assays demonstrated that there is a significant improvement of cell survival in devices with an amino acid internal compartment as compared to cells in depleted media with no amino acid supplementation (Figure 1). 50 SCIPC's were encapsulated in devices with and without the presence of amino acid devices. After 24 hours, 67.9% of encapsulated cells in depleted media survived while more than 95% of cells encapsulated in depleted media with the incorporation of glutamine or alanine devices survived.
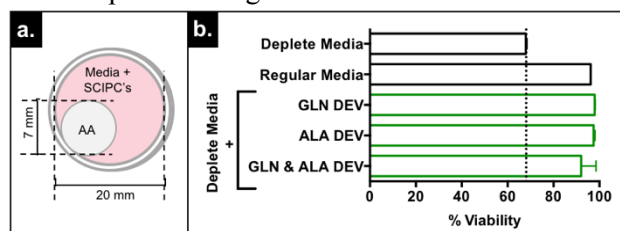
Figure 1. Schematic of device design (a). Cell survival benefit for encapsulated cells with amino acid devices after 24 hours (b).

Conclusions: The controlled release of alanine and glutamine within the inner compartment of the encapsulation device increases the viability of stem cell derived insulin producing cells in nutrient-lacking conditions. Currently, further tests are being conducted to assess cell viability and function at higher cell densities and longer time points. Also, on-going *in vivo* studies in immunodeficient NSG mice are being conducted to assess cell viability and function.

References: 1. Schweicher, J., Frontiers in Bioscience, 2014, 19, 49-76. **2.** Chang, R. ACS Nano, 2017, 11(8), 7747-7757. **3.** Nyitray, CE. ACS Nano, 2015, 9 (6), 5675-5682.

DYNAMIC ADHESOME GENE REGULATION IN SOMATIC CELL REPROGRAMMING

Tri Andrew Q. Phan, Zachary Reitz, Timothy L. Downing
Department of Biomedical Engineering, University of California, Irvine, CA
Contact: *tim.downing@uci.edu*

Introduction: Stem cells are known to sense and respond to their mechanical microenvironment. Previous studies have found that cell differentiation is heavily directed by mechanotransduction pathways.[1] Other evidence has implicated transmembrane protein anchors, such as integrins and adherens, in a number of cellular decisions including differentiation, survival, and proliferation.[2] Our lab has recently demonstrated that substrate topography can modulate the epigenetic state of mouse fibroblasts and facilitate somatic cell reprogramming.[3] However, the upstream effectors responsible for this phenomenon remain poorly understood. Here, we explore the effects of targeted RNA knockdown of ~100 genes found within the mammalian adhesome on induced pluripotent stem cell (iPSC) reprogramming efficiency. We hope to use the insights gained from this molecular screen to better understanding the influence of mechanical forces in somatic cell reprogramming.

Materials and Methods: For this study, we utilized an immortalized human fibroblast cell line (hiF-T) containing a doxycycline inducible OKSM gene cassette.[4] Our reanalysis of a previously published RNA-seq time course revealed that 104 of 346 integrin and cadherin adhesome genes are dynamically expressed during cellular reprogramming. To screen the effect of these genes on iPSC induction efficiency, three shRNAs per gene were designed and virally transduced into hiF-T cells before reprogramming was initiated. The impact of each shRNA was subsequently assessed by immunostaining for TRA-1-60, a known pluripotency marker. A secondary antibody HRP-reaction reporter followed by a whole-well image scan was used to quantify the number and coverage area of iPSC colonies. These values were averaged on a per gene basis and ordered for further analysis.

Results and Discussion: Here we show results from an RNAi screen of adhesome genes likely involved in the biophysical regulation of cell reprogramming. Surprisingly, over 90% of adhesome shRNA gene knockdowns increased colony count and area over shRNA controls. In terms of colony counts, our shRNA's improved by as much as 27-fold compared to controls. Of the 10% that decreased colony count, none reduced it by more than 3.8-fold when compared to the controls. Starker observations can be made in terms of colony coverage area, where increases in reprogramming efficiency of over 100-fold were observed. Ultimately, these results suggest a positive correlation between cellular reprogramming efficiency and adhesome gene suppression.
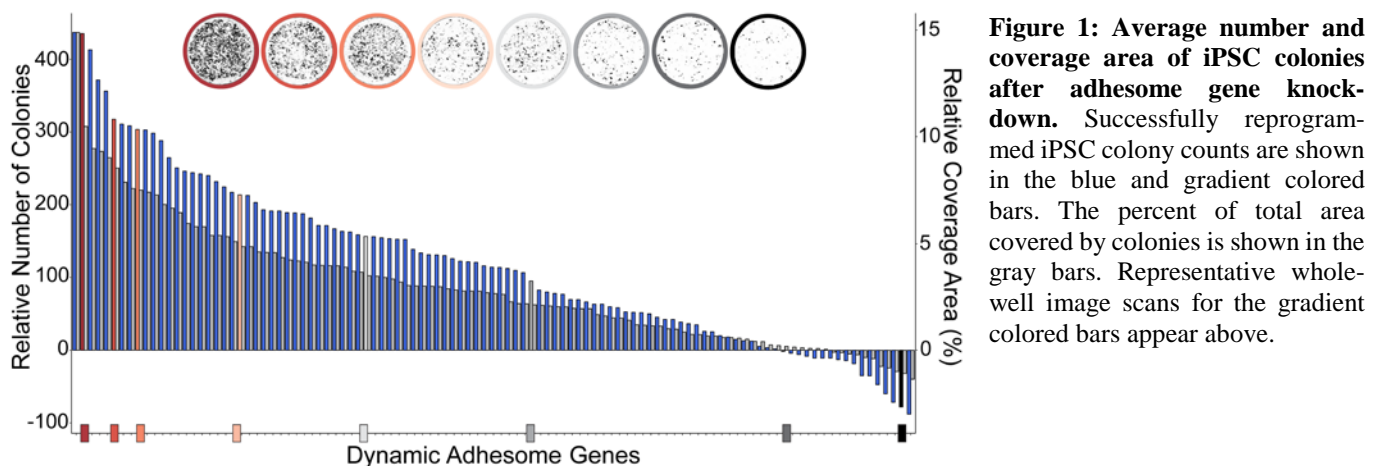
Figure 1: Average number and coverage area of iPSC colonies after adhesome gene knockdown. Successfully reprogrammed iPSC colony counts are shown in the blue and gradient colored bars. The percent of total area covered by colonies is shown in the gray bars. Representative whole-well image scans for the gradient colored bars appear above.

Conclusions: Our study reinforces the importance of mechanotransduction and the biophysical microenvironment in cellular reprogramming and reveals that reprogramming efficiency can be increased by inhibiting the expression of many relevant integrin and cadherin adhesome genes. These findings imply that cellular mechanosensing may act as a significant barrier to efficient somatic cell reprogramming. Further study of these mechanisms may enable a better understanding of somatic cell reprogramming and fate regulation more broadly.

References: 1. Engler, A. J., Sen, S., Sweeney, H. L. & Discher, D. E. *Cell* (2006) 2. Li, L., Bennett, S. A. L. & Wang, L. *Cell Adh. Migr.* (2012) 3. Downing, T. L. *et al. Nat. Mater.* (2013) 4. Cacchiarelli, D. *et al. Cell* (2015)

In Vitro Modeling of Variable Heart Diseases due to Lamin A/C Mutation via Patient induced Pluripotent Stem Cell-derived Cardiomyocytes

Mehrsa Mehrabi[1], Mira Asad[1], Danielle Beker[1], Halida Widyastuti[2], Cecilia Nguyen[2,] Linda A. Mccarthy[1,]
Michael V. Zaragoza[2], Anna Grosberg[1]

[1]Department of Biomedical Engineering, University of California, Irvine, [2]Depts. of Pediatrics- Genetics & Genomics Division and Biological Chemistry School of Medicine, University of California, Irvine

Introduction: Nuclear shape defects are a distinguishing characteristic in laminopathies, cancers, and other pathologies. According to numerous fundamental studies, there are many mutated genes that cause heart diseases, yet the practical diagnosis and treatment for them is scarce. A mutated Lamin A/C gene (*LMNA*) can cause dilated cardiomyopathy, arrhythmia, and heart failure. The *LMNA* encodes Lamin A/C proteins that make mesh like nuclear lamina under the nuclear envelope, and these proteins interact to impact the nuclear shape, stability, protein transduction, and DNA replication. Although, almost all nucleated cells in the human body have Lamin A/C in the nuclear lamina, we study patients who have Lamin A/C gene mutation with the main pathologies in the heart. Therefore, our goal is to understand the mechanisms of how an *LMNA* mutation can cause exclusively heart diseases. **Hypothesis:** We hypothesize that an *in vitro* model using induced Pluripotent Stem Cell (iPSC)-derived cardiomyocytes can differentiate between a population of patients whose major phenotype presentation is heart disease due to an *LMNA* mutation from the control population in structural and functional mechanisms.

Material and Methods: We have used *in vitro* tissue engineering techniques to interrogate the iPSC-derived cardiomyocytes tissue structures and function. PATIENT's and CONTROL's fibroblasts (from skin biopsy) were reprogrammed to iPSCs and differentiated to cardiomyocytes. The PATIENT and CONTROL iPSC-derived cardiomyocytes were cultured and immunostained for Nuclei, actin fibrils, and Sarcomere. The tissues were imaged with a confocal microscope, and the stained architectures were quantified. Moreover, for the functional assay, iPSC-derived cardiomyocytes were evaluated by the "Heart-on-a-Chip" device based on the muscular thin film (MTF) technology. The cardiomyocytes can either contract spontaneously or they can be paced using a myopacer at 0.5-2 Hz by field stimulation electrodes. The dynamics of the tissue constructs were recorded and analyzed using ImageJ and Matlab software. Data for PATIENTs and CONTROLs chips were collected and analyzed for frequency and stress as a function of time for all conditions tested.

Results and Discussion: Our data shows significant differences between iPSC-derived cardiomyocytes of PATIENTs and CONTROLs in frequency and active stress (Fig1). PATIENTs tissue do not respond to external electrical stimulation and they act independently from external stimulation (Fig1A), which can be due to *LMNA* mutation and could be a cause of heart disease initiation. Moreover, negative control has significantly higher developed force (Fig1B).
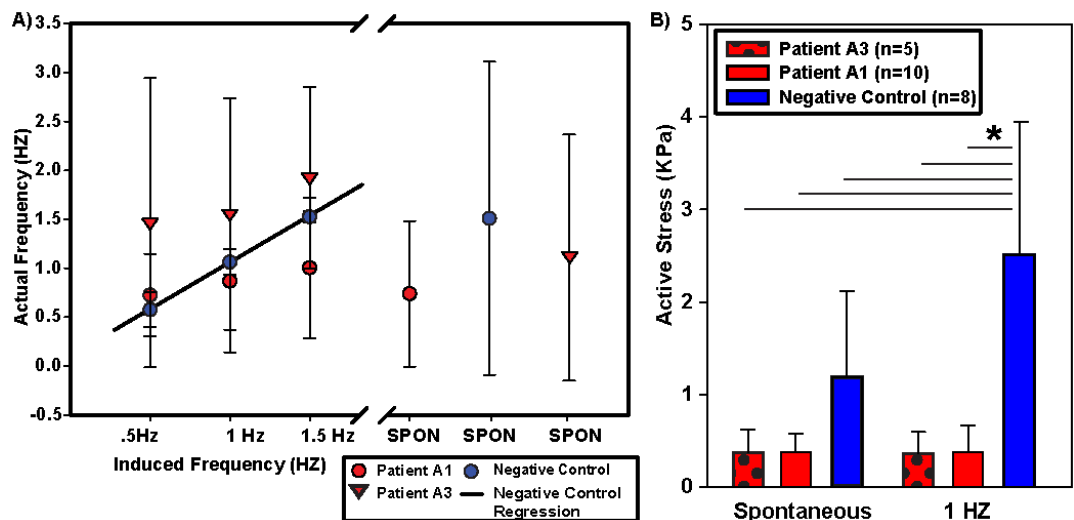
Figure1: A) iPSC-derived cardiomyocyte frequency B) Active stress

Conclusion: Our results demonstrate that it is possible to construct an iPSC-derived cardiomyocyte *in vitro* model that differentiates between our CONTROL and PATIENT population. Since, patients have severe symptoms exclusively in their hearts due to the *LMNA* mutation, investigating individual specific iPSC-derived cardiomyocytes shows better understanding of changing cells architectures caused by the mutation. By further investigating the structural and functional differences between PATIENTs and CONTROLs iPSC-derived cardiomyocytes, we can find the downstream mechanisms of LMNA mutation consequences in heart and find the proper treatments through drug screening and the other techniques by monitoring the function and structure of the iPSC-derived cardiomyocytes by using the "Heart-on-a-Chip" device.

DEEP LEARNING ACHIEVES AUTO-FOCUSING AND PHASE RECOVERY TO EXTEND THE DEPTH-OF-FIELD IN DIGITAL HOLOGRAPHIC MICROSCOPY

[1]Y. Wu, [1]Y. Rivenson, [1]Y. Zhang, [1]Z. Wei, [1]H. Gunaydin, [1]X. Lin, and [1]A. Ozcan

[1] University of California, Los Angeles, California 90095, USA

Contact: *wuyichen@ucla.edu*   *ozcan@ucla.edu*

Introduction: Digital holographic microscopy computationally reconstructs images of biological specimens from an intensity-only recording, without using any lenses. In its on-chip implementation, it decouples resolution from field-of-view (FOV) and can be made much smaller, lighter and lower cost than a conventional microscope. [1] However, to digitally reconstruct the sample image from its in-line hologram(s), auto-focusing and phase recovery are needed, which are time consuming to compute, and typically require 2-8 hologram measurements.[1] Here, we demonstrate a convolutional neural network (CNN) based approach that simultaneously performs both auto-focusing and phase recovery using a single intensity hologram.[2] This approach, termed HIDEF (Holographic Imaging using Deep learning for Extended Focus), significantly increases the computational efficiency (by > 30-folds) and reconstruction speed in holographic imaging and extends the depth-of-field (DOF) of the reconstructed images (by e.g., > 25 folds). We demonstrated the success of this approach by imaging various samples, including human breast tissue sections.

Materials and Methods: A deep CNN that separates the real image and twin image features of an object at different scales is designed and built using TensorFlow (see Ref.[2] for details). To train the HIDEF network, it was fed with pairs of randomly de-focused and back-propagated holograms, and their corresponding in-focus phase-recovered images. After its training, the neural network learned to automatically refocus different parts of the image and remove the twin image artifact, *both at the same time*, extending the DOF of digital holographic image reconstruction while performing phase recovery.

Results and Discussion: Fig. 1(a) compares the HIDEF reconstruction results against CNN input images from a single hologram and MH-PR (multi-height phase recovery) using eight holograms. The sample is a thin slice of a human breast tissue. CNN input images exhibit significant twin image and self-interference noise. MH-PR has a very limited DOF – even at a defocus distance dz = 5 µm, some of the fine features of the tissue are distorted. HIDEF, by inputting a single back-propagated hologram, retrieves high resolution, phase recovered images of the sample over a very large DOF ($|dz| \leq 100$ µm in this case). Fig. 1(b) quantitively compares different methods with MH-PR at correct focus using the structural similarity (SSIM) index,[2] averaged over 180 test FOVs. This comparison shows that HIDEF has significantly higher SSIM values compared to back-propagated images, owing to its auto-focusing and phase recovery capability. Compared to a CNN that trained with only in-focus images (green curve, Ref. [3]), HIDEF exhibits much higher SSIM values for de-focused holograms, over the range it was trained for ($\pm$ 0.1 mm or $\pm$ 0.2 mm).
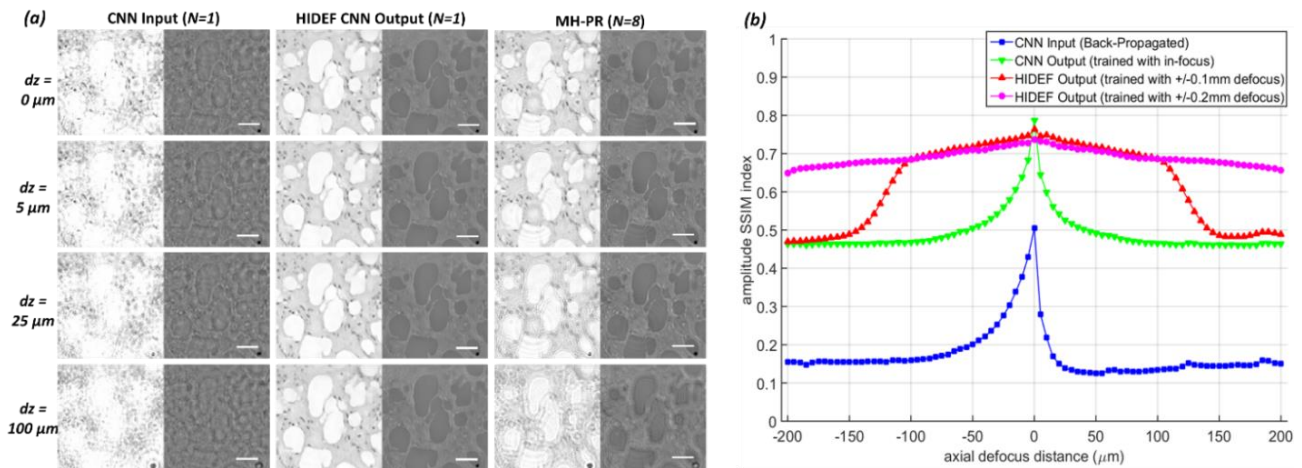
Fig. 1. (a) Comparison of HIDEF against free-space back-propagation (CNN input), and MH-PR, as a function of the axial defocus distance (dz). N is the number of the measured holograms. (b) SSIM values as a function of dz.

Conclusions: HIDEF significantly extends the DOF of holographic imaging while simultaneously performing phase recovery and auto-focusing using deep learning.

References: [1] Y. Wu and A. Ozcan, *Methods*, vol. 136, pp. 4–16, Mar. 2018.   [2] Y. Wu *et al.*, *ArXiv180308138 Phys.*, Mar. 2018. [3] Y. Rivenson et al., *Light Sci. Appl.*, vol. 7, no. 2, p. 17141, Feb. 2018.

DEVELOPMENT OF A FOCUSED X-RAY LUMINESCENCE TOMOGRAPHY (FXLT) IMAGING SYSTEM

[1]M.C. Lun, [1]W. Zhang, [1]Y. Zhao, [2]J. Anker, [3]W. Cong, [3]G. Wang, and [1]C. Li

[1]Department of Bioengineering, University of California, Merced, Merced, CA

[2]Department of Chemistry, Department of Bioengineering, Center for Optical Materials Science and Engineering Technology (COSMET) and Institute of Environmental Toxicology (Cu-ENTOX), Clemson University, Clemson, SC

[3]Department of Biomedical Engineering, Biomedical Imaging Center, Center for Biotechnology and Interdisciplinary Studies, Rensselaer Polytechnic Institute, Troy, NY

Contact: *cli32@ucmerced.edu*

Introduction: Recently, X-ray luminescence computed tomography (XLCT) has emerged as a hybrid molecular imaging modality and has shown great promises in overcoming the strong optical scattering in deep tissues. However, its high-resolution capabilities have not yet been implemented. In this work, using a superfine focused X-ray beam, we have designed a focused X-ray luminescence tomography (FXLT) imaging system for small-animals with both an anticipated spatial resolution of 150 μm and a high detection sensitivity of several μM. First, we discuss the system design, and then demonstrate the feasibility of this system from different perspectives, including the spatial resolution, molecular sensitivity, and methods to improve the scan-time for the case of narrow/pencil beam XLCT imaging, finally discussing some potential applications for this imaging system. Details of this work are currently summarized in reference 1.

Materials and Methods: Based on our previous studies, we designed the FXLT imaging system as shown in Fig. 1 below. To validate this system, we have performed numerical simulations (in MATLAB) and several physical experiments (using the prototype system described in [2]) to assess the imaging performance of the proposed system.
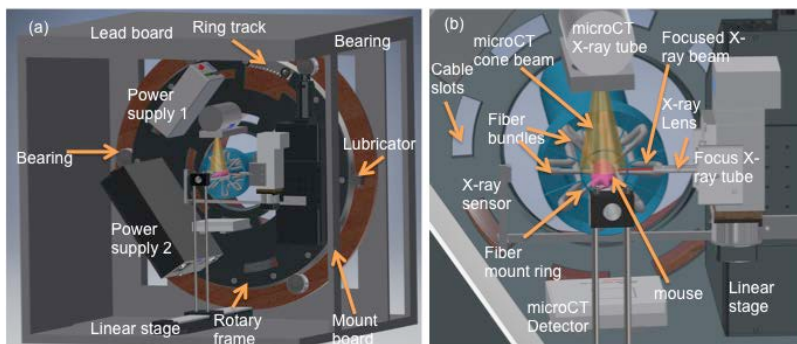
Figure 1: CAD model of the proposed FXLT imaging system. (a) Right front view and (b) zoomed in view.

Results and Discussion: Numerical simulations performed indicate that the proposed FXLT system can obtain a spatial resolution of 150 μm if we use a focused X-ray beam with a maximum diameter of 75 μm. Physical experiments performed with phantoms indicate an approximate molecular sensitivity of about 5 μM for depths of 10 mm. Also from our results, the scan time per transverse section can be reduced to approximately 120 seconds.

Conclusions: We have designed an FXLT imaging system with 150 µm spatial resolution and several µM molecular sensitivity for deeply embedded targets inside mice. We have estimated the FXLT imaging system performance with phantom experiments and numerical simulations. We have estimated that the scan time per transverse section imaging is about 120 seconds and the radiation dose will be around a typical CT scan range. Overall our results have indicated that the proposed FXLT imaging system has great potentials to be a powerful tool for the molecular imaging research community.

References:

1. M.C. Lun**,** W. Zhang, Y. Zhao, J. Anker, W. Cong, G. Wang, and C. Li, "*Development of a focused-X-ray luminescence tomography (FXLT) system,*" arXiv:1709.10186 [physics.med-ph]
2. W. Zhang, M.C. Lun, A.A. Nguyen, and C. Li, *"A focused x-ray beam based x-ray luminescence computed tomography,"* Jour. of Biomed. Opt., 22 (11), 116004 (2018).

TRANSFORMING FLIM INTO A HIGH-CONTENT MOLECULAR ANALYSIS PLATFORM

Maha K. Rahim[1], Enrico Gratton[1], Jered B Haun[1]
[1]Department of Biomedical Engineering, University of California, Irvine, CA
Contact: *mrahim@uci.edu*

Introduction*:* Tumors are complex and heterogeneous, and therefore diagnostic techniques will have to comprehensively assess molecular features across diverse cell types and functional states. Current methods that can provide both spatially-resolved and quantitative molecular interpretation of tissues are limited in multiplexing capacity or are complex and time-consuming. To address these limitations, we have developed a multiplexed imaging platform that utilizes fluorescence lifetime imaging microscopy (FLIM). Fluorescence lifetime refers to the duration of fluorescence light emission after excitation, and it can be leveraged to resolve fluorescent probes that have the same color. Moreover, the phasor approach to FLIM greatly simplifies lifetime analysis. Instead of fitting complicated exponential functions, the phasor approach provides a graphical representation that enables the unmixing of more than one lifetime using simple geometrical considerations. In this study, we are developing new methodologies to quantitatively detect 4 molecular probes within the same spectral window using FLIM and the powerful phasor method of lifetime analysis.

Materials and Methods: FLIM and phasor studies were performed using 4 different fluorescent probes that emit light within the same emission window, but have unique fluorescent lifetimes: rhodamine dye, bodipy-tmr dye, and two CdSe/ZnS quantum dots. Fluorescent probes were targeted to cancer biomarkers via monoclonal antibodies. FLIM images were analyzed using SimFCS software, whereby fluorescent lifetimes for each pixel in an image were placed as a point on the phasor plot. Pixels containing more than one fluorescent species exhibit lifetimes that are fractional contributions of each species; this information enabled unmixed quantification of each probe.

Results and Discussion: We performed FLIM on fluorescent probes in solution and analyzed lifetime using the phasor approach to confirm distinct phasor locations for each probe (Figure 1a). Next, we conjugated these probes to monoclonal antibodies targeting relevant cancer biomarkers. FLIM of targeted probes labeled onto NCI-H1650 cells demonstrated that phasor locations for each antibody conjugate closely matched the solution measurements. Simultaneous targeting of spatially separated biomarkers Ki67 (nucleus), cytokeratin (cytoplasm), and EpCAM (surface) resulted in a distinct phasor map with points corresponding to the lifetime of all three probes. Moreover, points on the phasor plot were traced back to image pixels, enabling clear visualization of targets within the cell (Figure 1b). We also targeted the cell surface markers EpCAM, Her2, E-Cadherin, and Transferrin Receptor on a panel of cell lines with varying biomarker expression levels, which resulted in distinct phasor locations that correlated well with expression levels measured by flow cytometry (Figure 1c). To our knowledge, this is the first demonstration in which 4 probes were resolved based only on fluorescence lifetime.
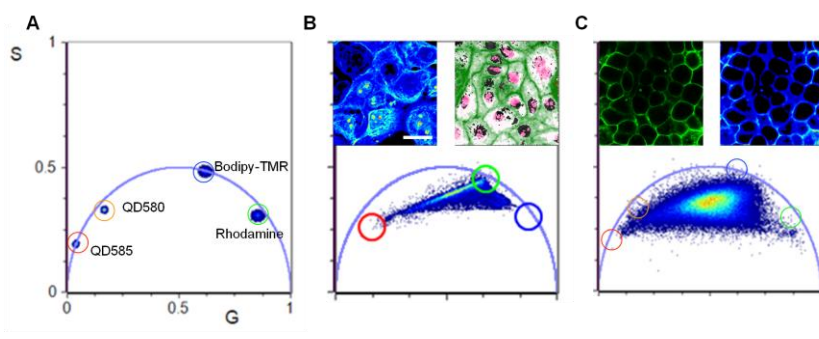
Figure 1. A) Phasor results for rhodamine, bodipy-TMR, QD580, and QD585 in solution measured by FLIM. B) Phasor results from simultaneous targeting of Ki67, cytokeratin, and EpCAM on NCI-H1650 cells with rhodamine, bodipy, and QD585 probes, respectively. C) Phasor results from simultaneous targeting of transferrin receptor, E-Cadherin, EpCAM, and Her2 on BT-474 cells with rhodamine, bodipy, QD580 and Q585 probes, respectively.

Conclusion: To fully maximize the potential of this technology, we will extend this detection platform to the other 4-8 spectral windows across the visible spectrum, resulting in detection capacity on the order of 16-24 targets. We will then utilize this approach for analysis of molecular markers in human cancer specimens. We are also creating a library of probes with distinct lifetimes. The extensive level of molecular information offered by our technology would make it possible to richly characterize heterogeneous tumor specimens to improve detection and enable host-cell subtyping, and rare cell detection.

ON-CHIP MICROSCOPY FOR 3D IMAGING OF OPTICALLY CLEARED TISSUE

[1,2,3]Yibo Zhang, [2,5]Yoonjung Shin, [2,5]Kevin Sung, [1]Sam Yang, [2]Harrison Chen, [1,2,3]Hongda Wang,
[4]Da Teng, [1,2,3]Yair Rivenson, [2,3,5]Rajan P. Kulkarni, and [1,2,3]Aydogan Ozcan
[1]Electrical and Computer Engineering Department, University of California, Los Angeles
[2]Bioengineering Department, University of California, Los Angeles
[3]California NanoSystems Institute, University of California, Los Angeles
[4]Computer Science Department, University of California, Los Angeles
[5]Division of Dermatology, Department of Medicine, David Geffen School of Medicine at
University of California, Los Angeles
Contact: *zybmax@ucla.edu ; ozcan@ucla.edu*

Introduction: The diagnoses of various diseases, including cancers, rely on traditional histopathology, where the tissue from a biopsy is micro-sectioned into sub-10-μm slices, stained, and evaluated using lens-based light microscopy. This process is high-cost, labor-intensive, low-throughput and results in a loss of 3D information inherent to cells and tissues. Recently developed tissue clearing techniques (such as CLARITY) offers the possibility to view large tissue volumes in 3D using fluorescence tagging and microscopy, which is promising to be used in clinical diagnosis. However, these approaches are also limited by high cost equipment and reagents, complex tissue processing procedures, limited throughput of fluorescence microscopy, and susceptibility to photo-bleaching and signal fading. To address these issues, we demonstrate a cost-effective and high-throughput tissue clearing and imaging procedure using a combination of the simplified CLARITY method (SCM) and lens-free on-chip microscopy, which is demonstrated to chemically clear and image a 0.2-mm thick mouse brain tissue over a wide field of view (FOV) of >20 mm^2.[1]

Materials and Methods: Mouse brain tissue was sectioned into various thicknesses (50-200 μm), chemically cleared using the SCM, and colorimetrically stained with diaminobenzidine (DAB). It was then loaded into a custom-made sample chamber filled with a refractive index matching solution (RIMS) and was imaged by our lens-free on-chip microscope (Figure 1(a)). This lens-free microscope uses a partially coherent light source for illumination, and a complementary metal-oxide-semiconductor (CMOS) image sensor to record the diffraction patterns of the sample. Pixel super-resolution (PSR) and multi-height phase recovery are used to computationally reconstruct the sample's image in 3D.[1]

Results and Discussion: As a proof of concept, we successfully imaged an optically cleared 200-μm-thick mouse brain tissue over a FOV of 20.5 mm^2 (Figure 1(b)), that is, a tissue volume of ~4 μL, which is four orders of magnitude larger than the imaging volume of a typical 20× microscope objective. The images of the cells distributed in the 3D volume are in good agreement with the images acquired by a 20× 0.75NA scanning bright-field microscope (Figure 1 (d)).
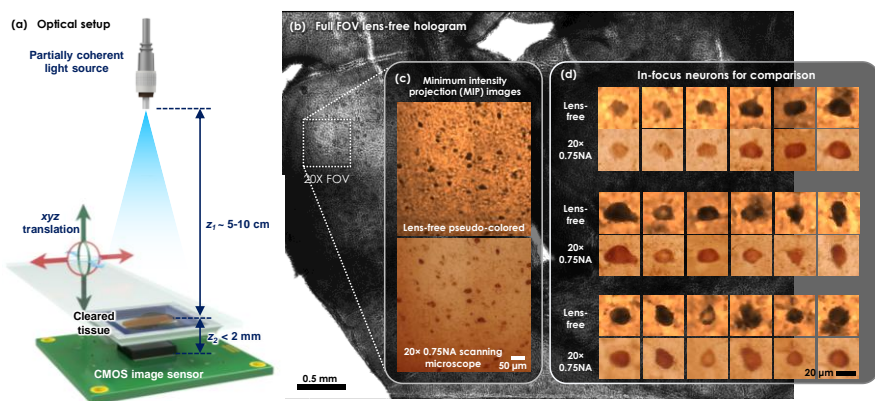
Figure 1. (a) Schematic of the lens-free on-chip microscope. (b-d) Imaging result of a 0.2-mm-thick cleared mouse brain tissue over a wide FOV of 20.5 mm^2, corresponding to a tissue volume of ~4 μL.

Conclusions: The presented tissue clearing and computational imaging procedure can potentially be used to reduce the cost and improve the throughput of pathological diagnosis, especially at resource-limited settings.

References: [1] Zhang, Y. *et al.* 3D imaging of optically cleared tissue using a simplified CLARITY method and on-chip microscopy. *Science Advances* **3,** e1700553 (2017).

BROADBAND SPATIAL FREQUENCY DOMAIN IMAGING USING A SUPERCONTINUUM LASER SOURCE

[1,2]M. Torabzadeh, [3]P. Stockton, [1,2]H. S. Yazdi, [1]G. T. Kennedy, [1,2]A. J. Durkin, [3]R. A. Bartels, [1,2]B. J. Tromberg

[1]Department of Biomedical Engineering, University of California, Irvine, CA
[2]Laser Microbeam and Medical Program, Beckman Laser Institute, Irvine, CA
[3]Colorado State University, School of Biomedical Engineering, Fort Collins, CO
Contact: *mtorabza@uci.edu*

Introduction: Hyperspectral imaging is a growing technique for medical applications such as diabetic foot ulcers and image-guided surgery. We have developed a Hyperspectral Spatial Frequency Domain Imaging (H-SFDI) system that quantifies and decouples sample's optical properties, absorption (μ_a) and reduced scattering (μ'_s). μ_a can be used to characterize tissue function [1] by calculating chromophore concentrations such as oxy/deoxyhemoglobin and μ'_s can be correlated with tissue structures such as collagen fibers [2-3].

Materials and Methods: Our H-SFDI system is based on integration of a supercontinuum laser source to a wavelength-tuning optical configuration. A folded Martinez configuration along with a slit mounted on a linear stage allows for tuning the central wavelength and bandwidth of the output beam [4]. The laser beam is then expanded, spatially modulated using a digital micro-mirror device, and projected onto a sample. Reflected light is finally captured with a scientific camera to generate a hyperspectral cube of optical properties in the 580-950nm range using the SFDI technique.

Results and Discussion: We measured a tissue simulating phantom with two absorbing dyes, Naphthol Green B and Nickel(II) Phthalocyanine, and their 50/50 % by volume mixture. Once μ_a spectra are calculated at each pixel, it is fitted to extinction coefficient spectra of its two constituents. Figure 1 shows concentration maps of these two dyes. As it was expected, concentration value of the mixture is measured to be almost half of its pure solution for both dyes.
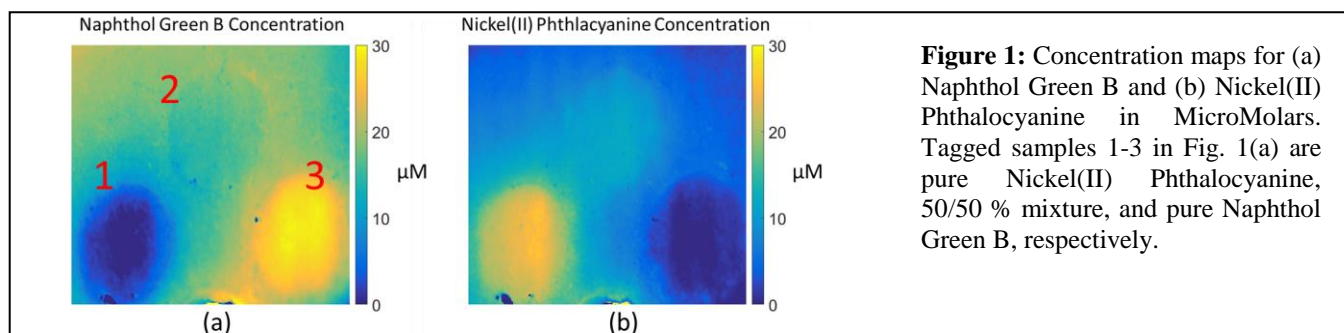
Figure 1: Concentration maps for (a) Naphthol Green B and (b) Nickel(II) Phthalocyanine in MicroMolars. Tagged samples 1-3 in Fig. 1(a) are pure Nickel(II) Phthalocyanine, 50/50 % mixture, and pure Naphthol Green B, respectively.

Conclusions: The proposed broadband H-SFDI instrument can decouple absorption contribution of multiple dominant chromophores in a tissue phantom. This work can be extended to biological samples such as human skin to quantify oxy/deoxyhemoglobin, melanin, water, and fat concentrations. Fine spectral resolution along with spatial frequency domain information can also provide opportunities for diffuse optical tomography approaches to characterize tissue function in 3D.

References:
1. Yazdi, Hossein S., et al. "Mapping breast cancer blood flow index, composition, and metabolism in a human subject using combined diffuse optical spectroscopic imaging and diffuse correlation spectroscopy." Journal of biomedical optics 22.4 045003(2017).
2. R. H. Wilson et al., "High-speed spatial frequency domain imaging of rat cortex detects dynamic optical and physiological properties following cardiac arrest and resuscitation." Neurophotonics 4(4), (2017).
3. M. Torabzadeh et al., "Compressed single pixel imaging in the spatial frequency domain"; Journal of Biomedical Optics 22(3), 030501 (2017).
4. M, Torabzadeh et al. "Hyperspectral characterization of tissue simulating phantoms using a supercontinuum laser in a spatial frequency domain imaging instrument." Design and Quality for Biomedical Technologies XI. Vol. 10486. International Society for Optics and Photonics, (2018).

INTEGRATING 4-D LIGHT-SHEET IMAGING WITH INTERACTIVE VIRTUAL REALITY TO RECAPITULATE DEVELOPMENTAL CARDIAC MECHANICS AND PHYSIOLOGY

C-C. Chang[1], Y. Ding[1,2], A. Abiri[2,3], P. Abiri[1,2], K. Baek[1], R. R. S. Packard[2], and T. K. Hsiai[1,2]

[1]Department of Bioengineering, University of California, Los Angeles, CA
[2]Division of Cardiology, David Geffen School of Medicine at UCLA, Los Angeles, CA
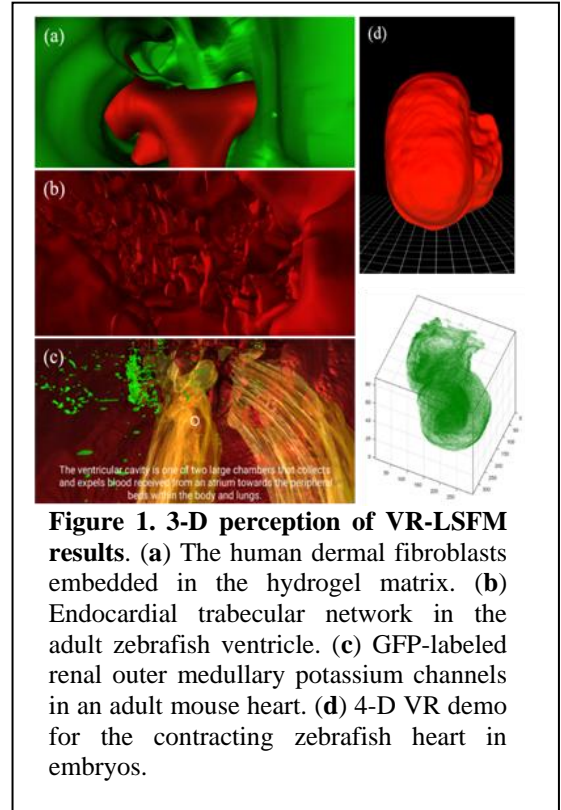[3]Department of Biomedical Engineering, University of California, Irvine, CA
Contact: *changc4@ucla.edu*

Introduction: Light-sheet fluorescence microscopy (LSFM) introduces rapid image acquisition with high axial resolution in capturing physiological events in the 3-dimensional (3-D) or 4-D (3-D spatial + 1-D temporal) domain. However, current visual methods are constrained from displaying 3-D architecture post volume rendering. Virtual reality (VR) enables us to integrate with advanced imaging to resolve the limitation of the current volume rendering technique for an immersive and interactive experience. We hereby integrate LSFM and VR to create a 3-D and 4-D interactive experience for the user. The VR-LSFM platform is further adapted to a smartphone through the Google Cardboard or Daydream viewer.

Materials and Methods: We built a dual-sided illumination LSFM system for acquiring 3-D image stack or 4D events. The images were preprocessing through variational stationary noise remover algorithm and deconvolution approach to enhance the image contrast. By applying manual segmentation and newly developed batch intensity normalized segmentation methods, we post-processed and converted the raw data to an editable 3-D object via an open file protocol. This proposed pipeline enabled us to integrate the image acquisition with data visualization, bypassing the conversion to vector images. We further applied deformable image registration to reconstruct the 4-D contracting heart in zebrafish embryos. Finally, we published all of the objects along with the scenes as a single installable application from the engine to the Android platform. This approach enabled us to run in VR-mode on the smartphone equipped with the Google VR viewer.

Results and Discussion: We are able to interrogate proliferating human dermal fibroblast cells in response to the physical and degradation properties of the hyaluronic acid hydrogel beads as a basis for wound repairs (**Figure 1(a)**). We are also able to navigate through the trabecular network in the adult zebrafish model of injury and regeneration (**Figure 1(b)**), and to quantify 4-D wall strain (space + cardiac cycle) in the embryonic zebrafish hearts. Furthermore, we succeed in detecting the spatial distribution of potassium channels underlying cardiac contractile function following gene modulation/therapy in the adult murine hearts (**Figure 1(c)**). In addition, we also developed another framework for dynamic VR application, that is, 4-D data in the VR mode (**Figure 1(d)**). Recapitulating LSFM imaging by VR introduces an interactive and immersive experience for navigating micro-environments for the study of developmental cardiac mechanics and physiology.

Figure 1. 3-D perception of VR-LSFM results. (**a**) The human dermal fibroblasts embedded in the hydrogel matrix. (**b**) Endocardial trabecular network in the adult zebrafish ventricle. (**c**) GFP-labeled renal outer medullary potassium channels in an adult mouse heart. (**d**) 4-D VR demo for the contracting zebrafish heart in embryos.

Conclusions: The VR-LSFM hybrid method establishes an efficient and robust platform to hold promises for the next generation of microscale interactions with live models at the cellular and material interface. This platform demonstrates the capacity for improving the understanding of developmental cardiac mechanics and physiology with an interactive and immersive method. This framework builds on the high spatiotemporal resolution provided by LSFM to offer user-directed acquisition and visualization of life science phenomena, thereby facilitating biomedical research and learning via readily available smartphones and VR headsets.

A NOVEL SYNTHETIC ARTIFICIAL CORNEA WITH BIOMIMETIC NANOTOPOGRAPHY, FROM DEVICE FABRICATION TO ANIMAL STUDY

Junming Cai, Kate Xie, Elena Liang, Priscilla Vu, Steven Carter, Albert Yee and Marjan Farid
University of California, Irvine, Irvine, CA

Summary: We report a novel design of a synthetic artificial cornea incorporating selective nanotopography to decrease bacterial adhesion. Our initial studies of partial-thickness implantation in the New Zealand white rabbit suggest that our fabrication protocol provides reproducible and durable nanopatterning on our implantable corneal device.

Introduction: An estimated 12.7 million people worldwide are awaiting implants and only under 0.02% of the needs were met with current procedure primarily due to procedure's dependency to donor corneal tissue. Currently available artificial cornea for treatment, the Boston Keratoprothesis (K-Pro), although widely used, still relies on donor grafts, requires complex assembly process and risks bacterial infection.

Materials and Methods: Artificial cornea prototypes were machined with polymethylmethacrylate (PMMA) and nanotopographic features were reversely imprinted onto designated part of the device surface. Scanning electron microscopy (SEM) was used to confirm the location and dimensions of the transferred features. Approved devices were implanted into the right eyes of two New Zealand white rabbits. The eyes were evaluated using Slit Lamp and anterior segment optical coherence tomography (AS-OCT) during a one month period. The rabbits were sacrificed at one month post-implantation. Bacterial cultures were obtained from implanted and control eyes. SEM was used to evaluate prototype surfaces and tissue interaction in fixed enucleated eyes.

Results: Our artificial cornea prototype was successfully implanted into the eyes of two rabbits. An increasing gap between the optic edge and corneal tissue was observed during the 4-week period. There were no instances of infection nor extrusion. SEM images showed gross preservation of the nanostructures on the central optic. No microbial growth was observed in cultures from either the eyes with the implants or control eyes.

Conclusion: We successfully developed a process to fabricate artificial cornea prototypes with reproducible and durable nanopatterning. These artificial cornea prototypes were successfully implanted and tolerated in rabbits via partial thickness implantation for one month. Our nanotopographic surface was durable in the eyes of the rabbits for one month. Further design modifications will be made to the artificial cornea prototypes to minimize gap formation and promote epithelial adherence to the surface of the implant, and antimicrobial properties of the prototypes will be further quantified.

"MICROFLUIDIC THERMOMETERS" FOR ANALYZING BIOMEDICAL SAMPLES

Brittney A. McKenzie and William H. Grover
Department of Bioengineering, University of California, Riverside, CA

Introduction: Measuring the temperature of a sample is a fundamental need in many chemical processes. When the volume of the sample is on the microliter scale (e.g., precious samples, or samples in microfluidic devices), accurate measurement of the sample temperature becomes challenging. We developed a "microfluidic thermometer" that can accurately measure the temperature of microliter-scale volumes of fluid with an uncertainty of a 0.26 °C using a simple microfluidic chip.[1] The microfluidic thermometer takes advantage of the fact that when two phases of a substance (for example, liquid water and ice) are present at the same location, the temperature of that location at equilibrium is precisely known (in this example, 0 °C). We previously demonstrated the technique to measure sample temperature and to identify unknown samples, and have now expanded the technique to be used as a way to analyze a wide variety of biomedical samples.

Materials and Methods: The thermometer system consists of a plastic 3D printed or milled microfluidic chip and a cooling source (thermoelectric cooler or liquid nitrogen). The channels of the chip are filled with liquid samples, including liquid standards, and a temperature gradient is formed across the chip by partially suspending it on or in the cooling source. Solid-liquid interfaces form in the channels and their positions along with the known freezing/melting points of the standards are used to calculate the temperature gradient along the chip. This gradient is then used to determine the freezing/melting point of an unknown sample at any position along the chip (Fig. 1A). The positions of these solid-liquid interfaces are also used to analyze and validate the relative purity of Oil (Olive and Peanut) samples and the quality of cough medicine samples.
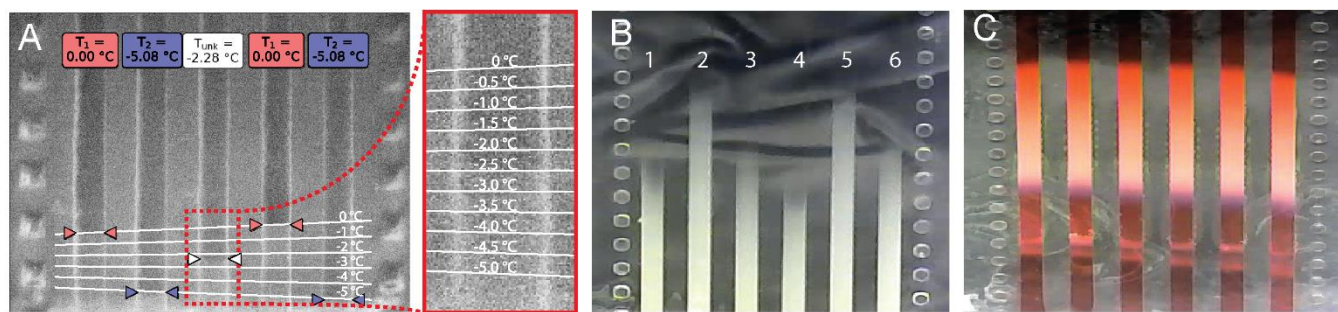
Fig 1. (A) The temperature gradient along the chip was used to determine the temperature of an "unknown" sample. (B) Pure olive oil (channels 1, 4) and peanut oil (channels 2, 5) were distinguished from a 50% mixture of the two (channels 3, 6). (C) The quality of different cough medicine lots in each channel was found to be consistent.

Results and Discussion: We were able to use the microfluidic thermometer chip to measure the freezing point of an "unknown" solution (Fig. 1A). The chip contained two standard solutions (deionized water, T = 0.00 °C; 8.0% (*m/m*) NaCl, T = -5.08 °C) in the first two and last two channels, as well as a simulated unknown solution in the middle channel (4.0% (*m/m*) NaCl). With our technique we determined the "unknown" sample's temperature to be -2.28 ± 0.26 °C, which is only 0.15 °C higher than the known literature value -2.43 °C. We also determined the purity of samples. After analyzing the interface positions of oil samples, we were able to distinguish pure oil samples from mixed oil samples (Fig. 1B). Finally we were able to determine the quality of samples (Fig. 1C). After analyzing the interface positions of the same cough medicine from different lots, we found that they were consistent and that their "fingerprint" could potentially be used to identify issues in the quality of lots by distinguishing dilute or adulterated samples.

Conclusions: The microfluidic thermometer provides a simple, label-free and probe-free method for precisely measuring the temperature of any fluid samples with minimal equipment. Since freezing point is an intrinsic property, the technique can also identify (or rule out) a substance by its freezing point, as well as determine the purity or quality of it. This technique is not limited to measuring near-freezing temperatures. By filling the microfluidic thermometer channels with other materials with different known freezing/melting temperatures (e.g., liquid oils that solidify at temperatures well above 0 °C), our chip can measure a wide range of temperatures. The thermometer is a versatile tool that can be used for many different applications.

References:
1. B. A. McKenzie and W. H. Grover. PLoS ONE 12(12), e0189430 (2017).

LASER GENERATED SHOCKWAVE TREATMENT INCREASES BACTERIAL CELL MEMBRANE PERMEABILITY *IN VITRO*

[1]Y. Chung, [1]W. Yao, [2]E.C. Kuan, [2]M.A. St. John, [1,3]W.S. Grundfest, and [1]Z.D. Taylor

[1]Department of Bioengineering, University of California, Los Angeles, CA

[2]Department of Head and Neck Surgery, University of California, Los Angeles, CA

[3]Department of Surgery, University of California, Los Angeles, CA

Contact: *ericchung95@g.ucla.edu*

Introduction: Bacteria in chronically infected wounds are often protected by biofilms keeping the wound from producing anatomic and functional integrity in a timely fashion. Current methods of biofilm debridement can be damaging to underlying tissue and lead to low patient tolerance. Laser generated shockwave (LGS) therapy is a novel debridement approach that is non-thermal, minimally invasive, and tissue-sparing. Laser ablation of titanium film is used to deliver purely compressive shockwaves into the biofilm. The reflected tensile wave disrupts the biofilm allowing for better antibiotic therapy. Due to the high compressive strength of tissue, the non-reflected compressive waves cause minimal damage to healthy tissue. In this study, we investigate, through flow cytometry, if LGS can also permeabilize bacterial cell membranes as permeabilization may aid in the absorption of antibiotics such as gentamicin that bind to bacteria's 16S rRNA.

Materials and Methods: The study utilized propidium iodide (PI) for the flow cytometer dyes, as PI permeates damaged cell membranes. Five solutions containing planktonic *S. epidermidis* underwent LGS treatment with a 1064nm Nd:YAG laser (laser density of 110.14 mJ/mm^2, pulse duration 9ns, spot size 3mm) with dye input times ranging from 0 to 20 minutes at 5 minute intervals. One solution each of all non-permeabilized (N) or all permeabilized (P) controls were included for comparison. The solutions were treated once in microcentrifuge tubes with shockwaves generated from laser ablation of titanium on polyimide substrates. Filters at 561nm and 488nm were used to analyze the cells under a SORP BD LSRII Analytic Flow Cytometer.

Group	PI Fluorescence (%)
Non-permeabilized control (N)	0.3
Permeabilized control (P)	99.2
Dyes added right after LGS (0-LGS)	6.1
Dyes added 5 min. after LGS (5-LGS)	6.0
Dyes added 10 mins. after LGS (10-LGS)	25.3
Dyes added 15 mins. after LGS (15-LGS)	26.2
Dyes added 20 mins. after LGS (20-LGS)	30.8

Table 1: A table showcasing the % of cells in each sample that were permeabilized, based on PI fluorescence compared to the non-permeabilized controls (N). There is a sharp contrast in PI fluorescence between the N and P group and between the N and treatment groups showcasing the permeabilization effect of LGS.

Results and Discussion: As seen in Table 1, the non-permeabilized control showed little absorption of PI, but all treated solutions showed stronger absorbance levels. 20 minutes after LGS treatment, the cells still demonstrated persistent uptake of PI. The permeabilized controls showed the highest level of PI absorbance.

Conclusions: The results suggest that LGS may have a direct permeabilization effect on the bacterial cells. The low PI values for the non-permeabilized control and higher PI fluorescence for the treated cells support this. Future studies need to assess the impact of multiple treatments to the bacteria. This data confirms that LGS can be a potentially useful adjunct to the treatment of bacterial biofilms in chronic wound and soft tissue infections by increasing antibiotic absorption.

ELECTROKINETIC SENSING OF IMMUNOGLOBULIN G: A PRELIMINARY STUDY OF IgG CONDUCTIVITY IN PHYSIOLOGICALLY-RELEVANT BUFFER

[1]A. Downs, [1]S. Pennathur

[1]Department of Mechanical Engineering, University of California, Santa Barbara, CA

Introduction: The immune system relies on antibodies to recognize and guide the destruction of harmful agents in the body, thus protecting the body from infection. Immunoglobulin G (IgG) is the most plentiful antibody in human serum, coordinating the immune response to numerous viruses, bacteria, and fungi. Changes in serum IgG levels indicate altered immune status, which can occur in conditions ranging from cancer and liver disease, to inflammation and immunodeficiency. Unfortunately, bulk IgG testing remains uncommon due to the high cost and analysis time the immunoassay demands. The present techniques require specific plates and buffers, as well as advanced lab equipment for optical detection. Creating a more accessible sensor could greatly improve monitoring of immune disorders and enable personalized treatment for immune-deficient patients. We propose to sense IgG directly, using electrical currents. Here, we present a preliminary study of sensing IgG within microfluidic channels using current monitoring.

Materials and Methods: Physiologically relevant concentrations of IgG (0-20 mg/mL) are suspended in 1X phosphate-buffered saline. Electrical current monitoring is performed using a Keithley 2410 connected to platinum electrodes inserted into wells at the end of 100 µm fused silica capillaries. A 1V potential drives flow of PBS through the capillary via electroosmosis. Upon reaching a stable current, solutions of 5, 10, and 20 mg/mL IgG are flowed through the capillary using 1V potential, and the resulting currents are measured. Average electrical currents are obtained by selecting at least three experimental trials, isolating data taken after over-potential has passed (400-500s), and calculating averages with pooled standard error.

Results and Discussion: Representative current monitoring plots for physiological concentrations of IgG are shown below. Figure 1a demonstrates the strong reproducibility of this technique: current monitoring curves for sequential trials are shown. Figure 1b demonstrates that electrical current decreases as a function of IgG concentration. This shift may result from: neutral IgG displacing charge carriers in the solution, screening of ions by charged IgG, IgG adhering to the glass surface and impacting the electric double layer, or a combination of these factors.
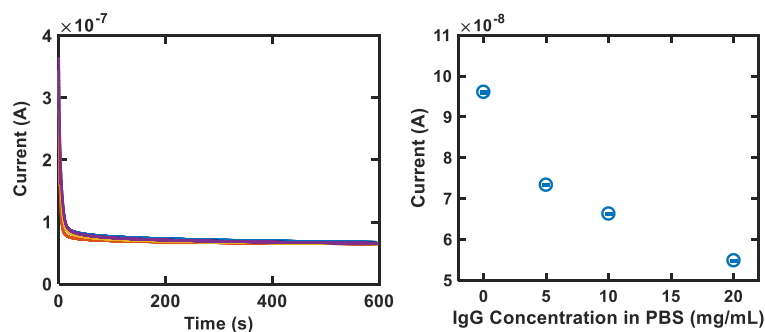
Figure 1: (a) Typical current monitoring curves for a given solution (10 mg/mL IgG in 1X PBS) over 4 sequential 10-minute trials.
(b) Stabilization current vs. IgG concentration (0-20 mg/mL IgG in 1X PBS) with pooled error.

Conclusions: This preliminary study suggests that there is a shift in electrical current (and as a result, conductivity) in solutions with varying concentrations of IgG. Future studies will determine whether this trend manifests in serum, and whether binding-mediated events in the microchannel can provide sensing specificity. By understanding the electrokinetic behavior of physiologically relevant IgG solutions, we hope to uncover a sensing mechanism that may prove amenable for the point of care due to the minimal user involvement, small sample size, and low power required.

CHARACTERIZATION OF PHOSPHATIDYLSERINE EXPRESSION ON ERYTHROCYTE-DERIVED NANOPARTICLES

J. C. Tang and B. Anvari

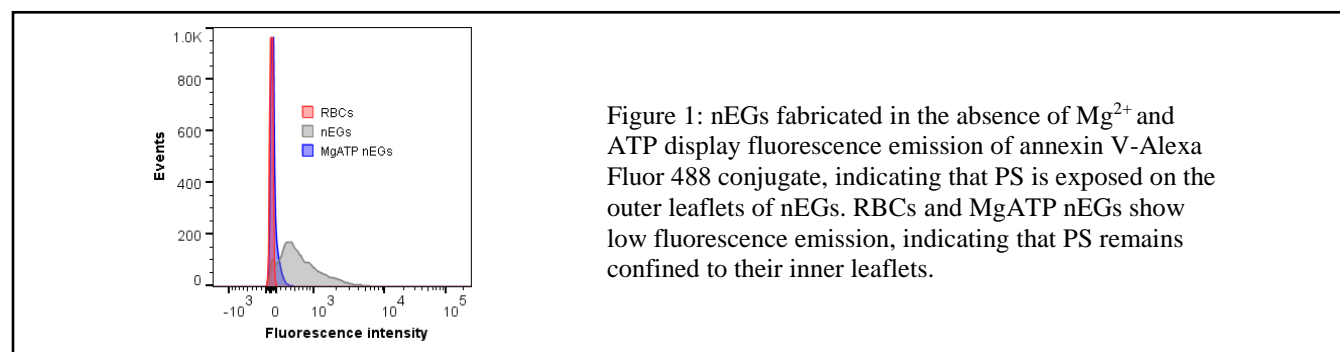Department of Bioengineering, University of California, Riverside, CA

Contact: *anvarib@ucr.edu*

Introduction: Nano-sized constructs derived from erythrocyte ghosts (nEGs) are a promising platform for delivery of payloads such as therapeutic molecules and imaging agents. An important consideration in fabrication of such construct is to maintain the surface characteristics of native erythrocytes to ensure biocompatibility and avoid recognition by the immune system.

A particularly important immunomodulatory marker is phosphatidylserine (PS), a phospholipid that is normally confined to the inner leaflet of the membrane bilayer, including those of the erythrocytes. Mg-ATP dependent "flippases" actively maintain this thermodynamically unfavorable lipid asymmetry.[1] Translocation of PS to the outer leaflet, in the case of damaged erythrocytes, serves as a signal for recognition by macrophages with subsequent removal from circulation. Thus, we investigated the effects of using Mg^{2+} ions and ATP during the fabrication of nEGs as a method to preserve the localization of PS to the inner leaflets.

Materials and Methods: To fabricate nEGs, whole human blood was centrifugally washed twice in ≈330 mOsm (1X) phosphate-buffered saline (5 min, 1600×g). Packed red blood cells (RBCs) were then re-suspended in hypotonic PBS (0.25X), and washed 15 times, resulting in formation of erythrocyte ghosts (EGs). The EGs were then re-suspended in 1X PBS and mechanically extruded until their diameter was approximately 100-200 nm. The resulting nEGs were then washed in 1X PBS for 1 hour, 100,000×g. In a similar process, we fabricated nEGs in presence of 3 mM Mg^{2+} and 3 mM ATP in steps involving 1X PBS or 0.25X PBS. We refer to such prepared constructs as MgATP nEGs. MgATP nEGs and nEGs were subsequently stained with annexin V-Alexa Fluor 488 conjugate for detection of PS using flow cytometry. As a negative control, we stained RBCs with the annexin V conjugate.

Results and Discussion: RBCs and MgATP nEGs labeled with annexin V-Alexa Fluor 488 conjugate showed minimal fluorescence, indicating that PS was not translocated to the outer leaflet of the membrane. However, nEGs fabricated without Mg^{2+} or ATP in the lysis buffer showed greater fluorescence signal, indicating the elevated expression of PS on the outer leaflet of these nano-constructs (Figure 1).

Figure 1: nEGs fabricated in the absence of Mg^{2+} and ATP display fluorescence emission of annexin V-Alexa Fluor 488 conjugate, indicating that PS is exposed on the outer leaflets of nEGs. RBCs and MgATP nEGs show low fluorescence emission, indicating that PS remains confined to their inner leaflets.

Conclusions: Nano-extruded erythrocyte ghosts (nEGs) fabricated in the presence of 3 mM Mg^{2+} and 3 mM ATP maintain the localization of PS to the inner leaflet of the constructs. Fabrication of nEGs without these additives results in translocation of PS to the outer leaflet, which may serve as a signal for recognition by macrophages.

References:

(1)   Connor, J.; Gillum, K.; Schroit, A. J., Maintenance of Lipid Asymmetry in Red-Blood-Cells and Ghosts - Effect of Divalent-Cations and Serum-Albumin on the Transbilayer Distribution of Phosphatidylserine. *Biochim Biophys Acta* **1990,** *1025* (1), 82-86.

MEASURING PROTEIN SECRETION FROM SINGLE CELLS AT SINGLE MOLECULE RESOLUTION USING QUANTUM DOTS

[1]Vanessa Herrera, [1]Ssu-Chieh Joseph Hsu, [1]Maha K. Rahim, [1,2]Wendy Liu, and [1,2]Jered B. Haun.
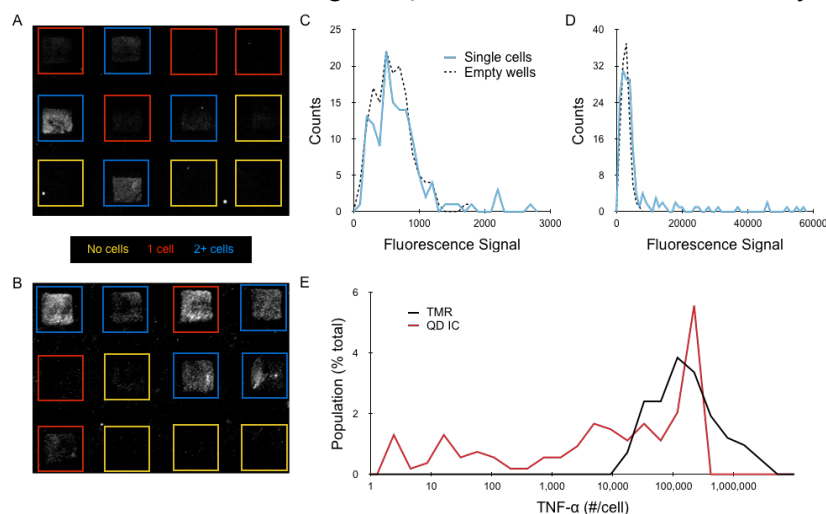[1] Department of Biomedical Engineering, University of California, Irvine, CA
[2] Department of Chemical Engineering and Materials Science, University of California, Irvine, CA

Introduction: Single cell analysis methods are becoming increasingly important since understanding how individual cells process information and respond to stimuli could lead to greater insight into cell heterogeneity and population behavior. One area that has only received limited attention is the detection of secreted products from single cells. Current methods only provide bulk information about the population or do not actually assess the act of secretion. To address these issues, single cell arrays have been developed that isolate single cells in picoliter microwells.[1] The wells are then covered with a glass slide containing immobilized antibodies to capture proteins secreted by individual cells, followed by removal of the glass slide and quantification by immunofluorescence. While this platform has proven powerful, a current limitation is that detection sensitivity is only in the ng/ml (pM) range. Nanomaterial probes have been shown to provide remarkable detection capabilities in cell-based detection applications; specially luminescent quantum dots (QD), with their bright and photostable signals. In this study, we test QD detection of TNF-α protein in single cell arrays.

Materials and Methods: Imaging experiments were performed using monoclonal anti-TNF-α capture antibody attached to glass slides using avidin/biotin chemistry. Monoclonal anti-TNF-α detection antibody was conjugated with NHS-TCO followed by reaction with Tz-QD and purification by gel filtration to yield QD IC antibody or modified with NHS-tetramehtylrhodamine to yield the TMR fluorescence antibody. Single cell experiments were conducted by seeding phorbol myristate acetate (PMA)-treated U-937 cells in microarrays and stimulating them with lipopolysaccharide (LPS) for 24 h. Cells in microwells were then imaged under bright field and the detection slide separated, stained with detection antibody (TMR or QD IC), and imaged under fluorescence microscope. Bright field and fluorescence images were then stitched, superimposed, and analyzed for mean intensity per microwell using ImageJ software.

Results and Discussion: The representative images in Fig 1 show TNF-α signal from single cell experiments using (A) TMR or (B) QD IC detection, where QD IC provided greater signal per microwell and higher number of positive microwells overall. Fluorescence signal was then quantified for empty (no cells) and single cell wells (Fig 1C and D). Signal from single cells largely overlaps empty wells for TMR, while QD IC had a significant number of single cell wells extending out to higher values. Only ~6% of single cells were detected using TMR, but the QD IC enabled detection of ~20% of single cells, for an increase of >3-fold. Fig 1E. displays the number of TNF-α molecules secreted per cell. For TMR, single cells had to secrete >10,000 molecules (30 pM) to be detected. In contrast, using the QD enabled detection down to only 2 molecules/cell (5 fM).

Conclusions: We have shown that QD nanoprobes dramatically improve detection of secreted products from single cells. Specifically, detection sensitivity was improved from ng/ml (pM) down to 3 fg/ml (180 aM) by switching from organic dyes to QDs in standard sandwich immunoassays. In single cell experiments, we found that our QD-based detection method increased the number of single cells that could be interrogated for TNF-α secretion by 3-fold relative to a traditional organic fluorophore, improving detection threshold from 10,000 molecules down to only 2. Results from this study will significantly expand the detection capacity of single cell secretion studies, enabling detection at earlier time points and/ or lower secretion rates. Future work will also focus on adding multiplexing capabilities.

Fig 1. Fluorescence images from single cell experiments for (**A**) TMR and (**B**) QD IC detection. Mean fluorescence intensity obtained in wells containing only single cells (solid blue line) or no cells/empty wells (dotted black line) for TMR (**C**) and QD IC (**D**). (**E**) Histogram showing the number of TNF-α protein secreted per cell as percentage of the total single cell population.

[1]Love *et al*. Nat Biotechnol 24, 703-707 (2006)

GENETICALLY ENCODED PHYB OPTOGENETICS IN ANIMAL CELLS

[1]P. Kyriakakis, [1]M. Catanho, [2]S. Devkota, [1]N. Hoffner, [1]V. J. Hu, [1]W. Thavarajah, [2]E. Bulger, [2]A. Auradkar, [2]L.E. Dozier [2]G.N. Patrick [2]W. McGinnis, [2]E. Bier and [1]T. P. Coleman
[1]Department of Bioengineering, University of California, San Diego, CA
[2]Division of Biological Sciences, University of California, San Diego, CA
Contact: *pkyriaka@ucsd.edu*

Introduction: In the past two decades, gene regulation systems have increased in specificity to the point of single cell modulation of virtually any gene. Combining the CRISPR/Cas system with optogenetics has allowed targeted illumination of cells to target genomic loci for regulation of transcription, generating knockouts, or perform site-specific gene insertions into DNA. However, such systems have no active "off switch" and use blue shifted light that penetrates tissue poorly. Phytochromes are photoreceptors that are reversely switchable with different wavelengths of light and absorb visible red and near-infrared light. However, the chromophore required for the vast majority of these optogenetic tools is not naturally produced in animal cells. Here we describe the engineering of the phytobilin metabolic pathway in animal cells and several genetically encoded PhyB optogenetic tools that we developed.

Materials and Methods: Zinc-PAGE assays were used to find the rate limiting factors for chromophore production and optimize the metabolic pathway for chromophores phycocyanobilin (PCB) and phytochromobilin (PφB) in animal cells. Luciferase-based gene expression assays were used to probe the gene activation levels and kinetics of the red light-regulated gene expression system. Red light controlled gene editing was assessed using *in vitro* DNA cutting assays as well as a "traffic light reporter" that changes the cells "color" depending on homology-dependent repair versus non-homologous end joining events.

Results and Discussion: With these advancements, we show that we can activate and deactivate genes using the Gal4-UAS system in an on-off switchable manner using red and far-red light respectively. We extend this system to work with a split Cas9 system allowing actively reversible control of Cas9 activity for the first time. We demonstrate the utility of this advancement by using light to restrict gene editing to a specific part of the cell cycle, leading to an increase in homology-directed repair. Using catalytically inactive mutants of Cas9, this system can also be adapted to regulate transcription of endogenous loci at short time scales.
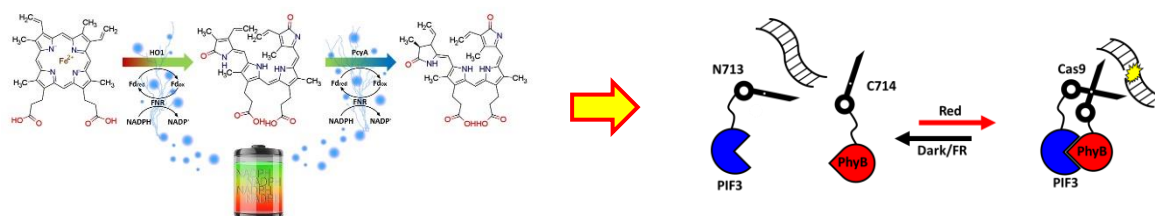
Figure 1: The phytobilin synthesis pathway for animal cells requires exogenous ferredoxin and FNR. Phytobilin chromophore production enables genetically encoded red and far-red light control of gene expression and gene editing.

Conclusions: Since the system uses red and far-red light, it also can facilitate gene modulation or gene editing several centimeters into tissue, paving the way for highly controlled *in vivo* gene expression and editing. Altogether, this variety of activities now controllable with red light demonstrates how genetically encoded reversible systems can be used to study many biological processes and engineer cells, tissues, and animal models.

DIPOLE MODULATION OF CHARGE TRANSFER

E. M. Espinoza,[1] M. Krzeszewski,[2] J. Clark[3], J. Derr[4], D. Gryko[2] and V. I. Vullev[1, 3, 4]

[1]Department of Chemistry, University of California Riverside, CA
[2]Institute of Organic Chemistry, Polish Academy of Sciences, Warsaw, Poland
[3]Department of Bioengineering, University of California Riverside, CA
[4]Department of Biochemistry, University of California Riverside, CA

Contact: *vullev@gmail.com*

Introduction: Molecular-level control of charge transfer is paramount for organic electronics and solar-energy conversion. Electromagnetic interactions, originating from the second strongest fundamental force in the universe, occur between charged particles. As electrostatic analogues of magnets, molecular electrets are dielectrics that contain ordered electric dipoles. Anthranilamides comprise non-native beta amino acids, and much like protein helices, they possess intrinsic dipole moments originating from ordered amide and hydrogen bonds. Unlike the protein helices, however, anthranilamides have a backbone of directly linked aromatic moieties providing pathways for highly efficient electron and hole transfer.[1-3] The dipole of even a single anthranilamide residue can rectify the kinetics of charge separation and charge recombination.[4] That is, the rates of electron transfer along the dipole are different from the rates against the dipole, and for a anthranilamide residue with an electron acceptor, that difference can be as large as an order of magnitude. Indeed, electric dipoles can play a key role in charge-transfer rectification.

Materials and Methods: For making charge transfer (CT) conjugates we use synthetic procedures developed in our lab.[5] Transient absorption spectroscopy is the principal tool that we employ for studying CT kinetics.

Result and Discussion: For a photosensitizer and an electron acceptor we used a diketopyrollopyrollo, DPP, molecule.[4] By attaching it to a side chain of a non-native amino acid, Aaa, we place DPP on the positive pole of the Aaa dipole (Figure 1a). Conversely, we place DPP at the negative pole of the dipole when we attach it to the N-terminus of the dipole (Figure 1b). These two conjugates allow us to demonstrate for the first time that the molecular dipole can not only enhanced rates of CT but also can completely suppress it when the acceptor is at the negative pole of the dipole (Figure 1c).
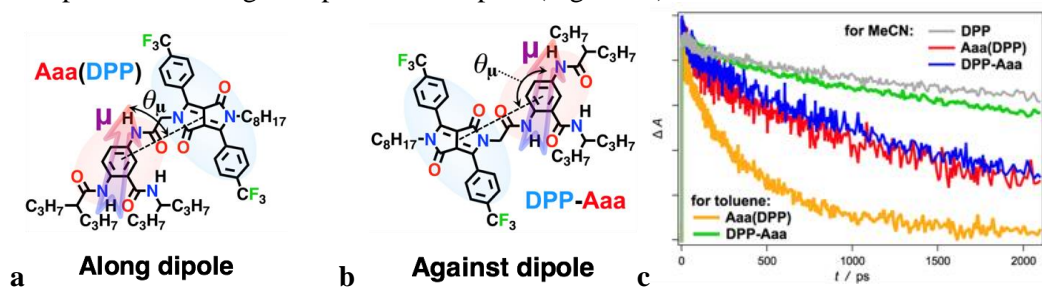
Figure 1. Anthranylamide dyad where the electron transfer is (a) along the dipole and (b) against the dipole. (c)Transient absorption kinetics showing the different rates of deactivation of DPP when it is a component of the two dyads.

Conclusion: Our studies show for the first time key design principles for harnessing dipole effects on CT: (1) place the dipole as close as possible to the donor or to the acceptor; (2) employ non-polar media; and (3) ensure that the thermodynamic driving forces in the absence of dipoles are as close as possible to zero. This discovery opens doors for guiding forward ET processes, while suppressing undesired backward electron transduction, which is of immense importance for molecular electronics and energy science.

References

1) Upadhyayla, S. et. al. *J. Phys. Chem. B* **2011**, *115* (30), 9473-9490
2) Xia, B. et. al. *J. Org. Chem*. **2013**, *78*, 1994-2004
3) Larsen, J. M. et. al. *Pure Appl. Chem.* **2015**, *87*, 779-792
4) Bao, D. et. al. *J. Am. Chem. Soc.* **2014**, *136*, 12966-12973
5) Purc, A. et. al. *J. Am. Chem. Soc.* **2016**, *138*, 12826-12832

ASSESSING CANCER HETEROGENEITY THROUGH PHENOTYPIC CELL SORTING

[1]K. Chen, and [1]S. Fraley

[1]Department of Bioengineering, University of California, San Diego, CA

Contact: *kec162@ucsd.edu*

Introduction: Cancer cells have diverse molecular profiles, even within an individual tumor. This heterogeneity presents a challenge for treatment, as differences between cells in a tumor can have important consequences on how the cells function and whether the cancer will progress. However, establishing the link between molecular heterogeneity and functional heterogeneity remains a challenge. Functional or phenotypic heterogeneity arises not only from genetic changes but also microenvironmental differences and reversible changes in cellular properties. Current approaches to studying cancer heterogeneity rely on sorting cells based on molecular markers of cell state, which do not reliably predict cell function. Here, we present a method we are developing that allows us to sort cells based on their functional state. Importantly, this technique can be used in physiologically relevant three-dimensional (3D) culture systems and potentially *in vivo*. This approach will enable us to enrich sub-populations and probe the biochemical differences between functional cell states.

Materials and Methods:
Dendra-2-LifeAct transfected MDA-MB-231 and MCF10A cells were embedded in 2.5 mg/mL rat tail collagen I (Corning) + 10 mg/mL PEG (Sigma) gels and cultured for one week. Cells displaying the phenotype of interest were photostimulated using a laser line at 405 nm using a Nikon Ti widefield microscope to photoconvert the Dendra-2-LifeAct within the cells. After photostimulation, the cells were extracted from the gel using collagenase and trypsin and sorted using a BD Influx flow cytometer. A control population of non-photostimulated cells was used as a control gate for sorting the cells expressing the photoconverted Dendra-2-Lifeact, and the sorted population was collected for re-culture or lysed for RNA extraction and sequencing.

Results and Discussion: We were able to successfully photoconvert cells of interest with minimal photoconversion of neighboring cells despite using a widefield microscope as opposed to a confocal microscope. (Figure 1) This allows us to photoconvert cells at a much higher throughput. The cells remain alive and healthy post-photoconversion and post-extraction from the collagen matrix.
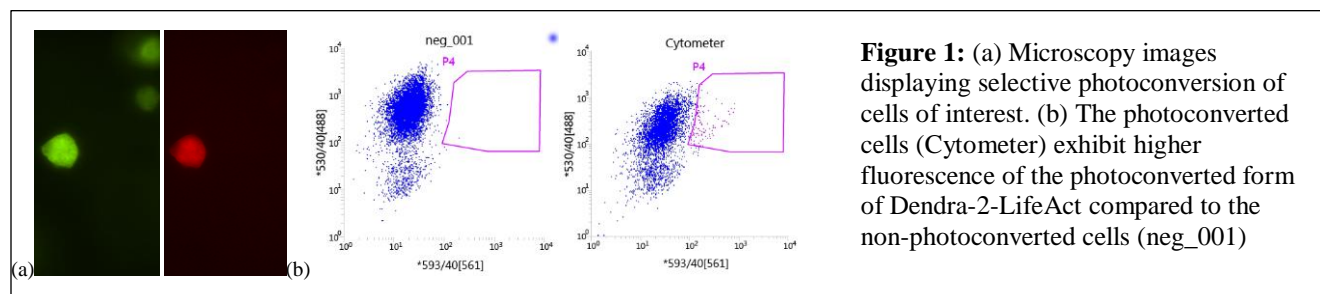
Figure 1: (a) Microscopy images displaying selective photoconversion of cells of interest. (b) The photoconverted cells (Cytometer) exhibit higher fluorescence of the photoconverted form of Dendra-2-LifeAct compared to the non-photoconverted cells (neg_001)

Our photoconverted cells display fluorescence above the negative gate when passing through the flow cytometer (Figure 1), and we confirmed expression of the photoconverted form of the Dendra-2-LifeAct in the cells we collected for re-culture. We plan to conduct RNA-seq for these different sub-populations to identify transcriptomic differences which may be responsible for the formation of particular 3D phenotypes.

Conclusions: We developed a powerful method capable of sorting out populations of cells based on phenotypic and functional behaviors. The availability of this technique allows us to sort out cell populations based on any visually measurable criteria without the need for traditional fluorescence labeling of specific proteins. This platform opens new opportunities for analysis of different cell populations because we can isolate and collect living, healthy subpopulations, instead of analyzing a heterogeneous population and identifying the subpopulations using genomic analysis downstream. We can amplify the signal we obtain by purifying these heterogeneous populations for the population of interest, and then perform biological assays such as RNA-Seq, or re-culture to observe different in-vitro behavior. We are also in the process of applying machine learning algorithms to automate the identification and photoconversion of sub-populations of interest so that this platform will have higher throughput.

DEVELOP SUMOYLATION INHIBITOR AS A NOVEL ANTI-INFLUENZA A VIRUS AGENT

Z. Xiong[1], Y. Song[1] and [1]J. Liao

[1]Department of Bioengineering, University of California, Riverside, CA

Contact: *zxion001@ucr.edu*

Introduction: Influenza A virus (IAV) is the major cause of world-wide pandemics associated with high morbidity and mortality. Besides, seasonal flu affects 20% world population and 250,000 to 500,000 people die from it worldwide every year. The anti-influenza drugs present the first line of protection against seasonal and pandemic influenza infections. The current two classes of drugs approved by FDA are amantadine-based M2 ion channel blocker and neuraminidase inhibitors. However, the rapid emergence of drug-resistant influenza variants has raised an urgent need of innovative strategies for development of new drugs with novel mechanism. Our recent study of the positive regulation of IAV replication by host cellular SUMOylation pathway reveals that SUMOylation cascade can serve as a novel cellular drug target that counteracts IAV drug resistance. Here, we report a fluorescence reporter strategy for surveillance of IAV replication in MDCK host cells which is more suitable for high-throughput assay than the traditional plaque assay, and identify a newly discovered SUMOylation inhibitor-STE as an effective host-directed influenza A antiviral agent.

Materials and Methods: The ambisense plasmids (pDZ) containing the eight influenza A viral segments were used for rescue of a commonly studied laboratory strain, influenza A/Puerto Rico/8/1934 (PR8). Plasmid pDZ-HA with a double-fluorescence reporter was created with a YPet-YPet tag flanked by packaging region (45 3' and 80 5' nucleotides) of PR8 HA vRNA segment (1). This pDZ-HA packaging plasmid with YPet-YPet insert was used in replacement of pDZ-HA for the generation of the PR8 viruses with Ypet-Ypet reporter in MDCK-HA cells. The growth rates of recombinant PR8 viruses with Ypet-Ypet reporter under treatments of SUMOylation inhibitor-STE, NEDDylation inhibitor-MLN4924 and ubiquitination inhibitor-PTR were evaluated by inoculating MDCK-HA cells at a MOI of 0.001, and after 48 hours incubation the cells were harvested for fluorescence measurement at an excitation wavelength of 475 nm, and emission wavelength of 530 nm.

Results and Discussion: The vast majority of the IVA intracellular life cycle is interfering with host proteins to take benefits from cellular metabolism and evade host antiviral response. There are a large variety of examples about SUMO pathway involving in viral protein functions in different aspects. After we elucidated the importance of H1N1 NS1 SUMOylation in promoting viral infection, we further studied the effect of our newly found SUMOylation inhibitor on virus growth via the double-fluorescence reporter strategy as described above. The result showed that SUMOylation inhibitor-STE can inhibit virus growth in a dose-dependent manner with IC_{50} at around 1 μM, while the other two ubiquitin-like pathway inhibitors, namely ubiquitination and NEDDylation inhibitors, did not show any effects on virus replication.
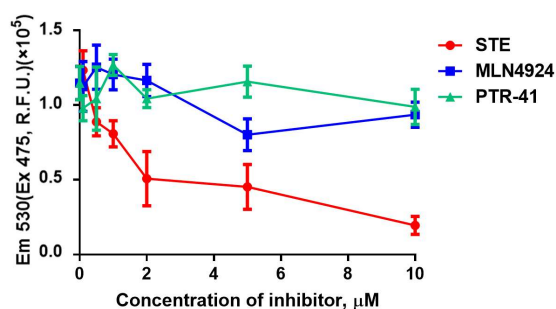
Figure 1: 0.1, 0.5, 1, 2, 5, 10 μM of SUMOylation inhibitor-STE, NEDDylation inhibitor-MLN4924 and ubiquitination inhibitor-PTR-41 was added to MDCK-HA cells 6 hours before infection of recombinant PR8 with Ypet-Ypet reporter. 48 hours post infection, the cells were harvested for fluorescence measurement to compare the virus growth rates with different ubiquitin-like pathway inhibitor treatments.

Conclusions: We have developed SUMOylation inhibitor as a novel anti-influenza drug agent, which targets host cellular SUMOylation pathway that is crucial for viral replication.

References:

1. **Marsh GA, Hatami R, Palese P.** 2007. Specific residues of the influenza A virus hemagglutinin viral RNA are important for efficient packaging into budding virions. Journal of virology **81:**9727-9736.

Poster #	Track	Rapid Fire	Lead Author	Affiliation	Title
17	Biomaterials and Drug Delivery	Yes	Yiping Guo	UC Merced	Photodynamic Therapy Excited by High Energy Photons from Cesium-137 Irradiator: in Vitro Studies
20	Biomaterials and Drug Delivery		Cody Combs	UC Irvine	Deformability of Individual Cells Probed by Optical Signal
23	Biomaterials and Drug Delivery		E Hong	UC Irvine	Measuring the Elastic Modulus of Ex Vivo Porcine Coastal Cartilage
26	Biomedical Imaging	Yes	Yibo Zhang	UCLA	Accurate-color Holographic Imaging of Pathology Slides Using Absorbance Spectrum Estimation
29	Biomedical Imaging		Mildred S. Cano-Velázquez	UC Riverside	Providing Long-term Optical Access to the Brain Using a Transparent Cranial Implant and Scalp Optical Clearing
32	Computational Bioengineering	Yes	Rohith Mohan	UC Riverside	Peptide Design for Theranostic Applications
35	Computational Bioengineering		Troy Alva	UC Riverside	Data-driven Models of Protein Secretion for Producing Biologics
50	Medical Devices and Instrumentation	Yes	J.M. Roper	UC Riverside	Injectable Polydiacetylene Biosensors for Disease Detection in Food Crops
53	Medical Devices and Instrumentation		P.I. Pai	UC Riverside	Photocatalytic Microreactors for Water Purification
56	Medical Devices and Instrumentation		Yuan-Yu (Ben) Hsueh	UCLA	Controllable Compression Model to Recapitulate Variable Functional Loss in Compressive Neuropathy
59	Medical Devices and Instrumentation		S.R. Corber	UC Riverside	Toward the Fabrication of Titanium Microneedle Arrays for Enhanced Optical Tissue Clearing
62	Medical Devices and Instrumentation		D.Z. Ash	UC Riverside	Grey-based Taguchi Optimization of Photoactive Tio2 for Catalytic Microreactor Applications
65	Medical Devices and Instrumentation		Heran C. Bhakta	UC Riverside	Measuring the Mass, Volume, and Density of Microgram-sized Objects in Fluid
2	Molecular & Cellular Engineering	Yes	D. O. Velez	UCSD	3d Collagen Architecture Modulates Degradability and Cell Adhesion
5	Molecular & Cellular Engineering	Yes	J. Clark	UCR	Room-temperature Solid-state Solvents for Molecular Photonics
8	Molecular & Cellular Engineering		Matthew Moldthan	CSU Northridge	Effects of Dod 3d Bioprinting on the Formability of Microspheres
11	Molecular & Cellular Engineering		Vipul Madahar	UC Riverside	Development of Fret Based Hts for Small Molecule Inhibitor of Atg4
14	Molecular & Cellular Engineering		Vasiliki Courelli	UCSD	Increased Levels of Intestinal Trypsin and Lipase in Human Blood Plasma Correlate with Clinical Biomarkers of Congestive Heart Failure
38	Neuroengineering	Yes	S.Tabatab	UC Davis	Designing a Tilt System to Test Balance and Learning Pattern in Rats with Spinal Cord Injury
41	Stem Cells and Regenerative Medicine	Yes	N. Sandhu	UC Riverside	Human Embryonic Stem Cell-derived 3d Model for the Study of Palatal Fusion
44	Stem Cells and Regenerative Medicine		K. Nguyen	UCSD	Elongated Cell Shape Directs Mesenchymal Stem Cell Differentiation to Smooth Muscle Cell via Mir-145
47	Stem Cells and Regenerative Medicine	Yes	A. P. Cabrera	UC Riverside	Impaired Lysosomal Exocytosis Contributes to Complement-mediated Vascular Injury Associated with Dry Amd

PHOTODYNAMIC THERAPY EXCITED BY HIGH ENERGY PHOTONS FROM A CESIUM 137 IRRADAITOR: *IN VITRO STUDIES*

[1]Y. Guo, [2]S. Sheng, [3]W. Zhang, [3]M. C. Lun, [3]S. Tsai, [3]W. Chin, [4]Roy Hoglund, and [1,3]C. Li*

[1]Department of Quantitative and Systems Biology, University of California, Merced, CA
[2]Tongji Medical College, Huazhong University of Science and Technology, Wuhan, P.R. China
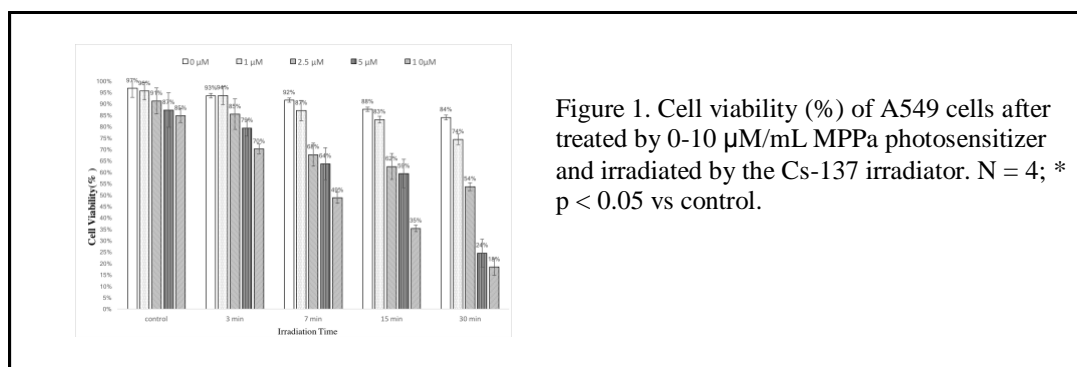[3]Department of Bioengineering, University of California, Merced, CA
[4]Department of Animal Research Services, University of California, Merced, CA
Contact: *cli32@ucmerced.edu*

Introduction: Photodynamic therapy (PDT) is a noninvasive cancer therapy method that has been clinically approved for many years. During PDT, photosensitizing agents will be excited by optical photons to generate reactive oxygen species which can kill nearby cancer cells. However, due to the strong optical scattering and absorption of tissues, optical photons can only penetrate tissues in few millimeters which results in the limited applications of PDT to superficial lesions. To overcome the limitation of penetration depth, we used high-energy photons to excite photosensitizers directly to enhance PDT, without any nanoparticles as energy mediators.

Materials and Methods: A Cesium-137 irradiator has been used as the high-energy photon source and a fiber pigtailed diode laser was used to validate the efficacy of photosensitizer MPPa. A549 Human lung carcinoma cells were firstly treated with different concentrations of MPPa (10μM/mL, 5μM/mL, 2.5μM/mL, 1 μM/mL and 0 μM/mL) and then exposed to high energy photons for 30 min, 15 min, 7 min to 3 min, respectively. Moreover, to evaluate the effects from possible plastic scintillation of cell culture plates, we have used both transparent and black 96-well plates in these studies.

Results and Discussion: The cell viability reduces when the photosensitizer concentration increases and the irradiation time increases. For the same photosensitizer concentration of 10 μM, the cell viability reduced to 70%, 49%, 35%, 18% for the irradiation times of 3, 7, 15, and 30 minutes respectively. The corresponding radiation doses are calculated to be 5.85, 13.65, 29.25 and 58.5 Gy.

Figure 1. Cell viability (%) of A549 cells after treated by 0-10 μM/mL MPPa photosensitizer and irradiated by the Cs-137 irradiator. N = 4; * p < 0.05 vs control.

Conclusion: Our results indicated that high-energy photons enhanced PDT is an efficient cancer therapy method without nanoparticles as energy mediators. The proposed method could overcome the penetration limitations and has potentials to be a safe, non-invasive, painless and low cost cancer treatment approach.

Reference:
1. Wilson, B. C. and Patterson, M. S., "The physics, biophysics and technology f photodynamic therapy." Phys. Med. Biol. 53, 61-109 (2008).
2. Chatterjee, D. K., Fong, L. S. and Zhang Y., "Nanoparticles in photodynamic therapy: An emerging paradigm" Adv. Drug Deliv. Rev. 60, 1627-1637 (2008).

DEFORMABILITY OF INDIVIDUAL CELLS PROBED BY OPTICAL SIGNAL

[1]Cody Combs, [1]Preston Hinkle, [1]Trisha M. Westerhof, [1]Yinghua Qiu, [1]David J. Malin, [1]Matthew L. Wallace, [1]Chih-Yuan Lin, [1]Zuzanna S. Siwy, [1]Edward L. Nelson,and [1]Peter Taborek,
[1]Department of Bioengineering, University of California, Irvine, Irvine, CA
Contact: *ccombs1@uci.edu*

Introduction: The deformability, or change in shape to an applied stress, is directly related to the internal structure of a cell. The structure of a cell can be dependent on a cell's phase, and can also be used as an identifier between cancerous and non-cancerous cells. Flow deformability cytometry has recently been developed to phenotype cells based upon mechanical properties. This technique utilizes hydrodynamic forces within micro-fluidic channels and high-speed optical detection in order to induce and detect the deformability of passing cells. Here, we present a study of two cancer cell lines, 293-T and HCT-116, using a non-traditional channel design which contains a central cavity, with two narrow entrances. This non-traditional design bidirectionally deforms cells and provides additional information on the elastic properties of a cell, such as relaxation time. The 293-T and HCT-116 cell lines studied formed two distinct populations according to these mechanical properties.

MEASURING THE ELASTIC MODULUS OF EX VIVO PORCINE COASTAL CARTILAGE

E Hong [1]; L Fossett[1,2]; W Moy[1,2]; P Borden[1,2]; K Hansen[1,2]; BJ Wong[1,2,3]
1 Beckman Laser Institute & Medical Clinic, Irvine, CA 92612, USA
2 Department of Biomedical Engineering, University of California - Irvine, Irvine, CA 92697, USA
3 Department of Otolaryngology - Head and Neck Surgery, University of California - Irvine, School of Medicine, Orange, CA 92868, USA
Contact: *ellenh1@uci.edu*

Introduction: Understanding the biomechanical properties of cartilage is integral for improving treatments and techniques for correcting cartilage defects caused by disease or damage. The mechanical properties of cartilage can be measured by using a myriad of techniques with additional parameters of testing, such as Poisson's ratio, specimen thickness, indenter radius, and scaling factors. There has been a demonstrated difficulty in obtaining reliable biomechanical measurements across different experiments that don't use identical experimental parameters. Elastic modulus is a frequently used measurement that describes a tissue's reaction to applied force, and it is representative of the physical nature of the tissue. The aim of this study was to design an efficient, accurate, and repeatable indentation protocol for measurement of elastic modulus of *ex vivo* porcine costal cartilage.

Materials and Methods: Pork rib cartilage was separated from the sternum and sectioned into 10mmx10mmx3mm pieces. The samples were then fitted into a custom 3D-printed acrylic jig that ensured constant hydration. A spherical indenter (d = 1 mm) was fitted into an ElectroForce 3200 mechanical testing unit with a 22.2N load cell to record force over time. Along with surface detection and preconditioning, the indentation protocol involved four step-wise deformations of 0.075mm (2.5%) to reach a maximum deformation of 0.3mm (10% strain). Each deformation was accompanied by a 5 minute hold to let the tissue equilibrate. Force and time data were collected and used to calculate elastic modulus using a derivation of Hayes solution which accounts for Poisson's ratio (v), indenter radius (a), scaling factor (k), skin thickness (h), and the slope of the stress-strain curve ($E_{measured}$). $E = \frac{E_{measured}(1-v^2)\pi a}{2hk}$

Results and Discussion: The average values of the instantaneous and equilibrium elastic modulus across four points of porcine costal cartilage specimens were calculated across all specimens (n=20), with instantaneous and equilibrium modulus showing values of 2.81±0.65 and 1.10±0.24 MPa, respectively. Plots of the standard error of measurement (SEM) and averages as a function of each additional value showed decreasing error and low standard deviation amongst averages, demonstrating the reliability of the testing method.
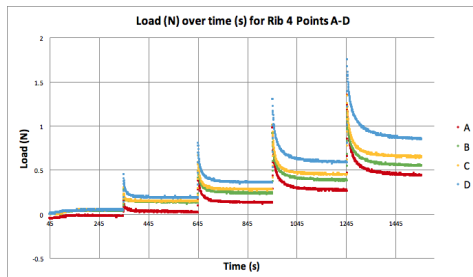
Figure 1. A sample plot of the data recorded. Each peak represents a deformation step and each letter represents a different point across the cartilage specimen (distance apart=1mm). Each point has a varied force response to the deformation, which speaks to the variation across the surface of one specimen. All other graphs (n=20) look similar in this varied distribution.

Conclusions: The protocol put forth aimed at producing an accurate, reliable, and efficient method for measuring the elastic modulus of costal cartilage. Going forward, this method can be expanded to look at the elastic moduli in different aspects of the porcine cartilage or in costal cartilage of other species, such as humans. Understanding basic biomechanical properties would lead to improvements in both research and clinical techniques that treat disease, defects, or damage.

ACCURATE-COLOR HOLOGRAPHIC IMAGING OF PATHOLOGY SLIDES USING ABSORBANCE SPECTRUM ESTIMATION

[1,2,3]Yibo Zhang, [1,2,3]Tairan Liu, [1]Yujia Huang, [4]Da Teng, [1]Yinxu Bian, [1,2,3]Yichen Wu, [1,2,3]Yair Rivenson, [1,2,3]Alborz Feizi, and [1,2,3,5]Aydogan Ozcan

[1]Electrical and Computer Engineering Department, University of California, Los Angeles, CA
[2]Bioengineering Department, University of California, Los Angeles, CA
[3]California NanoSystems Institute (CNSI), University of California, Los Angeles, CA
[4]Computer Science Department, University of California, Los Angeles, CA
[5]Department of Surgery, David Geffen School of Medicine, University of California, Los Angeles, CA

Contact: *liutr@ucla.edu; ozcan@ucla.edu*

Introduction: Digital holographic microscopy (DHM) has been used to image stained tissue sections for pathological diagnosis, which has various advantages such as cost-effectiveness, large fields-of-view, higher throughput, and the capability to generate amplitude and phase images of the sample. However, traditional methods for generating color images using DHM has suffered from color inaccuracies due to the use of narrow-band illumination sources, posing a major drawback for diagnostic pathology slide imaging. To address this issue, here we present an accurate-color holographic imaging approach based on absorbance spectrum estimation of histochemical stains, which can significantly improve the color accuracy and reduce the number of wavelengths when using DHM to image stained tissue samples.

Materials and Methods: In this work, a lens-free on-chip holographic microscopy setup (Figure 1(a)) with a multispectral illumination source is used for imaging. In the optimization step, for each given tissue sample, a hyperspectral image cube was acquired to generate the ground truth color image. The same hyperspectral cube was also used to calculate the spectral statistics of the sample, allowing for the estimation of the spectra of stained samples from a subset of measurements at arbitrary n wavelengths (Figure 1(b)). Then, wavelength optimization was performed for $n = 3, 4, 5,$ and 6, respectively, to minimize the average color error ($\Delta E*_{94}$ color distance metric) with respect to the ground truth when performing absorbance spectrum estimation-based colorization. After optimization was complete, the optimal three-wavelength set (illuminated *simultaneously*) was used to image samples with the same tissue type and stain.
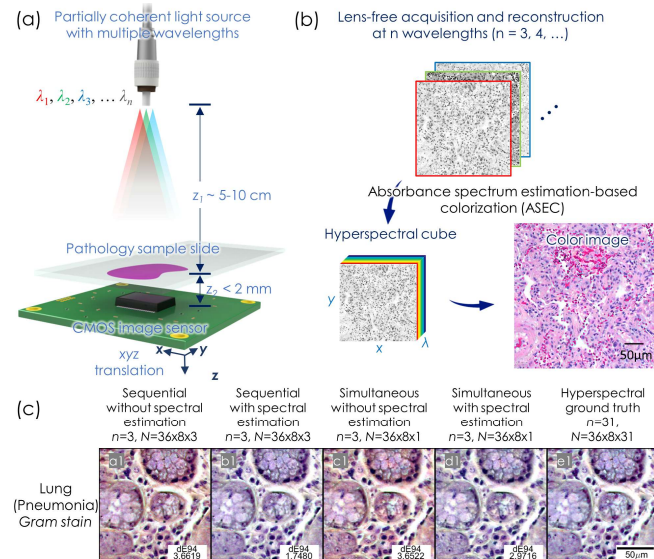
Figure 1: (a) Optical setup schematic. **(b)** Illustration of the accurate-color lens-free microscopy method. **(c)** Result of applying the spectrum estimation method in sequential and simultaneous illumination conditions. *n*: the number of the illumination wavelengths; *N*: the number of the holograms acquired for reconstructing each image.

Results and Discussion: We optimized and tested our colorization method on 25 pathology slide samples with different tissue-stain combinations. Figure 1(c) shows the imaging result of a Gram-stained lung tissue sample ($n = 3$). Compared to the direct RGB combination method (without spectral estimation), our method (with spectral estimation) significantly reduced the color inaccuracies with respect to the ground truth based on visual judgement. Quantitatively, for all 25 samples, our method improved the average $\Delta E*_{94}$ from 4.19 (sequential illumination) and 5.56 (multiplexed illumination) to 1.71 and 3.83, respectively. In addition, the color accuracy can be further improved using a larger number of wavelengths ($n = 4, 5,$ or 6) determined by our optimization results.

Conclusions: The presented absorbance spectrum estimation-based colorization method and wavelength optimization framework provide a practical guide for computational colorization and wavelength selection in holography, which can potentially lead to an improved diagnostic accuracy in pathology applications.

PROVIDING LONG-TERM OPTICAL ACCESS TO THE BRAIN USING A TRANSPARENT CRANIAL IMPLANT AND SCALP OPTICAL CLEARING

[1]Mildred S. Cano-Velázquez, [2]Nami Davoodzadeh, [3]Carrie R. Jonak, [2]David Halaney, [3]Devin K. Binder, [2]Guillermo Aguilar, and [1]Juan A. Hernández-Cordero

[1]Instituto de Investigaciones en Materiales, Universidad Nacional Autónoma de Mexico

[2]Department of Mechanical Engineering, University of California, Riverside, CA

[3]Division of Biomedical Sciences, School of Medicine, University of California, Riverside, CA

Contact: *mildred.cano.vel@gmail.com*

Introduction: Laser-based diagnostics and therapeutics show promise for many neurological disorders. But the poor transparency of cranial bone limits the spatial resolution and interaction depth that can be achieved. We addressed this limitation previously, by introducing a novel cranial prosthesis made of a transparent nanocrystalline yttria-stabilized-zirconia (nc-YSZ). By using optical coherence tomography and laser speckle imaging, we have demonstrated the initial feasibility of nc-YSZ implants for open scalp cortical imaging in an acute murine model. However, for our cranial implant to be successful as optical "window" for post-operatory and prolonged diagnostics and/or therapy, scalp scattering must be overcome. It is in this context that optical clearing agents (OCAs) can play an important role, as they may be applied topically to the skin to reduce scattering locally, temporarily and reversibly, prior to laser irradiation.

Materials and Methods: A set of in-vitro experiments including optical characterization of mouse dorsal skin, optically cleared dorsal skin, skull, and nc-YSZ implant were performed to compare the effect of OCA and/or the nc-YSZ implant on the optical transparency. Figure 1 shows three approaches for optical characterization experiments. The dorsal skin samples were topically exposed to PEG-400 (PEG) and Polyethylene Glycol (PG) as scattering reducer and penetration enhancer, respectively. To measure the optical transmittance optical spectrometry in visible (400-900 nm) and near infrared (1000-2500 nm) light was performed. The sampling system used for specular transmission measurements consists of a rail coupled with two fiber holder including collimating lenses. A space for placing the samples was incorporated on one of one the fiber holder.

Results and Discussion: In this study, three sets of quantitative comparison were performed to study the effect of OCAs and the nc-YSZ implant on optical transmittance enhancement. The optical transparency of dorsal skin was increased up to 90% after adding OCA. The optical transmittance through the nc-YSZ implant was higher compared to mouse skull sample in NIR wavelength range. Experimental results show OCA + implant has the optimal optical transparency increasing up to 3 times, in visible range, and 5 times, in NIR range, the transmitted light that could travel trough skin and skull without the application of OCA.
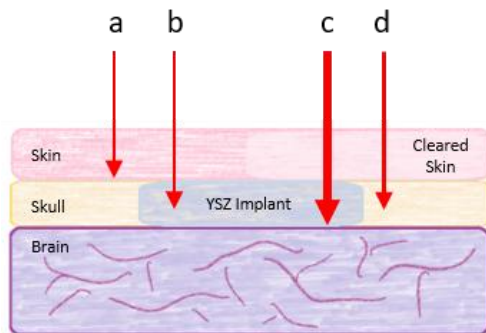
Figure 1: Three sets of comparison were performed to study: 1) effect of OCA in the skin (a vs d), 2) effect of the implant (d vs c), and 3) effect of OCA + nc-YSZ implant (b vs c).

Conclusions: The transparent nc-YSZ implants coupled with the OCAs, seek to ultimately provide opportunity for brain monitoring, over large areas, and on a chronically-recurring basis, without need for repeated craniotomies or scalp removal. While the current study represents only the first step towards realization of the long-term brain imaging through an implant, it is helpful to consider the opportunities this may eventually afford. For example, opportunity may arise for chronic monitoring of cerebral edema. Finally, it could provide a platform for development of new long-term optical monitoring modalities.

PEPTIDE DESIGN FOR THERANOSTIC APPLICATIONS

R.R. Mohan and D. Morikis
Department of Bioengineering, University of California, Riverside, CA
**Contact:** *rmoha004@ucr.edu*

Introduction: Within the complement system, the interaction between complement fragment C3d and complement receptor CR2 plays an important role as the link between innate and adaptive immunity. C3d is a marker for complement activation, but also functions to stimulate B cell activation and production of antibodies through its interaction with CR2. As unregulated complement response is implicated in several inflammatory disorders and other diseases, C3d can be utilized both as a biomarker for tracking disease progression as well as a target for inhibition due to its role as an opsonin and in augmenting B-cell mediated antibody production. By characterizing the C3d:CR2 interaction through *in silico* methods, we propose rational and combinatorial peptide design derived from key CR2 contacts with C3d.

Materials and Methods: The forces driving the C3d:CR2 interaction were examined through computational mutagenesis, molecular dynamics (MD) simulations, Poisson-Boltzmann electrostatic calculations, and free energy calculations. Persistent interactions and amino acids exhibiting significant energetic contributions to binding served as the basis for our rational peptide design. Three main sequence segments of CR2 were selected (Figure 1) from which peptides were derived through various cyclization schemes and point mutations. Experimental testing was carried out through microscale thermophoresis to characterize the binding affinity of the peptides. Subsequent iterative rational and combinatorial peptide design was implemented to optimize binding and improve solubility.
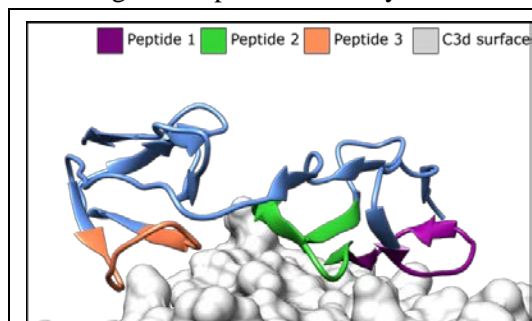
Figure 1: Molecular graphic of C3d:CR2 complex. C3d is shown in gray in a surface representation, while CR2 is in blue in ribbon representation. Locations of initial proposed peptides on CR2 are colored in purple (Peptide 1), green (Peptide2) and orange (Peptide 3).

Results and Discussion: Two CR2-derived peptides were identified that demonstrate binding to C3d (Figure 2). The structural stability of the peptides was retained by strategically introducing disulfide bridges. Both peptides were optimized for solubility and binding affinity by introducing critical amino acid replacements through rational design. Further rational and combinatorial design is in progress. Peptides with affinity for C3d are amenable to become potential diagnostic biomarkers by covalently attaching fluorophores.
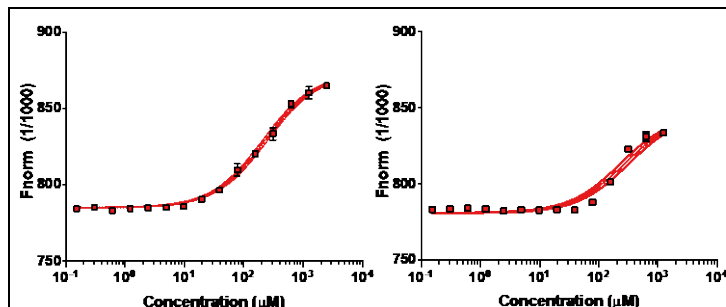
Figure 2: Concentration dependent binding curve of Peptides X (left) and Y(right) that demonstrate binding to C3d. Thermophoretic data is plotted as mean $\pm$ SEM (as error bars) from three replicate experiments, together with the fitted binding curve in red and the 95% confidence interval of the fitted binding curve represented as red dots. The calculated K_D of peptide X and Y are 269.8$\pm$22.3 µM and 228.8$\pm$11.4 µM respectively.

Conclusions: Only two complement-based therapeutics are currently on the market despite complement's involvement in the pathology of many chronic inflammatory and systemic autoimmune diseases. Peptides can be viable therapeutics as they represent a balance of properties between those of protein-based therapeutics and small drug-like compounds in terms of bioavailability, specificity, and production cost. The CR2-based peptides identified here establish a basis for C3d-targeting theranostic development and demonstrate the validity of our in silico workflow in protein engineering.

DATA-DRIVEN MODELS OF PROTEIN SECRETION FOR PRODUCING BIOLOGICS
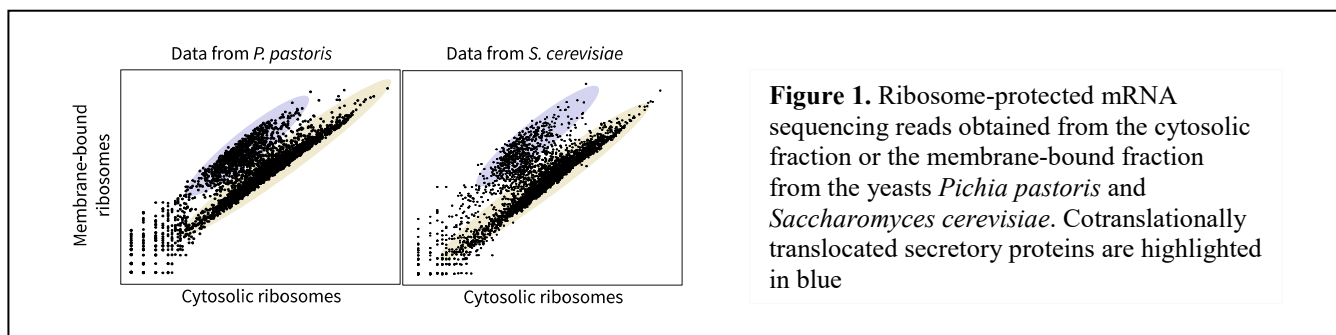
T. Alva, B. Lupish, and J.W. Chartron
Department of Bioengineering, University of California, Riverside, CA
Contact: *jchartron@engr.ucr.edu*

Introduction: Our overall goal is to generate enabling technologies to satisfy increasing demand for therapeutic proteins in the United States and around the world. Many therapeutic proteins must be secreted from eukaryotic hosts, whose cellular secretory pathways provide the molecular chaperones and enzymes necessary for folding and modifications. Our objective is to overcome the major bottleneck of protein secretion in yeast, which appears to be that nascent polypeptides are unable to enter the secretory pathway at the endoplasmic reticulum (ER). Polypeptides are directed to the ER by hydrophobic signal peptides that initiate translocation through Sec translocons located in the ER membrane. The choice of signal peptide significantly varies the yield of mature recombinant protein, and efficient signals from one species do not necessarily work in another. There are no models that can predict yields from the sequence of signal peptides, and so the link between signal peptides and translocation efficiency remains a crucial, but poorly understood, aspect of secretion.

Materials and Methods: We have developed a high-throughput sequencing based assay to globally measure entry into the secretory pathway of yeasts, without needing genetic modifications. Cells are cryogenically pulverized and ER-bound ribosomes are rapidly separated from cytosolic ribosomes by centrifugation. Ribosomes from both subcellular fractions are subject to ribosome profiling (Ribo-seq), providing quantitative measurements of cotranslational targeting to the ER. These data are then used to train machine learning algorithms that predict cotranslational translocation efficiency using gene sequence features and the translational state of the cell.

Results and Discussion: The experiment allows us to (i) quantify the efficiency cotranslational targeting for every gene, (ii) identify the set of proteins which must use posttranslational targeting *in vivo*, and (iii) identify host proteins that will compete for translocons during production phases (Figure 1). Our experimental design allows for several species to be investigated in parallel, allowing us to contrast the conservation of signal peptide sequence with its efficiency of driving cotranslational translocation. We will use the quantitative results from thousands of endogenous proteins across several species in order to train models predicting translocon flux from polypeptide sequence.

Figure 1. Ribosome-protected mRNA sequencing reads obtained from the cytosolic fraction or the membrane-bound fraction from the yeasts *Pichia pastoris* and *Saccharomyces cerevisiae*. Cotranslationally translocated secretory proteins are highlighted in blue

Conclusions: Most secreted proteins and proteins which reside in the secretory pathway are targeted to the ER cotranslationally. However, there is significant variation in the extent of cotranslational targeting that is conserved between species, even though the sequences of signal peptides are poorly conserved.

INJECTABLE POLYDIACETYLENE BIOSENSORS FOR DISEASE DETECTION IN FOOD CROPS

J.M. Roper[1], P. Viravathana[2], C. Roper[2], and H. Tsutsui[3]

[1]Department of Bioengineering, University of California, Riverside, CA
[2]Department of Plant Pathology, University of California, Riverside, CA
[3]Department of Mechanical Engineering, University of California, Riverside, CA

Contact: *htsutsui@ucr.edu*

Introduction: The Food and Agricultural Organization (FAO) of the United Nations (UN) estimates that 98% of the world's malnourished population, of nearly 870 million, reside in developing countries. Smallholder farmers, who often cultivate a plot of land smaller than two football fields, dominate agricultural production in developing countries. In order to alleviate global food shortages, low-cost and robust solutions must be provided to increase agricultural production and decrease crop loss. Crop loss due to disease can be particularly detrimental to smallholder farmers in developing countries, whose yield is often the sole source of food and income for their family. Rapid detection and identification of plant pathogens in diseased crops is essential for minimizing yield loss. Current diagnostic technologies, such as quantitative PCR (qPCR) and ELISA, are sufficiently sensitive and specific. These methods, however, require trained operators, expensive reagents, and require time-consuming processing of plant tissue, making these techniques impractical for smallholder farmers.

Under this project, we are developing an injectable, polydiacetylene (PDA) vesicle-based biosensor. PDAs are a class of amphiphilic polymers with environmentally responsive chromic and emissive properties. UV-polymerization of PDA vesicles results in a deep blue solution, which transitions to red in response to various environmental factors, such as pH, temperature change, and molecular binding. Conjugating pathogen-specific antibodies to the surface of liposomes allows for rapid detection of plant disease, allowing the farmer to take corrective action immediately loss (Fig. 1).
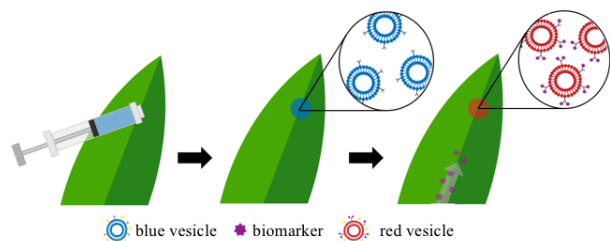
Figure 1. One-step detection of pathogen markers in live maize leaves. Pathogen responsive PDA vesicles are injected into leaf tissue. The vesicles undergo a transition in response to the pathogen biomarker binding to the antibody.

Materials and Methods: This study utilizes maize, a staple crop, and *Pantoea stewartii,* the causal agent of Stewart's wilt in sweet corn, as a model system. Here, we demonstrate that 10, 12-pentacosadiynoic acid (PCDA) liposomes, doped with dimyristoylphosphocholine (DMPC), can detect *P. stewartii*, when functionalized with anti-*P.stewartii* antibodies.

Results and Discussion: We demonstrate here that PCDA:DMPC liposomes functionalized with anti-*P. Stewartii* antibodies are able to detect 9.6×10^6 CFU•mL^{-1} in liquid culture and maintain specificity when liquid culture is spiked with plant extract. Preliminary results show that the blue to red color transition is visible with the naked eye in plant extract (Fig. 2).
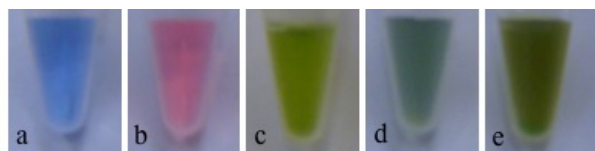
Figure 2. Colorimetric response of PDA liposomes in plant extract. (a) 1 mM PDA liposomes (negative control) and (b) heat-treated liposomes (positive control), color shift visible with naked eye. When maize leaf extracted (c) is added to the positive (d) and negative (e) control, the color shift is still detectable with the naked eye.

Conclusions: Thus far we have shown that *P. stewartii* can be detected *in vitro*. This proves feasibility for future work, where the PDA liposome sensor will be injected directly into plant tissue for rapid disease detection in food crops.

PHOTOCATALYTIC MICROREACTORS FOR WATER PURIFICATION

[1]P.I. Pairs, [2]D.Z. Ashby, [2]K. Xia, [3]T.C. Beaulieu, and [1,2,4]M.P. Rao

[1]Department of Materials Science and Engineering, University of California, Riverside, CA
[2]Department of Mechanical Engineering, University of California, Riverside, CA
[3]Department of Physics and Astronomy, University of California, Riverside, CA
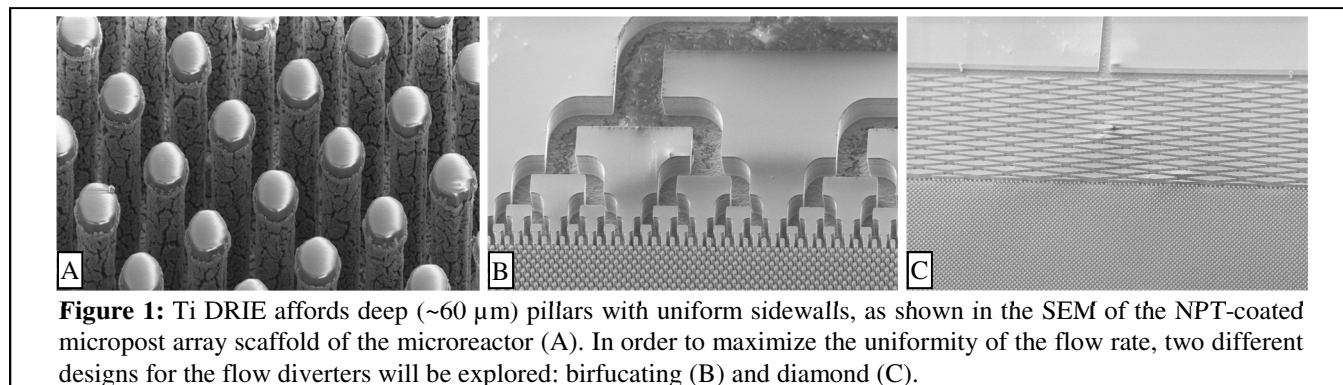[4]Department of Bioengineering, University of California, Riverside, CA
Contact: *pranee.pairs@email.ucr.edu*

Introduction: The World Health Organization reports that as of 2015, 844 million people lack drinking water services, 2 billion people are drinking from sources contaminated with feces, and 500,000 people die from diarrhea each year. Photocatalytic microreactors offer many advantages over traditional water purification systems including increased reaction rate and improved mass transfer. Furthermore, these devices can degrade waterborne pathogens that pass through microporous systems traditionally used in low-cost filtration systems.

While researchers have strived to improve the catalytic materials of these devices, less focus has been placed on the reaction chamber geometry as a means of increasing efficiency. Herein, we propose a microreactor that contains a high-density TiO_2-coated micropost array optimizing vacant space within the reaction chamber. The posts minimize diffusion distances between contaminants and catalytic sites without compromising the device size, resulting in increased reaction rate and throughput. The proposed microreactor would also be a sustainable alternative to the thermal reactors used for wastewater recycling on the International Space Station. Currently, these devices require extreme temperature and pressure that accelerates the wear of equipment, which presents a barrier to long-term space exploration.

Materials and Methods: The titanium micropost array is fabricated using standard photolithography procedures followed by Titanium Deep Reactive Ion Etching (Ti DRIE). Additional etching with hydrochloric acid removes the passivation layer formed during the Ti DRIE process. Taguchi design of experiments (DOE) optimized Nanoporous titania (NPT, TiO_2) is grown *in situ* by submerging the Ti-etched substrate in heated hydrogen peroxide. The NPT-oxidized substrate is then bonded to a quartz cover that is transmissible to UV light. The geometric features, *e.g.* pillar width, extent of undercutting, etch depth, NPT quality, and extent of NPT cracking are observed using Scanning Electron Microscopy (SEM). The photocatalytic efficiency of the microreactor is assessed via a methylene blue (MB) degradation experiment using UV-Visible Spectroscopy.

Results and Discussion: Preliminary Taguchi DOE experiments demonstrated that drop-cast P25 TiO_2 degrades MB 6.5% better than a comparable flat NPT film. We predict that integration of the micropost array in a microfluidic reactor will yield greater MB degradation due to the 3-fold increase in surface area. Figure 1 shows scanning electron micrographs of the micropost array, which serves as a proof-of-concept for the feasibility of microreactor fabrication. Following device assembly, we will analyze the effect of residence time, which is a parameter that allows us to compare the catalytic performance (*i.e.* MB degradation efficiency) with other reported microreactors.

Figure 1: Ti DRIE affords deep (~60 µm) pillars with uniform sidewalls, as shown in the SEM of the NPT-coated micropost array scaffold of the microreactor (A). In order to maximize the uniformity of the flow rate, two different designs for the flow diverters will be explored: birfucating (B) and diamond (C).

Conclusions: We present a microfluidic reactor capable of degrading organic compounds and pathogens by means of TiO_2 photocatalysis. It is expected that the high surface area afforded by the micropost array will yield greater MB degradation efficiencies than that observed with flat NPT films.

CONTROLLABLE COMPRESSION MODEL TO RECAPITULATE VARIABLE FUNCTIONAL LOSS IN COMPRESSIVE NEUROPATHY

[1,2,3]Yuan-Yu (Ben) Hsueh, [2,3]Si-Han Chen, [3,4]Chia-Ching (Josh) Wu

[1]Department of Bioengineering, University of California, Los Angeles, CA
[2]Division of Plastic Surgery, National Cheng Kung University Hospital, Tainan, Taiwan
[3] International Center for Wound Repair and Regeneration, National Cheng Kung University, Tainan, Taiwan
[4]Department of Cell Biology and Anatomy, National Cheng Kung University, Tainan, Taiwan
Contact: benyyhsueh@ucla.edu

Introduction: Persistent compressive neuropathy produces neuropathic pain resulting from structural and functional changes of nerve, hyper-inflammatory response, and vascular dysfunction due to hypoxia. Surgical nerve decompression for compressive neuropathy is the gold standard procedure and most patients have satisfied outcome in neuropathic pain relief, but some patients still have irreversible dysfunction with variable clinical manifestation such as hyper- or hypo-sensitives. In this study, we aim to establish different severity of nerve compressive injury by applying controllable forces on the sciatic nerve of rat.

Materials and Methods: The sciatic nerves of Sprague-Dawley rats (6-8 weeks) were exposed and tightened by 4 ligatures (approximately 1 mm between ligatures) under surgical suture skill. The tightening forces was real-time measured by mechanical force sensor. The locking-tied ligatures was utilized for the loosely compression and the sliding technique was applied to create tightly compression. The rats received periodic measurements for neuropathic pain and sciatic nerve function 4 weeks after nerve injury. The muscle atrophy and nerve degeneration were evaluated by histological assessments 1 month after nerve compressions.
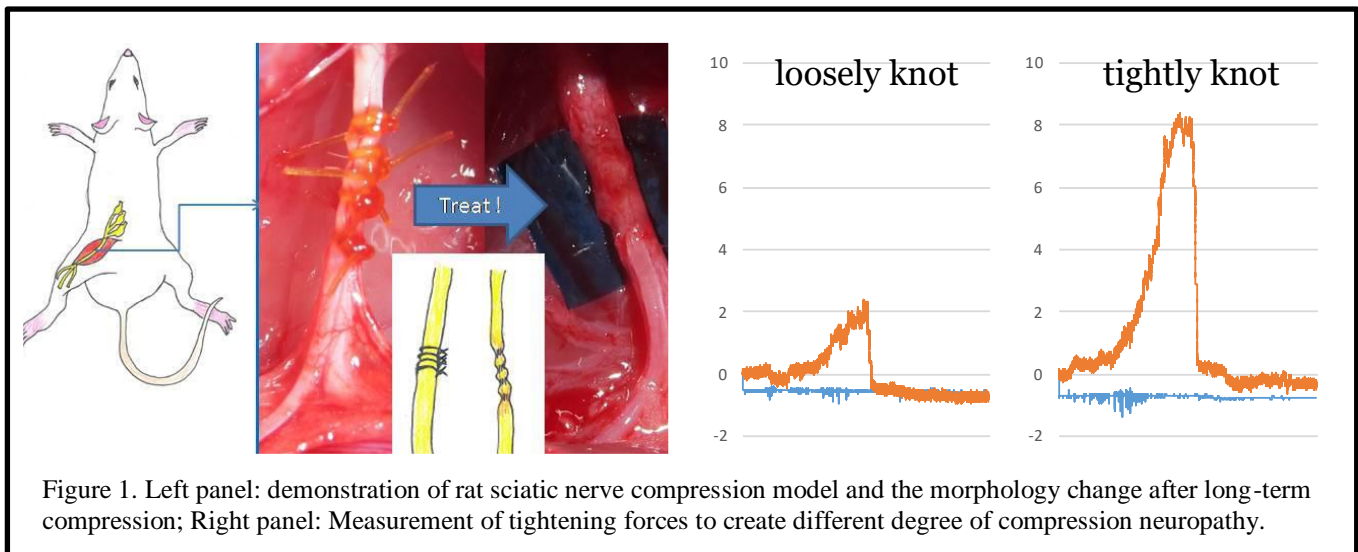
Figure 1. Left panel: demonstration of rat sciatic nerve compression model and the morphology change after long-term compression; Right panel: Measurement of tightening forces to create different degree of compression neuropathy.

Results and Discussion: This controllable animal model resulted in 2 significant pathological patterns that recapitulate the degree of functional loss in clinical patients of compressive neuropathy. The sensory abnormality was correlated to the force applied onto sciatic nerve. The von Frey tests demonstrated the tight compression induced acute sensation loss and motor dysfunction as well. On the other hand, the loose compression lead to hypersensitivity and neuropathic pain, without significant motor function deficit.

Conclusions: These results indicated the degree of mechanical force on nerve tissue can induce variable pathological deterioration on peripheral nerve. The clinically relevant model can help to investigate the pathogenesis of refractory compression neuropathy, providing alternative treatment of choice in the future.

TOWARD THE FABRICATION OF TITANIUM MICRONEEDLE ARRAYS FOR ENHANCED OPTICAL TISSUE CLEARING

[1]S.R. Corber, [2]Y. Leos, [1]D.Z. Ashby, [1,2]G. Aguilar, and [1,2,3]M.P. Rao

[1]Department of Mechanical Engineering, University of California, Riverside, CA

[2]Department of Bioengineering University of California, Riverside, CA

[3]Material Science and Engineering Program, University of California, Riverside, CA

Contact: Samantha R. Corber, *scorb003@ucr.edu*

Introduction: Optical Clearing Agents (OCAs) increase the transmittance of light through biological tissues, which represents a key step toward laser-based medical diagnostics and treatments. The stratum corneum (SC) is the key limitation to the transport of topically-applied OCA through the skin. While a bolus, subdermal injection overcomes the SC barrier, it can result in scarring and necrosis of the tissue; signifying a need for alternative drug delivery methods. In this study, we aim to increase the clearing efficacy of the OCA via active profusion through a hollow microneedle (MN) array.

Current materials being used to fabricate MN, such as silicon (Si), are non-ideal for intradermal drug delivery due to their non-optimal material properties. Titanium (Ti) is a promising surrogate material in this regard, due to its excellent biocompatibility and fracture toughness. The recent development of titanium deep reactive ion etching (Ti DRIE) has enabled the fabrication of small-scale, Ti-based biomedical devices. However, this micromachining technique was developed for anisotropic deep etching, which limits microdevice design and complexity, but provides opportunity for improvements in sidewall profile control. Herein, we explore the process parameter space of Ti DRIE, which represents a key step towards the realization of complex Ti-based MN devices that require multidimensional features. We also demonstrate the ultimate capability to produce the desired hollow, out-of-plane MN by replicating the process in silicon substrates.
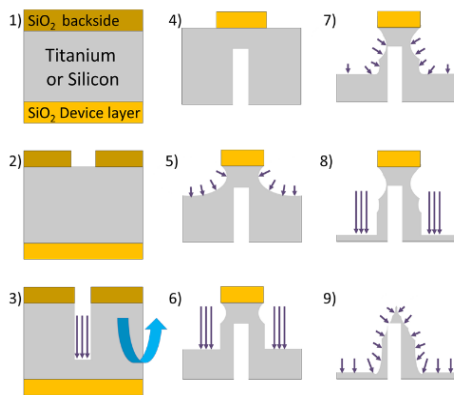
Figure 1. Process flow for MN fabrication.

1) SiO_2 is deposited on both sides of the substrate via Plasma Enhanced Chemical Vapor Deposition (PECVD).
2) Backside/needle lumen mask is patterned through photolithography and transferred to SiO_2 via Deep Reactive Ion Etch (DRIE).
3) Lumens are etched in substrate through anisotropic DRIE Bosch process (Si) or Ti-DRIE.
4) Device layer is patterned and the SiO2 mask etched.
5-9) Ultimate needle shape is realized through a series of anisotropic and isotropic etches performed through DRIE.

Materials and Methods: The process flow to produce Si or Ti out-of-plane MN arrays is shown in figure 1. The parameter space of the Ti-DRIE isotropic etch (represented in steps 5, 7, and 9) was optimized through exploration of the effect of temperature, pressure, and substrate power on the etch profile.

Results and Discussion: The process flow for out-of-plane MN arrays have been demonstrated using silicon. The vertical, lateral etch rate and selectivity has been measures as a function of the above mentioned parameters.

Conclusions: Progress has been made toward an isotropic titanium etch using Ti-DRIE; a key step toward the ultimate fabrication of Ti-based drug delivery systems. Using these MN arrays, we expect to improve upon previous OCA profusion methods with a simple, one-step active injection. This will further increase the overall distribution of OCA in the tissue, and inherently minimize issues with OCA transport, tissue necrosis, and scarring. We expect the applications of this device to extend beyond OCA delivery, such other transdermal drug delivery, interstitial fluid sampling, 3D cell culture microinjection.

GREY-BASED TAGUCHI OPTIMIZATION OF PHOTOACTIVE TiO$_2$ FOR CATALYTIC MICROREACTOR APPLICATIONS

[1]D.Z. Ashby, [2]Y. Jiang, [3]V. Nguyen, [1]K. Ply, [1]B.W.K. Woo, [4]P. Christopher, and [1,3,5]M.P. Rao
[1]Department of Mechanical Engineering, University of California, Riverside, CA
[2]Department of Chemical and Environmental Engineering, University of California, Riverside, CA
[3]Department of Bioengineering, University of California, Riverside, CA
[4]Department of Chemical Engineering, University of California, Santa Barbara, CA
[5]Materials Science and Engineering Program, University of California, Riverside, CA
Contact: *dashb001@ucr.edu*

Introduction: Astronaut crews aboard the International Space Station (ISS) rely on recycled water from cabin condensation and urine to sustain their daily water intake. An essential component of the Water Recovery System (WRS) is a thermal catalytic oxidation reactor operating at high pressure and temperature to eliminate volatile organic compounds. Deep space travel and long-term life support systems represent sensitive environments that could benefit from alternative reliable, low-cost, and low-energy instrumentation to achieve ambitious new goals. Interest in photocatalytic TiO$_2$ microfluidic reactors for applications in water treatment has grown considerably over the past decade. Advantages of microfluidic devices over traditional packed-bed thermal oxidation systems include: operation at standard temperature and pressure, increased surface area to volume ratio, and greatly reduced mass diffusion length, which can translate to enhanced performance on a miniature scale. However, low volumetric throughput remains a critical limitation in many applications, as does the difficulty associated with integrating TiO$_2$ uniformly within complex microfluidic device geometries.

Herein, we present our recent efforts to optimize growth of nanoporous TiO$_2$ (NPT) for use within Ti-based microfluidic devices. NPT is grown *in situ*, directly from the Ti channel surfaces, using a hydrogen peroxide-based oxidation process. Advantages over traditional shortcomings of microfluidic devices include: a) conformal coverage of complex geometries; b) high porosity yielding increased surface area and fluidic accessibility; and c) potential for scalable fabrication of large area photocatalytic devices with increased volumetric throughput.

Materials and Methods: A Taguchi design of experiments study was conducted to determine optimal NPT growth conditions for use on Ti micropillar scaffolding to further increase catalyst surface area, concept seen in figure 1. Grey relational analysis was applied to incorporate two performance metrics to produce an NPT film which maximizes reaction rate and minimizes NPT crack size. Methylene blue bulk reactor degradation was used to determine reaction rate and SEM contrast analysis was functionalized to find average crack size across samples.

Results and Discussion: Oxidation time proved to have the largest impact on both reaction rate and crack size independently. By applying grey relational analysis with equal weight for reaction rate and crack size we established a response table indicating the significance of each parameter's levels and determined the ideal sample conditions to be oxidation in 10% H$_2$O$_2$, at 80ºC, for 5 hours. This sample was tested and successfully yielded a performance within the confidence interval, demonstrating that these NPT growth conditions are the ideal balance of performance and film quality for use within a 3-D reaction chamber.
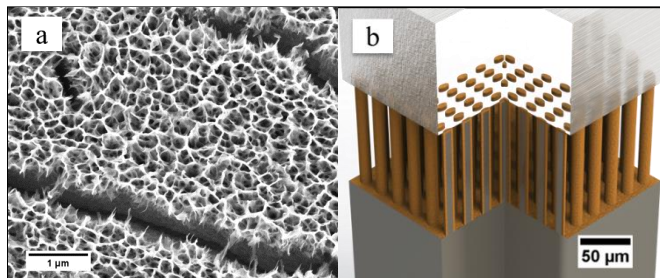
Figure 1: a) Scanning electron microscopy image of nanoporous titania (NPT) grown *in situ* on polished titanium foil. NPT has a highly porous, nanowire morphology ideal for photocatalysis applications.
b) A 3-D render of titanium microfabricated pillars serving as scaffolding for NPT growth. The micropillars occupy space within the reaction chamber and increase catalyst surface area to improve mass transfer and device performance.

Conclusions: Using Taguchi design of experiments and grey relational analysis we have optimized NPT for use in water purification applications. The parameter study led to a film that strikes a balance between maximizing reaction rate and minimizing crack size to produce an efficient, high-quality catalyst. Collectively, these results represent an important step towards our goal of developing robust, high-performance, multi-scale photocatalytic microreactors via complex channel geometries for increased mass and photon transfer efficiency.

MEASURING THE MASS, VOLUME, AND DENSITY OF MICROGRAM-SIZED OBJECTS IN FLUID

Heran C. Bhakta, Shivam Kardani, Vamsi K. Choday, Jessica Lin, and William H. Grover
Department of Bioengineering, University of California, Riverside
Contact: wgrover@engr.ucr.edu

Introduction: Measurements of an object's fundamental physical properties like mass, volume, and density can offer valuable insights into an object's composition or state. Conventional laboratory balances can easily measure the object's mass in the milligram scale, but for smaller objects in fluid (like biodegradable medical implants or drug-releasing particles), the fluidic environment of these objects is incompatible with conventional measurement techniques. In this work, we show a novel method for continuously monitoring the mass, volume, and density of any microgram-sized object in fluid. This sensor has immediate applications in different fields including materials science and drug product design.

Materials and Methods: We accomplish this using glass tubes bent into diving-board or tuning-fork shapes. The tubes are vibrated at their resonance frequency; this frequency is a function of the mass of the fluid contents of the tubes. When a particle flows through the tube (Fig. 1A), the resonance frequency of the tube briefly changes (Fig. 1C) by an amount proportional to the buoyant mass of the particle (Fig. 1D). In this manner, we can continuously and automatically measure the mass of any particle in fluid every few seconds with nano-gram resolution. Furthermore, by measuring a particle in fluids of different densities, we can also determine the volume and density of the particle. As a proof of concept, we measure the degradation rates of biomaterials, dissolution rates of over-the-counter medications, as well measure the skeletal properties of hydrogels.

Results and Discussion: As an initial proof of concept of our sensor, we measured the degradation rate of a model biomaterial. Figure 1E shows the buoyant masses of two millimeter-sized samples of magnesium metal as they degrade in different fluids. In neutral-pH physiologically relevant fluid (pH = 7.0; green) the sample of magnesium degrades relatively quickly and is effectively gone after 20 hours of continuous measurement in our sensor. We obtained a degradation rate of 0.14 h^{-1} for the magnesium sample in pH 7.0 buffer. However, when this experiment was repeated for a similarly-sized magnesium sample in a more-alkaline buffer (pH = 8.0; red), the sample took six times longer than the sample in pH 7.0 buffer with a degradation rate of 0.021 h^{-1} for pH 8.0. The magnesium reacts with acids to form magnesium ions and hydrogen gas; this reaction would be expected to accelerate the degradation of a magnesium sample at lower pH.
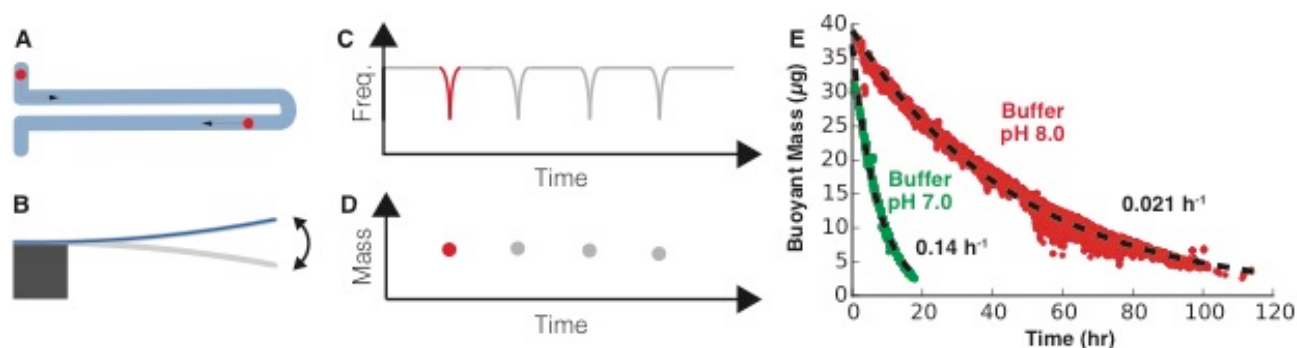
Figure 1. Using a vibrating glass tube to weigh objects in fluid. (A) The tube is bent into a "U" shape and a sample is passed through the sensor and resonated at its resonance frequency (B). As an object passes through the tube, the frequency changes are recorded over time (C) and mapped to buoyant mass using known calibrations (D). Using this method, we can directly measure the degradation rate of a sample biomaterial in different physiologically relevant fluids. Two millimeter-sized pieces of magnesium were measured in two different phosphate-buffered saline (PBS) solutions (E) [1].

Conclusion: We highlight the versatility of our sensor by using it in a variety of different proof-of-concept applications, including measuring the extremely slow degradation rates of a biodegradable magnesium material for medical implants, measuring the degradation rates of single particles of a controlled-release pharmaceutical, and by measuring skeletal properties of hydrogles. Our sensor's ability to make particle mass, volume, and density measurements continuously, in any fluidic environment, and with high sensitivity makes the sensor a powerful tool for many different fields.

3D COLLAGEN ARCHITECTURE MODULATES DEGRADABILITY AND CELL ADHESION

[1]D.O. Velez, [2]B. Tsui, [1]S. Ranamukhaarachchi, [3]H. Carter, and [1]S.I. Fraley
[1]Department of Bioengineering, University of California, San Diego, CA
[2] Bioinformatics and Systems Biology Program, University of California, San Diego, CA
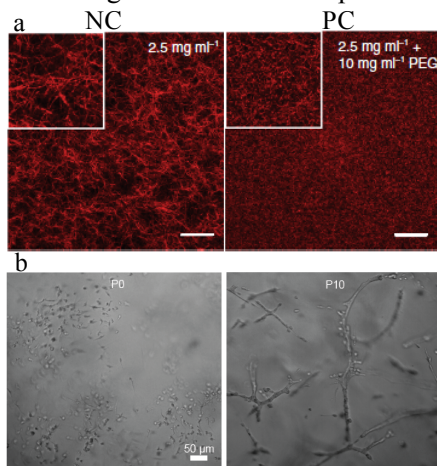[3] Department Medicine, University of California, San Diego, CA
Contact: *sifraley@ucsd.edu*

Introduction: Metastasis is the cause of 90% of cancer related deaths. An initial step in metastasis is the migration of cancer cells through collagen-rich tumor stroma and into the lymphatic or vascular systems. Despite an appreciation for the role of collagen in promoting tumor growth and progression, the field is generally lacking an understanding of how native collagen architecture, independent of stiffness and density, regulates cell migration and metastasis. We have developed a collagen matrix engineering technique to study the role of matrix architecture on cell-ECM interactions and cell migration outcomes.

Materials and Methods: The density of acid-extracted Type I collagen was held constant, and fibril architecture was tuned by the addition of free polyethylene glycol (PEG) during polymerization. PEG was then removed by washing. Biochemical assessment and quantitative microscopy were used to measure four core cell-ECM interactions (cytoskeletal polymerization, matrix remodeling, contractility, and adhesion) and cell migration.

Results and Discussion: PEG crowding (PC) created matrices with smaller pores, shorter fibers, and lowered degradability compared to non-crowded matrices (NC) (Fig. 1A). However, local and bulk stiffness was not significantly different. PC matrices triggered a migration response in breast cancer (BRCA) cells and several other cancer types, resulting in collective migration and the formation of multicellular network structures (Fig. 1B). We linked these structures to an aggressive clinical phenotype known as vasculogenic mimicry (VM) through phenotypic, histological, and transcriptional evidence. Clinically, the VM phenotype is correlated with advanced metastatic disease in 16 tumor types, but mechanistically, it is poorly understood. To better understand induction of this phenotype, we closely analyzed cell-ECM interactions. Cells initially interacting with PC matrices produced smaller and shorter-lived protrusions compared to cells embedded in NC matrices. Actin FRAP studies revealed that this difference in protrusion lifetime was not caused by differences in actin polymerization rates. TFM and protrusion-ECM displacement correlation showed that in PC architectures, cells fail to stabilize protrusions and sustain pulling force on the surrounding matrix. Likewise, FAK is significantly less phosphorylated, suggesting that adhesion is limited. Higher reactive oxygen species levels, lowered glucose consumption, and downregulation of mTOR signaling revealed that PC matrix architecture triggered oxidative and metabolic stress consistent with a low adhesion state. MMP inhibition led to lowered adhesive coupling in both conditions, suggesting that the PC matrix's resistance to degradation may be the feature driving cell stress and transdifferentiation.

Figure 1. (a) Reflection confocal micrograph of non-crowded (NC) 2.5 mg/ml collagen matrix (left) and 2.5 mg/ml collagen crowded with PEG (PC, right). (b) Brightfield micrographs of MDA-MB-231 cells cultured in NC and PC conditions after seven days.

Conclusions: These preliminary results suggest that collagen matrix degradability is regulated by fiber architecture, and that degradation activity modulates the extent of cell-ECM coupling. Thus, cells can experience low-adhesion stress even when surrounded by matrix. Low adhesion stress in 3D collagen leads to cancer transdifferentiation into an aggressive migratory phenotype.

Room-Temperature Solid-State Solvents for Molecular Photonics

John A. Clark, Eli M. Espinoza, James B. Derr, Frederic Guittard, Valentine I. Vullev

Department of Bioengineering, University of California, Riverside, CA 92521.

Contact: vullev@ucr.edu

Introduction: The optical properties of amyloid staining dyes, such as Thioflavin T (ThT) and 3,3'-diethylthiacyanine iodide (THIA), make them immensely attractive for fluorescence-based applications. THIA and ThT are rotamer dyes, dissipating energy via multiple non-radiative pathways. It results in parallel excited-state transient conformational changes, most of which do not undergo radiative deactivation, i.e. they do not fluoresce.[1] These dyes have a strong affinity for β-sheet proteins, such as amyloids and bacterial surface proteins.[3] Binding to proteins suppresses the degrees of torsional freedom of such rotameric dyes and prevents their non-radiative deactivation, increasing their fluorescence quantum yiled. That is, binding to bacteria causes emission enhancement of ThT and THIA, which is immensely promising for imaging, sensing and bioanalysis.[2] The discovery of such photoprobes that undergo emission enhancement, however, is serendipitous. Therefore, we develop glassy materials as novel room-temperature solid solvents for characterization of optical properties of photoprobes that are sensitive to binding and viscosity of the microenvironment.

Materials and Methods: Fluorescence spectroscopy and imaging were conducted as previously descirbed.[1-3] We compare the optical properties of ThT and THIA for liquid solvents, with those for solid solvents, such as polydimethylsiloxane (PDMS) and sucrose octaacetate (SOA). Bacterial staining tests, we used *E.coli*, *B. subtilis*, *B. megaterium*, and *E. aerogenes*.

Results and Discussion: Traditionally, flash-frozen organic solvents at liquid-nitrogen temperatures are used as solid-state glass media for spectroscopy tests. Molten SOA forms solid glass when cooled to room temperature and it has been our choice for testing solid-state optical medium. Loading the samples at elevated temperature, however, presents challenges. Recently, we discovered a means for loading molecular samples in a solid elastomer, PDMS, at room temperature. Interestingly, PDMS not only reproduces the emission enhancement that SOA induces, but also discourages ground state aggregates. Our studies reveal that suppression of the non-radiative decay processes are the reason for the PDMS-induced emission enhancement. Comparison between the results from the PDMS studies with our bacterial staining results validates our discovery that this elastomer can provide testing ground for biologically relevant microenvironment.

a   b
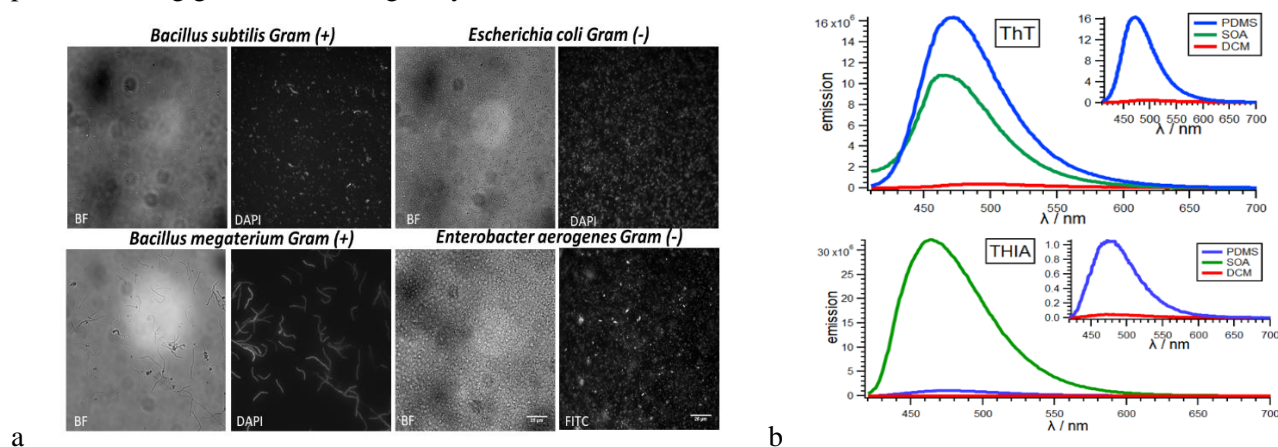
Figure 1. Optical features of ThT and THIA. a) Brightfield (BF) and fluorescence images of Gram (+) bacteria strained with ThT and Gram (-) species stained with THIA. b) Emission spectra of ThT and THIA for liquid and solid media (λ_{ex} (ThT) = 400 nm, λ_{ex} (THIA) = 410 nm).

Conclusions: By far, PDMS proves to be the best optically clear solid-state solvent for biological photoprobes. This discovery is a promising development for molecular spectroscopy and photonics.

References: 1) Upadhyayula, *et al.*, *Chem. Sci.* **2015**, *6*, 2237 2) Thomas et al *Langmuir* **2010**, *26* (12), 9756-9765 3) Xia, B et al, *J. Clinical Microbiol,* **2011**, *49* (8), 2966-2975

Effects of DOD 3D Bioprinting on the Formability of Microspheres

[1]Matthew Moldthan, [2]Ryan Meza and [3]Bingbing Li*

[1]Department of Manufacturing Systems Engineering and Management, California State University, Northridge, CA

[2]Department of Mechanical Engineering, California State University, Northridge, CA

[3]Department of Manufacturing Systems Engineering and Management, California State University, Northridge, CA

Contact: *bingbing.li@csun.edu*

Introduction: The growing number of people in need of organ transplants has increased steadily over the past few decades; however, the number of organ donors has not seen a large increase in about 10 years. This shortage of biocompatible, viable organs has lead to an increasingly large number of organ-failure related deaths. As organ donor waitlists continue to increase to an all-time high, 3D Bioprinting has emerged as a promising technological advancement to possibly solve this problem. Tissue engineering through freeform fabrication has provided an opportunity to have an unlimited supply of biocompatible tissues and organs using one's own cells. This opportunity has led to the development of various 3D Bioprinters, each requiring specific bioinks capable of securely encapsulating cells. In this study, the compatibility of various bioinks were examined using a Drop-on-Demand, piezoelectric inkjet 3D bioprinter. We tested the properties of various bioinks in relation to this device to determine optimal bioink composition and printing parameters.

Materials and Methods: To test various bioinks under extreme conditions, hydrogels were extruded on a MicroFab PH-46 (MicroFab, Plano, TX) micro dispensing subsystem. This system consists of a MicroFab Jet Driver responsible for controlling the DOD pulse, a MicroFab pneumatic controller used to adjust the back pressure, an 80um piezoelectric micronozzle used to extrude bioinks, and an imaging camera STC-MB33USB (SENTech America, Carrollton, TX) to observe the droplet formation process. Biomaterials used in this experiment include sodium alginate (0.5% w/v, 0.75% w/v, 1% w/v, and 1.25% w/v) and sodium alginate (0.5% w/v) with gelatin (0.1% w/v).

Results and Discussion: Through experimentation, it was found that all bioinks tested had good extrudability, however a time dependency was determined. The longer the hydrogel was exposed to the air at the orifice of the micro-nozzle, the more the hydrogel began to swell. Through studies it was determined that hydrogels with high water concentrations swell when exposed to air. A "tickle pulse" is needed to circulate the fluid at the nozzle orifice to prevent swelling. Various hydrogel concentrations and compositions, corresponding to various viscosities, correlate to different levels of extrudability. Hydrogels were extruded and tested against different printing parameters. These parameters were tested against the droplet size and speed to determine the effect on droplet formation.
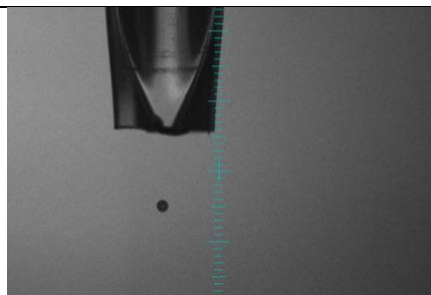

Figure 1: Microsphere formation of hydrogel consisting of 0.5% sodium Alginate

Conclusion: Sodium alginate based bioink has proven to be an adaptable material with a broad range of capabilities that are dependent on various printing parameters. All concentrations maintained good printability, provided they were extruded under favorable conditions.

DEVELOPMENT OF FRET BASED HTS FOR SMALL MOLECULE INHIBITOR OF ATG4

[1]V. Madahar, [2]C. Hariharan, and [3]J. Liao
[1]Department of Bioengineering, University of California, Riverside, CA
Contact:vmada001@*ucr.edu*

Introduction: Autophagy describes a process that removes misfolded proteins, damaged organelles, and even intracellular pathogens using double-membraned autophagosomes. Recently, autophagosome degradation has been observed to provide a source of nutrients for cancerous cells that are in a nutrient deprived and or oxidative stress environment, by processing damaged organelles and or proteins to use as a source of nutrients and energy. Thus, modulation of autophagy activity is a viable path for cancer therapy. Autophagy-related Gene 8 (ATG8)- Phosphatidylethanolamine (PE) system is tightly regulated by a cysteine protease Autophagy-Related Gene 4 (ATG4). Current methods for the assessment of ATG4 activity utilize SDS-PAGE and or in-vivo fluorescent assays, however SDS-PAGE studies are not suitable to high-throughput screenings, and in-vivo assays are vulnerable to false positives due to non-specific interaction. In this study we present a novel method for studying ATG4 activity and develop a platform for a high throughput screening for a small molecule inhibitor of ATG4 activity.

Materials and Methods: This study describes the development of a quantitative fluorescent assay, between the homolog Golgi-associated ATPase enhancer 16 kDa (GATE-16), a homolog of ATG8, and the cysteine protease ATG4. Förster's Resonance Energy transfer (FRET) between two fluorophores, such as the fluorescent proteins CyPet and YPet, provide a quantitative method for the assessment of ATG4 and ATG8 homolog interaction *in-vitro*. The protein complex is constructed with the FRET protein pair, CyPet and YPet bound to the amine and carboxy terminus of GATE-16, shown in figure 1a & 1b. To characterize the robustness of our assay, we measured the Z' factor for our HTS for a ATG4 inhibitor. Z' Factor is measured in the 384 well plate format, over three plates, 128 well repeats, and over the course of three days, using the FlexStation II 384 plate reader.

Results and Discussion: Protein complex, CyPet-GATE-16-YPet is cleaved at its glycine residue on the C-terminal by ATG4 resulting release of YPet and a loss of FRET, excitation at 414 nm while observing 475 nm and 530 nm emission, schematic shown in figure 1A**.** The protein complex is designed in a way that ATG4 activity can be correlated directly to the loss of EmFRET and increase in emission at 475 nm. The response of EmFRET over time with varying concentration of ATG4, provides evidence that over 30 minutes solely ATG4 changes the FRET signal, this provides confidence in the assessment ATG4 activity from this assay, figure 1B. The Z' factor was measured to be an average of 0.97 over the course of 3 days, and a total of 9 plates which meets the larger than 0.5 Z' factor criteria set by NIH guidelines for HTS, EmFRET reading provided in figure 1C.
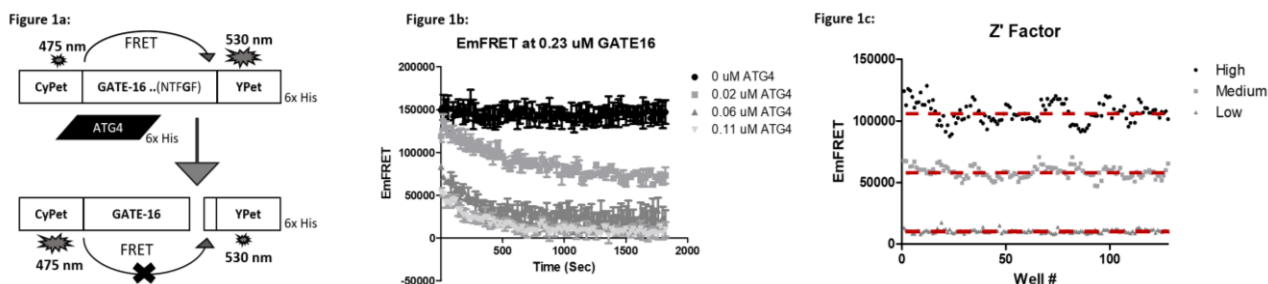
Figure 1A: Illustration of protein complex, FRET pair attached to the C and N terminal of the substrate GATE16.
Figure 1B: Calculated EmFRET shown over 30 mins, with varying concentrations of ATG4 protease.
Figure 1C: Plot of EmFRET over a 384 well plate, with 128 repeats of ATG4 to produce MAX, MID, and MIN signal.

Conclusions: We have developed a platform to investigate activity of the cysteine protease, ATG4, and to screen for small molecule inhibitors. Implementation of our FRET assay has provided a novel method to characterize protease activity, by measuring Kcat/Km and IC50 of an inhibitor. Future work is to establish this FRET assay *in-vivo* to further characterize the inhibitor for cytotoxicity and viability as an inhibitor.

INCREASED LEVELS OF INTESTINAL TRYPSIN AND LIPASE IN HUMAN BLOOD PLASMA CORRELATE WITH CLINICAL BIOMARKERS OF CONGESTIVE HEART FAILURE

[1]V. Courelli, [1]A. Courelli, [2]P. Mills, and [1]G. Scmid-Schönbein

[1]Department of Bioengineering, University of California, San Diego, CA

[2]Department of Family Medicine and Public Health, University of California, San Diego, CA

Contact: *vcourell@ucsd.edu*

Introduction: The fundamental tissue degrading mechanisms that lead to Congestive Heart Failure (CHF) accompanied by cardiac enlargement and hypertrophy, and increased heart rate are not completely understood. Our current research suggests that powerful digestive enzymes of the intestinal lumen may leak into the systemic circulation triggering or exacerbating CHF. We hypothesize that increased intestinal permeability due to CHF allows digestive enzymes typically found in the small intestinal lumen—such as pancreatic trypsin, lipase, and elastase—to cross the compromised intestinal barrier and enter the general circulation. Active digestive enzymes may trigger or exacerbate the degradation of cardiac tissue and contribute to cardiomyopathy and the systemic inflammation observed in CHF. Our objective is to determine the levels of pancreatic trypsin and lipase in blood plasma via western blot and investigate their correlation with clinical biomarkers of inflammation that were measured using ELISA assays as well as functional measurements of the heart function.

Materials and Methods (Figure 1)**:**
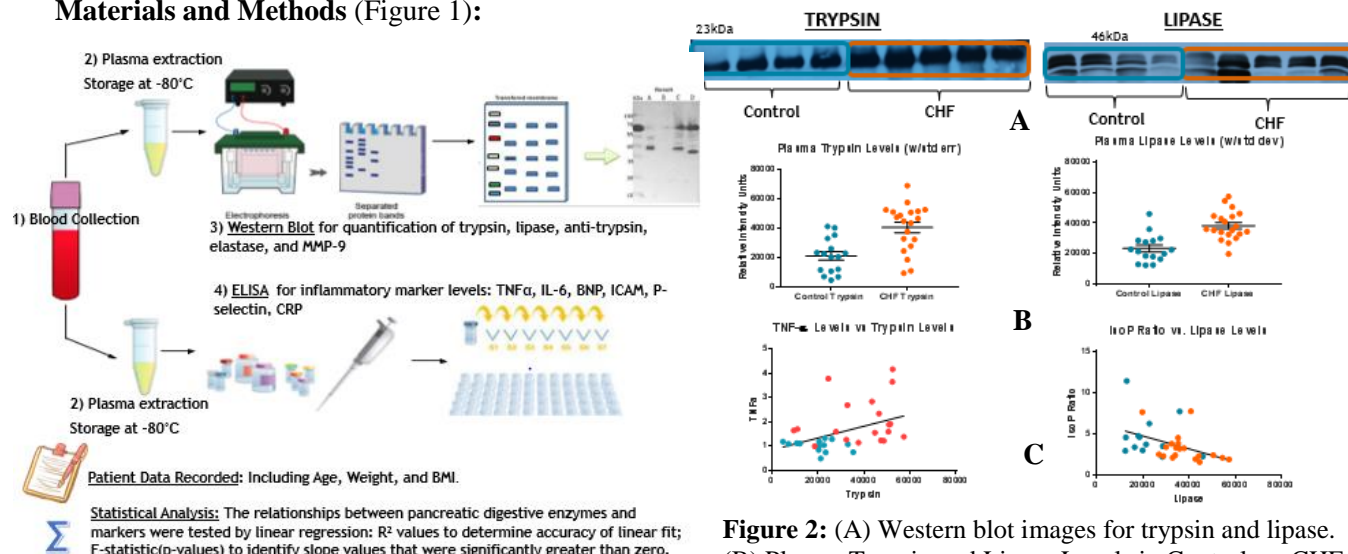
Figure 1: Illustration of the experimental protocol including blood plasma collection (human CHF and control patients), western blot and ELISA assays, and statistical data analysis.

Figure 2: (A) Western blot images for trypsin and lipase. (B) Plasma Trypsin and Lipase Levels in Control vs. CHF patients. (C) Significant positive trypsin correlation with TNF-α (p-value: 0.014) and significantly negative lipase correlation with isoproterenol ratio (p-value: 0.013).

Results and Discussion: Western Blots showed increased levels of MMP9, Lipase, Trypsin, and Anti-Trypsin in CHF patients compared to Control patients (Figure 2B), and no difference between the Elastase levels of CHF patients and Control patients. Correlation analysis of trypsin and lipase with several inflammatory biomarkers indicated significant positive correlation between plasma lipase levels and TNF-α (p-value: 0.002), IL-6 (p-value: 0.05), BNP (p-value:0.0002), CRP (p-value:0.016), neutrophil counts (p-value: 0.011), cardiac ejection fraction (p-value:0.02), and significant negative correlation with isoproterenol response (p-value: 0.013) (Figure 2C). It also showed significant positive correlation between plasma trypsin levels and TNF-α (p-value: 0.014), BNP values (p-value: 0.005), and neutrophil counts (p-value: 0.01). The results suggest that levels of pancreatic digestive enzymes in the systemic circulation of patients with congestive heart failure are elevated concurrently with a loss of physiological function and presence of inflammatory biomarkers.

Conclusions: Increased amounts of intestinal trypsin and lipase are present in the CHF patients' blood plasma, due to compromised permeability of the intestinal mucosal barrier of CHF patients, and correlate significantly with various functional and inflammatory CHF biomarkers.

Designing a Tilt System to Test Balance and Learning Pattern in Rats with Spinal Cord Injury

[1]S.Tabatabai,[2]L.Oelsner, [3]N. Evangelista, [4]N. Bridges, [5]K.Moxon

[1]Department of Biomedical Engineering, University of California, Davis, CA

Contact: staba@ucdavis.edu

Introduction: There are 17,000 new spinal cord injury cases a year with approximately 282,000 people in the US who are alive and have SCI as of 2016. Current treatments include physical therapy where patients learn how to use their muscles again to restore function. However, it is challenging to reteach patients because their way of learning changes after a spinal cord injury. In order to better understand how the ability to learn is affected by a spinal cord injury, we will observe neural signals of rats while they learn to balance and repeat consistent neural patterns. Learning patterns were observed from the firing rates and timing of indirect and direct neurons. We designed a tilt platform and data acquisition system that captures such neural data.

Materials and Methods: We designed both the hardware and software aspect of the system. The rat stands on a tilt platform which is connected to a servo motor to provide the tilts. Load cells beneath the platform acquire sensory information that is amplified and sent to MATLAB to be time stamped and analyzed offline. Meanwhile neural information is recorded by electrodes in the rat's brain. The neural data is amplified and sent to a Multichannel Acquisition Processor to be time stamped and recorded. The neural and sensory data is attained and organized in MATLAB. The tilt platform is controlled by LabVIEW. A classifier is created to recognize the neural patterns for each tilt type. The neural signals are compared to the classifier and the rat is punished if the signals do not correspond and rewarded if the signals match the classifier. The punishment is a steep tilt while the reward is leveling of the platform.

Results and Discussion: In learning animals, both direct and indirect neurons showed increases in single neuron information compared to control animals in the early phase. In the late phase, direct neurons increased information to levels above indirect neurons, while indirect neurons maintained information levels found in the early phase. Direct neurons used a combination of firing rate and timing differences to increase information while indirect neurons only modulated firing rate. Moreover, only direct neurons showed an increase in redundancy with practice. These results suggest that the cortex primarily uses a global strategy initially but transitions to a more local neuron strategy with practice. Learning animals showed an early phase of rapid performance improvements followed by a late phase of smaller performance improvements that eventually plateaued.
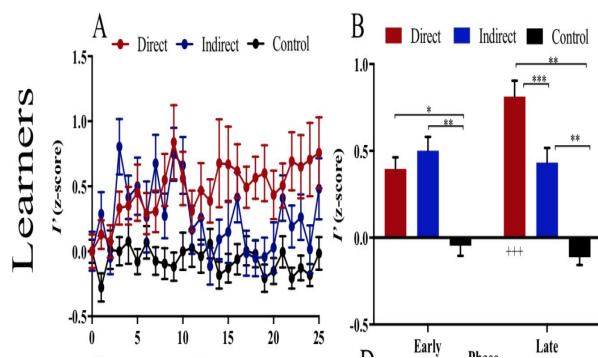
Figure A. Depicts the amount of information contained in direct and indirect neurons in learners over a period of time (in days). In this case, direct neurons contained more information that indirect neurons throughout the entire period.

Figure B. Depicts the overall trend in amount of information contained in direct and indirect neurons in the learners. Generalization of Figure A. Both direct and indirect neurons contained information on the task initially. However, in the later phase direct neurons were more involved in the task than indirect neurons.

Conclusion: The results from this study can contribute to the understanding of BMI learning and motor learning as well as the the development of a BMI as a neuroprosthetic for paraplegia. Since both direct and indirect neurons are used initially and then direct neurons are favored, a more effective BMI can be designed accordingly.

HUMAN EMBRYONIC STEM CELL-DERIVED 3D MODEL FOR THE STUDY OF PALATAL FUSION

[1]N. Sandhu, [2]M. Prasad, [2]J. Hackland, and [2]M. Garcia-Castro

[1]Department of Bioengineering, University of California, Riverside, CA

[2]Department of Biomedical Sciences, University of California, Riverside, CA

Contact: nsand006@ucr.edu

Introduction: Neural crest cells (NCC) contribute to many derivatives in the body, ranging from cells of the craniofacial region, such as cartilage and bone, and neurons of the peripheral nervous system[1]. Abnormalities in either the development or migration of NCC can result in a wide range of diseases. These are known as neurocristopathies and include cleft lip and palate[2]. Oral clefts occur in 1 in every 700 live births [3]. An adequate model is needed to study the effects of gene mutations and toxins on human palate development, one that is preferably constituted of cells from the correct ontogeny. A model from a recent report utilizes mesenchymal cells from the umbilical cord and primary epidermal keratinocytes from juvenile donors[4] rather than NCC as in the developing embryo. Unique to our system, each cell type is generated from hESC via developmentally relevant pathways: osteocytes and fibroblasts via a NCC intermediate, and epithelial cells directly from hESC. To study the causes of cleft palate we are developing a surrogate model of the embryonic human oral palate.

Material and Methods: NCCs are differentiated from hESCs (H1[5], fibroblasts and osteoblasts are differentiated from NCC[6] and epithelial cells are differentiated from hESCs[7]. The osteoblast spheres are generated using non-adherent AggreWell molds (Stem Cell Technologies), and each sphere is approximately 3000 cells in size. After formation Osteoblas**t** spheres are moved from the AggreWell molds into 96 well plates, one sphere per well and the fibroblasts and epithelial cells are then added sequentially **(Figure 1)**.
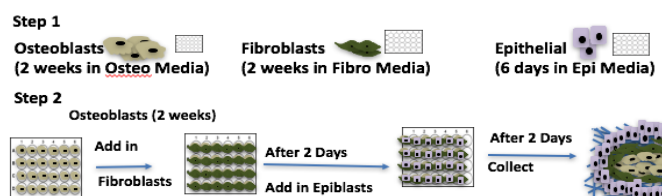
Figure 1. Formation of 3D palatal surrogate. Osteoblast spheres are moved into the 96 well plate, 3000 fibroblasts are added per well, and allowed to shake at 135 RPM under culture conditions. After 48 hours, they are moved to new 96 well plates and 3000 epithelial cells are added per well, and incubated at 135 RPM under culture conditions for 48 hours.

Results and Discussion: We have engineered 3D spherical structures that contain an osteoblast layer at the center that is surrounded by fibroblasts and coated with epithelial cells. **Each one of these cell types maintains their marker expression in both** 2D and 3D co-cultures **(Figure 2).**
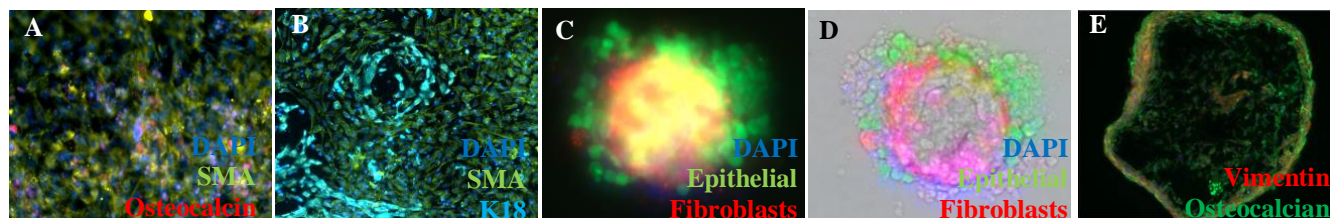
Figure 2: Sphere Formation and Derivatives A, B) Co-stains in a monolayer culture **A)** Fibroblasts (SMA) and osteoblasts (Osteocalcin) **B)** Fibroblasts (SMA) and epithelial cells (K18) **C-E)** Are images of triple co-culture spheres. **C)** Is a merged fluorescent image in which epithelial cells are labeled with DiO, and fibroblasts are labeled with DiI **D)** Modified version of C **E)** Fibroblasts (Vimentin) and osteoblasts (Osteocalcin)

Conclusions: We have demonstrated that it is feasible to make 3D structures similar to those that form during development using osteocytes that are derived from NCC. This model will be used to study the effects of gene mutations, or environmental toxins that lead to palatal clefting, and as such may lead to novel diagnostic and therapeutic approaches for cleft palate.

References: [1] Lee, Gabsang, et al. Nature protocols 5.4 (2010): 688-701 [2] Donoghue, Philip CJ, Anthony Graham, and Robert N. Kelsh.; Bioessays 30.6 (2008): 530-541. [3] Zuk, Patricia. Pediatric Research. 2008. 2 Tollemar, Viktor, et al. Genes & Diseases (2015). [4] Belair, David G., et al *PLoS one* 12.9 (2017): e0184155. [5] Leung, Alan W., et al. Development 143.3 (2016): 398-410. [6] Lee, Gabsang, et al. Nature protocols 5.4 (2010): 688-701. [7] Metallo, Christian M., et al. Stem cells 26.2 (2008): 372-380.

ELONGATED CELL SHAPE DIRECTS MESENCHYMAL STEM CELL DIFFERENTIATION TO SMOOTH MUSCLE CELL VIA MIR-145

[1]K Nguyen, [1]C Hoffman, [1,2]YT Yeh, [1,2]KC Wang, [1,2]S Chien
[1]Department of Bioengineering, University of California, San Diego
[2]Institute of Engineering in Medicine
Contact:khn001@ucsd.edu c2hoffma@ucsd.edu

Oral/Poster Consideration
Technical Track: Stem Cells and Regenerative Medicine
Award Consideration: Yes - Student/Postdoc

Introduction: Mesenchymal stem cells (MSC) are multipotent stem cells that are able to differentiate into various cell types, including smooth muscle cells (SMCs). MSC differentiation into SMC shows great therapeutic potential for repairing vascular damage. Smooth muscle cells contribute to the elasticity and composition of arterial walls and are invaluable for maintaining blood pressure in the body. Damage to vascular smooth muscle cells leads to various cardiovascular diseases (CVDs), which are the leading cause of death in the United States. Therefore, it is of prime importance to investigate the potential of using differentiated MSC for treatment of CVD. Upon their damage, SMCs switch from a contractile to a proliferative phenotype, thus losing their normal contractile ability. Previous studies have shown that cell shape and size can determine MSC fate. Here, we study the role of elongated cell shape in MSC-to-SMC differentiation and microRNA-regulation of the differentiation pathway.

Materials and Methods: We applied a soft-lithography technique to fabricate PDMS gels with microgrooves to produce the elongated MSC shape. MSCs derived from bone marrow were then seeded onto such PDMS gels. Western blot analysis and immunofluorescence staining were used to determine expression levels of SMC marker proteins. Then, gain and loss of function experiments of microRNA 145 (miR-145) were performed to determine the role of miR-145 in the regulation of the MSC-to-SMC differentiation pathway.

Results and Discussion: The MSCs cultured on these microgrooves showed a definite increase in the expressions of SMC markers α-SMA and SM22, in comparison to those on flat surfaces. Subsequent gain and loss of function experiments showed that the microgrooves induced MSC-to-SMC differentiation via downstream Krüppel-like factor (KLF4) regulation. Treatment with an inhibitor of Rho or Rho-associated protein kinase abolished the elongated-cell-shape-induced SMC marker expressions. These effects were restored by the overexpression of miR-145.
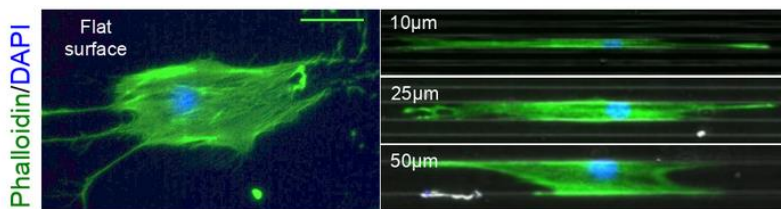
Figure 1: Immunostaining with phalloidin and DAPI to visualize nuclei and actin fibers of MSC seeded onto a flat PDMS gel, 10 µm, 25 µm, and 50 µm microgroove PDMS gels. The MSC are elongated in the microgrooved gels.

Conclusions: Our results show that miR-145 is critical in the cell-shape-induced MSC-to-SMC differentiation and has important potential for MSC-based therapy. These findings have the potential to advance stem cell based therapy by predicting MSC differentiation and preventing vascular disease progression from grafts and other vascular damage.

IMPAIRED LYSOSOMAL EXOCYTOSIS CONTRIBUTES TO COMPLEMENT-MEDIATED VASCULAR INJURY ASSOCIATED WITH DRY AMD

[1]Cabrera AP, [2]Stoddard J, [2]Neuringer M, [2]McGill TJ, [1]Ghosh K

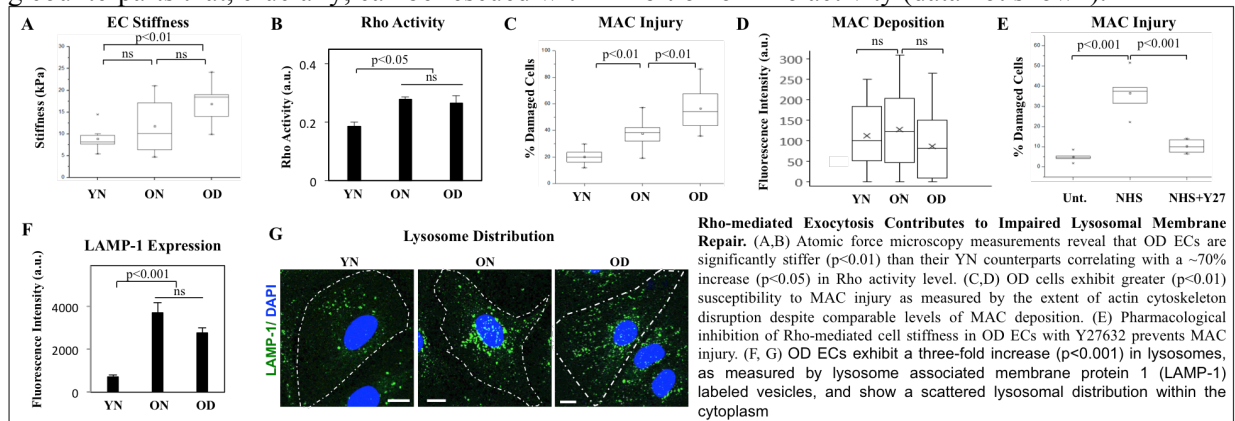[1]Department of Bioengineering, University of California, Riverside, CA

[2]Oregon National Primate Research Center, Oregon Health & Science University, Beaverton, OR, United States.

Contact: *acabrera@engr.ucr.edu*

Introduction: Age-related macular degeneration (AMD) is the leading cause of blindness in the aging population. Despite the prevalence of AMD, only 10-15% of those with advanced wet AMD benefit from current therapies. Thus, there is a need to develop treatments for early AMD. A notable feature of early AMD is choriocapillaris (CC) atrophy. Since complement activation, a major risk factor for dry AMD, leads to deposition of membrane attack complex (MAC; C5b-9) on the CC, it likely results in choroidal endothelial cell (EC) lysis and CC atrophy. Interestingly, however, MAC also deposits in CC of young non-AMD eyes, thus indicating that specific age-related factors may contribute to MAC-induced CC degeneration in AMD. Indeed, using a rhesus monkey model of early AMD, we have recently shown that choroidal ECs from old AMD eyes exhibit greater complement injury than their young non-AMD counterparts. Yet, precisely how aging increases MAC susceptibility remains unknown. Since lysosomal exocytosis protects cells from membrane injury, here we explored its role in EC susceptibility to MAC injury.

Methods: Stiffness of choroidal ECs isolated from eyes of young normal (6 yrs; YN), old normal (20 yrs; ON) and old rhesus monkeys with severe drusen (19 yrs; OD) was measured by atomic force microscopy (AFM) while Rho GTPase activity was quantified by Rho G-LISA. Susceptibility of choroidal ECs to MAC-induced injury was assessed by treatment with complement-competent serum, measuring C5b-9 deposition by immunofluorescence labeling, and quantification of actin cytoskeleton damage. To determine whether EC stiffness exacerbates MAC injury, pharmacological Rho/ROCK inhibitor (Y27632) was used to reduce EC stiffness. Since the exocytosis and membrane fusion of lysosomes promote the spontaneous repair of damaged cell membranes, immunofluorescence of lysosomal membrane protein LAMP1 was used to evaluate the role of membrane repair following MAC injury.

Results: AFM measurements revealed that OD ECs are significantly stiffer than their YN counterparts (Fig. A), which correlated with increased Rho activity (Fig. B). Further, OD cells exhibit greater susceptibility to complement injury, as indicated by greater disruption of actin cytoskeleton (Fig. C) despite comparable levels of MAC deposition (Fig. D). Remarkably, decreasing stiffness of OD ECs alone (by inhibition of Rho activity) reduced their susceptibility to MAC injury (Fig. E). Importantly, these MAC-susceptible OD ECs were found to exhibit a higher density and larger spatial distribution of LAMP-1-expressing lysosomes, thus indicating sub-optimal acidification (pH) of lysosomal hydrolases necessary for membrane repair. Time-lapse videos of GFP-labeled lysosomes further revealed that that OD ECs exhibit impaired lysosomal trafficking compared to their young counterparts that, crucially, can be rescued with inhibition of Rho activity (data not shown).

Rho-mediated Exocytosis Contributes to Impaired Lysosomal Membrane Repair. (A,B) Atomic force microscopy measurements reveal that OD ECs are significantly stiffer (p<0.01) than their YN counterparts correlating with a ~70% increase (p<0.05) in Rho activity level. (C,D) OD cells exhibit greater (p<0.01) susceptibility to MAC injury as measured by the extent of actin cytoskeleton disruption despite comparable levels of MAC deposition. (E) Pharmacological inhibition of Rho-mediated cell stiffness in OD ECs with Y27632 prevents MAC injury. (F, G) OD ECs exhibit a three-fold increase (p<0.001) in lysosomes, as measured by lysosome associated membrane protein 1 (LAMP-1) labeled vesicles, and show a scattered lysosomal distribution within the cytoplasm

Conclusion: Together, these findings implicate age-related and Rho-mediated EC stiffening as a key determinant of complement-mediated CC atrophy. Our ongoing work aimed at deciphering the molecular mechanisms underlying this phenomenon may lead to the identification of new therapeutic targets for dry AMD.

Saturday, June 23ʳᵈ

7:00 am – 12:00 pm	**Registration (Concourse 101)**
7:00 am – 9:00 am	**Exhibitor Setup (Concourse 101)**
7:00 am – 8:00 am	**Breakfast (Concourse 101 and Plaza)**
8:00 am – 8:50 am	**Plenary Talk 6: Dori Borjesson, Ph.D., Director, Veterinary Institute of Regenerative Cures, University of California, Davis (Ballrooms A and B)**
9:00 am – 11:00 am	**Poster Session III (MR 4 and MR 5)**
9:00 am – 9:30 am	**Rapid-Fire Poster Presentations (Ballrooms A and B)**
9:30 am – 11:00 am	**Undergraduate Student Capstone Design Competition (Ballrooms A and B)**
11:00 am – 11:10 am	**Coffee Break (Concourse 101 and Plaza)**
11:10 am – 12:00 pm	**Plenary Talk 7: Stan Rowe, Chief Scientific Officer, Corporate Vice President of Advanced Technology, Edwards Lifesciences (Ballrooms A and B)**
12:00 pm – 1:15 pm	**Lunch (Concourse 101 and Plaza)**
1:15 pm – 2:45 pm	**Biomedical Imaging 3 (MR 1)** Chair: Hyle Park, UC Riverside Co-Chair: Xiaoping Hu, UC Riverside
1:15 pm – 2:45 pm	**Biomaterials and Drug Delivery 2 (MR 2)** Chair: Huinan Liu, UC Riverside Co-Chair: Kaustabh Ghosh, UC Riverside
1:15 pm – 2:45 pm	**Molecular and Cellular Engineering 3 (Ballrooms A and B)** Chair: Bahman Anvari, UC Riverside
2:45 pm – 3:15 pm	**Student Awards and Closing Remarks (Ballrooms A and B)** **Xiaoping Hu, Ph.D., UC Riverside**

1:15 pm – 2:45 pm	**Biomedical Imaging 3 (MR 1)**
	Chair: Hyle Park, UC Riverside Co-Chair: Xiaoping Hu, UC Riverside
1:15 pm – 1:30 pm	D. Hadraba, Institute of Physiology, Czech Academy of Sciences Mechanical Testing of Connective Tissue From Nano to Macro
1:30 pm – 1:45 pm	Thompson Lu, UC Riverside Mechanical Characterization of Micron-sized Erythrocyte-derived Optical Particles by Quantitative Phase Imaging
1:45 pm – 2:00 pm	Eddy Salas, UC Irvine Pressure Induced Injury Detection Spatial Frequency Domain Imaging
2:00 pm – 2:15 pm	Padmaja Jonnalagedda, UC Riverside Segmentation based Data Augmentation in Deep Networks for Magnification Invariant Breast Cancer Detection
2:15 pm – 2:30 pm	Ameet Braganza, UC Los Angeles THz and mm-Wave Based Imaging of Ex Vivo Porcine Corneas and Preliminary Human Trials
2:30 pm – 2:45 pm	Andrew L. Trinh, UC Irvine Distinguishing Stem-Like Tumor-Initiating Cells in Malignant Glioma by Phasor Fluorescence Lifetime Microscopy
1:15 pm – 2:45 pm	**Biomaterials and Drug Delivery 2 (MR 2)**
	Chair: Huinan Liu, UC Riverside Co-Chair: Kaustabh Ghosh, UC Riverside
1:15 pm – 1:30 pm	Jin Hee Kwak, UC Los Angeles Bioengineered Osteogenic Protein NELL-1 Rescues Spaceflight-Induced Bone Loss
1:30 pm – 1:45 pm	Casey M. Gries, UC Riverside Crosslinked Salmonella Flagella as a Stabilized Vaccine Scaffold
1:45 pm – 2:00 pm	Claire Yu, UC San Diego Rapid Digital Light Processing 3D Bioprinting of Human Tissues with Tunable Decellularized Extracellular Matrix Bioinks
2:00 pm – 2:15 pm	Zachary Reitz, UC Irvine Epigenetic Consequences of Biomaterial Design on Macrophage Inflammatory Response
2:15 pm – 2:30 pm	Ross Chung, UC Riverside Antimicrobial Effects of Hydroxyapatite Coated Magnesium Implants Against S. aureus
2:30 pm – 2:45 pm	J.S. Yang, UC Riverside Predicting Direct Cerebral Delivery of Neuregulin-1 Using an Osmotic Transport Device to Reduce Edema
1:15 pm – 2:45 pm	**Medical Devices and Instrumentation 3 (MR 3)**
	Chair: William Grover, UC Riverside Co-Chair: Victor G. J. Rodgers, UC Riverside
1:15 pm – 1:35 pm	M. Aghaamoo, UC Irvine Hydrodynamic Micro-vortices in Droplet-based Microfluidics: Toward High Efficient Single Cell Encapsulation and Selective Releasing
1:35 pm – 1:55 pm	Christopher Hale, UC Riverside Reduction of Edema Following Spinal Cord Injury Using a Novel Device
1:55 pm – 2:15 pm	Daniel Bradbury, UC Los Angeles Equipment-Free Automation of Multistep Paper-Based Sensors
2:15 pm – 2:35 pm	Jeremy Lombardo, UC Irvine Microfluidic Device With Embedded Microporous Nylon Membranes for Efficiently Filtering and Dissociating Digested Tissue Into Single Cells
1:15 pm – 2:45 pm	**Molecular and Cellular Engineering 3 (Ballrooms A and B)**
	Chair: Bahman Anvari, UC Riverside
1:15 pm – 1:45 pm	Invited faculty speaker: Niren Murthy, UC Berkeley
	In Vivo Delivery of Cas9 Ribonucleoprotein and Donor DNA With Gold Nanoparticles
1:45 pm – 2:00 pm	J. Cheah, UC Davis
	Innovative Approach to Resolve Force-dependent Protein Interactions Using BioID
2:00 pm – 2:15 pm	Y. Pan, UC San Diego
	Mechanogenetics for the Remote and Non-invasive Control of Cancer Immunotherapy
2:15 pm – 2:30 pm	V. A. Morikis, UC Davis
	Mechanotransduction via High Affinity LFA-1 Promotes Assembly of Kindlin-3/RACK1/Orai1, a Complex That Signals Intracellular Calcium Flux
2:30 pm – 2:45 pm	E. M. Francis, UC Davis
	A Mechanoregulatory Role for Calcium Bursts in Human Neutrophils

MECHANICAL TESTING OF CONNECTIVE TISSUE FROM NANO TO MACRO

D. Hadraba[1,2,3,4], F. Lopot[2], R. Paesen[3], M. Ameloot[3], K. Jelen[2], M. Digman[4]

[1]Department of Biomathematics, Institute of Physiology, CAS, Czech Republic

[2]Department of Anatomy and Biomechanics, Charles University, Czech Republic

[3]Department of Biophysics, Hasselt University, Belgium

[4]Department of Biomedical Engineering, University of California, Irvine, CA

Contact: dhadraba@gmail.com

Introduction: Connective tissue is an inhomogeneous composite structure with high variability in mechanical properties. The mechanical properties originate in a hierarchical organization of proteins from which type I collagen plays the most evident role. This role seems to differ at each hierarchical level. For example, type I collagen triple helix returns the highest Young's modulus but only fibers are aligned into a zig-zag wavy pattern, termed the crimp pattern. The mechanical properties are also not stationary and alter with age or disease, and therefore, conducting an experiment on the crimp pattern behavior under mechanical load simultaneously with the measurement on the helical pitch angle of type I collagen molecule can provide a new insight into the clinical classification of connective tissue.

Materials and Methods: The rabbit tendons were gripped in an in-house built tensile instrument that was placed at the microscope stage. The tendons were imaged using polarized second harmonic generation microscopy at load-free and stretched states (Zeiss LSM 510 META, Zeiss, Germany; Mai Tai DeepSee, Spectra-Physics, USA). The results were analysed for the crimp pattern, the crimp pattern disappearance, the helical pitch angle differences with age, and the helical pitch angle changes with mechanical loading.

Results and Discussion: The crimp pattern parameters differed significantly with age. The crimp pattern disappearance with age could be related to a higher occurrence of non-sport related tendon ruptures. The crimp pattern, if present, also disappeared during the mechanical test before reaching the minimum detectable force and reappeared immediately after returning to the initial elongation. When searching for a difference in the helical pitch angle between the age groups, the results provided no evidence to reject the null hypothesis. However, it seemed that there was a trend towards the helical pitch angle increase with age (Figure 1). Finally, no significant difference was found when comparing the helical pitch angle (HPA) at load-free and stretched states. This results indicated that some other structures such as crosslinking can be responsible for the changes of mechanical properties.

a) HPA = 48.7° ± 0.8°   b) HPA = 49.8 ° ± 0.8°   c) HPA = 50.0° ± 0.4°
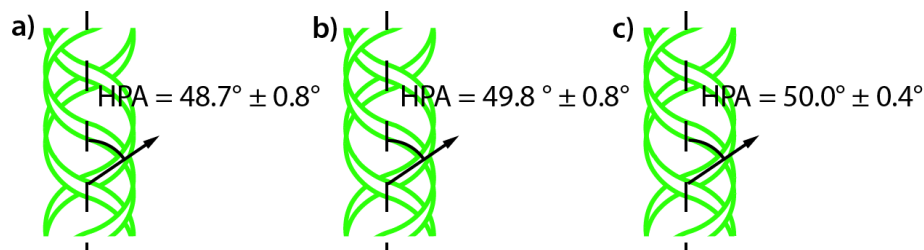
Figure 1: HPA of collagen molecule in flexor. (**a**) 1-month-old animals (n = 3). (**b**) 6-month-old animals (n = 4). (**c**) 18-month-old animals (n = 6). The HPAs are stated as mean ± SD.

Conclusion: The development and disappearance of the crimp pattern in connective tissue can provide an individual classification on the musculoskeletal apparatus. In contrary, the measurements on the helical pitch angle highlighted the rigidity of type I collagen molecule.

MECHANICAL CHARACTERIZATION OF MICRON-SIZED ERYTHROCYTE-DERIVED OPTICAL PARTICLES BY QUANTITATIVE PHASE IMAGING

T. Lu, J. Mac, and B. Anvari

Department of Bioengineering, University of California, Riverside

Introduction: We have developed constructs derived from erythrocytes that can be doped with various agents including the FDA-approved near infrared (NIR) dye, indocyanine green (ICG). We refer to these constructs as NIR erythrocyte-derived transducers (NETs). A particular feature of NETs is that their diameters can be tuned from micron to nano scale, making them potentially suitable for different biomedical imaging applications. A key question related to biodistribution of these particles relates to their mechanical characteristics. Herein, we quantify some of the mechanical properties of red blood cells (RBCs), hemoglobin-depleted erythrocyte ghosts (EGs), and micron-sized NETs (µNETs) using quantitative phase imaging.

Materials and Methods: EGs were fabricated by hypotonic treatment of RBCs. ICG at concentration of 25 µM in a hypotonic buffer was loaded into EGs to form µNETs. RBCs, EGs, and µNETs were seeded onto poly-D-lysine coated glass bottom dishes. After two hours of incubation at room temperature, samples were washed three times with phosphate buffer saline to remove loosely attached particles or cells. Quantitative phase maps of samples were then acquired using an interferometry platform developed in our laboratory [1]. Height (thickness) profiles of samples were determined from the phase maps through the relationship: $h = \lambda\varphi/(2\pi\Delta n)$ where h is the estimated height, φ is the phase at a given pixel, λ is the illumination wavelength (595 nm), and Δn is the refractive index mismatch between sample and medium. We determined the root mean square (RMS) of membrane height fluctuations as: $RMS = \frac{1}{N} \sum_{n=1}^{N}(h(t) - h_{mean})^2$ where $h(t)$ is the height at time t, h_{mean} is time-averaged height, and N is the number of image framed used in analysis. Membrane stiffness can be calculated from the RMS of membrane height fluctuations as $k_m = k_b T/(RMS^2)$ [2], where k_m is the membrane, k_b is Boltzmann's constant, and T is temperature.
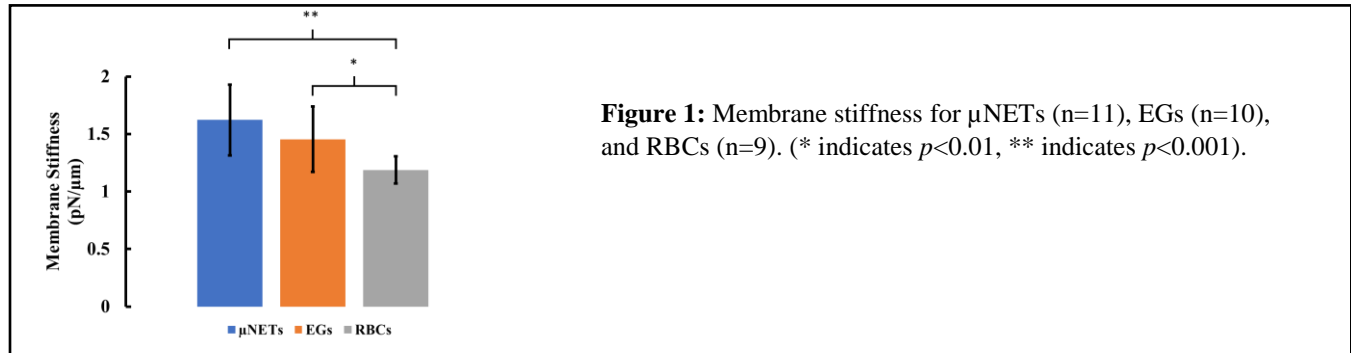
Figure 1: Membrane stiffness for µNETs (n=11), EGs (n=10), and RBCs (n=9). (* indicates $p<0.01$, ** indicates $p<0.001$).

Results and Discussion: Estimated fluctuations for µNETs, EGs and RBCs were ≈50 ± 5 nm, 53 ± 5 nm, and 59 ± 2 nm, respectively. Mean membrane stiffness values associated with µNETs, EG, and RBCs were 1.64 ± 0.31 pN/µm, 1.46 ± 0.28 pN/ µm, and 1.18 ± 0.12 pN/µm (Figure 1).

Conclusions: Our estimates of membrane stiffness based on the analysis of membrane fluctuations probed by quantitative phase imaging indicate that µNETs and EGs are less deformable than RBCs, suggesting that the fabrication of erythrocyte-derived particles can alter their mechanical properties from the native erythrocytes.

References:

1. M. Sarshar et al, Biomed. Opt. Express **7**, 1365–1374 (2016).

2. Y. Park et al. , Proc. Natl. Acad. Sci. **107**, 6731–6736 (2010).

PRESSURE INDUCED INJURY DETECTION SPATIAL FREQUENCY DOMAIN IMAGING

Chen, Jeffrey; Nguyen, Justin; Salas, Eddy; Torres, Damian; Thompson, Rachel
Mentors: Anthony J. Durkin, PhD., Robert H. Wilson, PhD., Rolf B. Saager, PhD., Rebecca Rowland
University of California, Irvine
wilsonrh@uci.edu

Introduction: Pressure ulcers are global health risk to hospitalized patients. This type of chronic wound typically forms in patients who are bedridden for extended periods of time resulting in constant pressure being applied over an area of skin [1]. Consequently, physiological factors including ischemia and waste accumulation lead to localized tissue necrosis [1]. Pathogenesis for these injuries originates beneath the skin where the ulcer develops and is generally detected through visual inspection only after the wound has progressed in stage. Visual inspection by a medical professional is the current clinical standard of care. In later stages, these wounds are significantly more expensive to treat due to the complex nature of care required [1]. Spatial Domain Frequency Imaging (SFDI) utilizes diffuse optics mechanics to extract quantitative, subsurface information from tissue allowing for early stage detection of pressure ulcers. We propose a portable, handheld device that employs SFDI for noninvasive detection of pressure ulcers in the subsurface of tissue. This device will image several millimeters beneath the skin and provide an accurate and quantifiable reading that will help healthcare providers determine the best option for treatment before the ulcer reaches the surface.

Materials and Methods: The imaging system's hardware consists of a grayscale camera, a projector, and four light sources at unique wavelengths (450, 550,700, and 850 nm). A computer using LabView performs the SFDI data acquisition protocol. The system works by individually shining a series of sinusoidal patterns at three different spatial frequencies (0-.2 mm^{-1}) and projecting them onto the tissue of interest. Each spatial frequency pattern will be projected at 3 phases (0, 120, and 240 degrees) and at the four separate wavelengths specified above, resulting in a total of 36 projected images. Each projected pattern will interact with the tissue and the backscattered light will be captured by the camera and processed after the image acquisition process. The processing algorithm will provide the user with tissue absorption and scattering coefficients. The tissue absorption coefficient can be mathematically modeled to provide tissue oxy-hemoglobin and deoxy-hemoglobin concentrations. Phantoms made of a mixture of liquid silicone, titanium oxide (to provide scattering), and India ink dye (to mimic absorption) will provide a method of validation of optical properties
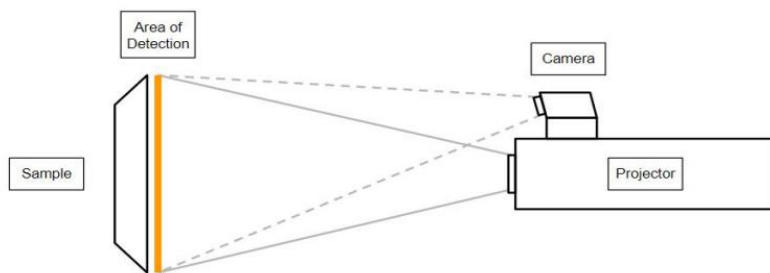
Figure 1. SFDI instrumentation for pressure ulcer imaging. Light is sent from each of 4 LEDs through a projector to send sinusoidal patterns onto the sample. Backscattered light creates images that are captured by the camera.

Results and Discussion: Currently, we have already accomplished many of our milestones. We have completed the Lab View acquisition code along with the MatLab processing and gamma correction codes; additionally, we have 3D printed camera and projector case. Moving forward, we have the hardware development and validation testing. The hardware requires the projector to be able to penetrate the epidermis and the dermis. By having three discrete wavelengths from three LEDs in the near infrared, we will be able to measure the subsurface tissue volumes and capture images of the superficial tissue. Silicone phantoms previously mentioned will be used to validate the effectiveness of visible light to interrogate superficial layers and near infrared to probe subsurface tissue layers. At the moment, we have acquired and demodulated images of human tissue. We are currently working on gathering the reflectance and scattering data.

Conclusions: Pairing SFDI with the materials used allows for a feasible approach to this project.

References:

Yafi, Amr., A.Y., Laser Surg. Med., 2017, 49:827-834

SEGMENTATION BASED DATA AUGMENTATION IN DEEP NETWORKS FOR MAGNIFICATION INVARIANT BREAST CANCER DETECTION

[1]Padmaja Jonnalagedda, [2]Daniel Schmolze, [1,3]Bir Bhanu

[1]Department of Electrical and Computer Engineering, University of California, Riverside
[2]Department of Pathology, City of Hope National Medical Center, Duarte CA
[3]Department of Bioengineering, University of California, Riverside

Contact: *sjonn002@ucr.edu*

Introduction: Histopathological images are the most trusted for breast cancer diagnosis compared to all other medical imaging techniques. Despite the advances in digital imaging techniques, a lot of the diagnosis is still performed manually by pathologists. The task is complicated and tedious, with pathologists having to analyze the same tissue at various magnifications for an accurate diagnosis. Furthermore, there are subtle distinctions among breast cancer images in texture, morphology etc., making cancer detection a complex task. Many researchers have proposed approaches for automatic breast cancer detection; however, their methods and results depend on the magnification at which the images were taken. To mitigate these issues, the authors propose a quantitative automated approach to detect cancer, independent of the image magnification level.

Materials and methods: The proposed method utilizes ResNet50, a deep learning architecture, for detection of cancer using the BreaKHis database [1]. It consists of 2480 benign and 5429 malignant tumor images (460x700 pixels, RGB images) at 4 magnification levels from 82 patients. In histopathology images, nuclei and surrounding area are indicators of tumor and its type. The proposed method leverages the location of these indicators. The images in the training set are subjected to clustering using a mixture of Gaussian models with three components. An image displaying one of the clusters contains only nuclei, called the *intermediate image*. In this intermediate image, a patch slides to find the area with the maximum number of nuclei. The patch size used here is 230x350 with 50% overlap. The patch size is chosen to preserve aspect ratio and obtain 2X magnified final image. From the original image, this area of interest is then extracted, resized to the size of original image and added to the training set. This has two advantages: (i) it balances the classes in training set by adding more images to the benign set, (ii) it adds randomly magnified images (zoomed images) to make training of magnification invariant model more robust. The images are divided into 70% train, 15% validation and 15% test sets (61 patients in training/validation, 21 for testing). The ResNet50 model was run on Python 3.6 and trained on an NVIDIA GeForce GTX1080 GPU.

Results and discussion: The performance of the proposed method is compared to a current method as well as random patch zooming to evaluate the impact of using the more informative patches to augment the training set. The accuracy of the detection method by Byramoglu et. al. [2] is 83%. The accuracy with the proposed method is $92.7 \pm 1.3\%$, with sensitivity $94.6 \pm 1.4\%$ and specificity $91.2 \pm 1.2\%$. Compared to this, using random patches gives as accuracy of $89.9 \pm 1.8\%$ with sensitivity $94.3 \pm 1.4\%$ and specificity $88.3 \pm 1.1\%$. The training time is 60-70 minutes and testing time per image is 0.25 seconds. These results are obtained for 10-fold cross validation testing.
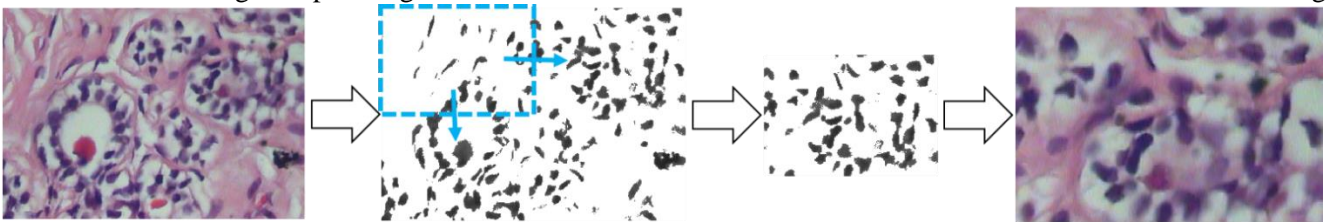

Figure 1: Original image → Intermediate image with sliding patch → Patch (mask) with most nuclei → Resized patch added to train set

Conclusions: The proposed approach provides better performance in magnification independent classification. Gaussian Mixture Model brings attention to areas with tumor nuclei that carry more information in tumor detection than data augmentation using random cropped patches from tissue images.

References:

[1] Spanhol, F., Oliveira, L., Petitjean, C. & Heutte, L. A dataset for breast cancer histopathological image classification. IEEE Transactions on Biomedical Engineering (TBME) 63(7), 1455–1462 (2016).

[2] Bayramoglu, N., Juho K., and Janne H. "Deep learning for magnification independent breast cancer histopathology image classification." In *International Conference on Pattern Recognition (ICPR)*, pp. 2440-2445, 2016.

THz and mm-Wave Based Imaging of *Ex Vivo* Porcine Corneas and Preliminary Human Trials

[1]A. Braganza, [2]S. Sung, [3]Z. Taylor, and [4]W. Grundfest

[4]Department of Bioengineering, University of California, Los Angeles, CA

Contact: *aabraganza@ucla.edu, junsung@ucla.edu*

Introduction: Terahertz (THz) wavelength radiation has unique properties for biomedical sensing and imaging. The THz band has both significant dielectric interactions with water as well as low photon energies while providing sufficient resolution limits for imaging of living tissue. We developed a novel THz imaging device for evaluation of tissue edema in *in vivo* human cornea. The imaging system acquires a map of the corneal surface with an acute sensitivity for corneal tissue water content (CTWC). CTWC is a critical measurement in full and partial corneal transplantation as well as corneal dystrophies that affect visual acuity of corneal stroma. We have previously demonstrated the abilities of this imaging technique by imaging *in vivo* rabbit corneas [1].

We designed and performed *ex vivo* porcine cornea imaging study. We aimed to detect changes in hydration over time and calibrate the THz sensing algorithm as well as to propose a metric to compare to for future clinical trials. In addition, we imaged four healthy human subjects demonstrated healthy CTWC profiles, which will later be used for comparison studies with the disease group.

Materials and Methods: The block-diagram and CAD rendering of the system are shown in *Figure 1.1* and *1.2* [2]. The imaging system acquired normal-incidence reflection image of the cornea using a novel scanning mechanism described in [2]. The system incorporated simultaneous 100 GHz and 525 GHz measurements that reached different depth into the cornea. *ex vivo* cornea specimens are resected from the unburnt, freshly harvested (< 72 hrs) porcine eyes. Specimens were weighed before and after the imaging to measure changes in water content. Images and weight measurements are acquired every five minutes.
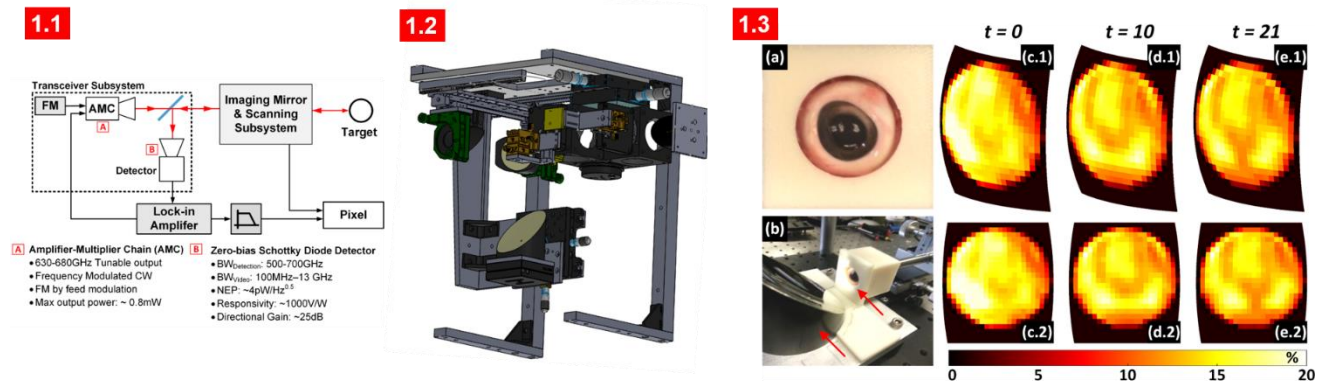
Figure 1 Study Overview: *1.1) Block diagram of system components 1.2) CAD Model of imaging system 1.3ab) Photographs of Porcine eye imaging setup 1.3c) Post processing images of the eye over time*

Results and Discussion: By comparing the images obtained from the system with the data regarding hydration we were able to see a correlation between the tissue water content and our images. The reflectivity vs lost water mass curve experimentally verified corneal electromagnetic properties [1]. The images shown in *1.3c* demonstrate clear changes over time based on hydration changes as the tissue dried.

Conclusions: Our experiments demonstrate a successful measurement of minute water content changes. Future works will focus on resolving absolute water content in healthy and diseased corneas. This system will soon be used in human clinical trials and we will assess the ability of this system to assist in diagnosing and monitoring various corneal diseases.

References

1. 1.Taylor, Zachary D., et al. "THz and mm-wave sensing of corneal tissue water content: in vivo sensing and imaging results." *IEEE transactions on terahertz science and technology* 5.2 (2015): 184-196.

2. Sung, Shijun, et al. "Optical System Design for Noncontact, Normal Incidence, THz Imaging of in vivo Human Cornea." *IEEE transactions on terahertz science and technology* 8.1 (2018): 1-12.

DISTINGUISHING STEM-LIKE TUMOR-INITIATING CELLS IN MALIGNANT GLIOMA BY PHASOR FLUORESCENCE LIFETIME IMAGING

[1]A.L. Trinh, [1]H. Chen, [2]Y. Chen, [3]Y. Hu, [3]Z. Li, [4]E.R. Siegel, [3]M.E. Linskey, [2]P.H. Wang, [3]Y.-H. Zhou, and [1]M.A. Digman

[1]Department of Biomedical Engineering, University of California, Irvine, CA
[2]UC Irvine Diabetes Center and Department of Medicine, University of California, Irvine, CA
[3]UC Irvine Brain Tumor Laboratory and Department of Surgery, University of California, Irvine, CA
[4]Department of Biostatistics, University of Arkansas for Medical Sciences, Little Rock, AR
Contact: *mdigman@uci.edu*

Introduction: Intra-tumoral heterogeneity is associated with therapeutic resistance of cancer. In particular, stem-like tumor initiating cell (STIC) subpopulations within malignant gliomas tumors have been shown to be responsible for treatment resistance and tumor recurrence. Therefore, there exists a need to monitor functional tumor subpopulations during treatment and cancer progression. Reduced nicotinamide adenine dinucleotide (NADH) is a metabolic coenzyme essential in cellular respiration. Fluorescence lifetime imaging microscopy (FLIM) of NADH has been demonstrated to be a powerful label-free indicator for inferring metabolic states of living cells. In this study, FLIM of NADH was applied to distinguish between malignant glioma subpopulations of STIC and tumor mass-forming cells (TMC). In addition, changes in the fluorescence lifetimes of NADH were compared to cellular respiration (oxidative phosphorylation and glycolysis), EGFR expression, and cell-growth rates.

Materials and Methods: Human glioblastoma-derived cell line U251 were enriched for STIC and TMC subpopulations by established cell culture conditions. U251 STIC subpopulations were cultured in neurosphere conditions, DMEM/F12 supplemented with EGF (20ng/mL), FGF (10ng/mL), and B27 (1%). U251 TMC subpopulations were cultured in serum-containing conditions, DMEM/F12 supplemented with FBS (5%). Enriched conditions were imaged by FLIM of NADH on a Zeiss LSM 710 microscope with incubation at 37°C and 5% CO_2. NADH was excited by an 80-MHz titanium:sapphire Mai Tai laser at 740nm. The NADH emission was collected by a 460/80 bandpass filter and a photomultiplier tube. FLIM data were acquired by an A320 FastFLIM box and analyzed by SimFCS software.

Results and Discussion: FLIM of NADH measured an increase in protein bound NADH in STIC enriched U251 cells. This was observed in both in vitro models and in xenograft models. TMC and STIC subpopulations were labeled with green and red fluorescent proteins, respectively. Labeled cells were mixed and implanted in a mouse intracranial xenograft model. Distinction by FLIM of NADH correlated with fluorescent protein labels, Figure 1. In addition, changes in NADH lifetimes correlated with cell growth rate.

Figure 1: Confocal fluorescence image of tumor xenograft (left) and the same section imaged by FLIM (right) with NADH fluorescence lifetime pseudo-colored. A higher fraction of bound NADH is represented as red, and free NADH is represented as white.
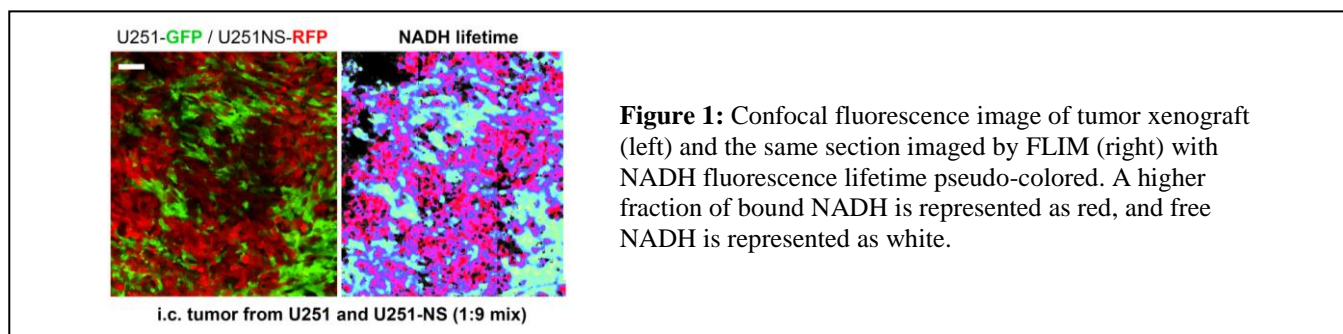
Conclusions: FLIM of NADH was able to distinguish STIC from TMC subpopulations in glioma tumors. Future studies can apply FLIM to monitor dynamic changes in tumor subpopulations during treatment.

References (optional):
Trinh, A. L., Chen, H., Chen, Y., Hu, Y., Li, Z., Siegel, E. R., Linskey, M. E., Wang, P. H., Digman, M. A., and Zhou, Y.-H. (2017). Tracking Functional Tumor Cell Subpopulations of Malignant Glioma by Phasor Fluorescence Lifetime Imaging Microscopy of NADH. *Cancers*, *9*(12), 168. http://doi.org/10.3390/cancers9120168

BIOENGINEERED OSTEOGENIC PROTEIN NELL-1 RESCUES SPACEFLIGHT-INDUCED BONE LOSS

[1]J.H. Kwak, [1]J. Shi, [1]P. Ha, [2]Y. Zhang, [1]H.C. Pan, [1]J.K. Kim, [1]E. Chen, [1]X. Zhang, [1,3]K. Ting, [2,3]B.M. Wu, [3,4]C. Soo

[1]Section of Orthodontics, School of Dentistry, University of California, Los Angeles, CA
[2]Department of Bioengineering, School of Engineering, University of California, Los Angeles, CA
[3]Department of Orthopaedic Surgery, University of California, Los Angeles, CA

[4]Division of Plastic and Reconstructive Surgery, University of California, Los Angeles, CA
Contact: *jkwak@dentistry.ucla.edu*

Introduction: NELL-1 is an osteogenic protein discovered by the UCLA Dentistry and Medicine scientists in prematurely fused cranial sutural bones in craniosynostosis patients. In collaboration with the UCLA Bioengineering scientists, NELL-1 has recently been engineered to enhance the pharmacokinetics to be tested as a systemic therapy to rescue spaceflight-induced osteoporosis (OP). Specifically, NELL-1 was PEGylated to enhance the *in vivo* half-life and was further engineered by conjugating it with inactive bisphosphonate (BP) as a bone-seeking molecule (hence named BP-NELL-PEG). The current project is funded by and collaborated with the Center for the Advancement of Science in Space (CASIS) and NASA, and is entitled the Rodent Research 5 (RR-5) mission. The mission signifies America's first live-return of rodents, the World's first live-return of drug treated rodents and first recovery model where the rodents that were returned to Earth were housed at UCLA for an additional month to continue therapy. The truly multi-centered and multi-disciplinary project has been successfully completed in late 2017 with all animals returning alive, healthy and happy and is currently in the process of data analysis. The ultimate objectives and applications of this project is in two folds. If proven successful in reversing spaceflight-induced bone loss, NELL-1-based therapy will demonstrate the potential to be used for space travelers, and to combat extreme cases of OP complicated by fracture and disuse atrophy on Earth.

Materials and Methods: 8 months old skeletally mature BALB/c female mice were used. 40 mice were flown to space and housed onboard the International Space Station (ISS) for 2 months receiving BP-NELL-PEG therapy or PBS control intraperitoneally every 2 weeks. Ground controls (n=40) were housed at the Kennedy Space Center (KSC), Florida, and treated the same. Mid-way through the experiment (after 2 injections), half of the Flight and Ground groups were returned live to UCLA to continue therapy for 2 additional biweekly injections. At 8 weeks post-treatment, all animals were euthanized for first-ever comparison of full-flight, live-return, and ground control groups treated with BP-NELL-PEG and control injections. Behavioral tests, DXA densitometer, microCT, RNA analysis, histology, immunohistochemistry, and FEM analysis were performed.

Results and Discussion: Following is partial data currently available. 1) Motor function analysis via Rota rod test showed that 4 weeks of spaceflight made the mice 20% weaker than ground controls, and they only recovered by 50% after spending 4 weeks on Earth. 2) DXA and microCT data showed that (a) spaceflight significantly reduced bone volume and density and (b) BP-NELL-PEG treatment in both ground and flight groups resulted in significant increases in all parameters. 3) Flow cytometry on BMSCs showed that microgravity is an inhibitor of stem cell proliferation. 4) ALP and TRAP staining on BMSCs showed that spaceflight significantly reduces OB differentiation and therapy significantly increases the differentiation of both OB and OC, but more of OB.
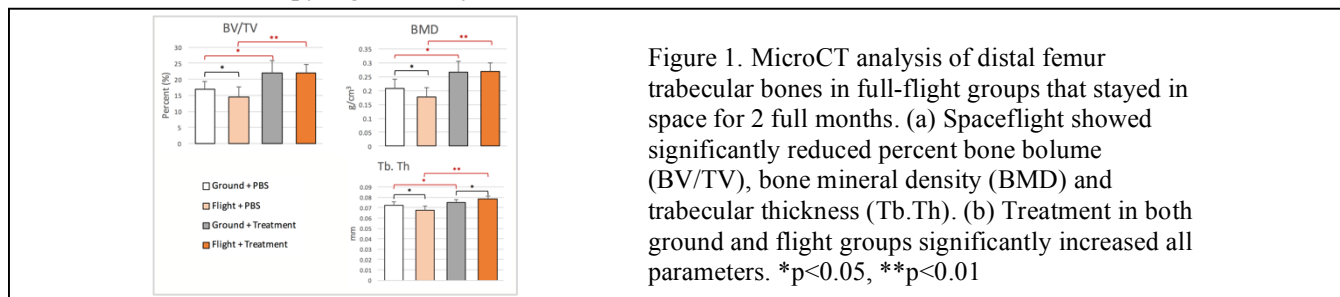

Figure 1. MicroCT analysis of distal femur trabecular bones in full-flight groups that stayed in space for 2 full months. (a) Spaceflight showed significantly reduced percent bone bolume (BV/TV), bone mineral density (BMD) and trabecular thickness (Tb.Th). (b) Treatment in both ground and flight groups significantly increased all parameters. *p<0.05, **p<0.01

Conclusions: NELL-1-based therapy (BP-NELL-PEG) has successfully reversed spaceflight-induced bone loss in mice, and demonstrated the potential to be used for long-duration space travelers and for patients with extreme cases of OP complicated by fracture and disuse atrophy on Earth.

CROSSLINKED SALMONELLA FLAGELLA AS A STABILIZED VACCINE SCAFFOLD

[1]C.M. Gries, [2]R.R. Mohan, [2]D. Morikis, and [1]D.D. Lo
[1]Division of Biomedical Sciences, School of Medicine, University of California, Riverside
[2]Department of Bioengineering, University of California, Riverside
Contact: casey.gries@medsch.ucr.edu

Introduction: Engineered protein adjuvants and vaccines constructed within the context of immune function are highly effective and can confer protection to a broad spectrum of human diseases. The bacterial flagellin protein is a proven vaccine adjuvant owing to both its TLR5 and inflammasome activation and, unlike other TLR agonists, production of a mixed Th1 and Th2 immune response. Additionally, flagellin can be engineered to contain multiple functional domains, as we have previously produced an effective hybrid protein in which the flexible (D3) domain of *Salmonella enterica* serovar Typhimurium flagellin (FliC) was replaced with a Dengue virus envelope protein[1]. Polymerized filaments of this conjugated flagellin hybrid provided a potent T helper cell-independent antibody response via activation of antigen receptors on B cells. In the current study we aim to produce and test a covalently stabilized polymerized flagella filament, providing additional immune efficacy through stabilized filaments, as well as stabilization for long term storage in lyophilized formulations.

Material and Methods: Modeling of FliC filament structure was performed using modeling software Chimera and Modeller. The *fliC* gene amplified from *S. enterica* Typhimurium IR715 was cloned into the Gateway® vector pENTR3C (Invitrogen). Primers encoding the desired SNPs were designed and amplified divergently from the sites of interest. Resulting flagellin constructs were expressed in the non-motile *S. enterica* Typhimurium Δ*fliC fljB*::Mu*d*Cm strain and stained with Alexa Fluor 488 carboxylic acid TFP ester (Invitrogen) for confocal imaging. Motility assays were performed on 0.5% agarose LB plates. Intact flagella was extracted from overnight cultures with vortex shearing and subsequent acetone precipitation. Centrifugation through 100K MWCO filters provided separation of monomeric vs. oligomeric filaments. Native- and SDS-PAGE (BioRad) was performed with equal amounts of flagellin according to established methods and was assessed with Imperial Protein Stain (Thermo Scientific). Caco-2 cells were cultured according to standard methods and luciferase expression from a NFkB reporter vector (Qiagen) was assessed using a Dual-Glo assay kit (Promega).

Results and Discussion: Computational modeling of the *S. enterica* flagellar filament identified a trio of candidate amino acid pairs for introducing intermolecular disulfide bonds. Cysteine replacements were performed pairwise, generating FliC variants FliC^{N5C,E454C}, FliC^{N38C,N430C} and FliC^{Q62C,Q97C}. Expressed in a *S. enterica* Typhimurium Δ*fliC* strain, each construct resulted in production of identifiable flagella, however microscopic analysis demonstrated structural abnormalities in FliC^{N5C,E454C}, and soft agar motility assays revealed that FliC^{N38C,N430C} and FliC^{Q62C,Q97C} were completely non-motility while FliC^{N5C,E454C} retained ~50% normal motility. To test for intermolecular crosslinking, SDS-PAGE demonstrated that, unlike wild-type, a large portion of the cysteine replacement filaments remained oligomerized, and were only depolymerized under reducing conditions. Finally, to examine the ability of crosslinked FliC filaments to induce an immune response, Caco-2 intestinal epithelial cells transfected with an NFkB reporter were treated with extracted flagellar filaments or monomers. Interestingly, monomeric FliC^{Q62C,Q97C} and FliC^{N5C,E454C} had significantly reduced NFkB induction, but the filaments retained nearly full induction, suggesting that the immune response to flagellar filaments may be unique from the monomeric protein.

Conclusions: This engineered filament will provide adjuvant activity, polymeric stimulation of immunity, and covalent stabilization, combined with an antigen to provide a potent and effective vaccine. Moreover, the advantages of covalently crosslinked FliC filaments apply not only to *in vivo* stability and immunogenic potency, but also to stability in formulation and long-term storage, a particular challenge for biologicals.

References:
1. Bennett KM, *et al*., Hybrid flagellin as a T cell independent vaccine scaffold. BMC Biotechnol. 2015;15:71.

RAPID DIGITAL LIGHT PROCESSING 3D BIOPRINTING OF HUMAN TISSUES WITH TUNABLE DECELLULARIZED EXTRACELLULAR MATRIX BIOINKS

[1]C. Yu, [2]X. Ma, [1]W. Zhu, [3]Z. Li, [4]P. Wang, [1]K. Miller, [5]J. Stupin, [5]A. Koreleva-Maharajh, [5]A. Hairabedian, and [1,2,4,5]S. Chen

[1]Department of NanoEngineering, University of California, San Diego, CA.
[2] Department of Bioengineering, University of California, San Diego, CA
[3]Department of Medicine, Keck School of Medicine of University of Southern California, CA
[4]Materials Science and Engineering Program, University of California, San Diego, CA
[5]Chemical Engineering Program, University of California, San Diego, CA
Contact: *chen168@eng.ucsd.edu*

Introduction: With the recent translation of decellularized extracellular matrices (dECMs) into bioinks to provide a biochemically complex microenvironment in 3D bioprinted tissues, their inherent mechanical weakness and limited printability has posed challenges regarding low resolution and structural fidelity. Here, we developed a novel approach to rapidly fabricate dECM-based tissue constructs possessing micron scale architectures using a custom digital light processing (DLP) 3D bioprinter. Moreover, cell-laden 3D dECM heart, liver, and kidney tissue constructs were 3D printed to provide a biomimetic microenvironment for the phenotypic maturation of human induced pluripotent stem cell (hiPSC)-derived cardiomyocytes (hiPSC-CMs), hepatocytes (hiPSC-Heps), and renal proximal tubule epithelial cells (hiPSC-RTPECs), respectively.

Materials and Methods: dECM bioinks were prepared from solubilized porcine decellularized heart, liver, or kidney tissues mixed with photocrosslinkable gelatin methacrylate (GelMA) or polyethylene glycol diacrylate (PEGDA). Characterization studies were performed to assess the physical stability, resolution, and mechanical properties of the printed tissue constructs. Viability of hiPSC-CMs, hiPSC-Heps, and hiPSC-RTPECs in tissue-matched constructs was assessed and phenotypic maturation was evaluated using immunohistochemical staining of tissue-specific markers and gene expression analysis compared to collagen I controls over 1 week in culture.

Results and Discussion: The bioprinted tissue constructs were physically robust in culture with micron level feature size and tunable modulus. Further, tissue-matched dECM bioinks maintained high viability of hiPSC-derived cells over 1 week (**Fig. 1**). Notably, higher expression of tissue-specific markers in hiPSC-derived cells cultured in their tissue-matched dECM bioinks compared to collagen I controls was observed. The patterned dECM bioinks also enabled cells to assume biomimetic organization into striated, lobular, and lumen-like structures predesigned for each of the heart, liver, and kidney tissue constructs, respectively.

Figure 1: Representative images of printed dECM-based tissue constructs. Digital patterns designed for each of the (a) heart, (b) liver, and (c) kidney constructs. Live/Dead™ viability staining of hiPSC-CMs, hiPSC-Heps, and hiPSC-RTPECs cultured in each of the tissue-matched dECM-based constructs. Scale bar = 1 mm.
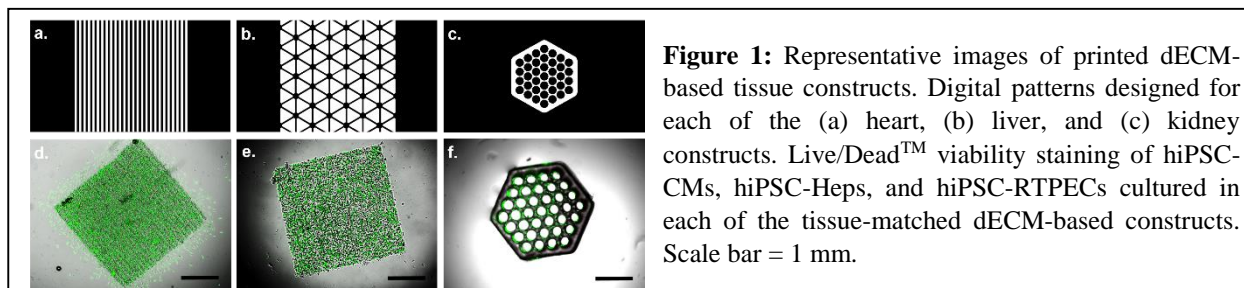
Conclusions: By applying a light-based approach to rapidly bioprint human scale tissues with next-generation dECM bioinks, the accurate design of personalized biomimetic tissues can be realized for various applications in tissue engineering, biology, regenerative medicine, and diagnostics.

EPIGENETIC CONSEQUENCES OF BIOMATERIAL DESIGN ON MACROPHAGE INFLAMMATORY RESPONSE

Zachary Reitz, Praveen K. Veerasubramanian, Hamza Atcha, Thuy Luu, Wendy Liu, Timothy L. Downing
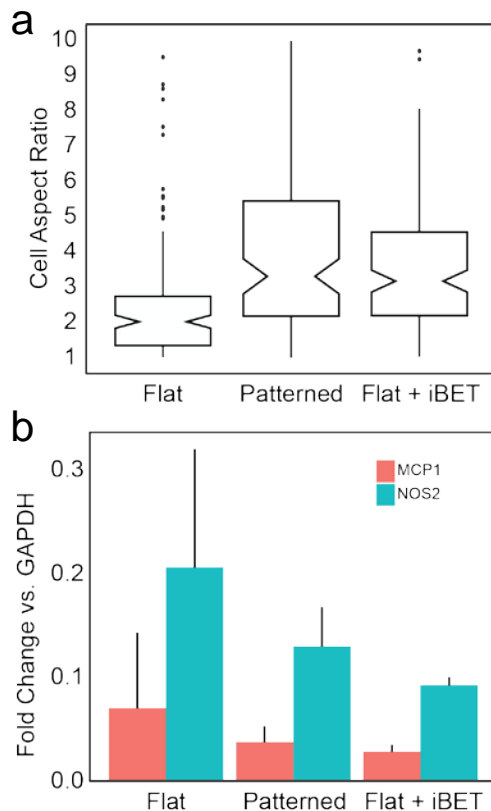Department of Biomedical Engineering, University of California, Irvine, CA
Contact: tim.downing@uci.edu

Introduction: Current evidence suggests macrophages play a leading role in regulating the integration of biomaterials after implantation by modulating the inflammatory and wound healing responses. Additionally, previous studies have shown microscale surface topography can directly influence macrophage behavioral patterns and consequently implant viability. However, the mechanisms by which these biophysical cues direct macrophage fate are not fully known. Furthermore, epigenetic mechanisms, which are known to induce transcriptional changes in macrophages during polarization, may directly facilitate this topography-induced regulatory relationship. Understanding the biophysical mechanisms at play will be key to improving implant material biocompatibility.

Materials and Methods: For this study we rely on murine bone marrow derived macrophages (BMDMs) generated through marrow extraction and a seven-day differentiation process. Afterwards, these cells are seeded atop either a uniform or micropatterned fibronectin surface, generated using microcontact printing. After a 2-hour adhesion period, the cells were stimulated with lipopolysaccharide (LPS) and interferon-γ (INFγ) at 1ng/ml each for 2 or 16 hours. Additionally, cells were treated 1 hour before and during stimulation with either sodium butyrate, a histone deacetylase (HDAC) inhibitor, or a BET inhibitor, which blocks BRD protein binding to acetylated histone tails. Morphological changes were characterized using phase-contrast microscopy. Transcriptional changes were measured using qRT-PCR and a Nanostring™ inflammation gene panel. Protein level responses were observed using immunofluorescence staining, western blotting, and ELISA.

Results & Discussion: Here we show a substantial decrease in key inflammatory genes MCP1 and NOS2, in stimulated macrophages at 2 and 16 hours, when cultured on the micropatterned versus uniform surfaces. The most effective surface geometry to elicit this change comprised of 5µm fibronectin stripes with 5µm PEG (non-adherent) spacings. The Nanostring™ panel confirmed these results and, with the help of gene set enrichment analysis tools, identified IL-6 as a potential regulator of the observed change. Additionally, MAPKAPK2, a gene critical to macrophage directed wound healing, appeared to be transcriptionally enhanced on the patterned surfaces at both time points. Furthermore, existing ChIP-seq datasets suggest LPS stimulation and sometimes BET inhibitors change histone acetylation levels at the transcriptional start sites of IL-6, related genes, and MAPKAPK2.

Figure 1: (A) Aspect ratio of BMDMs treated with 1ng/ml LPS & INFγ on a flat surface, with or without iBET, or on a 5x5µm patterned surface. (B) Expression ratio of MCP1 or NOS2 over GAPDH for the same conditions using qRT-PCR.

Conclusions: Our data suggests a possible epigenetic link between microscale surface geometries and inflammatory macrophage activation. Given that macrophages are key in determining modes of inflammation and wound healing, our findings have broad implications concerning innate immunity and biomaterial design. Furthermore, understanding the functional changes described here has the potential to elucidate the role macrophages play in various inflammatory disease states. Additionally, these findings may allow for macrophage activation to be purposefully governed through pharmaceutical or biophysical modulation.

ANTIMICROBIAL EFFECTS OF HYDROXYAPATITE COATED MAGNESIUM IMPLANTS AGAINST S. AUREUS

R. Chung [1], N.Y Nguyen [2], and H. Liu[2,3]

[1]Department of Biology, University of California, Riverside, CA

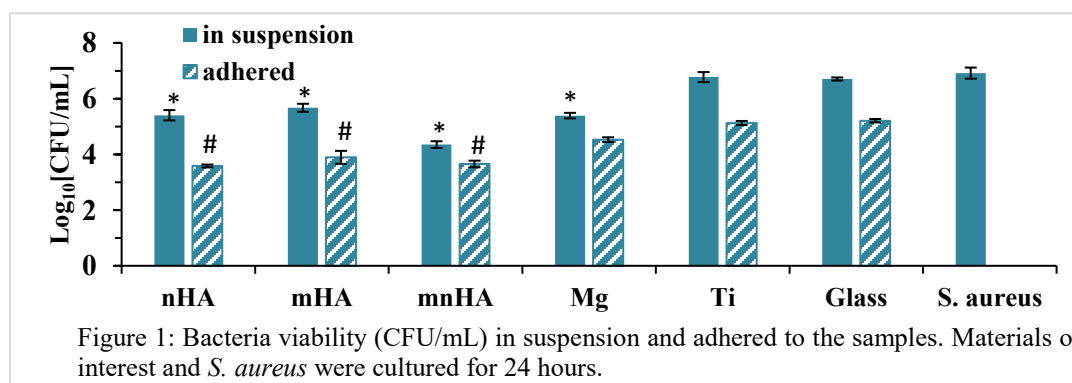[2]Department of Microbiology and Plant Pathology, University of California, Riverside, CA

[3]Department of Bioengineering, University of California, Riverside, CA

Contact: huinanliu@engr.ucr.edu

Introduction: Bacteria infections pose complications in orthopedic implants with high cost. When bacteria adhered to the implant, it can lead to biofilm formation, therefore leading to secondary surgery which can increase the cost. When biofilm forms, it is almost impossible to treat. Therefore, if we can use a degradable material that can prevent bacteria adhesion, no biofilm can form and no infection will occur. Currently, titanium (Ti) and its alloys are widely used, but there are recent reports stating that *Staphylococcus aureus* (*S. aureus*) can adhere to Ti. Magnesium (Mg) could be an alternative solution due to its antimicrobial property. Magnesium have mechanical properties and density that are more similar to cortical bone than Ti. However, Mg have fast degradation properties, it is necessary to have a coating to slow down the degradation for use in implant applications.

Materials and Methods: This study tests the antimicrobial properties of magnesium (Mg) coated with micro-hydroxyapatite (mHA), nano-hydroxyapatite (nHA), and a mixture of micro and nano hydroxyapatite (mnHA) against *Staphylococcus aureus* (*S. aureus*). Experimental controls were Mg, titanium, glass and *S. aureus*. The materials were cultured with *S. aureus* for 24 hours in revised simulated body fluid with 10% fetal bovine serum. After 24 hours of culture, solutions were collected and analyzed by quantification of colony forming units (CFU) with pH and ion concentration measurements. One set of materials were washed and sonicated to quantify the bacteria that adhered to the samples, and another set was fixed with 10% glutaraldehyde for imaging by a scanning electron microscope.

Results and Discussion: The resulting pH of coated and uncoated Mg displayed values close to 10, however, the Ti, glass, and broth controls fluctuated around 8.2. The difference in pH in the uncoated and coated Mg could possibly be attributed to Mg degradation. All the coated Mg, notably the mnHA and Mg had significantly lower CFU/ml in suspension than the control groups of Ti, glass and *S. aureus* (Figure 1). Additionally, coated Mg groups also had significantly less bacterial adherence to the samples. Notably the mnHA had the least *S. aureus* adhered to the sample. This could be because the mixture of the two nano and micro hydroxyapatite that caused the change in surface roughness, therefore inhibiting the bacteria adhesion.

Figure 1: Bacteria viability (CFU/mL) in suspension and adhered to the samples. Materials of interest and *S. aureus* were cultured for 24 hours.

Conclusions: All of the coated and uncoated Mg samples exhibited bactericidal effects against *S. aureus* in suspension, and prevented adherence compared to Ti and glass. Furthermore, Mg coated in mnHA displayed enhanced bactericidal effects compared to all other groups such as mHA, nHA, Mg, Ti, and glass. Mg coated with HA demonstrated promising results in antibacterial activity in both the inhibition of bacterial growth and bacterial adherence for orthopedic applications.

# PREDICTING DIRECT CEREBRAL DELIVERY OF NEUREGULIN-1 USING AN OSMOTIC TRANSPORT DEVICE TO REDUCE EDEMA

[1]J. S. Yang, B. D. Ford[2] and V. G. J. Rodgers[1]

[1]Department of Bioengineering, University of California Riverside, CA

[2]Department of Biomedical Sciences, University of California Riverside, CA

Contact: jyang033@ucr.edu

Introduction: Cerebral edema is a severe pathological state that involves an abnormal accumulation of fluid within the extracellular and intracellular space of the brain. It accounts for up to half of the mortality in all victims of traumatic brain injury (TBI) [1]. Current treatments such as decompressive hemicraniectomy can only reduce intracranial pressure. Our lab has developed a scalable osmotic transport device (OTD) that has been demonstrated to reduce cerebral edema following severe TBI and resulted in improved neurological outcomes in the mouse model [2]. We plan to use the device to deliver the neurorestorative compound neuregulin-1 (NRG-1) to reach critical tissue near the site of injury (Figure 1).
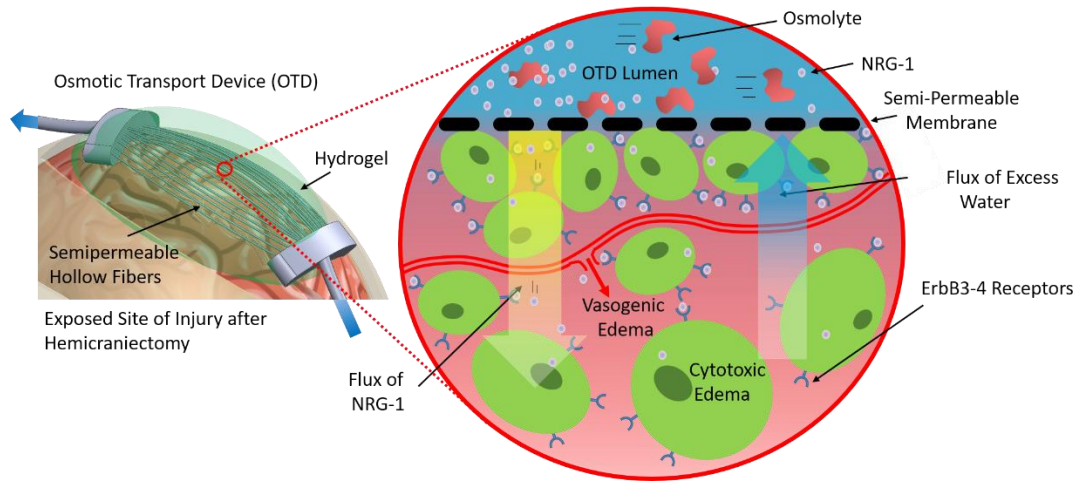
Figure 1. OTD eliminates edema and provide direct delivery of NRG-1 to the brain via diffusion.

In this work we determined a mathematical expression to predict the maximum therapeutic depth for various NRG-1 dosing. NRG-1 acts through the ErbB tyrosine kinase receptors which localize to the plasma membrane of various types of cells. ErbB molecules must dimerize to transduce signals across the plasma membrane [3]. NRG-1 transport in the tissue can be characterized by reaction-diffusion process with ligand-receptor binding kinetics.

Mathematical Methods: The governing equation is a 1-D Fickian diffusion for dilute solutions. The reactions in describe the net molar rate of formation of the ligand-receptor binding kinetics of NRG-1 and ErbB receptors.

Results and Discussion: The solution to the following differential equation allows us to interpret the time constant for NRG-1 delivery $\frac{\partial C_L}{\partial t} = D_L\left(\frac{\partial^2 C_L}{\partial x^2}\right) + R_L$ where $R_L = \left[2d_1\left(N_T - N_r - \left(\frac{1}{K_4}\right)N_r^2 - \left(\frac{C_L}{2K_2K_4}\right)N_r^2 - \left(\frac{C_L}{2K_2K_4K_i}\right)N_r^2 - \left(\frac{C_L^2}{K_2K_3K_4K_i}\right)N_r^2\right) - 2k_1C_LN_r\right] + \left[2d_2\left(N_T - N_r - \left(\frac{C_L}{K_1}\right)N_r - \left(\frac{1}{K_4}\right)N_r^2 - \left(\frac{C_L}{2K_2K_4K_i}\right)N_r^2 - \left(\frac{C_L^2}{K_2K_3K_4K_i}\right)N_r^2\right) - k_2C_L\left(N_T - N_r - \left(\frac{C_L}{K_1}\right)N_r - \left(\frac{C_L}{2K_2K_4}\right)N_r^2 - \left(\frac{C_L}{2K_2K_4K_i}\right)N_r^2 - \left(\frac{C_L^2}{K_2K_3K_4K_i}\right)N_r^2\right)\right] + \left[d_3\left(N_T - N_r - \left(\frac{C_L}{K_1}\right)N_r - \left(\frac{1}{K_4}\right)N_r^2 - \left(\frac{C_L}{2K_2K_4}\right)N_r^2 - \left(\frac{C_L}{2K_2K_4K_i}\right)N_r^2\right) - 2k_3N_T - N_r - \left(\frac{C_L}{K_1}\right)N_r - \left(\frac{1}{K_4}\right)N_r^2 - \left(\frac{C_L}{2K_2K_4}\right)N_r^2 - \left(\frac{C_L^2}{K_2K_3K_4K_i}\right)N_r^2\right]$, $N_r = f(C_L)$, and $C_L = C_{L_0} - \left(\frac{n}{N_A}\right)\left(N_T - N_r - \left(\frac{1}{K_4}\right)N_r^2\right)$.

Conclusions: This model provides the potential to express delivery of NRG-1 to the brain tissue via the OTD. Future development of the model will need to take the rate of endocytosis of the receptors and ligands into consideration.

[1] Donkin JJ, Vink R (2010). Current Opinion in Neurology, 23(3), 293-299.

[2] McBride DW, *et al.* (2014) *J. Neurotrauma* 31:1948-1954.

[3] Hiroshima M., *et al.* (2012) Proc Nat Acad Sci109(35), 13984-13989.

HYDRODYNAMIC MICRO-VORTICES IN DROPLET-BASED MICROFLUIDICS: TOWARD HIGH EFFICIENT SINGLE CELL ENCAPSULATION AND SELECTIVE RELEASING

[1,2]M.Aghaamoo, [1,2]G.K. Kurup, [1,2]A.P. Lee

[1]Department of Biomedical Engineering, University of California, Irvine, CA

[2] Center for Advanced Design & Manufacturing of Integrated Microfluidics (CADMIM), University of California, Irvine, USA

Contact: *maghaamo@uci.edu*

Introduction: Single cell analysis is an essential tool that benefits variety of fields ranging from fundamental biology to drug discovery. In recent years, there is a growing interest in the use of droplet-based microfluidics to encapsulate and confine single cells in individual droplets and perform wide range of analysis such as genome wide expression profiling, high throughput cytotoxicity screening, and other nucleic acid sequencing applications. Most of the conventional droplet-based single cell assays suffer from low encapsulation efficiency as they are dictated by Poisson statistics. To circumvent this, there have been a few droplet-based encapsulation techniques proposed that rely on either passive or active methods. However, most of these available techniques suffer from high complexity or low throughput. Here, we present a novel droplet-based microfluidics technique that takes advantages of hydrodynamics micro-vortices to initially trap cells and selectively release them into individual droplets. Using this method, we achieved 50% single cell encapsulation efficiency as well as size selective separation of blood components.

Materials and Methods: Soft lithography technique is employed to fabricate the PDMS-based microfluidic device. To study in detail the underlying physics, commercial CFD packages, ANSYS, were used to model droplet generation section. Specifically, two-phase flow nature of such physics is modeled using the explicit coupled level-set and volume of fraction (VOF) multiphase algorithms to track the interface between the dispersed and continuous phases. In addition, UCI HPC cluster were used to perform our computationally expensive models.

Results and Discussion: Our unique droplet generation design as well as optimized operational parameters (e.g. flow rates) create two symmetric three-dimensionally confined hydrodynamic vortices before the droplet generation orifice. Such a unique physics at droplet generation section results in a critical size above which the cells will be trapped at the micro-vortices. The cells can be then selectively released by increasing the critical size that is dependent on the flow rates of dispersed and continuous phase. Cell trapping leads to an increase in the local concentration of cells in the micro-vortices before encapsulation and consequently increases the efficiency >10 times.
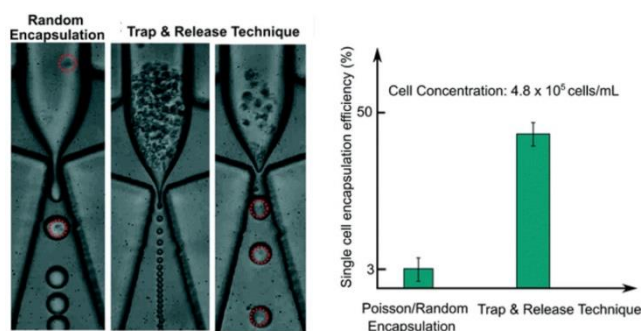
Figure 1: Comparison between single cell encapsulation based on the conventional Poisson-based method and our trap & release technique [1]

Conclusions: Our unique technique based on the hydrodynamics micro-vortices in droplet-based microfluidics enables selective trap and release capability that results in single cell encapsulation efficiency of up to 50%.

References: 1. G. Kamalakshakurup and A. P. Lee, *Lab on a Chip*, 2017, **17**, 4324-4333.

REDUCTION OF EDEMA FOLLOWING SPINAL CORD INJURY USING A NOVEL DEVICE

[1]Christopher S. Hale, [2]Jennifer Yonan, [2]Devin Binder, [1]Victor GJ Rodgers

[1]Department of Bioengineering, University of California, Riverside, CA
[2]Department of Biomedical Sciences, University of California, Riverside, CA
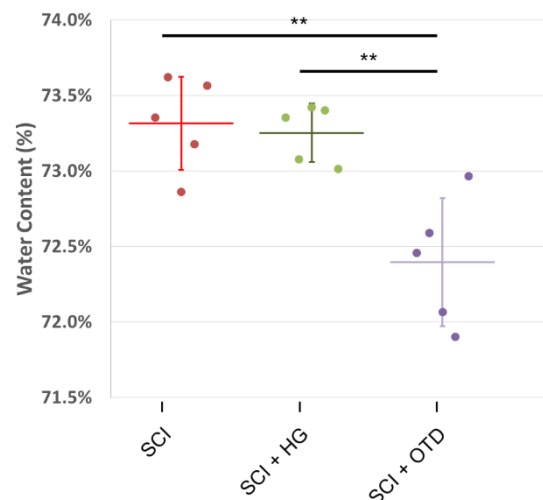**Contact:** vrodgers@engr.ucr.edu

Introduction: Currently in the U.S., there are 450,000 people living with spinal cord injury (SCI) with an estimated additional 11,000 individuals added each year. This injury leaves many people with pain and/or loss of control over parts of their body.[1] When spinal cord injury occurs it is accompanied by disruption of the blood-spinal cord barrier and subsequent leakage of fluid and proteins, which results in tissue swelling at the site of injury.[2] Tissue swelling at the injury site appears to develop in close association with necrosis at the lesion epicenter, and spreads bidirectionally along the cord within 24 to 48 hours after trauma.[3] A greater extent of spinal cord tissue swelling, evaluated by magnetic resonance imaging, has also been correlated with worse neurological outcome.[4-5] Typically, no treatment is given to the patient beyond immobilizing the spine to prevent further injury. This effort is passive and relies on the biological function of the patient for recovery.

We have designed a device to treat SCI by removing water from injured tissue via osmotically driven flux. The device is in contact with the injured tissue through a hydrogel applied to the tissue to facilitate water flux and ensure that the device and the tissue remain in contact. The device contains a solution chamber with a semipermeable membrane, separating the chamber form the hydrogel. Inside the solution chamber a protein solution creates an osmotic gradient between the injured tissue and the solution chamber, drawing water out of the tissue and into the chamber to reduce tissue swelling.

Materials and Methods: SCI experiments begin with a Sprague Dawley female rat, between 8-10 weeks old, being anesthetized before a T8 laminectomy is performed. After the spinal cord has been exposed, a 250 kD contusion is performed. The OTD is then placed on top of the injury site before the surgical site is closed. Following site closure, if applicable, the device is connected to 350 g L^{-1} BSA solution in aCSF at pH 7.4 and a flowrate of 25 μL min^{-1}. Treatment lasts 3 h before the animal is sacrificed and water content is measured by 48 h tissue drying.

Figure 1: Water content percentages for injured spinal cord tissue. The injured tissue treated with the device shows significant reduction in water content compared to injured-untreated and injured-nonfunctional device.

Results and Discussion: Uninjured (SCI) had a spinal cord water content of 73.3 ± 0.05% [Figure 1]. Injured animals treated with a nonfunctional device (SCI + HG) showed a similar water content (73.3 ± 0.19%) to that of the untreated animals. However, animals treated with the device (SCI + OTD) show a significant reduction (72.4 ± 0.42%) compared to both injured animals (SCI) and injured animal with a non-functional device (SCI + HG).

Conclusion: The *in-vivo* treatments provide evidence that the device is able to reduce tissue water content, after spinal cord injury, using only 3 hours of treatment. Next we plan to move to a 3 day treatment and look at how the water content changes over a longer edema time frame.

[1]American Association of Neurological Surgeons (2015)
[2]Whetstone WD, Hsu JY, Eisenberg M, et al. J Neurosci Res 2003;74:227–239.
[3]Tator CH, Fehlings MG. J Neurosurg 1991;75:15–26.
[4]Flanders AE, Schaefer DM, Doan HT, et al. Radiology 1990;177:25–33.
[5]Flanders AE, Spettell CM, Friedman DP, et al. AJNR Am J Neuroradiol 1999;20:926–934.

EQUIPMENT-FREE AUTOMATION OF MULTISTEP PAPER-BASED SENSORS

Daniel W. Bradbury[1], April A. Pan[1], Milad Azimi[1], Cecilie H. Falktoft[1],
Alexia J. Diaz[1], Benjamin M. Wu[1,2], and Daniel T. Kamei[1]
[1]Department of Bioengineering, University of California, Los Angeles, CA 90095
[2]School of Dentistry, University of California, Los Angeles, CA 90095
Contact: *kamei@seas.ucla.edu*

Introduction: The lateral-flow immunoassay (LFA) is an inexpensive, paper-based diagnostic device with the potential to rapidly detect disease biomarkers at the point-of-care. While the LFA has many advantages, its sensitivity is inferior to laboratory-based assays. Recently, our group discovered the phenomenon of aqueous two-phase system (ATPS) separation on paper, in which a well-mixed ATPS solution separates into its macroscopic phases and concentrates a target biomarker as it flows through a paper membrane. Coupling of this concentration step with the LFA resulted in an improved sensitivity. Here, we have developed a new technology to improve the LFA sensitivity even further by extending the functionality of ATPS separation on paper beyond biomarker preconcentration and using it for the tunable, automated delivery of signal enhancement reagents across the LFA detection zone. We have called this technology the **A**TPS-automated **C**oncentration and **E**nhancement of the **L**ateral-**F**low immuno**A**ssay (ACE-LFA).

Materials and Methods: ATPSs were made from poly(ethylene glycol-*ran*-propylene glycol) and either sodium sulfate or potassium phosphate. For the enzyme-based approach, alkaline phosphatase and antibodies specific to *Chlamydia trachomatis* (CT) were conjugated to gold nanoparticles. For the nanozyme-based approach, antibodies specific to *Escherichia coli* (*E. coli*) were conjugated onto in-house made porous, platinum nanoparticles. These conjugates were dehydrated onto the test strips for storage. To run the conventional LFA, a test strip was dipped into a sample of bacteria in PBS. To run the ACE-LFA, a test strip was dipped into an ATPS containing bacteria and chromogenic substrates. Nitroblue tetrazolium/5-bromo-4-chloro-3'-indolyl phosphate was used for the enzyme-based assay, while hydrogen peroxide and 3,3'-diaminobenzidine were used for the nanozyme-based assay.
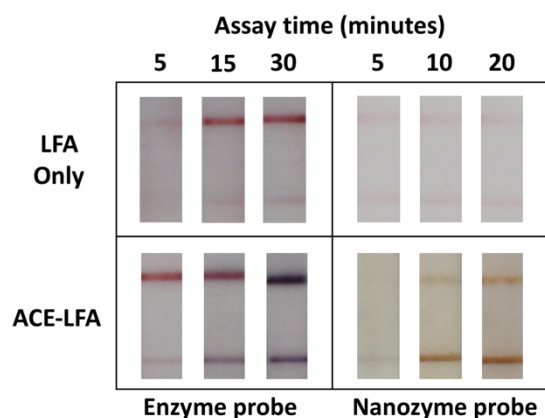
Figure 1. Time series images of the LFA only and the ACE-LFA. The enzyme probe assay was tested with 10 ng/uL of CT and the nanozyme probe assay with 10^6 colony forming units (CFU)/mL of *E. coli*.

Results and Discussion: We have shown that small, relatively hydrophobic substrates partition preferentially into the polymer-rich phase, while larger bacteria partitions into the smaller salt-rich phase and is thus concentrated. When the ACE-LFA test strip was dipped into the ATPS, the ATPS separates into its two macroscopic phases as it flows. First, the leading, salt-rich phase containing the concentrated bacteria solubilized the conjugates, and delivered them to the LFA test zone where they could bind to the test and control lines. This was followed by the lagging, polymer-rich phase which delivered the substrates to initiate the signal enhancement reaction. Because the substrates partitioned favorably into the polymer-rich phase, premature signal enhancement was avoided. Using the enzyme-based approach, the ACE-LFA demonstrated improved signal generation over the conventional LFA, ultimately leading to a 30-fold improvement in the LFA detection limit for CT within 30 minutes. We also incorporated a nanozyme-based enhancement reaction with the ACE-LFA, where an improved signal was observed when detecting for *E. coli* and therefore we expect an improvement in detection limit as well. This nanozyme-based approach not only eliminated the need for expensive and unstable enzymes, but it also enhanced the signal faster than the enzyme-based approach (Fig. 1).

Conclusions: We have demonstrated the first use of an ATPS to automate sequential reagent delivery. Additionally, to our knowledge, this is the first integration of both automated biomarker concentration and a signal enhancement reaction in a single paper-based device. We believe this technology will serve as an important platform for the development of other automated, highly sensitive paper-based assays.

MICROFLUIDIC DEVICE WITH EMBEDDED MICROPOROUS NYLON MEMBRANES FOR EFFICIENTLY FILTERING AND DISSOCIATING DIGESTED TISSUE INTO SINGLE CELLS

[1][#]Xiaolong Qiu, [1][#]Jeremy Lombardo, [1]Trisha Westerhof, [1]Edward Nelson, [1]Elliot Hui, and [1]Jered Haun [1]University of California, Irvine, [#]These authors contributed equally to this work; **Contact:** *jalombar@uci.edu*
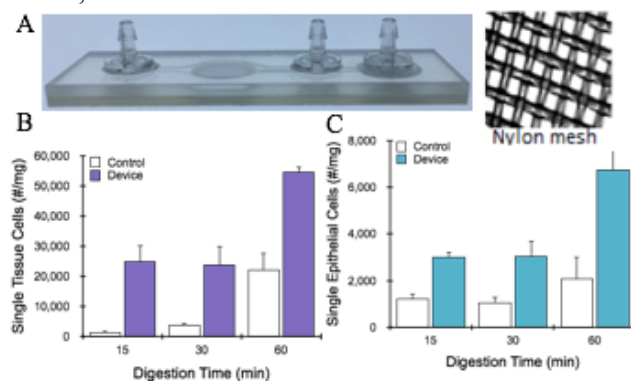
Introduction: Tissues are increasingly being analyzed at the single cell level in order to characterize cellular diversity and identify rare cells. Single cell analysis efforts are greatly hampered, however, by the need to first break down these tissues into a single cell suspension. Specifically, current dissociation methods are inefficient, leaving a significant portion of the tissue as aggregates that are either filtered away or left to confound analysis. Here, we present a simple and inexpensive microfluidic device that simultaneously filters large tissue fragments and aggregates and dissociates smaller aggregates and clusters into single cells, thereby improving both single cell yield and purity. The device incorporates two nylon mesh membranes with well-defined, μm-sized pores that perform the filtration and dissociation tasks at different size scales.

Materials and Methods: Microfluidic devices were fabricated using a commercial microfabrication process offered by ALine, Inc. Briefly, fluidic channels and openings for filters and hose barbs were etched using a CO_2 laser onto acrylic and polyethylene terephthalate (PET) layers using. The device layers, as well as a 50 and a 15 μm pore size nylon mesh membrane, were then pressure laminated together to form a single device (Fig. 1A). The 50 μm membrane was intended for filtration of large tissue fragments and cellular aggregates. We hypothesized that the smaller pores could help maximize single cell recovery and purity by further dissociating smaller aggregates as they travel through the nylon mesh, and preliminary experiments indicated that 15 μm pores were optimal. These double filter devices were tested using murine kidney, liver, and mammary tumor tissues. Tissues were scalpel minced to ~1 mm^3 pieces, digested in collagenase for 15, 30 or 60 min, repeatedly pipetted and vortexed to mechanically disrupt aggregates, washed by centrifugation into PBS+, and then introduced to the device. Cell counts were obtained using flow cytometry using a sequential gating scheme to identify live and dead tissue cells from leukocytes, red blood cells, and non-cellular debris.

Results: The number of single tissue cells recovered per mg kidney tissue after 15, 30, and 60 min collagenase digestion is shown in Fig. 1B. At 15 and 30 min digestion times, device treatment increased cell counts compared to controls by 5- to 10-fold. After a more thorough 60 min digestion, single tissue cell numbers for the control increased substantially, to more than 20,000/mg, while device treatment enhanced single tissue cell recovery by 2.5-fold. Notably, the filter devices produced similar numbers of single tissue cells after a brief 15 min digestion as the control at 60 min. Filter devices were then tested using murine mammary tumor tissue. Both 15 min and 30 min controls produced about ~1000 single epithelial cells per mg tumor tissue, and this only rose to ~2000 cells/mg after 60 min digestion (Fig 1C). Device treatment enhanced single cell recovery by approximately 3-fold at all time points. Viability after device treatment remained similar to controls for all time points for both kidney and mammary tumor experiments (data not shown).

Figure 1. A) Filter device and micrograph of nylon mesh. **B)** Kidney tissue single cell counts. **C)** Tumor epithelial tissue single cell counts.

Conclusions: To improve single cell analysis of tumor tissues, we designed and fabricated a simple and cheap microfluidic device that dramatically improves the quality of single cell suspensions obtained from digested tissue samples. Our experimental results demonstrate that these filter devices are capable of liberating more single cells from minced and digested murine kidney and mammary tumor tissues, often by a factor of 3- to 5-fold. Moreover, the numbers of single cells that could be obtained after a brief 15 min digestion and device treatment was comparable to a full 60 min digestion, which holds exciting potential to accelerate tissue processing work flows and to preserve the natural phenotypic state of cells. We are currently exploring integrating upstream tissue processing capabilities, such as our hydro-mincing digestion device[1] to extend the work to cm-scale samples and our branching channel dissociation devices[2] to maximize single cell recovery.

References: 1. Qiu et al., Microfluidic device for rapid digestion of tissues into cellular suspensions. *Lab Chip,* 2017, 17, 3300-3309; 2. Qiu et al., Microfluidic channel optimization to improve hydrodynamic dissociation of cell aggregates and tissue. *Lab Chip,* 2015, 15, 339-350.

IN VIVO DELIVERY OF CAS9 RIBONUCLEOPROTEIN AND DONOR DNA WITH GOLD NANOPARTICLES

Niren Murthy

Department of Bioengineering, University of California, Berkeley

Invited Presentation

Cas9 based therapeutics have the potential to revolutionize the treatment of genetic diseases because of their ability to generate homologous DNA recombination (HDR) and correct DNA mutations. However, viral gene therapy is currently the only delivery technology available for generating HDR *in vivo* with Cas9, and is challenging to bring into clinical trials because of off-target DNA damage and immunogenicity. In this presentation, I will describe a non-viral Cas9 delivery vehicle, termed CRISPR-Gold, which can induce HDR *in vivo* by directly delivering Cas9 protein, gRNA, and donor DNA. CRISPR-Gold is composed of gold nanoparticles assembled with the Cas9/gRNA ribonucleoprotein (RNP) complex, donor DNA, and an endosomal disruptive polymer. We have been able to demonstrate that CRISPR-Gold can correct the DNA mutation that causes Duchenne muscular dystrophy (DMD) in mdx mice via HDR, with an efficiency of 5.4% after an intramuscular injection and with minimal levels off-target DNA damage. In addition, we demonstrate that CRISPR-Gold can improve muscle strength and lower tissue fibrosis in mdx mice. CRISPR-Gold is the first example of a non-viral delivery vehicle that can generate HDR in vivo and has tremendous potential for treating DMD and other genetic diseases caused by single base pair mutations.

INNOVATIVE APPROACH TO RESOLVE FORCE-DEPENDENT PROTEIN INTERACTIONS USING BIOID

Joleen Cheah and Soichiro Yamada
Department of Biomedical Engineering, University of California, Davis.
Contact: syamada@ucdavis.edu

Introduction: Cells are constantly under various forms of mechanical stress, such as shear forces from the surrounding fluid, tensile forces through external interactions, and contractile forces generated by the internal cytoskeleton. Migrating cells are especially susceptible to mechanical stress as these cells must maneuver through dense ECM and obstacles to reach their destination. Cells' ability to appropriately respond to and overcome mechanical perturbations is a critical component in cancer metastasis. Thus, understanding the molecular mechanism governing how cells sense forces and resolving pathways activated by such stressors will provide crucial insight into metastatic cancer cells' physiology and identify potential therapeutic targets to deter cancer progression. We developed a unique technique using proximal biotin identification (BioID) along with a cell stretch device to induce a force-sensitive response in cells and identify novel force-dependent protein interactions.

Materials and Methods: Traditional approaches to resolve protein binding partners, such as co-immunoprecipitation, are incapable of detecting force-dependent protein interactions since no forces are present during the isolation of protein complexes. Recently, BioID has emerged as an alternative to immunoprecipitation to identify protein interactions [1]. In this method, a mutant biotin ligase promiscuously labels proximal binding partners in situ (Fig. A) [2], and thus, does not require stable protein interactions during isolation, making this an ideal approach to identify mechano-sensitive protein complexes. To induce a force-sensitive response, we designed and built a large-scale stretch device that cyclically stretches cells adhered on a thin, elastic PDMS membrane. Cells stably expressing mutant biotin ligase (BirA*) tagged to zyxin, a force-sensitive protein (Fig. B) were plated on the stretch chambers. Once adhered, cells were incubated with biotin and cyclically stretched to 20% for 16 hours. Biotinylated proteins are then isolated using an optimized protein purification protocol [3]. The purified proteins are analyzed using liquid chromatography-tandem mass spectrometry.

Results and Discussion: By comparing proteins differentially biotinylated in control and stretched cells, we have identified potential force-sensitive binding partners of zyxin. In the zyxin screen, we found greater levels of biotinylated CRKL, TUBB3, SVIL, and COPG2 and lower levels of biotinylated HSPH1 and DCTN1 in the stretched cells (Fig. C). We then verify and characterize these candidate proteins using biochemical techniques and live-cell imaging to visualize change in the protein's localization in real time from an applied force. With a small-scale stretch chamber manufactured in the lab and manipulation of cells using a micropipette needle, we are able to test a protein's mechano-response to different forms of forces.

Conclusion: With our unique approach combining BioID and the custom large-scale stretch device, we can resolve the network of force-dependent protein interactions and construct a force-sensitive interactome. This knowledge can reveal how normal mechanotransduction is disrupted in cancer cells and highlight pathways responsible for enhancing metastatic abilities.

Figure: A) BioID schematic. B) Cells expressing GFP-zyxin before and after induced force-sensitive response with microneedle. Stretch direction (arrow) and zyxin accumulation (arrowhead) shown. C) Proximal proteins of zyxin identified by mass spectrometry. Log-log plot of protein intensity in control against stretch samples.

References:
1. Roux, K.J., D.I. Kim, and B. Burke, Curr Protoc Protein Sci, 2013. **74**: p. Unit 19 23.
2. Ueda, S., et al., PLoS One, 2015. **10**(3): p. e0122886.
3. Cheah, J.S. and S. Yamada, Biochem Biophys Res Commun, 2017. **493**(4): p. 1522-1527.

MECHANOGENETICS FOR THE REMOTE AND NON-INVASIVE CONTROL OF CANCER IMMUNOTHERAPY

Yijia Pan[1], Sangpil Yoon[3], Jie Sun[4], Ziliang Huang[1], Changyang Lee[3], Molly Allen[1], Yiqian Wu[1], Ya-Ju Chang[1], Michel Sadelain[4], K. Kirk Shung[3*], Shu Chien[1,2*] & Yingxiao Wang[1*]

[1]Department of Bioengineering & Institute of Engineering in Medicine, [2]Department of Medicine, University of California, San Diego, La Jolla, CA 92093, USA, [3]Department of Biomedical Engineering, University of Southern California, Los Angeles, CA 90089, USA, [4]Memorial Sloan Kettering Cancer Center, New York, NY 10065, USA

Contact: *yiw015@eng.ucsd.edu*

Introduction: While cell-based immunotherapy, especially chimeric antigen receptor (CAR)-expressing T cells, is becoming a paradigm-shifting therapeutic approach for cancer treatment, there is a lack of general methods to remotely and non-invasively regulate genetics in live mammalian cells and animals for cancer immunotherapy within confined local tissue space. To address this limitation, we have identified a mechanically sensitive Piezo1 ion channel (mechanosensor) activatable by ultrasound stimulation and integrated it with engineered genetic circuits (genetic transducer) in live HEK293T cells to convert the ultrasound-activated Piezo1 into transcriptional activities. We have further engineered Jurkat T cell line and primary T cells to remotely sense the ultrasound wave and transduce it into transcriptional activation for the CAR expression to recognize and eradicate target tumor cells.

Materials and Methods: We combined 2MHz ultrasound stimulation and FRET imaging to stimulate and monitor the engineered cells (Figure 1). We further engineered genetic transducing modules by molecular cloning. HEK293T cells, Jurkat T cell line, human primary T cells, Toledo cells, Nalm6 tumor cells were used to demonstrate functionality of the system and T cell tumor killing efficiency.

Results and Discussion: We could detect mechanochannel Piezo1 activation in HEK 293T cells upon ultrasound stimulation (Figure 1). We then transmitted the Piezo1 activation to control gene activation by engineered genetic transducing modules. We further applied this system to remotely control the CAR production in Jurkat T cells and primary T cells. Upon ultrasound stimulation Jurkat T cells can express CAR and engage with antigens on the target tumor cells for T cell activation. Primary T cells can express CAR upon ultrasound stimulation and increase the killing efficiency on tumor cells.

Conclusions: In conclusion, we developed the remoted controlled gene activation system and demonstrated its function in primary T cells. This approach is modular and can be extended for remote-controlled activation of different cell types with a high spatiotemporal precision for therapeutic applications.
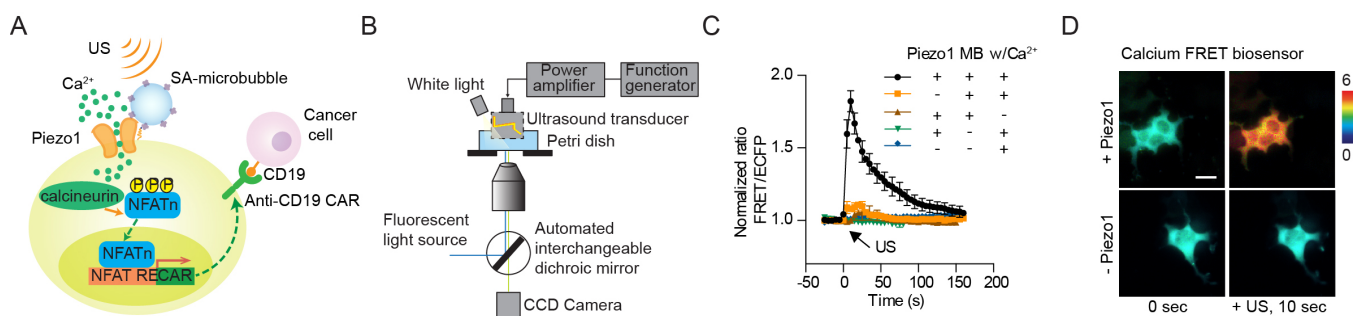
Figure 1: Design of synthetic genetic circuits remotely activatable by ultrasound. (*A*) Schematic drawing of ultrasound-induced cell activation and gene expression. (*B*) Diagram of an integrated system of ultrasound stimulation and FRET imaging. (*C*) The time courses of normalized FRET/ECFP ratio (mean ± S.E.M.) of a D3cpv calcium biosensor in HEK293T cells before and after 5 sec ultrasound stimulation under different conditions. (*D*) Representative FRET/ECFP ratio images of D3cpv calcium biosensor in HEK293T cells expressed with (top panels) or without (bottom panels) Piezo1 before (left) and after (right) ultrasound stimulation. Scale bar represents 20 µm.

Mechanotransduction via high affinity LFA-1 promotes assembly of Kindlin-3/RACK1/Orai1, a complex that signals intracellular calcium flux

Vasilios A. Morikis[1], Myung Hyun Jo[2], Taekjip Ha[2], and Scott I. Simon[1*]

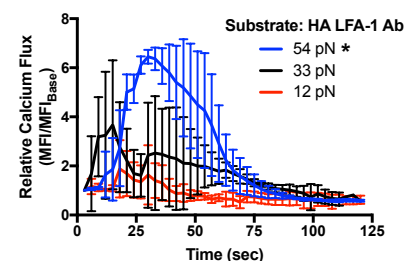[1]Department of Biomedical Engineering UC Davis, [2]Department of Biophysics and Biophysical Chemistry JHU

Introduction: Lymphocyte function associated antigen-1 (LFA-1) is a heterodimeric transmembrane integrin present on the neutrophil surface that is essential for innate immune function including recruitment to, and migration through inflamed endothelium to the site of tissue insult. To form adhesive bonds with intracellular adhesion molecule-1 (ICAM-1), LFA-1 must shift conformation from low affinity (LA) to a high affinity (HA) state. Within focal sites of adhesion, LFA-1/ICAM-1 bonds are capable of transducing mechanical signals that superpose with signaling via bound chemokine receptors to amplify calcium flux by several orders of magnitude over stimulation with chemokine alone. The objective of this study is to elucidate the nature of focal transmission of force through LFA-1 from the outside-in to the beta-subunit cytoplasmic domain, where Kindlin-3 promotes a physical linkage with the calcium release activated channel (CRAC) Orai1. We hypothesize that transmembrane force detection occurs through HA LFA-1/ICAM-1 bonds that induce assembly of an intracellular complex between Kindlin-3, receptor for activated-C kinase 1 (RACK1), and Orai1 within lipid raft domains rich in paxillin. Further, a characteristic threshold in the magnitude of tension is necessary to trigger the assembly of this signaling complex that promotes calcium flux, subsequent neutrophil shape change, and migratory functions.

Materials and Methods: In order to predict the tensile forces experienced by HA LFA-1/ICAM-1 bonds as they resist the drag of fluid shear stress, we employed a tension gauge tether (TGT) platform. ICAM-1 is immobilized to a surface through a well-defined noncovalent bond that ruptures at a defined force following receptor engagement. TGT tethers are constructed from two complimentary strands of DNA such that the strength of the bond is precisely engineered by the geometry of where the LFA-1 ligand is placed in relation to the substrate bound avidin/biotin bond. Estimated rupture forces of a 21-base pair DNA is ~12 pN when unzipped at adjacent points and increases to ~54 pN when dissociated under shear at distant points of attachment. To determine the molecular force thresholds necessary to activate formation of macromolecular LFA-1/Kindlin-3/RACK1/Orai1 complexes a microfluidic, vascular mimetic device was annealed to the surface of the TGT-ICAM-1 tether substrate. Neutrophils were flown over the substrate under physiological shear stress, upon arrest and bond tension, calcium flux and shape change were observed. Spatial association between HA LFA-1/ICAM-1 bonds and cytosolic Kindlin-3 and RACK1 was quantified before and after shear was applied using total internal reflection fluorescence microscopy (TIRF).

Results and Discussion: Neutrophils formed focal adhesions via HA LFA-1/ICAM-1 and upon application of shear flow to exert tension on bonds, elicited a maximum flux in calcium. Under these conditions, neutrophils transition from a round to a spread morphology associated with directional F-actin polymerization that initiates shape polarization. TGT-ICAM-1 tethers with at a threshold strength of 54 pN elicited a peak in calcium flux that was 6-fold higher than 12 pN, and 2-fold greater than 33 pN tethers (Figure 1). These data indicate that the magnitude of tensile forces acting on LFA-1/ICAM-1 bonds regulates local calcium release. Below a bond force of 33 pN, calcium flux occurred infrequently with an irregular profile, which coincided with inefficient shape change. HA LFA-1 focal bond cluster number and area was equivalent between all three TGT tether strengths. Under static conditions or stabilizing LFA-1 at a low affinity with antibody treatment even in presence of tension, blocked calcium flux. To further elucidate the mechanism of mechanosignaling, neutrophils were captured on a substrate of ICAM-1 via HA LFA-1 and a shear was applied prior to co-immunoprecipitation with anti-LFA-1. Pulldown of Kindlin-3 and RACK1 to HA LFA-1 under force conditions are enhanced by 100x and 30x respectively when compared to static conditions. Additionally, we confirmed the requirement of a focal adhesion complex between Kindlin-3, RACK1, and HA LFA-1 by knocking out each in neutrophil-like HL60. Force applied to HL60 deficient in Kindlin-3 and/or RACK1 exhibited diminished calcium flux commensurate with pharmacological inactivation of Orai1. Thus, force acting on HA LFA-1 promotes a complex of LFA-1/Kindlin-3/RACK1/Orai1 that is required for calcium flux.


Figure 1. Neutrophil were allowed to settle on a substrate of 54, 33, or 12 pN TGT functionalized with HA-inducing LFA-1 antibody and calcium flux (Rhod-2) was observed under continuous force conditions.

Conclusion: We report on mechanotransduced regulation of local calcium flux at the region of adhesive contact of neutrophils at the endothelial surface where LFA-1/ICAM-1 bonds form in shear flow. This sensitivity to tensile force and the subsequent spatial calcium flux promotes neutrophil shape change and motility, indicating that force acting on HA LFA-1/ICAM-1 bonds a is a key step in informing the neutrophil on where and when within inflamed vessels they should arrest and transmigrate.

A MECHANOREGULATORY ROLE FOR CALCIUM BURSTS IN HUMAN NEUTROPHILS

Emmet A. Francis and Volkmar Heinrich
Department of Biomedical Engineering, UC Davis
Contact: *eafrancis@ucdavis.edu*

Introduction: Global bursts in cytosolic calcium concentration are among the most conspicuous signaling events in immune cells. While they are associated with a variety of vital processes from phagocytosis to cell migration, their precise physiological role remains unclear. For instance, some past studies have implied that G-protein coupled receptor (GPCR) engagement is sufficient to trigger calcium bursts, but other studies clearly show that neutrophils can respond to GPCR activation by chemoattractants without exhibiting calcium bursts. On the other hand, these bursts frequently accompany adhesion-mediated processes in which cells expand their surface area dramatically, which suggests that calcium bursts play a mechanoregulatory role in immune cells. We here investigate the cause-effect relationship between mechanical behavior and calcium bursts in human neutrophils.
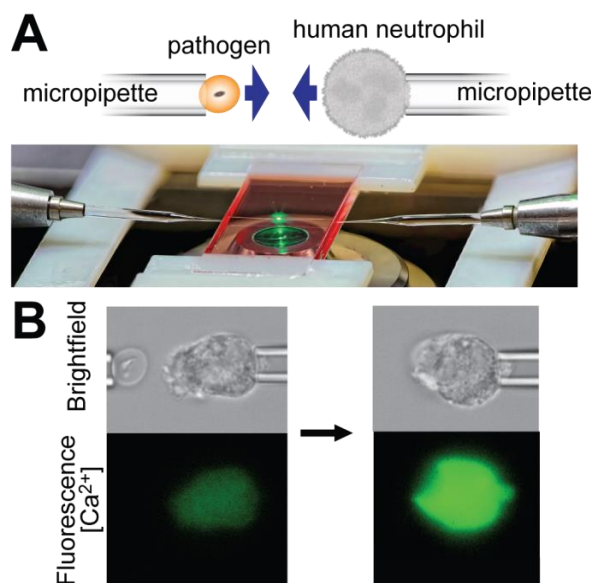
Figure 1. A: Experimental setup. B: Neutrophil exhibits a calcium burst during phagocytosis, but not during pure chemotaxis.

Materials and Methods: Our single-cell experiments combine micropipette manipulation (Fig 1A) with fluorescence imaging of cytosolic calcium concentration. The use of micropipettes enables us to separately inspect chemotaxis, adhesion, and phagocytosis during one-on-one encounters between human neutrophils and pathogenic particles (see sample movies online[1]). Alternatively, we can eject a known concentration of chemoattractant toward the cell from the opposing pipette. Our setup also allows us to monitor the surface area and cortical tension of cells and to quantify cell morphology by measuring cell extension or contraction along the axis defined by the micropipette.

Results and Discussion: We found that pseudopod extension during complement-mediated pure (i.e., adhesion-free) chemotaxis neither requires nor causes calcium bursts[2] (Fig 1B). In these experiments, cell surface area never increased more than ~30% during pure chemotaxis, a value that coincides with the known amount of cortical slack in neutrophils. This indicates that adhesion and membrane tension play a vital role in calcium burst induction.

In other experiments, we induced calcium bursts by stimulating neutrophils with supraphysiological levels of the chemoattractant C5a. This led to axial contraction of the cell, indicating an increase in cortical tension and/or an inward pulling force. Phagocytosis assays in which we altered the strength and/or dynamics of calcium signals by treating cells with 1 mM caffeine further supported the mechanoregulatory role of calcium bursts. In these assays, neutrophils often pushed phagocytic targets outwards before engulfing them, indicative of weakened structural linkages between the actin cytoskeleton and the cell membrane. Therefore, calcium bursts appear to regulate the lock or release events of these cytoskeleton-membrane anchors.

Conclusions: Our findings demonstrate that there is a close relationship between mechanical behavior and calcium dynamics in immune cells. In general, calcium bursts in neutrophils are induced during adhesive processes and are associated with larger surface area expansions and higher cortical tension. Furthermore, altered calcium signals change cell morphology during phagocytosis. Therefore, we propose that calcium bursts control the mechanical behavior of immune cells by modulating the strength of cytoskeleton-membrane anchors.

References: 1. https://www.youtube.com/user/HeinrichLab 2. Francis, E. A. and V. Heinrich, *Sci. Signal.* 2018, Vol. 11, Issue 521, eaal4289.

Poster #	Track	Rapid Fire	Lead Author	Affiliation	Title
18	Biomaterials and Drug Delivery	Yes	Melissa Xu	UC Merced	Dynamics of Liposome Formation on Cellulose Paper
21	Biomaterials and Drug Delivery		Justin Stanley Plaut	UCSD	Detection of Nucleation Core Mineralization Within Hydrated Matrix Vesicles by Physicochemical Analyses
24	Biomaterials and Drug Delivery		Victoria Wu	UI Chicago	Ceramic Nanoparticles for Advanced Biomedical Applications: From Bone to Brain
27	Biomedical Imaging	Yes	Aniruddha Ray	UCLA	Holographic Microscopy Monitors the Degradation of Drug Loaded Nanoparticles
30	Computational Bioengineering	Yes	Alfredo Lucas	UCSD	Use of Logistic Regression to Determine Parameter Ability for Recovery Prediction in Experimental Rat Hemorrhagic Shock Model
31	Computational Bioengineering	Yes	Reed Harrison	UC Riverside	Missense Single Nucleotide Polymorphism Disrupts a Coevolved Pair and Adversely Affects Pattern Recognition in Complement Factor H
33	Computational Bioengineering	Yes	Nehemiah Zewde	UC Riverside	Complement System Models for C3 Glomerulopathy and Therapeutic Intervention
36	Computational Bioengineering		Rohaine Hsu	UC Riverside	Mathematical Modeling of Hereditary Angioedema
48	Medical Devices and Instrumentation	Yes	E.M. Werner	UC Irvine	High Density Normally Closed Elastomeric Membrane Valves for Microfluidic Digital Logic
51	Medical Devices and Instrumentation	Yes	S.V. Kardani	UC Riverside	Characterizing Hydrogels with Vibrating Tube Mass Sensors
54	Medical Devices and Instrumentation		Ramsey Batarseh	UC Riverside	The Development of a Novel Osmometer for the Study of Macromolecular Crowded Environments
57	Medical Devices and Instrumentation		B.W.K. Woo	UC Riverside	Development of Titanium-based Stents for Treating Coronary Heart Disease
60	Medical Devices and Instrumentation		R. Geoghegan	UCLA	Development of a Transoral Robotic Surgery Training Platform
63	Medical Devices and Instrumentation		Brent Kalish	UC Riverside	Modifying Wicking Speeds in Single- and Double-sided Laser-etched Paper-based Microfluidic Channels
66	Medical Devices and Instrumentation		H. Winet	UCLA	Four Mechanisms of Evolution and Their Implications for Bioengineering
3	Molecular & Cellular Engineering		Taylor Hanley	UC Riverside	Erythrocyte-derived Nano-particles Functionalized to Target Epha2 Receptors
6	Molecular & Cellular Engineering		Kyle Jacobs	UC Davis	Visualizing Real-time Changes in Force-dependent Protein Interactions
9	Molecular & Cellular Engineering		Richard Tran	UC Irvine	The Effect of Heart's Mechanics Environment on Cells with the Lamin a/c Mutation and Its Relation to Heart Disease
12	Molecular & Cellular Engineering		Jiayu Liao	UC Riverside	Develop a Universal Fret Technology Platform for Quantitative Systems Biology
15	Molecular & Cellular Engineering		Ziliang Huang	UCSD	A Light Inducible Gene Activation System Toward Controllable Cell- Based Therapeutics
39	Neuroengineering		Holly M. Howarth	UCSD	Peripheral Nerve Lengthening as a Method for Regeneration and Repair
42	Stem Cells and Regenerative Medicine	Yes	A. Witmer	UC Riverside	Inferring Stem Cell Protein Expression from Dynamic Colony Morphology Using Machine Learning Algorithms

HOLOGRAPHIC MICROSCOPY MONITORS THE DEGRADATION OF DRUG LOADED NANOPARTICLES

[1,2]Aniruddha Ray[*], [3]Shuoran Li, [2,3]Tatiana Segura, and [1,2]Aydogan Ozcan[#]

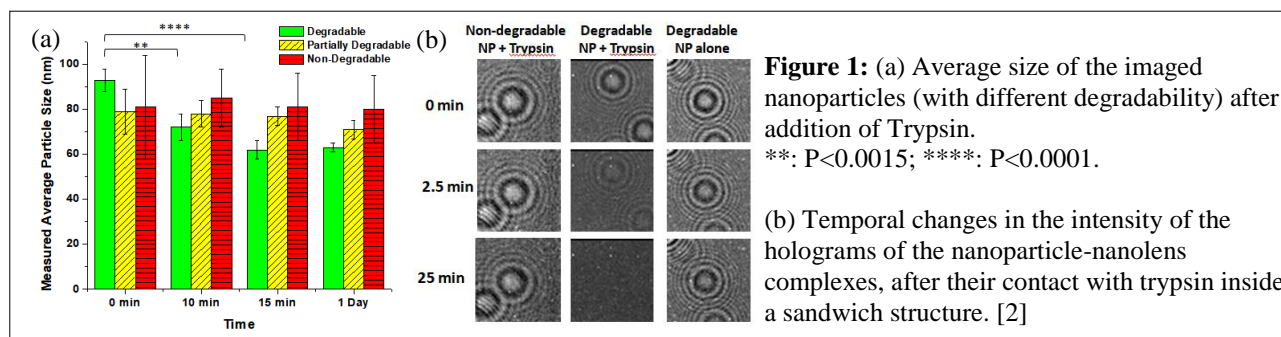[1]Electrical and Computer Engineering Department, University of California, Los Angeles, USA.
[2]Bioengineering Department, University of California, Los Angeles, USA.
[3]Department of Chemical and Biomolecular Engineering,University of California, Los Angeles,USA.
Contact:[*]rayani@ucla.edu [#]ozcan@ucla.edu

Introduction: Degradable nanoparticles have been extensively used for different therapeutic applications, particularly in oncology, cardiology and tissue healing. Tuning the degradability of the nano-capsules allows precise control of the drug delivery and release, thereby regulating the dosage. The most common method of characterizing the degradation process is indirect and involves quantifying the amount of drug released from the capsules. Direct methods such as electron microscopy, atomic force microscopy, light scattering and chromatography have been used for quantifying the changes to the nanoparticle matrix, but they have several limitations. Here we present two novel methods, based on computational holographic microscopy, to monitor this phenomenon in any type of nanoparticles. The first approach involves holographic monitoring of the size of the nanocapsules as they undergo degradation. The second method involves directly monitoring the changes to the nanoparticle matrix, when the particles are placed in contact with an enzyme (trypsin), responsible for degradation, inside a sandwich structure. These techniques enable high throughput characterization of nanoparticles using very small quantities of sample volume (<20nL per test).

Materials and Methods: The microscope was built using 3D-printed parts and low-cost optical components. Low-cost fiber coupled LEDs, controlled using a micro-controller, were used as light sources to illuminate the sample. The light from the fiber was filtered through a band pass filter (@532nm) prior to irradiating the sample. An inverted CMOS imaging chip placed close to the sample (<1 mm) was used to record the in-line holograms (i.e., the interference between the directly transmitted wave and scattered wave from the nanoparticles). These holograms were then digitally back-propagated to the object plane to computationally reconstruct the image of the nanoparticles and accurately size them [1].We also utilized nanolenses to enhance the optical scattering from the nanoparticles. These nanolenses were created by evaporating and condensing polyethylene glycol (PEG) on a substrate containing the nanoparticles.

Figure 1: (a) Average size of the imaged nanoparticles (with different degradability) after addition of Trypsin.
**: P<0.0015; ****: P<0.0001.

(b) Temporal changes in the intensity of the holograms of the nanoparticle-nanolens complexes, after their contact with trypsin inside a sandwich structure. [2]

Results and Discussion: We used polymer nanoparticles containing a vascular endothelial growth factor, which is used for treatments in cardiology, tissue healing etc. The degradation rate of these polymer nanoparticles was controlled by using different cross-linkers. We observed a significant reduction in the size of the nanoparticles synthesized with degradable cross-linkers as compared to the non-degradable or even partially degradable cross-linkers, after adding trypsin (Fig. 1) [2]. For continuously monitoring the degradation process we created a sandwich structure by placing trypsin coated coverslip on a substrate containing the nanoparticle-nanolens complexes. We observed a rapid change in the hologram intensity for the degradable nanoparticles [2].

Conclusions: Two different high-throughput and cost effective methods for characterizing the degradation rate of drug loaded nanoparticles are presented; these techniques will be useful during the nanoparticle based drug development and testing phase.

References:[1] E. McLeod *et al. ACS Nano*, 2015, 9, 3265–3273.
[2] A. Ray *et al. ACS Photonics*, 2017, 4 (5), 1216–1224.

DETECTION OF NUCLEATION CORE MINERALIZATION WITHIN HYDRATED MATRIX VESICLES BY PHYSICOCHEMICAL ANALYSES

[1,3]J.S. Plaut, [3]A. Strzelecka-Kiliszek, [3]S. Pikuła, [4]S. Mebarek, [4]R. Buchet, [1,3]S. Esener, [6]J.L. Millan, and [5,6]M. Bottini
[1]Department of Bioengineering, University of California San Diego, La Jolla, CA
[2]Cancer Early Detection Advanced Research Center, Oregon Health and Science University, Portland, OR
[3]Department of Biochemistry, Nencki Institute of Experimental Biology, Warsaw, Poland
[4]Institut de Chimie et Biochimie Moléculaires et Supramoléculaires, Université Lyon 1, Villeurbanne, France
[5]Department of Experimental Medicine and Surgery, University of Rome Tor Vergata, Rome, Italy
[6]Sanford Burnham Prebys Medical Discovery Institute, La Jolla, CA
Contact: *jplaut@ucsd.edu, massimo.bottini@uniroma2.it*

Introduction: Matrix vesicles (MVs) are a class of extracellular vesicles released by mineral-competent cells. MVs are thought to mediate both physiological and ectopic mineralization processes in cartilage, bone, and other tissues by forming crystalline minerals in the MV lumen by a Ca^{2+} and P_i driven process. A nucleation core (NC) containing Ca^{2+}-P_i complexed with proteins and phospholipids is believed to be the primary site of mineralization. Experimental evidence of MV mineralization and the NC has been limited to analyses on artifact-prone dried samples. We show by hydrated dynamic light scattering (DLS) and quantitative atomic force microscopy (AFM) that the size and moduli of MVs increase and single, punctate features present in all of the MVs are obscured during the mineralization process. This demonstrates the potential for DLS and AFM to dynamically track MV maturation.

Materials and Methods: MVs were isolated from growth plates and epiphyseal cartilage of 17-day chicken embryos by collagenase IA treatment in synthetic cartilage lymph (SCL) buffer and then serial centrifugation and ultracentrifugation. Hydrodynamic diameter and zeta potential of MVs were measured via DLS on a Malvern Zeta Sizer ZSP. Dried energy dispersive X-ray (EDX) spectra were collected on a Jeol JEM-1400 TEM with an Oxford INCA system. Quantitative AFM data was acquired using calibrated Peakforce-HiRs-F-A probes in Peakforce Tapping mode on an Icon scanner of a Bruker Fastscan System. MVs were captured onto poly-L-ornithine-coated mica and imaged in SCL. "MV+Ca^{2+}" data were acquired 24 h after addition of 2 mM $CaCl_2$ to the "MV neat" sample.

Results and Discussion: The diameter of MVs increased significantly after addition of Ca^{2+} (**Fig. 1A**, p<0.0001). Zeta potential showed no significant change (-8.8 ± 0.8 to -8.7 ± 1.2 mV) and suggests mineralization occurred within the MV lumen (Ca^{2+}-P_i minerals are typically < -14 mV). This is complemented by the significant increase in the Ca / P ratio of MV internal aggregates as determined by EDX. (**Fig 1B**, p<0.05). Fluid AFM showed a significant increase in the moduli of MVs after incubation with Ca^{2+} (**Fig. 1C**, p<0.05). Representative modulus maps show that high modulus regions appear after Ca^{2+} treatment (**Fig. 1D**) and representative height maps suggest that these regions arise from the maturation of a punctate feature within the MV that is the NC (**Fig 1E**).
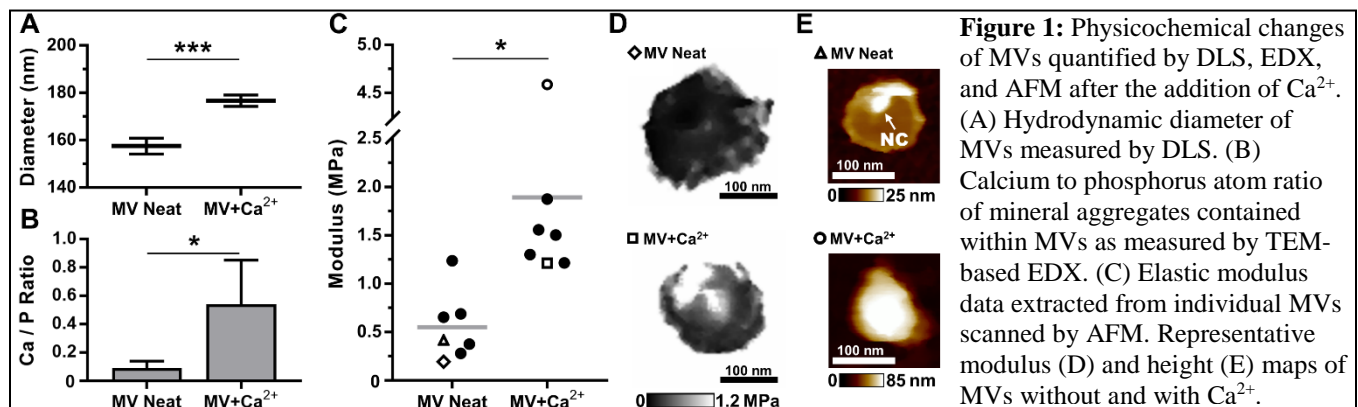
Figure 1: Physicochemical changes of MVs quantified by DLS, EDX, and AFM after the addition of Ca^{2+}. (A) Hydrodynamic diameter of MVs measured by DLS. (B) Calcium to phosphorus atom ratio of mineral aggregates contained within MVs as measured by TEM-based EDX. (C) Elastic modulus data extracted from individual MVs scanned by AFM. Representative modulus (D) and height (E) maps of MVs without and with Ca^{2+}.

Conclusions: We applied fluid AFM for the morphological and nanomechanical characterization of MVs and observed the NC in hydrated conditions for the first time. The increase in size and elastic modulus of MVs after addition of Ca^{2+} supports the prevailing hypothesis that crystalline minerals grow within MVs until they rupture the vesicle. We envision that this approach will enable the differential characterization of NC maturation in MVs released in physiological and pathological processes, including breast calcification, arthritis, and atherosclerosis.

Ceramic Nanoparticles for Advanced Biomedical Applications: From Bone to Brain

Victoria M. Wu[1], Vuk Uskoković[1,2]

[1] 7 Park Vista, Irvine, CA 92604, USA

[2] Department of Bioengineering, University of Illinois, Chicago, IL 60607-7052, USA

Structural complexities of ceramics are the key to explaining their display of a broad range of interesting properties, yet the control of these complexities has not been harnessed to the fullest extent and translated to the medical domain. In the first part of the lecture I will talk about our work on calcium phosphate nanoparticles and the control of their physical and chemical properties to yield new properties relevant for various biomedical applications, ranging from tunable drug delivery kinetics to gene delivery to cancer cell targeting to intrinsic antibacterial activity. This will be placed in the context of an ongoing effort in my lab to expand the application repertoire of calcium phosphate nanoparticles beyond their traditional use as components that impart osteoconductivity and high compressive strength to tissue engineering constructs. In the second part of the lecture I will talk about our work on the use of composite nanoparticles modeled after the stratified structure of the planet Earth for permeation of the blood-brain barrier and brain tumor targeting.

USE OF LOGISTIC REGRESSION TO DETERMINE PARAMETER ABILITY FOR RECOVERY PREDICTION IN EXPERIMENTAL RAT HEMORRHAGIC SHOCK MODEL

[1]A. Lucas, [1]A.T. Williams, [1]P. Cabrales

[1]Department of Bioengineering, University of California, San Diego, CA

Contact: *allucas@ucsd.edu*

Introduction: Hemorrhagic shock (HS) severely decreases oxygen (O2) delivery and induces cardiovascular collapse. It is of interest for clinicians to estimate the potential of recovery during the early onset of a shock event as that would determine whether resources should be expended in environments of material shortage such as warzones and low resource communities. Multiple parameters, such as mean arterial pressure (MAP) and blood pressure, are traditionally monitored during shock as a means of estimating the potential for recovery. In this study we used a logistic regression model to determine the ability of systemic hemodynamics, cardiac function, and blood gas parameters in determining the ability of successful HS recovery.

Materials and Methods: Packed red blood cells (pRBCs) stored in AS-3 after leukorfiltration were created from donor Sprague-Dawley rats. pRBC units were randomly stored under either 1) conventional; 2) anaerobic; or 3) anaerobic/hypercapnic conditions. Rats (150-200g) were hemorrhaged to 50% of blood volume, held in hypovolemia for 30 minutes, and resuscitated to recover blood pressure to 90% pre-hemorrhage with pRBC stored for either 1 or 3 weeks. Systemic hemodynamic, cardiac function, and blood gas parameters were monitored during shock and resuscitation. The percent resuscitation (%Res) corresponding to the percentage of the animal's original blood volume infused at the end of recovery, was used to create two classes of subjects with %Res=50% set as the threshold. A binary classification, logistic regression model was created with all measured parameters as features, and trained on random instances. The weights with an above threshold contribution assigned to each parameter after an L2 norm cost function minimization were extracted and matched with the corresponding features creating a reduced feature vector. A Monte Carlo approach was applied for n=100 trials of the previously described procedure to get a distribution of the most commonly selected features. The performance of the new feature vector was assessed by another logistic regression model with a 5-fold cross-validation.

Results and Discussion: The top 3 features chosen by the model in order of increasing number of occurrences were: lactate at 30 minutes into shock, mean arterial pressure at 30 minutes into shock and contractility at baseline (Figure 1). The model trained using these three features had a mean cross-validation accuracy of 90.2%, significantly above the 66.9% accuracy (p<0.001) for a baseline classifier trained with random features. A final test set accuracy of 88.5% was obtained.

Conclusions: It has been shown that a logistic regression model can be effectively used for the determination of important parameters for the prediction of successful recovery after shock in an experimental rat hemorrhagic shock model.
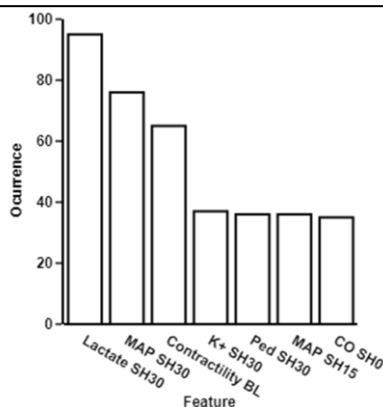
Figure 1: Distribution of features selected by the proposed model. Note that the features differ from those commonly associated with HS resuscitation monitoring such as heart rate.

MISSENSE SINGLE NUCLEOTIDE POLYMORPHISM DISRUPTS A COEVOLVED PAIR AND ADVERSELY AFFECTS PATTERN RECOGNITION IN COMPLEMENT FACTOR H

[1]R.E.S. Harrison, [1]D. Morikis

[1]Department of Bioengineering, University of California, Riverside, CA
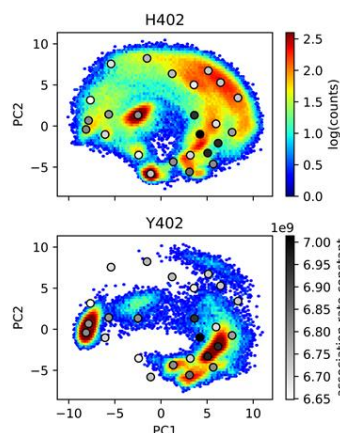
Contact: dmorikis@ucr.edu

Introduction: A single nucleotide polymorphism, tyrosine 402 to histidine (Y402H), within the gene encoding complement Factor H (FH) predisposes individuals to acquiring age-related macular degeneration (AMD) after aging. This polymorphism has been shown to significantly reduce binding of the FH splice variant named FHL-1 to heparin, C-reactive protein, and products of oxidative stress, negatively impacting pattern recognition. Structurally, 20 short consensus repeats (SCR) joined linearly by short linker sequences comprise FH, while FHL-1 contains only the first 7 SCR. FHL-1 is thought to be an important regulator of complement in the macula where it can diffuse more freely through Bruch's membrane than FH. SCR7 from FHL-1 and FH contains position 402 and exhibits a net positive charge that promotes association with negatively charged heparin molecules found in the extracellular matrix. Since the Y402H mutation results in decreased affinity of SCR7 for heparin, we hypothesized that the mutation results in side-chain rearrangements of amino acids involved in heparin binding.

Materials and Methods: To assess the evolutionary importance of position 402, we retrieved 44,511 orthologous SCR domains. These sequences were filtered to eliminate redundancy and ensure high coverage with human SCR7 leaving 4,940 sequences. Direct coupling analysis (DCA) was performed for every pair of columns from the final multiple sequence alignment. To evaluate side chain rearrangements, we retrieved initial structures of SCR7 from the Protein Databank (PDB) for SCR7^{Y402} (PDB: 2jgx) and SCR7^{H402} (PDB: 2uwn) and performed multiple molecular dynamics (MD) simulations for a total of 35 μs per SCR7 isoform. Then we constructed a Markov chain describing probabilities of transitioning between 100 conformational states for each isoform through discretization of MD trajectories with independent component analysis and K-means clustering. To validate structures from Markov chains we compared expected C_α and C_β chemical shifts from SPARTA+ to known chemical shifts from nuclear magnetic resonance (NMR) experiments. To evaluate differences in predicted association rate constants, we performed 10,000 rigid-body Brownian dynamics (BD) simulations with hydrodynamic interactions for each of 200 representative structures to simulate heparin (dp12, PDB: 1hpn) associating to SCR7^{Y402} and SCR7^{H402}.

Results and Discussion: DCA identified coevolved pairs Y402-I412 (score 0.91, p-value 8.8 x 10^{-7}) and V429-P438 (score 1.01, p-value 4.0 x 10^{-8}). In general DCA scores greater than 0.7 are predictive of contacts in protein structure. V429-P438 is a contact between beta strands in SCR7 structures while no contact is observed between Y402 and P438. MD, however, suggests transient contacts between Y402 and I412 in SCR7^{Y402} with a probability of 25.6%. This contact is less frequent in SCR7^{H402} with a probability of 3.7%. Notably, we observe different conformational sampling between SCR7 isoforms as the network representation for the SCR7^{Y402} Markov chain is more modular than for SCR7^{H402}. Structures from communities in the SCR7^{Y402} network show switching between the PDB conformation of Y402 and a conformation in contact with I412, while the SCR7^{H402} network does not exhibit this behavior. Predicted chemical shifts for each Markov chain agree with experimentally determined values and suggest that the SCR7^{Y402} model outperforms the reference PDB structure.

Figure 1: Free energy landscapes for the side chain position of residue 402 in SCR7^{H402} (top) and SCR7^{Y402} (bottom). Regions of low energy are observed more frequently (upper color bar). After superposing all structures from MD, position vectors for atom $N_{\varepsilon 2}$ in H402 and O_η in Y402 are decomposed with principle component analysis and projected onto the first two components. Association rate constants are annotated in the landscape with circles shaded according to the mean value in a particular region (lower color bar). Only Y402 samples a minimum with a high association rate constant.

Finally, BD simulations suggest that conformations of SCR7 with the coevolved contact between position 402 and I412 associate faster with heparin than those with position 402 in a more solvent-accessible orientation (**Figure 1**).

Conclusions: The Y402H polymorphism disrupts a coevolved contact and structural dynamics of SCR7 in FH and FHL-1. As a result SCR7^{H402} predominantly samples conformations with low predicted heparin association rate constants, while SCR7^{Y402} frequently samples conformations with high predicted rate constants. As heparin density changes with aging, this decreased pattern recognition in SCR7^{H402} may confer risk for developing AMD.

COMPLEMENT SYSTEM MODELS FOR C3 GLOMERULOPATHY AND THERAPEUTIC INTERVENTION

Nehemiah Zewde[1], Manuel Galvan[2] Mingjun Huang[2], Dimitrios Morikis[1]*

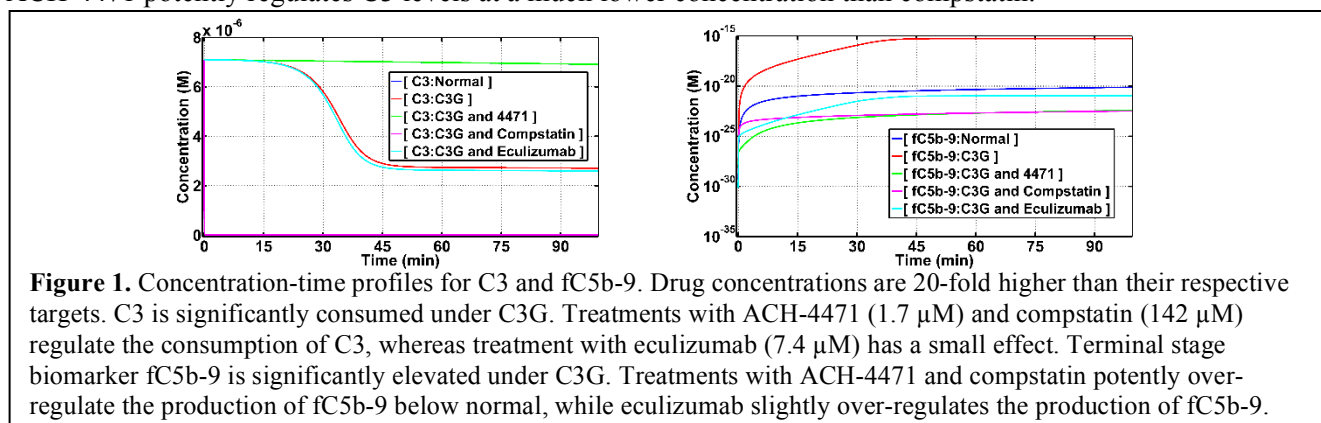[1]Department of Bioengineering, University of California, Riverside, CA, USA

[2]Achillion Pharmaceuticals, New Haven, CT, USA

Contact: *dmorikis@ucr.edu*

Introduction: The complement system plays a major role in the fight against microorganisms and removal of impaired host-cells. Activation of the complement system is balanced under homeostasis by various mechanisms including negative regulators such as Factor H (FH) and FH-like protein 1 (FHL-1) that prevent its uncontrolled activation and hence protecting healthy host cells from damage. Impairment of complement regulation tilts the homeostasis balance in favor of over-activation that leads to autoimmune and inflammatory diseases. C3 glomerulopathy (C3G) is one example where the disease manifests in glomerulus due to the dysfunction of complement regulation. Although it is widely known that the hallmark of C3G is the dysregulation of alternative pathway (AP) of the complement system, there is a lack of a systems level understanding on how perturbations of complement regulators lead to C3G. Here, we present a model of AP dysregulation for C3G that is based on previous mathematical modeling of complement system that includes activation, propagation, regulation/dysregulation, and termination [1,2].

Materials and Methods: Our mathematical model is composed of 290 ordinary differential equations (ODEs) with 142 kinetic parameters that describe the dysfunctional dynamics between complement activation and regulation for C3G. The disease state of C3G is generated by impairing the key complement AP regulators FH and FHL-1. We then perform a comparative assessment of the normal (homeostasis) state and C3G state by generating concentration-time profiles of key complement biomarkers C3, C3a-desArg, C5, C5a-desArg, Factor B (FB), Ba, Bb, and terminal assembly of fluid phase membrane attack complex (fMAC). Moreover, we evaluate the effect of complement inhibitors, ACH-4471 (an oral small molecule inhibitor of Factor D), compstatin (a peptide inhibitor of C3), and eculizumab (an antibody inhibitor of C5) at two concentrations, 1:1 and 20:1 drug to target ratio, in restoring the complement biomarker dynamics from the C3G state to the normal state.

Results and Discussion: We show that dysregulation of AP leads to consumption of complement proteins C3, C5, and FB, and consequently elevation of the cleavage products, C3a-desArg, C5a-desArg, Ba, and Bb, and terminal assembly of fC5b-9 (Fig. 1). Treatment with ACH-4471 and compstatin regulate early and terminal stage biomarkers, C3a-desArg, Ba, and Bb, C5a-desArg, and fC5b-9, compared to eculizumab that regulates only terminal stage biomarkers, C5a-desArg and fC5b-9. The results indicate that the degree of restoration to the normal state from the C3G state depends on the point of inhibition and drug/target concentration ratio and ACH-4471 potently regulates C3 levels at a much lower concentration than compstatin.

Figure 1. Concentration-time profiles for C3 and fC5b-9. Drug concentrations are 20-fold higher than their respective targets. C3 is significantly consumed under C3G. Treatments with ACH-4471 (1.7 µM) and compstatin (142 µM) regulate the consumption of C3, whereas treatment with eculizumab (7.4 µM) has a small effect. Terminal stage biomarker fC5b-9 is significantly elevated under C3G. Treatments with ACH-4471 and compstatin potently over-regulate the production of fC5b-9 below normal, while eculizumab slightly over-regulates the production of fC5b-9.

Conclusions: Overall, our data are in agreement with the complement serological profile in clinical C3G population, and our model suggests that inhibitors targeting at the early stage of complement cascade may be sufficient for restoring the dynamics of all biomarkers.

References: [1] Zewde N, Gorham RD Jr, Dorado A, Morikis D (2016) Quantitative modeling of the alternative pathway of the complement system, *PLOS ONE* 11:e0152337. [2] Zewde N, Morikis D (2017) A Computational Model for the Evaluation of Complement System Regulation under Homeostasis, Disease, and Drug Intervention. *bioRxiv* 225029.

MATHEMATICAL MODELING OF HEREDITARY ANGIOEDEMA

[1]Rohaine Hsu, [1]Nehemiah Zewde, [1]Dimitrios Morikis
[1]Department of Bioengineering, University of California, Riverside, CA
Contact: *dmorikis@ucr.edu*

Introduction: Hereditary angioedema (HAE) is a rare genetic disorder that affects 1 in 10,000 to 1 in 50,000 people. Episodes of swelling occur in multiple parts of the body, such as in the hands, feet, airway, and gastrointestinal tract. It is an autosomal dominant hereditary disease with 75% of cases due to genetic history, whereas 25% are due to a random mutation [1]. HAE is associated with components of the classical pathway of the complement system. The complement system is part of the innate immune system that functions as a defense mechanism against foreign pathogens, but also contributes to inflammatory and autoimmune diseases when self-regulation is failing. Complement components C1-Inhibitor (C1-INH) and C4 are used as clinical diagnostics for HAE. HAE Type I, affecting 85% of patients, is associated with low levels of C1-INH and C4 concentrations. Type II, affecting 15% of patients, has normal or elevated levels of C1-INH concentration, and low levels of C4 concentration. However, C1-INH is dysfunctional due to mutations affecting the reactive center loop in the SERPING1 gene. The functional activity of C1-INH in type II is low [1, 2].

Materials and Methods: A system of ordinary differential equations representing biochemical reactions of the classical and alternative pathways of the complement system was used to mathematically model HAE Type I [3, 4]. Different levels of C1-INH concentration were tested in the model to observe the behavior of other complement components. The concentration of C1-INH at homeostasis was considered the normal state. The initial concentration of C1-INH was then modified at various percentages, 50%, 30%, 20%, 10%, 5%, and 0% to simulate HAE Type I (Figure 1A). Concentration-time profiles for complement components were generated.

Results and Discussion: For HAE Type I patients, low levels of C1-INH concentrations range from 5% to 30% of normal concentration (Figure 1A) [5]. Clinical diagnostics define a lower normal level of C4 concentration to be 0.68μM [6, 7]. Our model shows that for concentrations of 0% to 30% of normal C1-INH, the concentration of C4 is below its normal range (Figure 1B). For 0% to 20% of normal C1-INH concentration, abnormal levels of C4 concentration are apparent at short time scales, whereas longer time scales (i.e. >2000 min) are needed to generate abnormal levels of C4 at 30% of normal C1-INH concentration.
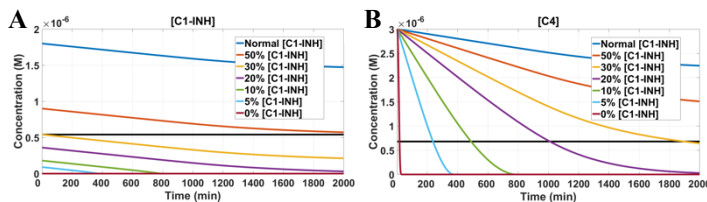
Figure 1: (A) Concentration-time profiles of C1-INH for different initial concentrations with respect to normal. Low levels of C1-INH for HAE Type I are below 0.54μM, 30% of normal C1-INH concentration (horizontal line). **(B)** Concentration-time profiles of C4 for different initial C1-INH concentrations. Normal levels of C4 concentration are above 0.68μM (horizontal line).

Conclusions: Our model shows that low levels of C1-INH concentration result to low levels of C4 concentration. When C1-INH concentrations are 0% to 30% of its normal concentration, C4 concentrations fall below its normal range. The results of the mathematical model are in agreement with clinical diagnostics for HAE Type I [5]. Modeling HAE Type II is ongoing. Our mathematical model can serve as the basis for the development of a computational diagnostic tool for disease state and progression, tailored to patient-specific clinical data.

References: [1] US Hereditary Angioedema Association – The Disease https://www.haea.org/HAEdisease.php. **[2]** Piñero-Saavedra M, González-Quevedo T. The genetics of hereditary angioedema: A review. J Rare Dis Res Treat. 2017;2(4):14–19. **[3]** Zewde N, Gorham RD Jr, Dorado A, Morikis D. Quantitative Modeling of the Alternative Pathway of the Complement System. PLOS ONE. 2016;11(3): e0152337. **[4]** Zewde N, Morikis D. A Computational Model for the Evaluation of Complement System Regulation under Homeostasis, Disease, and Drug Intervention. bioRxiv. 2017. doi:10.1101/225029. **[5]** Johnston DT. Diagnosis and Management of Hereditary Angioedema. J Am Osteopath Assoc. 2011;111(1):28–36. **[6]** Complement C4 – https://www.labcorp.com/test-menu/23021/complement-csub4-sub. **[7]** Arlaud, GJ, Colomb, MG. Complement: Classical Pathway. In eLS, (Ed.). 2001. doi:10.1038/npg.els.0000510.

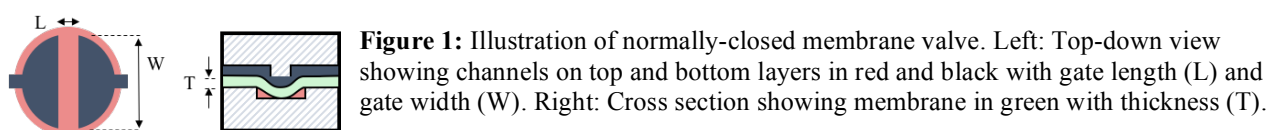# HIGH DENSITY NORMALLY CLOSED ELASTOMERIC MEMBRANE VALVES FOR MICROFLUIDIC DIGITAL LOGIC

[1]E.M. Werner, [1]E.E. Hui

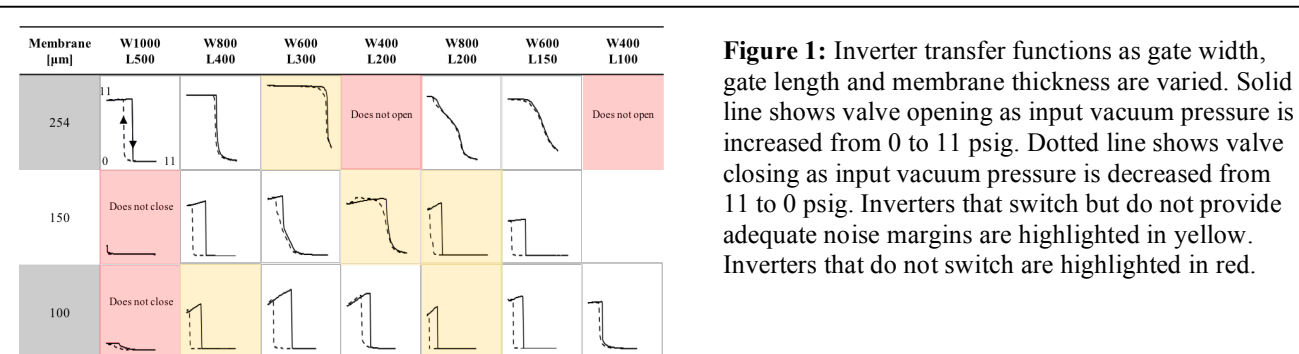[1]Department of Biomedical Engineering, University of California, Irvine, CA

Contact: *eehui@uci.edu*

Introduction: Microfluidic logic can reduce the off-chip instrumentation required to operate lab-on-a-chip devices, but the complexity of such systems has been limited by the relatively large size of individual logic gates. We present normally closed elastomeric membrane valves that occupy less than one third of the area of previously reported miniaturization efforts [1] and demonstrate their suitability for use in microfluidic digital logic circuits. Past examples of logic circuits built with these valves were limited by their large size and low speed of operation [2]. In previous work, micro milling was used to reduce logic gate size. Valve diameter and aspect ratio were optimized, but the minimum valve diameter was ultimately limited by the thickness of the membrane. In this study, we investigate valves fabricated with thinner membranes and specifically control for gate length while varying aspect ratio.

Materials and Methods: Pneumatic inverter gates were fabricated from an elastomeric sheet sandwiched between two pieces of patterned plastic as previously described [1]. Valve gate width was varied from 1000 to 400 μm, with a gate length of either 0.5 or 0.25 times the gate width (Figure 1). Chips were assembled using commercially available silicone membranes with a thickness of 254 μm (Bisco HT6240), 150 μm, or 100 μm (Silpuran 2030). Inverter transfer functions were collected by sweeping input vacuum from atmospheric pressure to 11psig and back. Each point on the transfer function curve was measured at steady state.

Figure 1: Illustration of normally-closed membrane valve. Left: Top-down view showing channels on top and bottom layers in red and black with gate length (L) and gate width (W). Right: Cross section showing membrane in green with thickness (T).

Results and Discussion: Our results show that valves with larger gate widths fail to completely close when the membrane is too thin, while valves with smaller gate widths fail to open when the membrane is too thick (Figure 2). Thinner membranes allow sufficient noise margins at smaller gate widths, allowing us to shrink the valve of a logic gate without compromising logic function. While inverters with membranes thinner than 100 μm were successfully fabricated and operated, hand-assembly was unreliable and fabrication methods should be improved for robust logic circuit function with membranes thinner than 100 μm.

Figure 1: Inverter transfer functions as gate width, gate length and membrane thickness are varied. Solid line shows valve opening as input vacuum pressure is increased from 0 to 11 psig. Dotted line shows valve closing as input vacuum pressure is decreased from 11 to 0 psig. Inverters that switch but do not provide adequate noise margins are highlighted in yellow. Inverters that do not switch are highlighted in red.

Conclusions: Decreased valve size and the coinciding increase in speed of operation will support more capable and more complex control logic integrated into lab-on-a-chip devices.

References: [1] P. N. Duncan, S. Ahrar, and E. E. Hui. Lab Chip, 2015, 15, 1360–1365. [2] W. H. Grover, R. H. C. Ivester, E. C. Jensen, R. A Mathies. Lab Chip, 2006, 6, 623-631.

CHARACTERIZING HYDROGELS WITH VIBRATING TUBE MASS SENSORS

S.V. Kardani, H.C. Bhakta, and W.H. Grover
Department of Bioengineering, University of California, Riverside, CA
Contact: *wgrover@engr.ucr.edu*

Introduction: Hydrogels are a type of biomaterial that has gained momentum over the past decade because of their unique properties that make them similar to biological tissue. The hydrophilic skeletal structure can be designed to release solution on demand in response to certain chemical, environmental, or physical stimuli. Utilizing these principles, hydrogels are currently being used as drug delivery systems to release drugs within the body at specific locations. Although hydrogels are used in many applications, there are several drawbacks to current analysis techniques that require physical property measurements like mass, volume, and density of the skeletal material. Conventional techniques require expensive equipment along with a large sample size to be able to be measured on a laboratory scale. Previously, our lab developed a sensor that can measure the mass, volume, and density of objects with microgram precision in liquid environments (Figure 1A). The sensor is a glass tube that vibrates at its natural resonance frequency, which is inversely proportional to its mass (Figure 1B). [1] In this work, we developed a technique to directly measure hydrogel characteristics without altering the physical structure of the hydrogel itself.

Methodology: The buoyant mass measured in the vibrating tube mass sensor is a function of the differences in densities between the fluid inside the tube and the density of the object flowing through it. Because the density of the fluid within the porous hydrogel is the same, only the buoyant mass of the material is measured. With an additional buoyant mass measurement using a different fluid with known density, we can calculate the apparent mass, volume, and density of the hydrogel's skeletal material as shown in Figure 1B. As a proof-of-concept, we used commercially available agarose powder to make hydrogel samples varying in concentrations from 1.5% to 2.5%. Each hydrogel is passed through the tube while immersed in water first then deuterium oxide (D_2O; 1.10 g/mL) as the secondary fluid. The samples are passed back and forth every thirty seconds through the vibrating tube sensor for 100 passes.

Results and Discussion: Buoyant mass measurements of agarose hydrogels were measured using the vibrating tube mass sensor in H_2O and D_2O. With the known fluid densities, and buoyant mass measurements, dry mass, dry volume, and dry density can be calculated. Figure 1C shows example data of dry density measurements collected in our sensor. As expected, we noticed similar dry density measurements throughout all concentrations.
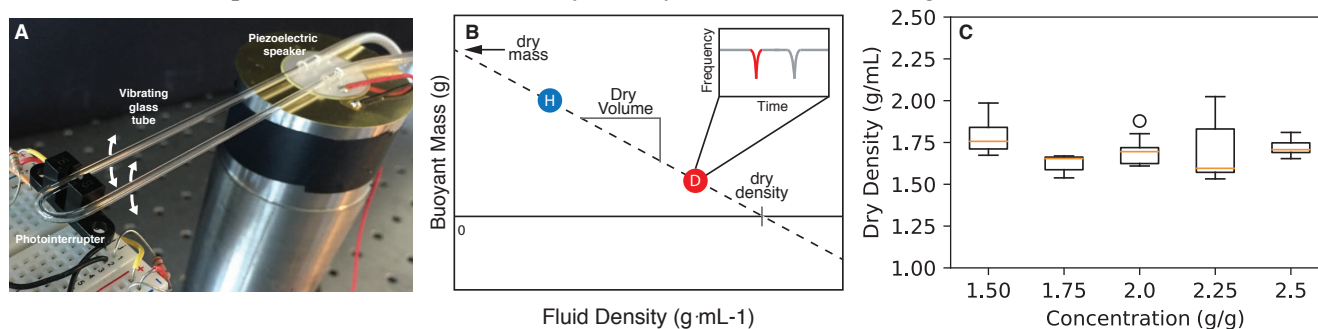
Fig 1. (A) A glass tube is bent into a "U" shape and is vibrated at its natural resonance frequency. The frequency is inversely proportional to the buoyant mass of an object. (B) With two buoyant mass measurements in different fluid densities, the dry mass, volume, and density can be calculated. (C) Agarose hydrogel measurements show consistent dry density values for all concentrations as expected.

Conclusion: The technique can drastically improve the quality of hydrogel characterization data. Our method solves both issues by making these measurements without the drying the hydrogel and maintaining its structural integrity while reducing sample size because of the microgram resolution of our sensor. In this manner, our method should accelerate the development of novel hydrogels for important applications in agriculture, drug delivery, and biomaterials.

References:
1. Shirin Mesbah Oskui, Heran C. Bhakta, Graciel Diamante, Huinan Liu, Daniel Schlenk, and William H. Grover. PLOS ONE 12 (4): e0174068 (2017).

THE DEVELOPMENT OF A NOVEL OSMOMETER FOR THE STUDY OF MACROMOLECULAR CROWDED ENVIRONMENTS

Ramsey Batarseh, Christopher S. Hale, and Victor G. J. Rodgers
Department of Bioengineering, University of California Riverside
Contact: rbata001@ucr.edu

Introduction: Many cellular systems contain high concentrations of proteins in solution, but their interactive behavior in concentrated or crowded conditions remains nebulous. While these systems tend to be difficult to model, their osmotic pressure, when deciphered properly, can be used to determine the interactions and properties of the system components.

The current method for obtaining osmotic pressure data is through an osmometer.[1] Consisting of two chambers, a protein chamber and a solvent chamber separated by a semi-permeable membrane, an osmometer restricts the flow of proteins between the solutions while allowing solvent to flow freely. In order to create a pressure-concentration curve, solutions with various protein concentrations need to be evaluated. Unfortunately, due to the amount of protein needed and its related expense, there is a limited amount of literature of near saturation osmotic pressure data.

Methods: A novel concentrating osmometer has been developed based on this same 2-chamber concept, but with the ability to concentrate or dilute the protein solution. This allows for the drastic reduction of the amount of protein needed, and therefore the cost required to obtain a complete pressure-concentration profile of a protein or macromolecular crowded environment. Additionally, this device is able to reduce the time needed to obtain profiles from a few weeks to a few days. This device was then tested using bovine serum albumin (BSA) in 0.15 M NaCl to compare to conventionally obtained data.[2] The data was regressed upon (TableCurve 2D, Systat Software (San Jose, CA)) using the Free Solvent Model (FSM) to obtain hydration and ion binding. The FSM treats proteins with its bound salt (ion binding) and water (hydration) as a macromolecule. The osmotic pressure of the system is related to the mole fraction of the unbound water in the solvent chamber over the unbound water in the protein chamber.[1]

Results: Figure 1 shows the data obtained from the concentrating osmometer compared to conventionally obtained data. Regressing on the concentrating osmometer data gave back a hydration of 1.33 ± 0.059 g g^{-1} and an ion binding value of 10.6 ± 0.95 mol mol^{-1}. Conventional osmometer data has a regressed hydration value of 1.11 ± 0.030 g g^{-1} and ion binding value of 7.7 ± 0.57 mol mol^{-1}.[1] Comparing these results, the concentrating osmometer hydration and ion binding values were found to be slightly higher but within reason.

Figure 1: Osmotic pressure data obtained from the concentrating osmometer compared to conventional osmometer data. The Free Solvent Model (FSM) has been fitted to each respective of set to obtain hydration and ion binding values.[2]

Conclusion: We observe a magnitude of order reduction in the amount of protein and time required to obtain a complete pressure-concentration profile. This translates to an even greater reduction in the cost associated with obtaining a profile.

[1]Yousef MA, Datta R, Rodgers VGJ. *AIChE J.* 2002; **48**:913-917.
[2]Vilker VL, Smith KA. *J. Colloid Interface Sci.* 1981; **79(2)**: 548-566.

DEVELOPMENT OF TITANIUM-BASED STENTS
FOR TREATING CORONARY HEART DISEASE

[1*]B. W. K. Woo, [2*]C. Roach, [1]K. Mensink, [1]R. A. Peck, [1]D. Z. Ashby, [12]S. N. Mathaudhu, and [123]M. P. Rao

[1]Department of Mechanical Engineering, University of California, Riverside, CA
[2]Materials Science and Engineering Program, University of California, Riverside, CA
[3]Department of Bioengineering, University of California, Riverside, CA
Contact: *mprao@engr.ucr.edu*
*Contributed Equally

Introduction: Coronary heart disease has been recognized as the leading cause of mortality around the world. Although stenting has become the standard of care for the treatment of coronary artery disease, serious adverse responses such as restenosis and late stent thrombosis continue to challenge its safety and efficacy.

Rational design of nanoscale stent surface topography (i.e. nanopatterning) may provide a new means for addressing these issues by facilitating, rather than delaying, healing. Using our novel titanium deep reactive ion etching technique, we have previously demonstrated the fabrication of planar Ti substrates patterned with precisely-defined nanoscale surface gratings, which have been shown to promote significant enhancement of endothelial cell response *in vitro*. We have also demonstrated the ability to incorporate these structures onto the surfaces of Ti-based stents that are compatible with balloon catheter deployment.

Despite these successes, one of the key remaining challenges is the relatively low strength of commercially pure (CP) Ti which may yield devices that are unable to resist vascular recoil and/or maintain sufficient wall apposition. Herein, we report our efforts to address this limitation through exploration of a severe plastic deformation technique known as high-pressure torsion (HPT) processing for material strength enhancement.

Materials and Methods: Samples (10 mm in diameter and 1 mm thick) were obtained from CP Grade 1 and Grade 2 Ti substrates via wire electrical discharge machining. After removing redeposited brass, samples were processed with 1, 2, and 4 turns of HPT under 1 and 2 GPa of pressure, and then polished down to 1 um diamond slurry and colloidal silica. Each sample was then analyzed with x-ray diffraction for composition and phase identification. Finally, Vickers hardness testing was performed to evaluate processed materials' strength versus similarly polished CP Ti that did not undergo HPT.

Results and Discussion: Pressure, purity, and number of turns were analyzed to optimize the HPT processing parameters for creating Ti substrates with enhanced strength. As illustrated in Fig. 1, HPT processing enabled a significant increase in Vicker's Hardness values from ~95 (unprocessed) to ~247 (Processed, Grade 1) kgf/mm^2, which represents an increase of ~160%.

Results of High-Pressure Torsion Processing
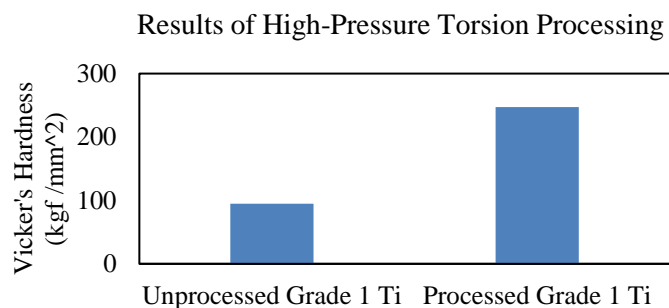
Figure 1: Vicker's Hardness values for commercially pure, grade 1 titanium processed through high-pressure torsion with 4 turns under 1 GPa of pressure. Unprocessed, grade 1 titanium included as a control.

Conclusions: Using HPT processing, we have demonstrated the ability to significantly enhance the material strength of our CP Ti substrates. This represents a considerable extension to our development of Ti-based cardiovascular stents by enabling CP Ti to compete as a viable material in devices that require higher material strength. Overall, these results represent important steps towards our goal of developing a new therapeutic platform where Ti-based stents, enhanced with HPT and nanopatterning, can be used to treat coronary artery disease without the need for pharmacological interventions.

DEVELOPMENT OF A TRANSORAL ROBOTIC SURGERY TRAINING PLATFORM

[1]R. Geoghegan, [2]A. Singh, [1]T. Le, [1]W. Grundfest and A. Mendelsohn[3]
[1]Department of Bioengineering, University of California, Los Angeles, CA
[2]Department of Mechanical Engineering, University of California, Los Angeles, CA
[3]Department of Head and Neck Surgery, University of California, Los Angeles, CA
**Contact:** rory.geoghegan@ucla.edu

Introduction: Transoral Robotic Surgery (TORS) provides a minimally invasive method of resecting pharangeal and laryngeal tumors. Given the relatively tight confines of the aerodigestive tract, an effective training program is critical to the successful adoption of TORS in head and neck surgery. Currently, TORS training utilizes animal and cadaveric models due to the lack of an appropriate dry lab training platform. We aimed to develop an anatomically accurate training platform to simulate tumor resection from the base of the tongue while recording force application to sensitive structures.

Materials and Methods: 3D modelling software (Meshmixer, Autodesk, CA) was used to create a model of the human head including the aerodigestive tract. The model was designed to enable integration of a force sensing system and synthetic tissue. A 3D printer (Series 1 Pro, Type A Machines, CA) was used to manufacture the physical model from polylactic acid filament. Normal force sensors (FlexiForce A101, Tekscan, MA) were integrated into the model via a magnetic mounting system enabling force measurement from the upper and lower back molars, lips and tongue. Data from the sensors is recorded using a microcontroller (Arduino Due, Arduino LLC, Italy) and custom designed software. The tumor model consists of a 10 mm silicone ball implanted into synthetic tissue (LifeLike BioTissue, Canada). This model is housed in a removable cartridge to facilitate rapid setup between training sessions. Preliminary testing was performed using the Da Vinci surgical system (Intuitive Surgical Inc., CA) to resect the synthetic tumor while recording force application to the upper and lower back molars, lips and tongue.

Results and Discussion: Figure 1 shows the training platform during testing with the Da Vinci surgical system. The user was able to visualize and resect the tumor model from the synthetic tissue using a Maryland grasper and curved scissors (Fig. 2). The training platform was found to provide an environment that mimics both the appearance and physical constraints of the aerodigestive tract. Moreover, force application on each sensor was successfully recorded. Surgical performance can be evaluated using this data and a recording of the training session. The sensor data is particularly useful for assessing instrument collision with sensitive structures outside the field of view provided by the Da Vinci camera.
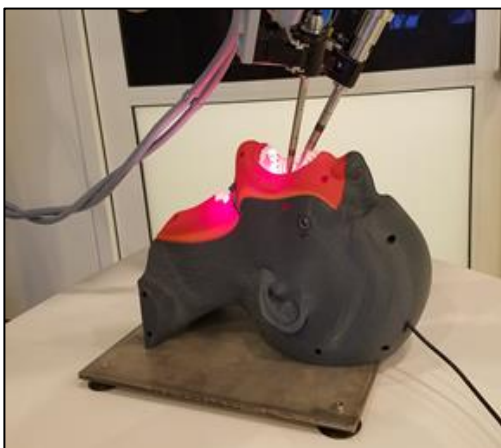
Fig 1: The Da Vinci surgical system operating on TORS Training Platform
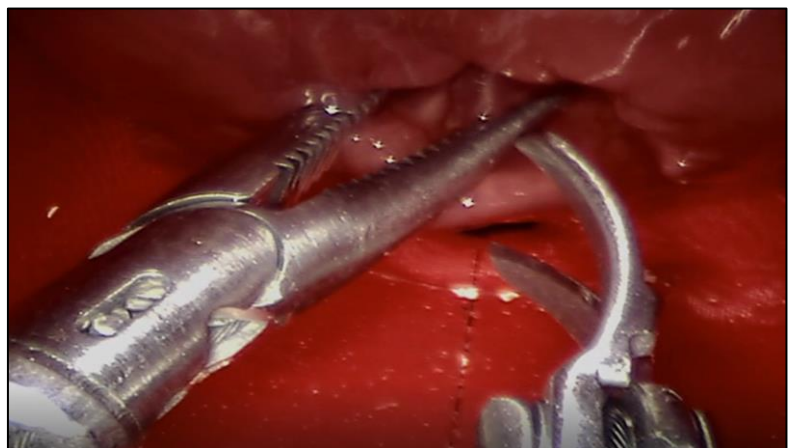
Fig 2: Tumor resection with a Maryland grasper and curved scissors

Conclusion: We have developed a novel training platform to facilitate the acquisition of TORS-specific skills. Future work will include integration of a real-time feedback system and a critical assessment of the overall utility of this platform as part of a surgical training program.

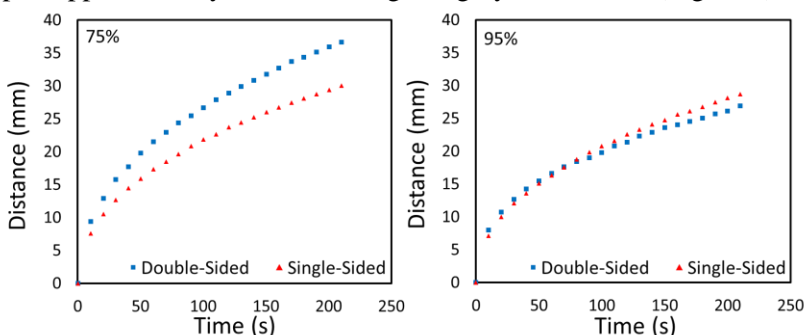# MODIFING WICKING SPEEDS IN SINGLE- AND DOUBLE-SIDED LASER-ETCHED PAPER-BASED MICROFLUIDIC CHANNELS

Brent Kalish, Mick Kyle Tan, and Hideaki Tsutsui

Department of Mechanical Engineering, University of California, Riverside, CA

Introduction: in recent years, paper-based microfluidics has become an increasingly attractive platform to develop diagnostic devices. Lateral flow devices are the most basic devices, where liquid wicks from one end to the other, where a qualitative or semi-quantitative color change is displayed. These devices are suitable for simple detections; however, for more complex reactions, different, more complex device architectures are required. These often involve the sequential delivery of reagents or wash buffers to different reaction zones. Much of the research into flow control on paper has focused on introducing delays to slow the wicking of certain liquids or channels. Delays are not ideal for all devices, as small sample volumes can be particularly susceptible to volume loss due to evaporation. The present study demonstrates the use of a CO2 laser to etch the surface of the paper to achieve both increases and decreases in wicking speeds over unetched paper. The degree of etching, controlled by the grayscale value of the image rastered onto the paper, dictates the overall impact on the paper's wicking speeds.

Materials and Methods: All channels were patterned and etched using a 30W CO_2 laser (Epilog Zing 16) onto Whatman #1 Chromatography and Whatman Grade 1 Filter paper. The laser raster settings were 13% power, 45% speed, 500 dpi, and Floyd-Steinberg dithering and the vector settings were 7% power, 60% speed, and 5000 Hz. Double-sided channels were etched on one side of the paper and then flipped over and etched and cut out. Wicking experiments were performed in a humidity-controlled chamber kept at 55% RH and 23°C. DI water was used as the wicking fluid and all channels were 3 mm wide. Mass loss measurements were taken by measuring the mass of 5 cm by 5 cm squares etched at each grayscale value.

Results and Discussion: In both papers, the fastest wicking speeds were found to be at 75-80% in both single- and double-sided channels. Wicking speeds decreased as the etching levels increased up until the highest grayscale values, 100%for single-sided and 95%for double-sided (double-sided channels disintegrated at 100%), which were dramatically slow than even the unetched channels. However, the difference in relative wicking speeds of the single and double-sided were greatest at 75and nearly identical at 95% (Figure 1). As expected, little mass was lost at low grayscale values, less than 2% at 50%, increasing up to approximately 38% at the highest grayscale values (Figure 2).

Figure 1: Wicking speeds of single- and double-sided 3mm channels etched at 75% and 95%. At low etching percentages, double-sided channels are much faster, but the difference decreases at higher percentages. N=3.
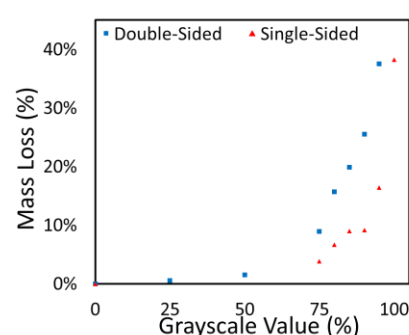
Figure 2: Mass loss of single- and double-sided 5cm squares of Whatman Chr 1. N=10.

Conclusions: This work details the use of laser etching as a means to control the wicking speed of liquids in paper-based microfluidic devices. Overall wicking times can be both increased or decreased depending on the degree and sidedness of the laser etching. Further research is required to develop a more complete understanding of the mechanism behind the changes in wicking speeds, which will in turn allow for more precisely tuned paper-based microfluidic devices.

FOUR MECHANISMS OF EVOLUTION AND THEIR IMPLICATIONS FOR BIOENGINEERING

H. Winet

Departments of Orthopaedic Surgery and Bioengineering, University of California, Los Angeles

Contact: *hwinet@g.ucla.edu*

Charles Darwin's theory that natural selection is the mechanism driving evolution of life on earth was the greatest discovery of science, according to James Watson, the co-discoverer of DNA's structure. The genes that the scientific world became aware of in 1900, after Darwin's death, had to be incorporated into his basic adapta-tion model to form a neo-Darwinian paradigm. Neo-Darwinism, like any scientific theory continues to evolve as data accumulates. It has spawned 3 more mechanisms, all gene-linked. The total of 4 are, with sample bioengi-neering implications:

1) ***Adaptation by natural selection***. Fecundity (production of fertile offspring) is the core event that defines suc-cessful adaptation. Each organism presents to its environment a phenotype that may or may not be fecund. If it is, its genotype is adapted for that environment, but only to the extent that the genes involved were necessary for achieving fecundity at the time it was being attempted. *Bioengineering implication*: Artificially bred organisms used for lab research have been removed from a selective environment, and their systemic adaptations (immunity, circulation, instinctive behavior, nervous system, endocrine system, etc.) that form feedback loops with each or-gan have not been allowed to respond to natural environmental pressures, being in a protected vivarium. These organisms may, accordingly, be poor predictors for the freer living humans they model. As a result, pre-clinical research data may be less relevant than those from wild species for studies of product efficacy. Safety study data would be less effected as toxicity tends to be easily detectable at the tissue level.

2) ***Non-adaptive mutation conservation***. Each genotype has genes that code or regulate structures or functions that do not contribute to natural selection. If these genes are conserved, by definition they cost the organism too little to affect its evolution. An example would be male nipples that are present in all male mammals. A subtler example, that may be adaptive only under certain circumstances, is redundancy. More than one structure may perform the same function. Two (or more) circulatory paths may supply the same organ, one being considered a collateral. More than one molecule may perform the same function. Initiation of production of inflammatory acute phase proteins can be performed by at least 5 different cytokines. *Bioengineering implication*: Engineers often assume that the organ/tissue/chemical they are studying is the only one performing a particular function. It is easy to reason from this premise that the performer is optimized for the function. Yet, there may be parts of the performer that are useless but cost it so little they are conserved. Also, the performer may have a redundant part-ner that serves as a backup when the main actor is injured. If an optimized system model is created upon which experiments are to be based, the falsely limited experimental design may yield irrelevant results. Also, patients needing personalized medicine may differ in the degree to which their regulator genes activate redundant struc-tures or functions. Ignoring their needs will reduce personalization.

3) ***Chromosomal recombination.*** The invention of sex about 550 million years ago accelerated evolution by al-lowing genes from two (or more) individuals to be mixed. A further source of variation was the ability of chro-mosomes to exchange parts, creating new gene combinations. Relocation of a gene to a new genotypic environ-ment affects its expression. This recombination form of gene redistribution may or may not be adaptive or con-served. It requires no new mutations to produce an unpredicted offspring genotype. *Bioengineering implication*: This could have a major impact on personalized medicine. Attempts to predict potential genotypes of offspring based on parental genotype will be less effective if chromosomal recombination is ignored.

4) ***Genetic drift***. This mechanism becomes evident where there is significant geographic isolation. The environ-ment may have a subtle effect on fecundity that appears only after many generations. The drift may be driven by accumulation of non-adaptive mutations that were accidently more plentiful at the time of geographic isolation. The Hardy-Weinberg Law has been used to measure this effect. *Bioengineering implication*: Medical devices for detecting (or treating) infectious diseases in third world countries may have to be recalibrated if there is genetic drift in the infectious agent such that a change in the critical epitope of its produced antigen propagates through the population. Models predicting the direction of such drift may have to be developed. Alternatively, one may frequently monitor genetic drift of the pathogen in each locality to detect Major Histocompatibility Complex I changes.

ERYTHROCYTE-DERIVED NANO-PARTICLES FUNCTIONALIZED TO TARGET EPHA2 RECEPTORS

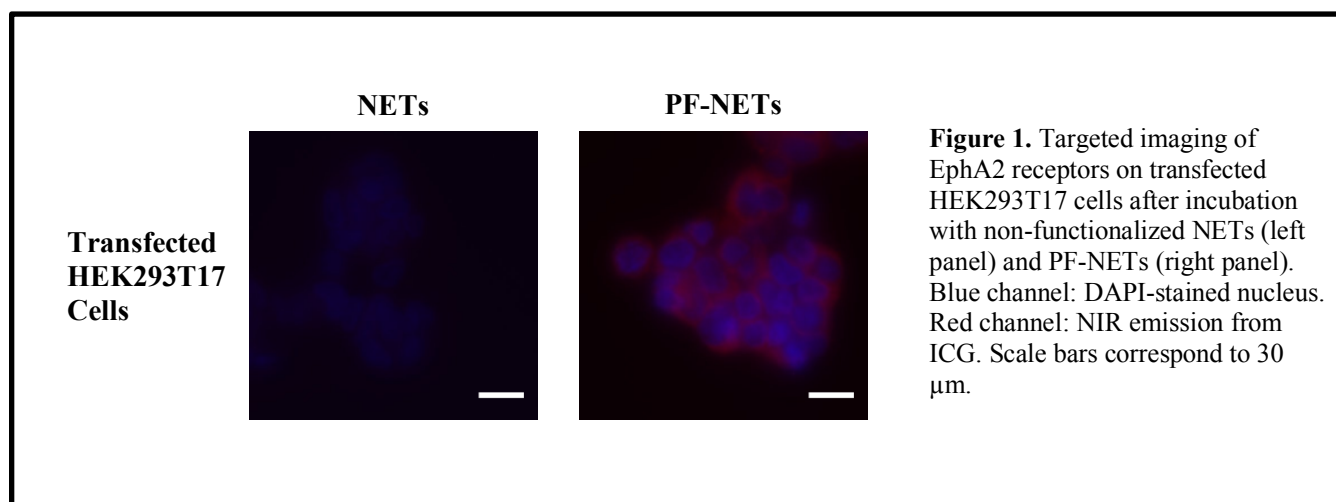[1]T. Hanley, [2]A. Farouk-Salem-Abdalla, [2]L. Gambini, [2]M. Pellecchia, and [1]B. Anvari
[1]Department of Bioengineering, University of California, Riverside, CA
[2]Department of Medicine, University of California, Riverside, CA
Contact: *anvarib@ucr.edu*

Introduction: Over-expression of the erythropoietin-producing human hepatocellular (Eph) receptors is associated with a variety of solid tumors [1]. We have engineered nanoparticles with the goal of targeting the EphA2 sub-class receptor for theranostic applications. These nanoparticles are derived from erythrocytes and doped with the FDA-approved near infrared (NIR) chromophore indocyanine green (ICG) [2], and are functionalized with a peptide to target the EphA2 receptors. We refer to these particles as peptide-functionalized NIR erythrocyte-derived transducers (PF-NETs). We present data demonstrating the successful targeting of PF-NETs to cells that over-express the EphA2 receptors.

Materials and Methods: PF-NETs were fabricated from hemoglobin-depleted erythrocyte ghosts (EGs). EGs were incubated with a PEG lipid linker, and then manually extruded to form nano-sized particles. These particles were then loaded with ICG in a hypotonic buffer, and subsequently functionalized with the peptide via a reductive amination reaction. Resulting PF-NETs were characterized by absorption and fluorescence spectroscopy, and dynamic light scattering. PF-NETs and non–functionalized NETs were incubated with HEK293T17 cells transfected with a lentivirus to induce overexpression of EphA2 receptors for 30 minutes at 4°C in the dark. Cells were then stained and imaged by fluorescence microscopy.

Figure 1. Targeted imaging of EphA2 receptors on transfected HEK293T17 cells after incubation with non-functionalized NETs (left panel) and PF-NETs (right panel). Blue channel: DAPI-stained nucleus. Red channel: NIR emission from ICG. Scale bars correspond to 30 µm.

Results and Discussion: Increased NIR emission was observed from the transfected HEK293T17 cells incubated with PF-NETs (Figure 1). These results suggest that PF-NETs were effective in targeted imaging of EphA2 receptors on transfected HEK293T17 cells.

Conclusions: We have successfully fabricated functionalized nanoparticles that can target and fluorescently image cells that overexpress EphA2 receptors. These nanoparticles present a potential platform for theranostic applications aimed at image-guided therapeutics that target the EphA2 receptors.

References: [1] S. Wang, W. J. Placzek, J. L. Stebbins, S. Mitra, R. Noberini, M. Koolpe, Z. Zhang, R. Dahl, E. B. Pasquale, M. Pellecchia, "Novel Targeted System To Deliver Chemotherapeutic Drugs to EphA2-Expressing Cancer Cells." J. Med. Chem. **55**, 2427-2436 (2012). [2] B. Bahmani, D. Bacon, B. Anvari, "Erythrocyte-derived photo-theranostic agents: hybrid nano-vesicles containing indocyanine green for near infrared imaging and therapeutic applications." Sci. Rep. **3**, 2180(2013).

VISUALIZING REAL-TIME CHANGES IN FORCE-DEPENDENT PROTEIN LOCALIZATION

[1]K. Jacobs and [1]S. Yamada
[1]Department of Biomedical Engineering, University of California, Davis
Contact: *syamada@ucdavis.edu*

Introduction: Cells constantly sense and respond to mechanical forces exerted by surrounding cells and their extracellular matrix through a biochemical process referred to as mechanotransduction. This response is thought to be crucial in regulating cellular functions and driving metastatic migration of cancer cells[1]. Thus, understanding these force dependent responses is of great interest to elucidate potential disease progression mechanisms. Since traditional methods do not allow for identification of force-dependent protein-protein interactions, these protein dynamics have not been extensively studied. Using an in situ proximal biotinylation approach, we are in the process of identifying force-dependent protein candidates surrounding zyxin, a force sensing protein that responds to mechanical stretch by interacting with actin stress fibers[2]. To visualize the real-time changes in subcellular localization of these candidates under mechanical strain, we developed cell substrate stretch devices to apply large strain while viewing the cells on a confocal microscope.

Materials and Methods: The microscope-mounted stretch device was fabricated using laser-cut acrylic and Delrin sheets, a servo motor, and a servo controller. The elastomeric stretch chambers were manufactured by laser cutting polydimethysiloxane (PDMS) and the PDMS membrane was attached by plasma bonding (Figure 1A). Madin-Darby Canine Kidney (MDCK) cells were plated, stretched for different stretch durations and magnitudes, and then fixed and stained for zyxin and phalloidin.

Results and Discussion: We systematically varied stretch magnitude from 20% to 40% to determine the optimal degree of stretch for a mechanosensitive response. The maximum stretch of the first generation of the device – 25% – did not yield a clear mechanosensitive response, however at 40% stretch, there was a clear localization of zyxin to actin stress fibers (Figure 1B). This response at a high degree of stretch may suggest that cells require even more exaggeration of mechanical forces to elicit a response than previously thought. We are currently revising the device to increase the magnitude of stretch to visualize the candidate proteins under these conditions.

Conclusion: A new generation of the cell stretch device that optimizes the degree of stretch that is required to induce a mechanosensitive response greatly simplifies the visualization of cells in force bearing conditions. Using this device combined with the biochemical screens, our approach will unravel the network of force-dependent protein-protein interactions within the cell.

Figure 1: Microscope-mounted cell stretch device and cell stretch experiment with MDCK epithelial cells. (A) Cell stretch device mounted on confocal microscope and image of device showing mechanical mechanism (pseudocolored). Arrows indicate direction of stretch. (B) MDCK cells uniaxially stretched. Zyxin colocalization with actin stress fibers increased following application of 40% stretch. Arrow indicates direction of stretch. Scale bar: 10μm

References:
1. Jaalouk, D. E. & Lammerding, J. Mechanotransduction gone awry. *Nat. Rev. Mol. Cell Biol.* **10,** 63 (2009).
2. Ueda, S., Blee, A. M., Macway, K. G., Renner, D. J. & Yamada, S. Force Dependent Biotinylation of Myosin IIA by α-Catenin Tagged with a Promiscuous Biotin Ligase. *PLoS One* **10,** e0122886 (2015).

THE EFFECT OF HEART'S MECHANICS ENVIRONMENT ON CELLS WITH THE LAMIN A/C MUTATION AND ITS RELATION TO HEART DISEASE

[1]R. Tran, [1]A. Ochs, [1]L. McCarthy, [2]C. Nguyen, [1]M. Siemens, [3,4]M. Zaragoza, [1]A. Grosberg
[1]Department of Biomedical Engineering, University of California, Irvine, CA
[2]Department of Neurobiology
[3]Department of Pediatrics, Division of Genetics & Genomics
[4]Department of Biological Chemistry

Introduction: Although mutations in the Lamin A/C (LMNA) gene can cause a variety of devastating diseases, the disease mechanisms are still unknown. Lamin A and C proteins play a crucial role in forming a meshwork under the nuclear membrane, providing the nucleus with mechanical integrity as well as interacting with other proteins for gene regulation. In this study, we have identified three unique families with variations of the LMNA mutation, which primarily results in the phenotype of heart disease. Despite having a LMNA mutation, these patients do not have symptoms like that in Hutchinson-Gilford progeria syndrome or Emery-Dreifuss muscular dystrophy where areas affected are more general like the skin and all muscles. It is a mystery why a mutation to the protein in every nucleus of the body in the case of these families manifests as a disease of only the heart. We hypothesized that the cyclic strain cardiomyocytes are constantly exposed to within the heart is an important factor that differentiates heart cells from others in the body. Thus, we predicted that non-contracting cells from these patients will be indistinguishable from cells originating from control populations unless they have undergone cyclic stretch.

Materials and Methods: In order to test this, a stretcher device was used to induce cyclic strain upon cells with and without the LMNA mutation. After culturing both static and stretch conditions in parallel, the cells were fixed, immunostained, images, and analyzed to collect variables such as nuclei defectiveness, nuclear eccentricity, and nuclear area.

Results and Discisson: Preliminary results indicate a difference in the phenotype presented by stretched cells from individuals with and without the LMNA mutation. For example, stretching generally causes increased eccentricity of the nuclei, but elongation was found to be greater in both stretch and static conditions for cells with the LMNA mutation when compared to those without.
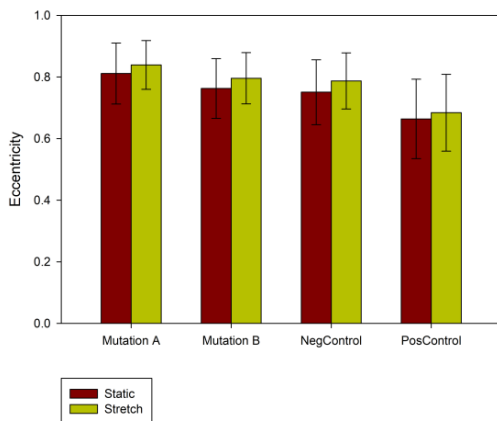
Figure 1: Eccentricity of the nuclei before stretch (red) and after stretch (yellow). All groups are significant to one another. Mutations A and B refer to the two different families with the LMNA mutation. The negative control contains both related and unrelated negative controls. Positive control refers to cells from a patient with Hutchinson-Gilford progeria syndrome.

Conclusion: Such changes to nuclear shape could be playing a role in gene expression regulation. Thus, there is a possibility that the unique mechanical environment of the heart affects cells with the LMNA mutation differently from those in the rest of the body.

DEVELOP A UNIVERSAL FRET TECHNOLOGY PLATFORM FOR QUANTITATIVE SYSTEMS BIOLOGY

Jiayu Liao[1,2,3,4,*], Zhehao Xiong[1,&], George Way[1], Vipul Madahar[1], Ling Jiang

[1]Department of Bioengineering, Bourns College of Engineering,[2]the Stem Cell Center, [3]Institute for Integrative Genome Biology and [4]Biomedical Science, University of California at Riverside, CA 92521,

Introduction: Systems Biology provides systematic and quantitative approaches to understand and monitor biological pathways, networks and even whole organisms. Traditionally, differential equation method has been widely used in systems biology to monitor a series of biological reactions or signal transduction cascades. However, in these differential equations, the kinetics parameters often come from various assays or hypothetic methods due to the lack of robust method(s) or an universal method to determine those parameters.

Materials and Methods: We have developed, for the first time, an universal method-quantitative Förster resonance energy transfer (FRET) assays, based on our new three-step absolute FRET signal analysis method, to determine various biological parameters. We used SUMOylation (small ubiquitin-like modifier or SUMO) as a model system to develop this novel methodology. The SUMO peptides covalently modifies proteins and regulates their activities in diverse cellular processes, such as signal transduction, cell cycle and DNA replication. The SUMO conjugation occurs through an enzymatic cascade of a series of ligases, E1, E2 and E3 after the SUMO peptides are matured from precursors by a family of SENP (Sentrin-specific) proteases. The SUMOylation cascade involves several common biological reactions, namely endopeptidase activity, isopeptidase activity, protein-protein interactions, enzyme-catalyzed transfer reactions and scaffold protein-involved catalyzed reactions. We labeled all the proteins in the SUMOylation cascade with FRET pair and determine kinetics parameters in each step reaction of the cascade.

Results and Discussion: We are able to determine K_ds of protein interactions in the SUMOylation cascade and K_{cat}/K_M of endopeptidase, isopeptidase and enzyme-catalyzed SUMO transfer reactions using one assay method-quantitative FRET. The results, coming from one assay method, are compatible in both measurement and variation.

Conclusions: An uniform assay platform based on quantitative FRET analysis has been developed to determine various biochemical reaction parameters in the SUMOylation cascade. The results from this uniform assay platform are compatible to each other with similar sensitivity and variation. This universal assay platform can provide a novel assay technology platform to determine reliable kinetics parameters for quantitative systems biology in a high-throughput mode.

Figure 1. Quantitative FRET assay platform to determine various biochemical kinetics parameters for quantitative systems biology. A. Fluorescence spectrum analysis to determine absolute FRET signal in three-step assay. B. SUMO1-Ubc9 protein-protein interaction K_d determination. C. Substrate CyPet-PreSUMO1-YPet digestions by SENP1(left) and K_{cat}/K_M determinations(right). D. Quantitative systems biology of SUMoylation cascade.

A LIGHT INDUCIBLE GENE ACTIVATION SYSTEM TOWARD CONTROLLABLE CELL-BASED THERAPEUTICS

[1]Ziliang Huang, [1]Yiqian Wu, [1]Yijia Pan, [1]Molly Allen, [1]Ya-Ju Chang, [1,2]Shu Chien, and [1,2]Yingxiao Wang

[1]Department of Bioengineering, University of California, San Diego, CA
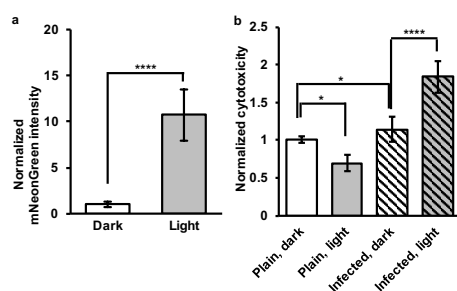[2]Institute of Engineering in Medicine, University of California, San Diego, CA

Contact: *yiw015@eng.ucsd.edu*

Introduction: T cells engineered to express chimeric antigen receptors (CARs) on cell surface can recognize and engage with target cancer cells with redirected specificity. This CAR T cell-mediated immunotherapy is under intensive investigation as a revolutionary therapy for cancer. However, adverse effects have been reported, including on-target off-tumor cytotoxicity, cytokine release syndrome and tumor lysis syndrome. One of the solutions is to engineer on/off-switchable cells to achieve high-precision control over their activation. Optogenetics utilizing genetically encoded dimerizers has been applied to remotely activate gene expression. Here, we developed a new blue light-mediated light-inducible nuclear translocation and dimerization (LINTAD) system for gene regulation to control cell activation, by integrating a LOV2-based light-inducible nuclear localization signal with CRY2-CIB1 dimerization. We demonstrated light-controllable gene expression and functional modulation in HEK 293T and Jurkat T cell lines. We further applied the LINTAD system in primary human CAR T cells and showed that the light-stimulated cells possessed a significantly stronger cytotoxicity against target cancer cells than the non-stimulated ones. We also extended the LINTAD system to activate the expression of the TNF-related apoptosis-inducing ligand (TRAIL) in HEK 293T cells, and observed a gain of cytotoxicity upon light stimulation. Therefore, our newly developed LINTAD system can serve as an efficient and general tool to remotely and non-invasively control gene activation in live cells for therapeutic applications.

Materials and Methods: Human peripheral blood mononuclear cells (PBMCs) were isolated from buffy coats (San Diego Blood Bank) using Ficoll gradients (Amersham Biosciences). For lentiviral transduction, cells were first activated for 72 h using 2 mg/L phytohemagglutinin (Thermo Fisher) in complete RPMI medium. The cells were then transduced with concentrated lentivirus at a MOI of 10 for each construct by spinoculation on Retronectin (Takara)-coated plates at 1,800 g, 32 °C for 1 h.

Results and Discussion: We have demonstrated that the LINTAD system can be used to control gene expression in HEK 293T and Jurkat cell lines (Figure 1a). Through delivering the LINTAD system into PBMCs, the activity/cytotoxicity of CAR-T cells can be controlled by blue light illumination (Figure 1b).

Figure 1: (a) Light-inducible mNeonGreen expression in HEK 293T cells transfected with LINTAD. Dark, without light treatment. Light, with 24 hr blue light illumination (n=20). (b) Light-inducible cytotoxicity of PBMCs. Plain, without infection. Infected, cells infected with LINTAD system. Dark, without light treatment. Light, with 24 hr blue light illumination. ($n = 9$).

Conclusions: In summary, we have developed a light-inducible gene activation system LINTAD by combining the light-inducible nuclear translocation and CIB1-CRY2 dimerization. We have demonstrated that LINTAD has high efficiency in controlling gene expression in mammalian cells, and that it can remotely and non-invasively regulate the activation of CAR T cells for cancer immunotherapy with high spatiotemporal precision.

PERIPHERAL NERVE LENGTHENING AS A METHOD FOR REGENERATION AND REPAIR

[1]H.M. Howarth, [2]A. Kadoor, [2]R. Salem, [2,3]E. Blevins, [2]M. Esparza and [1,2,3]S.B. Shah

[1]Department of Bioengineering, University of California, San Diego;

[2]Department of Orthopedic Surgery, University of California, San Diego;

[3] Research Service, Veterans Affairs San Diego Healthcare System, San Diego, La Jolla, CA
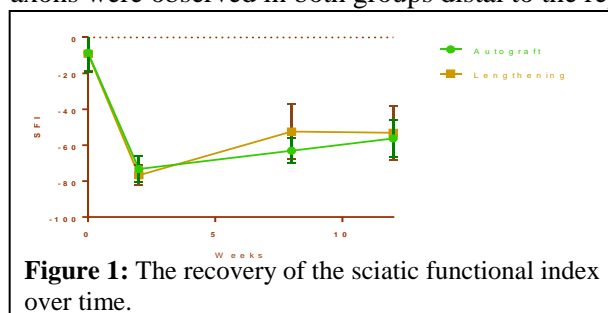
Contact: *sbshah@ucsd.edu*

Introduction: Individuals with peripheral nerve injuries often do not recover full sensorimotor function, especially for injuries of substantial severity or following delayed repair. For small nerve gaps (typically <20mm in a human or <2mm in a rat), an end-to-end repair is preferred, even under slight tension.[1,2] Autologous or synthetic grafts/conduits are used to bridge larger gaps, to eliminate tension at the site of repair.[3] However, because axons must grow into, through, and out of the graft to reach their targeted end organs, the efficiency of regeneration and functional recovery may be impaired. Instead, we propose the application of a novel device for gradual stretching of the proximal nerve stump towards the distal stump, to enable an end-to-end repair. This strategy builds on data that tensile loading accelerates the growth of axons.[4]

Materials and Methods: All animal experiments were approved by our Institutional Animal Care and Use Committee (IACUC). A 1cm gap was created in the sciatic nerve of Lewis rats (n = 16). In the autograft (gold standard) group (n = 8), the transected nerve segment was reversed and sutured to the proximal and distal stumps. Rats recovered for twelve weeks. In the experimental (device) group (n = 8), the proximal stump of the sciatic nerve was secured to the lengthening device, and the nerve was stretched 1 mm/day for two weeks. After stretching, the device was removed, nerve ends trimmed, and an end-to-end repair of the nerve was performed. Rats recovered for ten more weeks. During recovery, sciatic functional index (SFI) was measured at 2, 8, and 12 weeks after injury, using a digital gait analysis system (Treadscan). For tissue analysis, sciatic nerves and muscles innervated by the sciatic nerve were harvested at the terminal time point. Tissue was weighed and fixed in 10% formalin, followed by sucrose in 1X PBS. Tissue was then snap-frozen using liquid nitrogen cooled isopentane. 10 μm cross sections of nerve and muscle were immunolabeled using anti-laminin rabbit polyclonal antibody (Sigma-Aldrich) and anti-β-tubulin isotype III mouse monoclonal antibody (Sigma-Aldrich). Images were acquired using a Leica SP5 confocal microscope using 10X and 63X objective lenses. Differences between means were assessed using mixed two-way ANOVA (within factor: time; between factor: treatment). Tukey's HSD post-hoc test was used to compare individual means

Results and Discussion: In both groups, SFI improved over time after surgery (Figure 1), though not to pre-operative levels. While there was no significant difference in SFI between the device and autograft groups, there was significant improvement between two and eight weeks in the device group (p < .0001) but not the autograft group (p < .2316), suggesting improved recovery with nerve lengthening. Also, rats in the autograft group were more likely to display a contracture (7/8 in autograft vs. 3/8 in device with contracture), a feature confirmed by a significantly shorter paw length in autograft group compared to device group. Regenerated axons were observed in both groups distal to the repair site; preliminary data suggest more axonal growth into the peroneal branch of the sciatic nerve in the device group, which is consistent with reduced contracture.

Figure 1: The recovery of the sciatic functional index over time.

Conclusions: Nerve lengthening is a viable method for repairing large gaps in peripheral nerves. Nerve lengthening resulted in equal or better functional improvement compared to autograft groups, with reduced likelihood of contracture. This suggests a greater number and/or a more even distribution of axons into the branches of the sciatic nerve. In future studies, our approach will be extended to more complex injury scenarios in the future, including bridging of longer gaps and lengthening across nerve gaps after chronic nerve injury.

References :
1. Sunderland, IR et al. (2004). Ann Plastic Surg, 53(4), 382-387; 2. Hentz, VR et al. (1993). J Hand Surg (Am), 18(3), 417-425; 3. Vaz, KM et al. (2014). Neur Regen Res, 9(16), 1498; 4. Bray, D (1984). Dev Biol, 102(2), 379-389.

INFERRING STEM CELL PROTEIN EXPRESSION FROM DYNAMIC COLONY MORPHOLOGY USING MACHINE LEARNING ALGORITHMS

[1]A. Witmer, [2]B. Bhanu, [3]P. Talbot
[1]Department of Bioengineering, University of California, Riverside
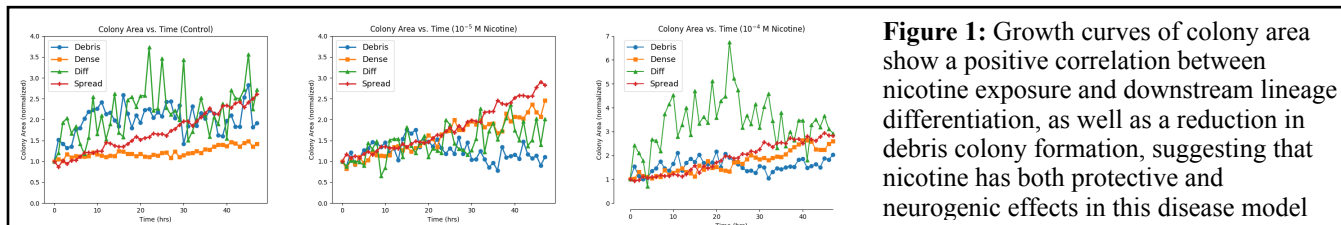[2]Department of Electrical and Computer Engineering, University of California, Riverside
[3]Department of Molecular and Systems Biology, University of California, Riverside
Contact: *adam.witmer@email.ucr.edu*

Introduction: The following abstract details collaborative works between the departments of Bioengineering, Electrical and Computer Engineering, and Molecular and Systems Biology, as well as a proposal for the continuation of the Ph.D thesis of Adam Witmer. These works center around the design of machine learning/ computer vision algorithms for the automated analysis of video microscopy data collected during stem cell toxicology experimentation. The goal of this work is to use deep convolutional neural networks (CCN) to determine the effects of cigarette and cigarette alternatives on human embryonic stem cell growth by modeling dynamic morphological features of stem cell colonies under toxic exposure. Motivation for this project stems from the need for unbiased, standardized quality control and analysis methods for stem cell projects involving live cellular microscopy. The need to characterize dynamic properties of colony development prohibits the use of invasive data collection techniques (i.e. fluorescent staining, genomic/proteomic profiling, flow-cytometry) via sacrifice of cell colonies. To date, two projects have been submitted as conference publications that address two problems relating to this issue: 1. classification of heterogeneous colony populations into homogeneous subclasses, and; 2. generation of synthetic data to supplement indispensable experimental data points. These projects, summarized below with supporting evidence, have provided insights into both the effects of toxicants on diseased stem cell colonies and the design of experimental protocol for the successful completion of the proposed projects.

Materials and Methods: Data for these projects comes from the laboratory of Dr. Prue Talbot in the form of time-lapse, phase contrast microscopy videos of induced pluripotent stem cells (iPSC) expressing the Huntington's disease phenotype. This data was collected to test the hypothesis that exposure to nicotine during culture has a neurogenic/-protective effect on the development of diseased iPSC development. It is noted that upon visual observation of colony growth over a 48 hour period, that pluripotent colonies begin to change towards downstream progenitor and differentiated lineages including neuron like formations. These projects address the need to automatically quantify changes that are difficult to determine using by-hand analysis methods.

Results and Discussion: For this purpose, a patch based classification method employing CNN is implemented to localize four morphologically homogeneous colony subtypes composing contiguous heterogeneous populations. Results suggest a positive correlation between concentration of nicotine exposure and overall increase in colony area classified as downstream lineages over time (Figure 1). Secondly, a synthetic dataset is generated using Generative Adversarial Networks (GAN) to supplement the number of real biological data points that must be irreplaceably used to train the CNN. It is noted that the addition of 500 synthetic images to a limited real dataset increases the confidence of a the classifier in its probabilistic predictions by 2% as well as slightly increasing the true positive rate of classification of real images.

Figure 1: Growth curves of colony area show a positive correlation between nicotine exposure and downstream lineage differentiation, as well as a reduction in debris colony formation, suggesting that nicotine has both protective and neurogenic effects in this disease model

Conclusions: Findings have proven the efficacy of CNN for the analysis of stem cell toxicology experiments and have influenced the synergistic design of cell culture and model based experimental protocols for the continuation of the thesis work. The goal of the proposed work is to track colony development and protein expression using only live cell colony morphology that is validated via proteomic profiling and immunocytochemistry. This work will be used to uncover the effects of cigarette toxins on underlying stem cell biology, and can be expanded to include other experimental protocols involving stem cells such as differentiation or therapeutic drug testing.

LOW-INTENSITY PULSED ULTRASOUND INCREASES COLLAGEN PRODUCTION IN BOVINE ANNULUS FIBROSUS CELLS

[1]D. Horne, [2]P. Jones, [2]M. Adams, [2]C. Diederich, [1]J. Lotz

[1]Department of Orthopaedic Surgery | [2]Department of Radiation Oncology, University of California, San Francisco, CA

Introduction: Low back pain (LBP) is the most common musculoskeletal condition, affecting 80% of the population at some point in their lifetime. Common causes of LBP include annulus fibrosus (AF) tears and herniations of the intervertebral disc (IVD). The standard treatment for IVD herniation is discectomy; however, the reherniation rate following discectomy is reported to be up to 21%, likely due to inefficient healing of the remaining AF defect. Oftentimes, surgeons opt to leave the AF defect to heal on its own. However, the IVD has limited healing capacity due to it being sparsely cellularized and having a poor blood supply.

Currently, there is no effective treatment to repair AF damage that effectively promotes tissue regeneration. Recently emerging biologic therapies, such as growth factor injection, have been introduced clinically with variable success. The primary limitations of these invasive intra-discal injection procedures are their sustainability and biological safety concerns. These findings indicate a clinical need for an effective noninvasive therapy for repairing annular defects.

Mechanical stimulation of IVD cells may be a safer therapeutic mechanism that could be used alone or in conjunction with other forms of biological treatments. It is well known that IVD cells respond to mechanical stimulation by increasing proteoglycan and collagen synthesis. Low-intensity pulsed ultrasound (LIPUS) is a mechanical stimulus that is potentially both noninvasive and regenerative. LIPUS has been shown to stimulate matrix metabolism in several cell types including IVD cells. However, the efficacy demonstrated in these *in-vitro* studies are highly variable and do not consider several confounding factors. Nonetheless, detailed descriptions of system characterization and LIPUS parameters are largely missing from published work. These deficiencies have likely contributed to the lack of experimental reproducibility and successful transfer to *in-vivo* conditions.

In this study, a custom LIPUS *in-vitro* exposimetry system was designed and characterized to mitigate potentially confounding factors including ultrasound beam inhomogeneity, beam reflections, and temperature rise within the target sample. This fully characterized system was used to test the hypothesis that collagen synthesis in annulus fibrosus cells can be increased by LIPUS mechanical energy.

Materials and Methods: Bovine AF cells were encapsulated in 1.2% sodium alginate beads at a density of 4×10^6 cells/mL. Twelve alginate beads per well (one sample) were cultured in 6-well plates with 3mL of supplemented DMEM. There were 12 total samples divided among 3 treatment groups: control, BMP-7, and LIPUS. The BMP-7 group received media supplemented with 200ng/mL of Human Bone Morphogenetic Protein-7 (BMP-7). The LIPUS group was exposed to a LIPUS waveform (1.5MHz frequency, 600mW/cm^2 spatial peak intensity, 1kHz pulse repetition frequency, and 20% duty) for 20 minutes each treatment day. To simulate the environmental conditions without LIPUS, control and BMP-7 samples were placed in the LIPUS exposimetry system for 20 minutes with the ultrasound turned off. All samples were cultured for 14 total days, with treatments taking place on 8 of the 14 days. On day 14, beads were collected and collagen content was evaluated by hydroxyproline assay.

Results and Discussion: BMP-7 treatment demonstrated greater total collagen per bead compared to control by 85.3% ($2.18 \pm 0.20\mu g$ vs $1.18 \pm 0.14\mu g$). LIPUS treatment demonstrated greater total collagen per bead compared to control by 98.2% ($2.33 \pm 0.26\mu g$ vs $1.18 \pm 0.14\mu g$). There was no significant difference between the BMP-7 and LIPUS groups.

Conclusions: The findings of this study provide evidence that LIPUS exposure can increases collagen production in bovine annulus fibrosus cells at a magnitude similar to BMP-7 treatment. These results suggest that LIPUS treatment may be an effective noninvasive therapy for enhancing IVD repair.

Figure 1: LIPUS and BMP-7 groups demonstrated greater total collagen compared to the control group (n=6). Collagen content was normalized by number of beads in well.

We never stop seeking

At Illumina, we are driven to know more—to relentlessly search for the answers that will advance the understanding of genomics to improve human health. And we realize we can't do it alone. We're counting on the next generation of scientific minds to help us keep up the momentum. As the leading developer of genomic solutions and services, we help accelerate genetic research and its use in the fields of cancer, hereditary disease, reproductive health, infectious disease, forensics, and agriculture. Together, we'll realize the promise of personalized medicine.

www.illumina.com/careers

Proud to be a supporting sponsor of the UC Bioengineering Symposium.

FOUNDED ON INNOVATION AND COLLABORATION

Innovation and collaboration are central to who we are. Since the late 1940s, we have been working with others to alleviate pain, restore health, and extend life.

Today, we are a medical technology leader offering therapies and solutions that enable greater efficiency, access, and value — for healthcare systems, providers, and the people they serve.

Medtronic
Further, Together
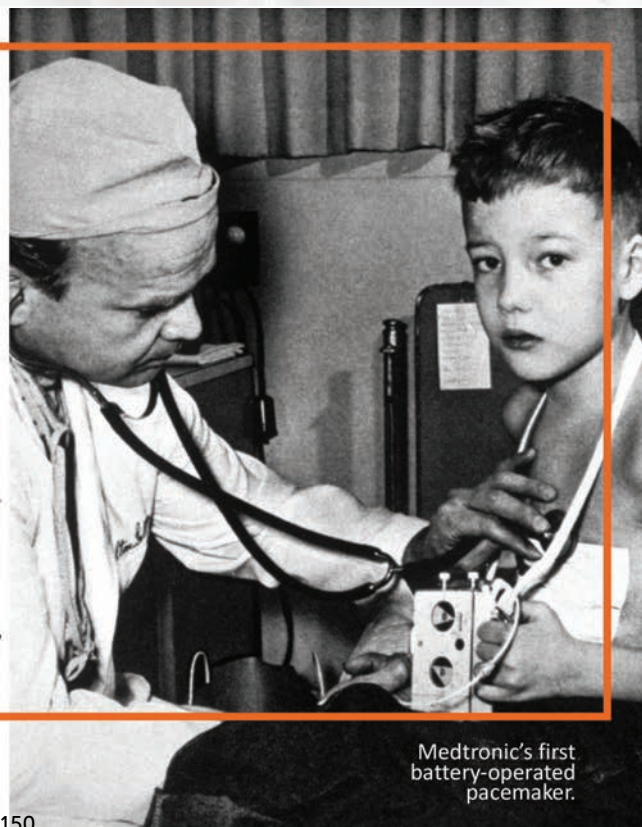
Medtronic's first battery-operated pacemaker.

Thank you to our Sponsors

We greatly appreciate the support from the following sponsors:

(**Bold** indicates oral presentation page number)

Symposium Organization Committee

Xiaoping Hu (Meeting Chair)

Joshua Morgan

Dimitrios Morikis

Victor G. J. Rodgers

Nancy Ford (Administrative Coordinator)

Angela Meluski (Marketing and Media Coordinator)

UCR

Marlan and Rosemary Bourns College of Engineering
Bioengineering

205 Materials Science and Engineering
900 University Avenue, Riverside, CA 92521
www.bioeng.ucr.edu | **(951) 827-4303**